Issues of Localized Corrosion in Additively Manufactured 316L Stainless Steel

---

A

Dissertation

Presented to

the faculty of the School of Engineering and Applied Science

University of Virginia

---

in partial fulfillment

of the requirements for the degree

Doctor of Philosophy

by

Duane Armell Tungpalan Macatangay

August 2022

APPROVAL SHEET

This

Dissertation

is submitted in partial fulfillment of the requirements
for the degree of

Doctor of Philosophy

Author: Duane Armell Tungpalan Macatanga

This Dissertation has been read and approved by the examing committee:

Advisor: Robert Kelly

Advisor:

Committee Member: Ji Ma

Committee Member: Gary Koenig

Committee Member: Bicheng Zhou

Committee Member: Richard Martukanitz

Committee Member:

Committee Member:

Accepted for the School of Engineering and Applied Science:

Jennifer L. West, School of Engineering and Applied Science

August 2022

Abstract

Additive manufacturing (AM) is a class of material fabrication methods that has exciting applications in the production of metal alloys such as austenitic stainless steels. In addition to opportunities in material and energy use reduction, the AM process offers opportunities in microstructure control and the refinement of mechanical properties such a strength, ductility, and toughness. AM processes such as laser powder bed fusion (LPBF) and direct energy deposition (DED) create materials with complex microstructures that tend to have spatial variations in composition. As works on AM corrosion are limited, there is a motivation to understand the electrochemical behavior of AM alloys such as 316L. This work is thus divided into three main parts:

(1) A holistic assessment of corrosion phenomenology in AM 316L

(2) An investigation of the effect of LPBF processing parameters on the corrosion behavior

(3) An investigation of intergranular corrosion and sensitization behavior of heat-treated LPBF 316L

The goal of the first part of this work is to gain a holistic view of understanding electrochemical behavior in AM 316L with particular emphasis on localized/selective corrosion due to the non-equilibrium microstructure of AM alloys. A range of testing environments were utilized from boiling acidic solutions to chloride solutions that induce pitting corrosion. Whether it is through the DED or LPBF process, local differences in elemental composition were observed to be a driving force for preferential corrosion. Distinctions were also able to be established in comparing the phenomenology between active and transpassive dissolution. Overall, it is it shown how local chromium and molybdenum differences drive preferential corrosion whether it is in respect to cellular dendritic structures in the LPBF material or ferrite in the DED material.

While the first part of the work emphasizes the effect of oxidizing behavior on AM corrosion morphology, the second part explores the effect of LPBF processing parameters on susceptibility to surface reactivation. The volumetric energy density (VED) was used as a tool to explore variations in LPBF processing. The double loop potentiokinetic reactivation (DLEPR) testing was used to make this comparison. While it was found that material printed at lower VED favored global reactivation, it was ultimately found that the VED alone cannot be used as a tool in predicting susceptibility to global reactivation. It was ultimately found that conditions that promote rapid solidification lead to materials that have greater susceptibility to reactivation such as materials printed at higher speed at constant VED.

Unlike the first two foci of the dissertation which explore corrosion in as-printed AM material, the third portion focuses on a phenomenon that is relevant to stainless steels exposed to elevated temperatures: sensitization and intergranular corrosion. Like the previous chapter, it was found that VED alone is not adequate to predict susceptibility to sensitization and intergranular corrosion. The deleterious effect of porosity and grain refinement is also established from this study.

The work performed in these studies are of scientific and technological importance. Stainless steels like 316L have diverse applications such as aerospace, naval, and biomedical. This diversity is also reflected in the range of standardized testing environments that are used in screening these alloys. This situation ultimately reflects a need to explore the electrochemical behavior of these materials. In the area of LPBF processing, this work is relevant as complement to other work that highlight the effect of processing on mechanical properties providing potential to gain a more holistic understanding of in-service performances of these alloys. As there is great

motivation to implement post-processing techniques that involve exposure at elevated temperatures, this work addresses a knowledge gap involving intergranular corrosion.

Acknowledgements

First and foremost, I want to thank my advisor Dr. Robert Kelly for really taking a chance on me and hiring me to do a very interesting project. Dr. Kelly was my MSE 2090 professor in 2014 and was impactful in starting me on the path to studying materials science and engineering. His dedication to teaching and mentoring has allowed me to grow not only as a researcher but an active member of the community. When I first started my PhD, there were very limited studies on the corrosion of additively manufactured alloys, and this was project was a learning curve for both of us and I could not have asked for a better advisor and colleague to tackle this challenge with. Dr. Kelly always empowered me and recognized my abilities even when my research frustrations got amplified by the stresses from a global pandemic.

I want to acknowledge my committee for putting in the time and effort in providing me with multi-faceted guidance on my research. The constructive criticism and interest conversations are greatly appreciated.

I want to thank ALL of the professors who served as my instructors during my undergraduate and graduate career at UVA MSE. Having been involved with the department since 2014, I think it is fair to say that a significant amount of my scientific background has been shaped by my interactions with my instructors. I believe that these interactions have allowed me to refine my ability to critically think and present information with confidence and finesse. I promise to always take and utilize these lessons in the next chapter of my life.

I want to acknowledge my friends and colleagues in the ~~third floor~~ Center for Electrochemical Science and Engineering. I want to thank fellow members of the Kelly group

(Utibe, Carolina, Pedro, Rebecca, Ryan, Victor, and Armando) for the productive (and sometimes intense) discussions about corrosion science. Our projects are insanely different from each other, but I have learned so much from everyone whether it is through discussions about my research or their research. I want to send a special shout out to Jeroen Deijkers for training me as an undergraduate research assistant and ~~coercing~~ encouraging me to applying for graduate school. I want to thank the students of UVA MSE for further broadening my knowledge and understanding of materials science. It is also critical that I acknowledge the individuals from my undergraduate years who I started this MSE journey with: Sama Mir, Jonathan Venezuela, and Jill Ferguson. I also want to acknowledge my friends from the chemistry department who have either helped refine my understanding of chemistry or gave me the chance to refine my ability to teach chemistry: Dr. Kevin Welch, Dr. Dave Metcalf, and Dr. Laura Serbulea. I also want to thank my professors in the Department of Biomedical Engineering for equipping me with the broad perspectives to analyze and solve problems from an engineering perspective.

I want to thank my family over at the East Rivanna Volunteer Fire Company for the level of support that they have provided me during my PhD degree. Like with my advisor, I am thankful for the level of trust that my captains placed upon me in letting me perform firefighting and emergency medical services for Albemarle County. This experience has improved my level of confidence in my abilities, and I believe it is fair to say that some of the technical skills I have learned as a volunteer first responder have been helpful in allowing me to refine certain tasks I have had to perform as a graduate research assistant. For example, knowing how to tie knots that are used in ladders came in very handy during my boiling acid experiments!

Lastly, I want to thank the ones closest to me for the amount of love and support that they have provided me during my graduate studies. I want to thank my parents and siblings for always

supporting me and making sacrifices to make sure that I have a high-quality education. I want to thank Nick, Baby, and Bean for always providing me with love and comfort even when the frustration of my research would get to me. Even though one of them likes to unnecessarily scratch and bite, I still love them. I want to further thank Nick for coming in the lab with me every now and then to help me with sample prep.

Table of Contents

surfaces depicted are oriented perpendicular to the build direction. The surfaces shown are oriented perpendicular to the build direction.

Fig. 5.9. Cross-sections of sensitized wrought material showing damange along the normal-rolling plane after testing in boiling sulfuric acid and ferric sulfate are shown (a) before and (b) after etching in Carpenter's etch. Cross sections for the transverse-rolling plane (c) before and (d) after etching are also shown.

Fig. 5.10. Cross-sections of sensitized LPBF material showing damage along the orientation perpendicular to the build direction after testing in boiling sulfuric acid and ferric sulfate for LPBF materials A1 (a) before and (b) after etching, A3 (c) before and (d) after etching, A8 (e) and (f) before and after etching, and A9 (g) before and (h) after etching.

Fig. 5.11. Graph depicting damage depth along the surface perpendicular to the build direction from cross sectional analysis as a function of measured of corrosion rate from the boiling sulfuric acid and ferric sulfate test for select LPBF materials. Damage depths are shown for the wrought material in the NT and NR plane.

Fig. 5.12. Scatterplot showing relationship between recorded DOS value from the DL-EPR test and the corrosion rate from the boiling sulfuric acid and ferric sulfate test.

List of Symbols

AM Additive Manufacturing

ASTM American Society for Testing and Materials

DED Direct Energy Deposition

DOR Degree of Reactivation

DOS Degree of Sensitization

GB Grain boundary

IGC Intergranular Corrosion

IGSCC Intergranular Stress Corrosion Cracking

LPBF Laser Powder Bed Fusion

SCE scanning calomel electrode

VED Volumetric Energy Density

To our future patients:

We got this.

1 Abstract

Additive manufacturing (AM) is a class of material fabrication methods that has exciting applications in the production of metal alloys such as austenitic stainless steels. In addition to opportunities in material and energy use reduction, the AM process offers opportunities in microstructure control and the refinement of mechanical properties such a strength, ductility, and toughness. AM processes such as laser powder bed fusion (LPBF) and direct energy deposition (DED) create materials with complex microstructures that tend to have spatial variations in composition. As works on AM corrosion are limited, there is a motivation to understand the electrochemical behavior of AM alloys such as 316L. This work is thus divided into three main parts:

(1) A holistic assessment of corrosion phenomenology in AM 316L

(2) An investigation of the effect of LPBF processing parameters on the corrosion behavior

(3) An investigation of intergranular corrosion and sensitization behavior of heat-treated LPBF 316L

The goal of the first part of this work is to gain a holistic view of understanding electrochemical behavior in AM 316L with particular emphasis on localized/selective corrosion due to the non-equilibrium microstructure of AM alloys. A range of testing environments were utilized from boiling acidic solutions to chloride solutions that induce pitting corrosion. Whether it is through the DED or LPBF process, local differences in elemental composition were observed to be a driving force for preferential corrosion. Distinctions were also able to be established in comparing the phenomenology between active and transpassive dissolution. Overall, it is it shown

how local chromium and molybdenum differences drive preferential corrosion whether it is in respect to cellular dendritic structures in the LPBF material or ferrite in the DED material.

While the first part of the work emphasizes the effect of oxidizing behavior on AM corrosion morphology, the second part explores the effect of LPBF processing parameters on susceptibility to surface reactivation. The volumetric energy density (VED) was used as a tool to explore variations in LPBF processing. The double loop potentiokinetic reactivation (DLEPR) testing was used to make this comparison. While it was found that material printed at lower VED favored global reactivation, it was ultimately found that the VED alone cannot be used as a tool in predicting susceptibility to global reactivation. It was ultimately found that conditions that promote rapid solidification lead to materials that have greater susceptibility to reactivation such as materials printed at higher speed at constant VED.

Unlike the first two foci of the dissertation which explore corrosion in as-printed AM material, the third portion focuses on a phenomenon that is relevant to stainless steels exposed to elevated temperatures: sensitization and intergranular corrosion. Like the previous chapter, it was found that VED alone is not adequate to predict susceptibility to sensitization and intergranular corrosion. The deleterious effect of porosity and grain refinement is also established from this study.

The work performed in these studies are of scientific and technological importance. Stainless steels like 316L have diverse applications such as aerospace, naval, and biomedical. This diversity is also reflected in the range of standardized testing environments that are used in screening these alloys. This situation ultimately reflects a need to explore the electrochemical behavior of these materials. In the area of LPBF processing, this work is relevant as complement to other work that highlight the effect of processing on mechanical properties providing potential

to gain a more holistic understanding of in-service performances of these alloys. As there is great motivation to implement post-processing techniques that involve exposure at elevated temperatures, this work addresses a knowledge gap involving intergranular corrosion.

2 Introduction

2.1 Background

2.1.1 The Additive Manufacturing of Metallic Alloys

Additive manufacturing (AM) is a family of 3-D printing techniques that allows for the creation of geometrically complex structures. Techniques such as laser powder bed fusion (LPBF) and direct energy deposition (DED) are forms of additive manufacturing in which materials are fabricated by melting and rapid solidification. 3-D printing takes place due to the occurrence of melting and solidification on a layer-by-layer basis allowing for the fabrication of geometrically complex parts that are not produced from conventional casting techniques[1–3]. Additive manufacturing also helps minimize the amount of post-process machining that is conventionally done with wrought alloys allowing for savings in material waste and energy use[4–7]. Multiple industries from aerospace to naval are currently looking into opportunities in using AM alloys [8–10].

LPBF and DED are two forms of additive manufacturing that have been applied to the fabrication of metallic alloys such as austenitic stainless, martensitic stainless steels, aluminum alloys, and many other systems [1,3,9]. During LPBF, a high energy laser is applied to a powder bed on a layer-by-layer basis to construct parts. In the case of DED, material in the form of wire or powder is melted with a focused energy source and is deposited by nozzle on a surface [3,9].

Enthusiasm over the development of additive manufacturing has led to copious amounts of studies across multiple alloy systems with emphasis on microstructure control and enhancement of select mechanical properties. SLM alloys of various alloys such as titanium, aluminum, and stainless steels have shown great refinement in mechanical properties such as ductility, strength,

hardness, and toughness[10–16]. The motivation to study AM materials is greatly enhanced due to improvements in these properties compared to those of conventionally wrought alloys. While the research in the mechanical properties is growing, corrosion studies are limited. It is well-known in the AM community that AM materials have non-equilibrium compositional heterogeneities in the microstructure[13,17,18]. The development of these structures in AM alloys provides motivation to investigate localized corrosion mechanisms.

2.1.2 Stainless Steel Metallurgy and Solidification

Austenitic stainless steels such as 304L and 316L have garnered attention in AM due to mechanical properties such as high strength and ductility[19–21]. 316L is a stainless steel that is nominally composed of the FCC austenitic phase. Table. 1 provides the composition of stainless 316L[22,23]. As with all steels, 316L is alloyed with carbon which contributes to solid solution strengthening. 316L, however, is designed to be a low-carbon stainless steel to mitigate issues such as grain boundary sensitization and intergranular corrosion. Nickel is added as an austenitic stabilizer which aids in the formation of the FCC phase. Manganese is also an austenitic stabilizer and helps in improving hot working properties, strength, and toughness[22–24].

Table 2.1 Nominal composition of 316L stainless steel [22]

Element	Fe	C	Mn	Si	Cr	Ni	Mo	P	S	N
Weight Percent	Bal.	0.030 max	2.00 max	0.75 max	16.00-18.00	10.00-14.00	2.00-3.00	0.045 max	0.030 max	0.10 max

Chromium and molybdenum are two alloying elements of great importance in the corrosion-resistant properties of steels such as 316L [24,25]. Stainless steels have a minimum chromium concentration of 16 wt.% due to the passivating effects of chromium[24]. In aqueous environments such as seawater, a Cr_2O_3 film forms and acts as a passive film[24]. However, too much alloyed chromium leads to the stabilization of the more brittle ferrite phase[24–27]. It is also

well-known that aggressive anions such as chlorides can result in passive film breakdown and result in forms of localized corrosion including pitting and crevice corrosion. Molybdenum improves resistance to pitting and crevice corrosion in chloride containing environments[25,28]. In environments that promote active corrosion such as acidic solutions, molybdenum has also been shown to decrease the uniform corrosion rate. Although chromium and molybdenum are known to improve corrosion properties in environments such as seawater, these alloys can be deleterious to the corrosion properties of these materials in environments that promote transpassive dissolution such as fuming nitric acid [29–31].

Fig. 2.1 depicts a thermodynamic phase diagram that is important in predicting the phase composition and the potential microstructure of austenitic steels like 316L. Using the orange line as reference for the 316L effective composition, it clear that the austenitic phase is the expected phase for these alloys at low temperatures though the presence of ferrite should not be surprising due to the stability at higher temperatures [32]. In the case of LPBF processing, rapid cooling from the liquid phase results in high cooling rates ($\sim \geq 10^5$ K/s) and small traces of ferrite have been observed due to the limited amount of time at high temperatures that would promote the formation of the ferritic phase [32–34]. Processes such as DED have lower cooling rates ($\sim 10^3 - 10^4$ K/s), creating for thermal conditions that may allow for the formation of the ferrite phase at high temperatures [34]. Multiple studies performed for DED materials have recorded the formation of skeletal and lathy ferrite such as that seen in traditional works on welding of stainless steel. Due to the compositional differences that may result from AM processes especially in terms of critical elements like chromium and molybdenum, issues of selective/localized corrosion become a concern.
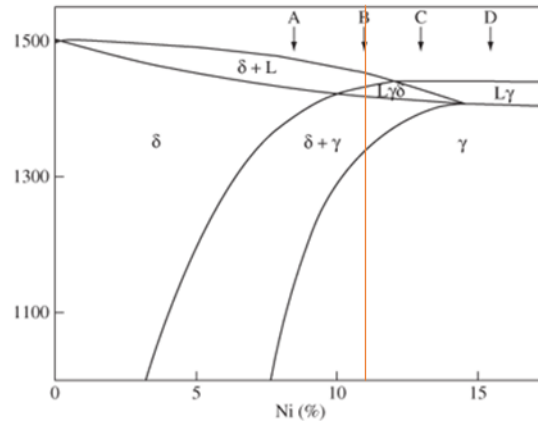
Figure 1. Temperature (°C) vs. nickel content (in wt. (%)). Section through Fe-Ni-Cr phase diagram at 19 wt. (%) Cr showing four solidification modes[3].

Fig. 2.1. Fe-Ni-Cr phase diagram depicting stability of relevant phases in stainless steel grades such 316L [36].

Solidification microstructure is controlled by solidification rate, cooling rate (R), undercooling, temperature gradients (G), and concentration. The solidification behavior in turn influences microstructural properties such as the size and shape of grains as well as the extent of chemical segregation. During welding or casting, the resulting microstructure can be either equiaxed, columnar, dendritic, or a combination due to the development of protrusions along the solid-liquid interface. These solidification microstructures can be rationalized using solidification theory[35–37]. According to this theory the ratio G/R controls the solidification microstructure and as the ratio G/R decreases, a microstructure that is more compositionally heterogenous is formed due to a lower degree of diffusional mixing in the liquid phase. Compositionally heterogenous microstructural features such as cellular dendrites tend to form at higher solidification velocities and lower temperature gradients. Fig. 2.3 shows TEM micrographs and EDS maps of these cellular structures and highlights compositional heterogeneities as well as dislocation arrangements that exist in LPBF stainless steel though multiple works have reported these heterogeneities [32,38].

The volumetric energy density (VED) is a parameter that is often used in additive manufacturing to describe the energy input in an AM build [9]. The VED is defined by the

following equation where P is the laser power, v is the scan speed, h is the hatch spacing, and t is the layer thickness:

$$VED = \frac{P}{vht}$$

Although multiple studies have criticized limitations of VED in predicting material features such as porosity, mechanical properties, and grain size, generalizations are able to be made[39–41]. For example, materials printed with low VED tends to lead to materials with high porosity due to incomplete melting of powder or incomplete fusion of material during the liquid state [11,21]. At high volumetric energy densities, the formation of key-hole porosity may lead to materials that are not fully dense [1,3,9,42]. Nevertheless, the discussion of these parameters highlights the importance of AM processing in resulting microstructure and properties.

Although there are dramatic differences between traditional welding and SLM, there is overlap in the two processes due to solidification being the main origin of microstructure control. The solidification process leads to complexities in the microstructure such as composition heterogeneities, which can lead to non-uniform corrosion. These fundamentals of solidification are important in understanding SLM microstructure and its effect on localized corrosion.
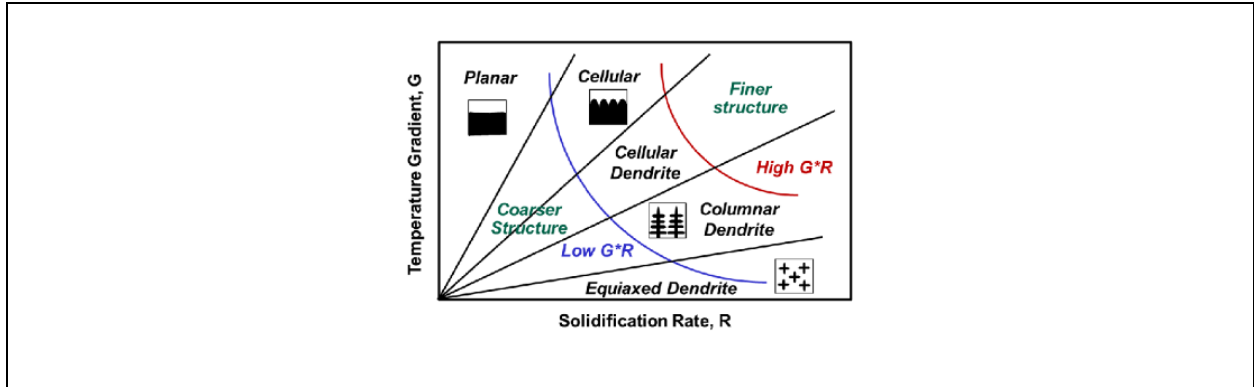
Fig 2.2. (a) Schematic depicting the effect of temperature gradient and solidification rate on resulting solidification microstructure.
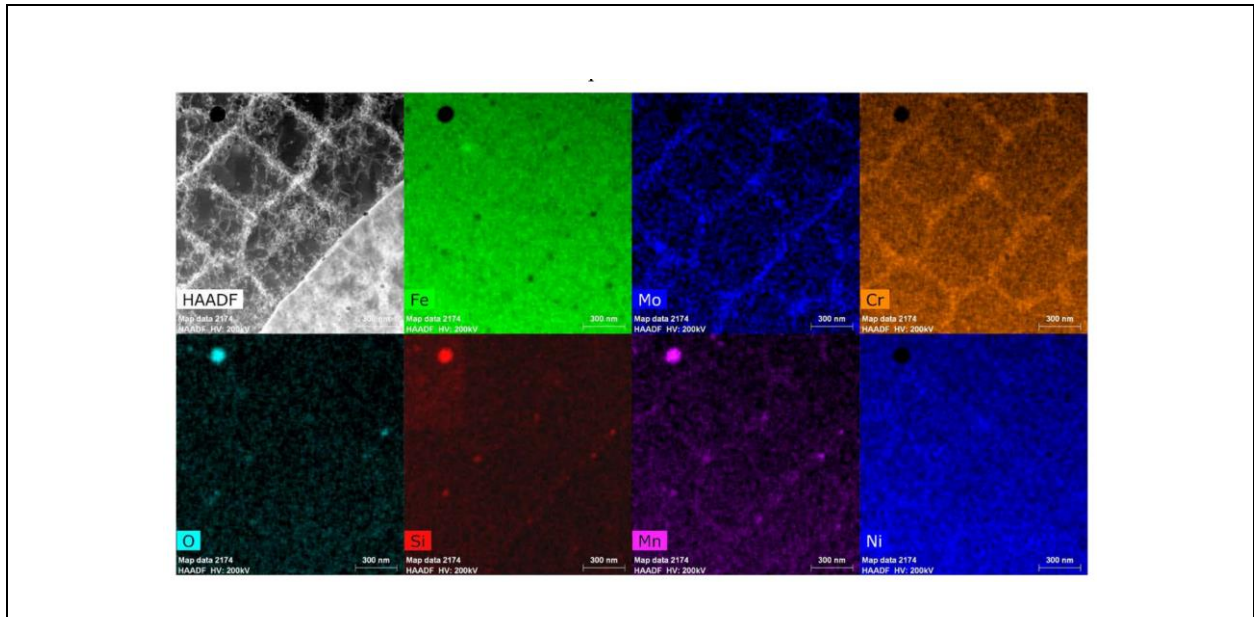
Fig. 2.3. HAADF and STEM-EDS maps of cellular structures in LPBF 316L [38].

2.1.3 Sensitization and Intergranular Corrosion

   In addition to pitting corrosion, another point of concern in steels such as 304 and 316L is intergranular corrosion due to grain boundary sensitization. Mostly an issue in welding, sensitization takes place during prolonged periods at a range of $450^{o}C – 800^{o}C$ in which chromium carbides ($Cr_{23}C_6$) preferentially form at the grain boundaries[43–45]. The formation of these carbides results in chromium depletion at areas adjacent to the grain boundaries. This depletion results in localized galvanic coupling between the chromium depleted region and the matrix[46–48]. Intergranular corrosion leads to significant mass loss in a material due to grain fall out from

grain boundary attack in corrosive media. Under mechanical loading, sensitization can lead to intergranular stress corrosion cracking (IGSCC) [48–50]. Fig. 2.4 Shows a cross-sectional image of type 304 steel that has undergone intergranular corrosion [51].

Alloying allows for mitigation against sensitization and intergranular corrosion. Steels such as 304L and 316L are contain relatively low amounts of carbon. This low carbon content assists in delaying the intergranular formation of chromium carbides. Alloying elements such as titanium and niobium are implemented in some stainless steels to form their respective carbides and compete with chromium carbide precipitation[47]. Although it leads to greater resistance to pitting corrosion, the presence of nitrogen in stainless steels (and even duplex stainless steels) can also lead to sensitization due to the formation of chromium nitrides[21,52]. Chromium nitride formation also results in a chromium-depleted region that would make an alloy susceptible to localized corrosion[47,48,53,54].

Microstructural features dictate an alloy's susceptibility to sensitization and intergranular corrosion. Although grain refinement is known to improve material strength and durability, studies of sensitization on stainless steels have shown an inverse relationship between grain size and susceptibility to grain boundary sensitization, i.e., smaller grained stainless steels are more susceptible to sensitization [55,56]. Smaller grains also lead to a damage morphology with a higher amount of grain-fall out [47-48]. At the same time, some studies have shown that smaller grain sizes lead to a lesser degree of chromium depletion. Studies investigating the effect of grain orientation have shown that low angle grain boundaries, twin boundaries, and CSL grain boundaries tend to be more resistant to sensitization compared to high angle grain boundaries[57–60]. An increase in the amount of cold work leads to a higher degree of intragranular precipitation of carbides due to preferential nucleation at dislocations [50,61,62].

10
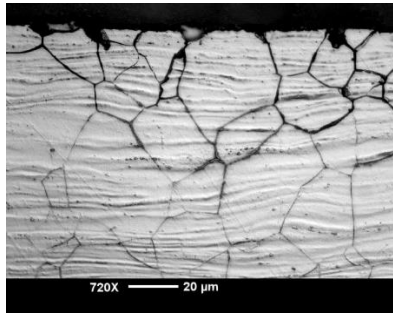
Fig. 2.4. Cross sectional image of type 304 steel that has undergone intergranular corrosion [43].

2.1.4 AM Microstructure and Preliminary Corrosion Results

The microstructure of AM alloys is different and more complex from those of conventionally wrought stainless steels. Grain size reduction with respect to the wrought counterpart is one signature of SLM alloys. LPBF 316L, for example, has a grain size of 10 um while a grain size of 30-60 um is common for conventionally wrought 316L[63]. In terms of the grain structure, elongated grains are observed along the build direction while columnar grains are observed orthogonal to the build direction[1,17,64,65]. Increased surface roughness and porosity are also observed in SLM alloys[66,67]. In conventionally wrought 316L, MnS inclusions have been known to be initiators for pitting corrosion. In LPBF 316L, these MnS inclusions are substituted with Mn-Si oxides and have resulted in reduced pitting susceptibility[47,55,68]. A decrease in the repassivation potential has been observed for LPBF 316L with greater porosity[58]. Nevertheless, multiple studies have discussed the deleterious nature of AM porosity to susceptibility to localized forms of corrosion such as crevice and pitting corrosion [68,69].

Solute segregation is an issue with solidification-based processing such as welding and SLM. Cellular structures have been observed in the characterization of SLM alloys. For example, in Al-Si-Mg alloys, silicon-rich cell structures are observed which leads to localized galvanic coupling[16,70,71]. In the case of stainless steels, cellular structures are observed with Mo or Cr enrichment at the cell boundaries. Such behavior was attributed to inhomogeneities in solute

distribution. Although multiple works have reported that the corrosion behavior of SLM 316L is enhanced compared to the wrought material, other works have also reported that the SLM material has worse performance in comparison to the wrought material [69,72–74].

Previous works have qualitatively reported observations of selective corrosion in additively manufactured alloys. In testing the behavior of LPBF materials by galvanostatic etching, for example, selective corrosion was observed to take place at the melt pool boundaries and cellular dendritic interiors though crystallographic dissolution was observed in the case of the wrought counterpart [75,76]. Other work has also found differences in corrosion behavior from different parts of the build and has been attributed to spatial variations in thermal conditions [76]. In comparing relative susceptibility to passive film breakdown in acidic, reducing environments, it has been found that materials with lower volumetric energy densities have greater susceptibility [77]. Little is known about intergranular corrosion in these additively manufactured alloys, but multiple works have reported that AM alloys are more susceptible while other works have reported that the AM counterpart is less susceptible [75–78].

Other microstructural features are worthy of noting in SLM materials although extensive corrosion studies on these other features have not been conducted. Surface roughness is particularly high since it is in the range of 10 – 30 um and is higher than one would receive from methods such as milling[79]. The rapid cooling rates and uneven heat distribution leads to the generation of residual stresses in SLM materials[14,17,80]. X-ray methods have shown that stresses tend to be compressive at the bottom of the build and tensile at the top of the build [65]. At the length scale range of 70-100 nm, complex dislocation networks have been observed [65].

The high dislocation density in SLM materials have been proposed to be one of the mechanisms for strengthening in SLM 316L as well as other alloys [65].

2.2 Key Unresolved Issues

Works on AM corrosion have primarily been focused on behavior in chloride solutions especially in relation to pitting and crevice corrosion [42,78,81,82]. However, work focusing on the corrosion behavior of AM in a broad range of environments, such as ones focused on behavior under transpassive conditions, is lacking in the literature. Therefore, there is motivation to further understand AM behavior in a broad range of environments and understand selective corrosion regarding the non-equilibrium microstructure of AM materials.

Within the literature, there seems to be inconsistency in the comparison between wrought and AM LPBF corrosion behavior. Some works may present the additive counterpart as more resistant to pitting corrosion [72], while others have reported the wrought material as more resistant. It is clear from the literature that the processing parameters have a significant impact on the microstructure and mechanical properties of AM materials. However, little work has been performed that investigates the effect of AM processing on corrosion properties.

In the area of intergranular corrosion and sensitization, there is very little work that has been performed that investigates the phenomena. Due to the prospects of using post-processing techniques such as hot isotactic pressing (HIP), there is value in understanding the effects of thermal processing on AM corrosion[1,3,9,20]. Sensitization and susceptibility to intergranular corrosion may be a consequence from thermal treatments and there is therefore a need to understand the mechanism of IGC in AM alloys as well as recognizing trends between processing parameters and sensitization/IGC susceptibility.

2.3 Objectives

Given these knowledge gaps, this dissertation has the following objectives:

- To compare the corrosion behavior between additively manufactured 316L to conventionally wrought 316L across a broad range of environments

- To understand the behavior of LPBF and DED 316L in a broad range of environments and relate corrosion behavior to the underlying non-equilibrium microstructure

- To understand the relationship between LPBF processing and susceptibility to surface activation and localized corrosion

- To understand IGC phenomenology in heat treated LPBF alloys and to understand the relationship between LPBF processing and sensitization/IGC susceptibility

2.4 Thesis Organization

Chapter 3 focuses on the LPBF and DED microstructure from the rapid solidification process and establishes a framework for predicting corrosion morphology based on environmental conditions. The main theme of this chapter is the distinction between active corrosion and transpassive dissolution. There is emphasis on how these varying environmental conditions affect selective corrosion in these varying AM processes. Environments that are relevant in the area of standardized testing are used to test hypotheses relevant to the compositional nature of cellular dendritic structures.

Chapter 4 focuses on the effect of LPBF processing on the localized corrosion susceptibility of LPBF 316L. Whereas Chapter 3 investigated the behavior of LPBF across a broad spectrum of environments and electrochemical potentials, corrosion behavior in chapter 3 will focus on the active behavior of LPBF 316L through the double-loop potentiokinetic reactivation rest in sulfuric acid and potassium thiocyanate. The concept of volumetric energy density is utilized to study the effect of LPBF laser parameters such as laser power and speed on susceptibility to global surface reactivation. As the DL-EPR technique is traditionally used in

studying the susceptibility of stainless steels to intergranular corrosion, a series of modifications to the DL-EPR technique were performed in order to further expand its utility in this work.

Chapter 5 focuses on intergranular corrosion and sensitization phenomena in LPBF 316L. Whereas the previous two chapters focused on the behavior of as-built LPBF material, this chapter focuses on the corrosion behavior of LPBF 316L after exposure to thermal conditions that are known to induce grain boundary sensitization in wrought 316L. In addition to describing the phenomena of LPBF 316L intergranular corrosion, the effect of processing parameters on sensitization/IGC susceptibility was investigated. The validity of traditional mass-loss testing and potentiodynamic testing in application to sensitized LPBF alloys were assessed in this chapter.

Additionally, the dissertation from time to time will incorporate orientation in regards to the additive manufacturing process. Fig. 2.5 shows the convention that will be used in this dissertation when discussing the build direction. The build direction is referred to as the direction in which the material grows after the addition of powder and laser treatment. When talking about LPBF materials, surfaces will be either be referred to as parallel or normal to the build direction.
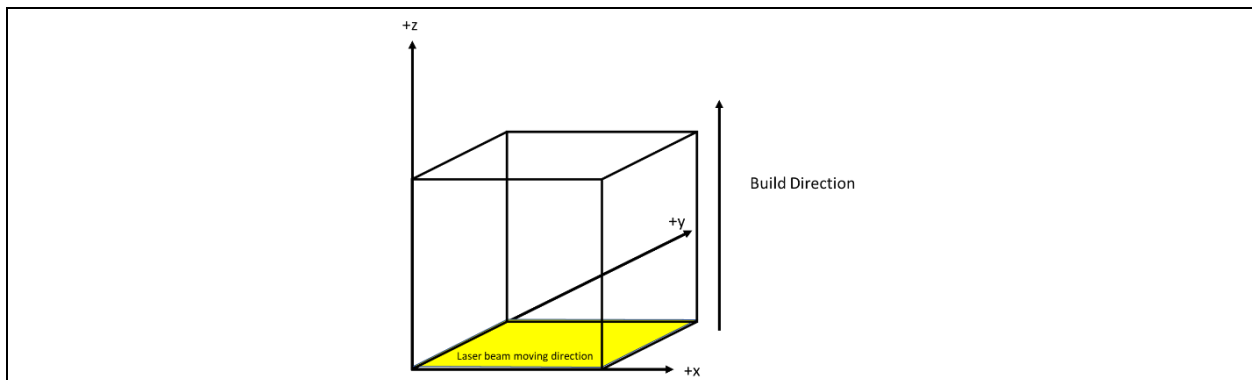
Fig. 2.5. Schematic highlight the build direction in regard to LPBF processing. In this schematic, as material is growing in the +z direction, the build direction is parallel to the +z direction. The scan direction will then be in the plane that contains the +x and +y directions.

The appendix shows published works that discuss observations of localized corrosion on LPBF 316L.

2.5 Citations

1. H. Sahasrabudhe, S. Bose, and A. Bandyopadhyay, in *Advances in Laser Materials Processing* (2018), pp. 507–539.
2. S. Pityana and S. Africa, 10 (2014).
3. D. D. Gu, W. Meiners, K. Wissenbach, and R. Poprawe, **57**, 133 (2013).
4. P. Zhang and Z. Liu, Materials and Design **100**, 254 (2016).
5. J. Ma, J. D. Harstvedt, D. Dunaway, L. Bian, and R. Jaradat, Journal of Cleaner Production **192**, 55 (2018).
6. J. M. Flynn, A. Shokrani, S. T. Newman, and V. Dhokia, International Journal of Machine Tools and Manufacture **101**, 79 (2016).
7. K. Kellens, R. Mertens, D. Paraskevas, W. Dewulf, and J. R. Duflou, Procedia CIRP **61**, 582 (2017).
8. B. Vandenbroucke and J. Kruth, Rapid Prototyping Journal **13**, 196 (2007).
9. D. Herzog, V. Seyda, E. Wycisk, and C. Emmelmann, Acta Materialia **117**, 371 (2016).
10. T. M. Mower and M. J. Long, Materials Science and Engineering A **651**, 198 (2016).
11. Y. Zhong, L. E. Rännar, L. Liu, A. Koptyug, S. Wikman, J. Olsen, D. Cui, and Z. Shen, Journal of Nuclear Materials **486**, 234 (2017).
12. Q. Chen and G. A. Thouas, Materials Science and Engineering R: Reports **87**, 1 (2015).
13. M. L. Montero Sistiaga, S. Nardone, C. Hautfenne, and J. Van Humbeeck, 27th Annual International Solid Freeform Fabrication Symposium - An Additive Manufacturing Conference. Solid Freeform Fabrication Symposium 558 (2016).
14. P. Hanzl, M. Zetek, T. Bakša, and T. Kroupa, Procedia Engineering **100**, 1405 (2015).
15. K. Kunze, T. Etter, J. Grässlin, and V. Shklover, Materials Science and Engineering A **620**, 213 (2014).
16. L. Thijs, K. Kempen, J. P. Kruth, and J. Van Humbeeck, Acta Materialia **61**, 1809 (2013).
17. X. Z. Xin, N. Xiang, J. Chen, D. Xu, and B. Wei, Journal of Materials Science **47**, 4813 (2012).
18. L. E. Murr, E. Martinez, J. Hernandez, S. Collins, K. N. Amato, S. M. Gaytan, and P. W. Shindo, Journal of Materials Research and Technology **1**, 167 (2012).
19. F. Bartolomeu, M. Buciumeanu, E. Pinto, N. Alves, O. Carvalho, F. S. Silva, and G. Miranda, Additive Manufacturing **16**, 81 (2017).
20. D. P. Guillen, D. C. Pagan, E. M. Getto, and J. P. Wharry, Materials Science and Engineering A **738**, 380 (2018).
21. C. Pauzon, E. Hryha, P. Forêt, and L. Nyborg, Materials and Design **179**, (2019).
22. S. Uns and S. W. Nr, 9 (2013).
23. Aalco, 1 (2013).
24. S. J. Kropschot and J. Doebrich, Usgs 1 (2010).
25. G. O. Ilevbare and G. T. Burstein, Corrosion Science **43**, 485 (2001).
26. A. Pardo, M. C. Merino, A. E. Coy, F. Viejo, R. Arrabal, and E. Matykina, Corrosion Science **50**, 1796 (2008).
27. N. U. Obeyesekere, Trends in Oil and Gas Corrosion Research and Technologies 215 (2017).
28. P. Gong, X. G. Liu, A. Rijkenberg, and W. M. Rainforth, Acta Materialia **161**, 374 (2018).
29. A. Fattah-Alhosseini and N. Attarzadeh, International Journal of Electrochemistry **2011**, 521384 (2011).
30. G. Song, Corrosion Science **47**, 1953 (2005).

31. B. Laurent, N. Gruet, B. Gwinner, F. Miserque, K. Rousseau, and K. Ogle, Electrochimica Acta **258**, 653 (2017).

32. J. W. Elmer, S. M. Allen, and T. W. Eagar, Metallurgical Transactions A **20**, 2117 (1989).

33. G. R. Mirshekari, E. Tavakoli, M. Atapour, and B. Sadeghian, Materials & Design **55**, 905 (2014).

34. G. T. Gray, V. Livescu, P. A. Rigg, C. P. Trujillo, C. M. Cady, S.-R. Chen, J. S. Carpenter, T. J. Lienert, S. J. Fensin, C. M. Knapp, R. A. Beal, B. Morrow, O. F. Dippo, D. R. Jones, D. T. Martinez, and J. A. Valdez, *L2 Milestone 5433: Characterization of Dynamic Behavior of AM and Conventionally Processed Stainless Steel (316L and 304L)* (Los Alamos, NM (United States), 2016).

35. H. Inoue, T. Koseki, S. Okita, and M. Fuji, Welding International **11**, 876 (1997).

36. H. Inoue and T. Koseki, Nippon Steel Technical Report 62 (2007).

37. V. Shankar, T. P. S. Gill, S. L. Mannan, and S. Sundarlsan, Sadhana - Academy Proceedings in Engineering Sciences **28**, 359 (2003).

38. P. Deng, H. Yin, M. Song, D. Li, Y. Zheng, B. C. Prorok, and X. Lou, JOM **72**, 4232 (2020).

39. P. Ferro, R. Meneghello, G. Savio, and F. Berto, The International Journal of Advanced Manufacturing Technology **110**, 1911 (2020).

40. F. Caiazzo, V. Alfieri, and G. Casalino, Materials **13**, 538 (2020).

41. K. G. Prashanth, S. Scudino, T. Maity, J. Das, and J. Eckert, Materials Research Letters **5**, 386 (2017).

42. J. R. Trelewicz, G. P. Halada, O. K. Donaldson, and G. Manogharan, Jom **68**, 850 (2016).

43. J. H. Lee, K. T. Kim, Y. S. Pyoun, and Y. S. Kim, Corrosion Science and Technology **15**, 226 (2016).

44. M. Terada, M. Saiki, I. Costa, and A. F. Padilha, Journal of Nuclear Materials **358**, 40 (2006).

45. H. Sidhom, T. Amadou, H. Sahlaoui, and C. Braham, Metallurgical and Materials Transactions A: Physical Metallurgy and Materials Science **38**, 1269 (2007).

46. A. S. M. Paroni, N. Alonso-Falleiros, and R. Magnabosco, Corrosion **62**, 1039 (2006).

47. S. M. Bruemmer, Corrosion **42**, 27 (1986).

48. A. Almubarak, W. Abuhaimed, and A. Almazrouee, International Journal of Electrochemistry **2013**, 1 (2013).

49. L. Huang, K. Wang, W. Wang, J. Yuan, K. Qiao, T. Yang, P. Peng, and T. Li, Engineering Failure Analysis **92**, 392 (2018).

50. V. Kain, in *Stress Corrosion Cracking*, edited by V. S. Raja and T. Shoji (Woodhead Publishing, 2011), pp. 199–244.

51. S. Ahmad, M. L. Mehta, S. K. Saraf, and P. Saraswat, 3 (1981).

52. G. Hu, P. Wang, D. Li, and Y. Li, Materials Science & Engineering A **752**, 93 (2019).

53. A. Scheil, (2017).

54. A. Pardo, M. C. Merino, M. Carboneras, A. E. Coy, F. Viejo, R. Arrabal, and J. A. Mu??oz, EUROCORR 2004 - European Corrosion Conference: Long Term Prediction and Modelling of Corrosion 1 (2004).

55. R. V. Taiwade, R. Shukla, H. Vashishtha, A. V. Ingle, and R. K. Dayal, ISIJ International **53**, 2206 (2013).

56. R. Singh, S. G. Chowdhury, B. Ravi Kumar, S. K. Das, P. K. De, and I. Chattoraj, Scripta Materialia **57**, 185 (2007).

57. T. Kuníková, H. Wendrock, K. Wetzig, and D. Hrivňaková, Materials and Corrosion **55**, 437 (2004).

58. M. Ziętala, T. Durejko, M. Polański, I. Kunce, T. Płociński, W. Zieliński, M. Łazińska, W. Stępniowski, T. Czujko, K. J. Kurzydłowski, and Z. Bojar, Materials Science and Engineering A **677**, 1 (2016).

59. A. King, G. Johnson, D. Engelberg, W. Ludwig, and J. Marrow, Science (1979) **321**, 382 (2008).

60. S. Q. Zhu and S. P. Ringer, Acta Materialia **144**, 365 (2018).

61. Project Management Institute, *11 11.1* (1996).

62. S. PEDNEKAR and S. SMIALOWSKA, CORROSION **36**, 565 (1980).

63. A. Ahmadi, R. Mirzaeifar, N. S. Moghaddam, A. S. Turabi, H. E. Karaca, and M. Elahinia, Materials and Design **112**, 328 (2016).

64. A. Yadollahi, N. Shamsaei, S. M. Thompson, A. Elwany, and L. Bian, International Journal of Fatigue **94**, 218 (2017).

65. E. Liverani, S. Toschi, L. Ceschini, and A. Fortunato, Journal of Materials Processing Technology **249**, 255 (2017).

66. A. Yadollahi, N. Shamsaei, S. M. Thompson, and D. W. Seely, Materials Science and Engineering A **644**, 171 (2015).

67. Z. Lei, J. Bi, P. Li, Q. Li, Y. Chen, and D. Zhang, Optics and Laser Technology **108**, 409 (2018).

68. G. Sander, S. Thomas, V. Cruz, M. Jurg, N. Birbilis, X. Gao, M. Brameld, and C. R. Hutchinson, J Electrochem Soc **164**, C250 (2017).

69. M. A. Melia, H.-D. A. Nguyen, J. M. Rodelas, and E. J. Schindelholz, Corrosion Science **152**, 20 (2019).

70. T. Maeshima and K. Oh-ishi, Heliyon **5**, e01186 (2019).

71. X. Liu, C. Zhao, X. Zhou, Z. Shen, and W. Liu, Materials and Design **168**, 107677 (2019).

72. G. Sander, S. Thomas, V. Cruz, M. Jurg, N. Birbilis, X. Gao, M. Brameld, and C. R. Hutchinson, Journal of The Electrochemical Society **164**, C250 (2017).

73. G. N. Nigon, O. B. Isgor, and S. Pasebani, Journal of The Electrochemical Society **167**, 141508 (2020).

74. K. M. Mantrala, M. Das, V. K. Balla, Ch. S. Rao, and V. V. S. Kesava Rao, Front Mech Eng **1**, 1 (2015).

75. D. A. Macatangay, S. Thomas, N. Birbilis, and R. G. Kelly, Corrosion **74**, 153 (2018).

76. D. A. Macatangay, G. W. Kubacki, and R. G. Kelly, JOM (2022).

77. D. A. T. Macatangay, J. M. Conrades, K. L. Brunner, and R. G. Kelly, Corrosion **78**, 13 (2022).

78. M. Laleh, A. E. Hughes, W. Xu, N. Haghdadi, K. Wang, P. Cizek, I. Gibson, and M. Y. Tan, Corrosion Science **161**, 108189 (2019).

79. E. Yasa and J. P. Kruth, Procedia Engineering **19**, 389 (2011).

80. T. Simson, A. Emmel, A. Dwars, and J. Böhm, Additive Manufacturing **17**, 183 (2017).

81. G. Sander, J. Tan, P. Balan, O. Gharbi, D. R. Feenstra, L. Singer, S. Thomas, R. G. Kelly, J. R. Scully, and N. Birbilis, Corrosion **74**, 1318 (2018).

82. G. W. Kubacki, J. P. Brownhill, and R. G. Kelly, Corrosion **75**, 1527 (2019).

3 Overview of Corrosion Phenomenology in Additively Manufactured 316L

3.1 Abstract

Additive manufacturing of metallic alloys like 316L have presented opportunities in the construction of complex geometries, control of microstructure, and the refinement of mechanical properties. This study is focused on corrosion phenomenology in additively manufactured 316L fabricated through direct energy deposition (DED) and laser powder bed fusion (LPBF). By testing across a broad array of oxidizing environments, the impact of local compositional differences due to the additive process was understood. Additionally, phenomenological distinctions between active dissolution and transpassive dissolution were able to be constructed regarding LPBF and DED 316L. Ultimately, observations of preferential corrosion were connected to the segregation of the critical corrosion suppressing elements chromium and molybdenum.

3.2 Introduction

Additive manufacturing technology such as laser powder bed fusion (LPBF) and direct energy deposition (DED) are methods of great interest due to opportunities in material conservation as well microstructure control and the improvement of mechanical properties[1–6]. LBPF uses a high-energy laser to melt powder on a build plate which undergoes rapid solidification whereas DED uses a laser to melt material (wire or powder) which is then directly deposited through a nozzle [1,7]. These fabrication methods involve melting followed by rapid solidification and usually result in the formation of complex, non-equilibrium microstructural features such as cellular dendritic structures [5,8–10]. There is also motivation in applying these technologies to the fabrication of austenitic stainless steel such as 316L to refine properties such as strength, ductility, toughness, and corrosion resistance [2,4,6,11–13].

Most work on AM corrosion have been focused on pitting corrosion and usually focus on structural features such as lack-of-fusion porosity and residual stress [1,14–16]. Dramatic

differences in cooling rates develop during the solidification process for both DED (10^3-10^4 K/s) and LPBF ($>10^5$ K/s) [17–19]. The compositional differences associated with these microstructural features provide motivation to understand the electrochemical behavior of these structures as well as how corrosion phenomenology varies with electrochemical conditions. Previous work on LPBF 316L have shown how preferential dissolution takes place along melt pool boundaries and the interior of the cellular dendritic structures in ammonium persulfate, hydrochloric acid, and sulfuric acid environments [16,20–27]. Due to the broad application of stainless steels and the diversity of environments that are used in standardized corrosion testing, it is important to broaden the discussion of AM corrosion phenomenology to various environmental and electrochemical conditions. For example, while lower potentials in acidic solutions may promote active corrosion, the application of higher potentials may promote transpassive dissolution and therefore a potentially different corrosion mechanism [28–30].

This manuscript is focused on the electrochemical behavior of additively manufactured 316L across a wide array of testing environments of varying oxidizing behavior. Environments such as boiling nitric acid and ferric chloride were chosen due to the widespread use of these chemical environments in the standardized testing of wrought austenitic stainless steels [31–33]. Whether it is through laser powder bed fusion or direct energy deposition, the solidification process results in complex microstructural features and it is critical to determine how these features dictate selective corrosion behavior, particularly in the test environments that are used as defaults for stainless steels. Proposed hypotheses involving the role of composition and dislocation structures are further tested by using characterization methods and validated through comparison of electrochemical behavior between wrought steels that have varying compositions and different degrees of dislocation density reflective of AM microstructural features. By performing these tests,

a main goal of this study is to propose holistic mechanisms of selective corrosion in additively manufactured 316L while comparing behavior to the conventionally wrought counterpart.

3.3 Experimental

3.3.1 Material Information and Preparation for Electrochemical Testing

AISI 316L powder manufactured by EOS with a particle size distribution of 10-53 um was used for the following build. Samples were printed with dimensions of 20 mm x 20 mm x 60 mm. The 20 mm x 20 mm base was oriented perpendicular to the build direction. As post-processing techniques such as hot-isotactic pressing and stress relieving were not performed, all LPBF material used in this chapter were tested in the as-built state. It should also be noted that the following set of build parameters were considered to be default by the system manufacturers. Table 3.2 shows the build parameters for the LPBF material.

DED 316L was fabricated by using a commercial M450 Meltio printer. The feedstock was a 316L wire with a 0.9 mm diameter and the build atmosphere was high purity argon. The following scan parameters were used: a total power of 800 W, a travel speed of 7 mm/s, a deposition rate of 16.31 mm/s.

Wrought AISI 316L and 317L from North American Stainless were used for comparison. Table 3.1. shows the composition of the wrought material and the powder used for the LPBF process.

Table. 3.1. Composition of Wrought, LPBF Material, and DED Material.

Element	Analysis Method	Wrought 316L Composition (Wt. %)	Wrought 317L Composition (Wt. %)	LPBF Process Powder Composition (Wt. %)	DED Process Material Composition
Fe	-	Balance	Balance	Balance	Balance
Cr	ICP	16.7	18.26	18.62	16.8
Ni	ICP	10.2	11.5	14.04	11.0
Cu	ICP	<0.1	<0.1	< 0.1	<0.1
Mn	ICP	1.99	1.85	1.65	1.95
Si	ICP	0.86	0.52	0.37	0.32
Mo	ICP	1.99	3.01	2.77	2.30
C	Combustion	0.006	0.003	0.007	0.002
S	Combustion	0.006	0.008	0.005	0.004
P	ICP	< 0.010	<0.010	< 0.010	<0.010
N	Fusion	0.04	0.08	0.07	-

Table 3.2. LPBF 316L Processing Parameters for LPBF Material

	LPBF Material
Power (W)	195
Scan Speed (mm/s)	1083
Hatch Distance (mm)	0.09
Layer thickness (mm)	0.02
Volumetric Energy Density (J/mm^3)	100
Gas Environment	Argon

3.3.2 Microstructure Characterization

Electron backscatter diffraction (EBSD) was performed to construct grain and phase maps of LPBF material. A Thermo Scientific Scios DualBeam™ was used to obtain EBSD maps.

A Themis 60-300 kV transmission electron microscopy of LPBF material was performed. STEM-EDS was used to construct compositional maps. High angle annular dark field imaging was utilized to investigate the dislocation structures of LPBF material.

A Quanta 650 scanning electron microscope was used to characterize corrosion surfaces after electrochemical testing. Secondary imaging was used to investigate corrosion surfaces.

Energy dispersive spectroscopy was used in characterizing the corrosion morphology of DED material to identify elemental distribution.

3.3.3 Behavior in Sulfuric Acid Environments

The active behavior of LPBF 316L, DED 316L, wrought 316L, and wrought 317L in 1 M H_2SO_4 was investigated with the addition of 0.01 M KSCN. Potassium thiocyanate was added due to how it induces active corrosion on the surface of Fe-Ni-Cr alloys [34,35]. Samples were ground to 1200 grit. To investigate the effects of residual stress on bulk active behavior, a scan was also performed for solution-annealed wrought 316L and compared to the behavior of as-built wrought 316L. Scanning electron microscopy was performed to assess corrosion morphology for all materials with exception of wrought 317L and solution-annealed wrought 316L.

The transpassive behavior of LPBF 316L, DED 316L, wrought 316L, and wrought 317L in 1 M H_2SO_4 was investigated through potentiodynamic scanning. Samples were ground to 1200 grit. After an open circuit potential hold for 30 minutes, the working electrode was scanned from 0.05 V below the open circuit potential to 1.2 V vs. SCE. Scanning electron microscopy was performed to assess corrosion morphology.

Zero resistance ammeter was performed to investigate the galvanic relationship between wrought 316L and 317L under active conditions in 1 M H_2SO_4 and 0.01 M KSCN. The galvanic current and potential were recorded for an exposure time of 24 hours. In the experimental set up, wrought 316L served as the working electrode.

3.3.4 Mass Loss Testing in Boiling Acid Solutions

Due to the use of boiling acid environments in certain standardized tests, two boiling acid mass-loss experiments were performed. Both testing environments environments as well as the overall experimental set up were derived from ASTM A-262 [31]. Table 3 shows the amount of

reagent used for each boiling test while Table 4 shows the weight percent of reagent used in each boiling test. An Erlenmeyer flask with solution was heated with a hot plate. Teflon tape and glass cradles were used to suspend the samples during the boiling test. Boiling chips were added to the solution to promote boiling. A reflux system was developed by using an Alihin condenser to promote the condensation of vapors back into the liquid phase and maintain acid concentration constant. Teflon and vacuum grease were placed along the interface of the condenser and the neck of the flask to create a tight seal. In both testing environments, the hot plate was used to promote boiling. Solution was checked in 12-hour increments to make sure there was little to no decrease in solution volume.

Table 3.3. Amount of reagent used in boiling test solutions.

Solution 1 (Provided by ASTM A262 Practice B)		Solution 2 (Provided by ASTM A262 Practice C)	
Reagent	Reagent Amount	Reagent	Reagent Amount
Deionized water (H_2O)	472 mL	Deionized water (H_2O)	108 mL
Concentrate Sulfuric Acid (H_2SO_4)	800 mL	70 wt.% Nitric Acid (HNO_3)	1000 mL
Ferric sulfate hexahydrate ($Fe_2(SO_4)_3 * 6H_2O$)	50.0 grams		

Table 3.4. Weight percent of reagents in boiling test solutions.

Solution 1 (Provided by ASTM A262 Practice B)		Solution 2 (Provided by ASTM A262 Practice C)	
Reagent	Composition (Weight Percent)	Reagent	Composition (Weight Percent)
Water (H_2O)	47.3	Water (H_2O)	35
Sulfuric Acid (H_2SO_4)	50.4	Nitric Acid (HNO_3)	65
Ferric sulfate $Fe_2(SO_4)_3$	2.3		

For all boiling tests, samples of approximate dimensions 20 mm x 20 mm x 2.5 mm were prepared. In the case of LPBF samples, the 20 mm x 20 mm square base is oriented perpendicular to the build direction. All faces were ground to a finish of 1200 grit with SiC paper Mass loss was recorded by measuring the mass before and after exposure to boiling acid solutions for 48 hours. Mass loss is expressed in units of mm/year and was calculated by the following standard formula [31]. Post-test scanning electron micrographs were taken.

$$Corrosion\ Rate = \frac{87660W}{Atd}$$
Equation 1

Corrosion rate is in units of mm/year, W is mass loss in grams, A is area in cm^2, t is exposure time in hours and d is the density of 316L in units of g/cm^3. In the case of chromium-nickel-molybdenum steels, a density value of 8 g/cm^3 was used.

3.3.5 Behavior in Chloride Environments

Wrought and LPBF 316L ground to 1200 grit with SiC paper. Samples were mounted in epoxy and were allowed to cure for a minimum of 12 hours. Samples were tested in a 0.6 M NaCl solution at room temperature. After exposure under open circuit conditions for 15 minutes, a potentiostatic hold was performed at 0.6 V vs. SCE for 600 seconds and the current was recorded. Additionally, scanning electron microscopy was performed with specific attention towards pit morphology.

To investigate the transpassive behavior of 316L in sodium chloride, a potentiostatic hold was performed at 1.65 V vs. SCE for 600 seconds for both wrought and LPBF 316L. The current was recorded and post-test scanning electron micrographs were obtained.

Full-immersion testing in 6 wt.% ferric chloride was performed as provided by ASTM G-48 [33] for wrought and LPBF 316L. Samples were ground to 600 grit and were immersed in the ferric chloride solution for 72 hours. In addition to recording mass loss, scanning electron micrographs of corrosion pits were taken. Chloride experiments were only performed for wrought and LPBF 316L.

3.4 Results

The results section are organized by describing corrosion phenemonology in sulfuric environments and a distinction is made for behavior at high potentials and low potentials. In order to determine the effect of local differences in dislocation density and composition, the behavior of wrought alloys that captured local compositional differences were then tested. Electrochemical results for the DED material is described in a way that discusses the effect of local changes in composition. Lastly, behavior in relevant boiling acid solutions and chloride environments is

discussed in a way that makes a distinction in corrosion morphology between low and high electrochemical potentials.

3.4.1 Potentiodynamic Behavior in Sulfuric Acid Environments

Fig. 3.1 shows polarization scans of wrought and LPBF 316L in 1 M H_2SO_4 and 0.01 M KSCN. It is observed that the measured current for wrought material is larger than that of the LPBF 316L throughout the active range (~-0.4 V(SCE) to ~-0.15 V(SCE)) above which there is a drastic drop in current due to passive film formation. It is also observed that the passive current for the LPBF material is greater than that of the wrought material.
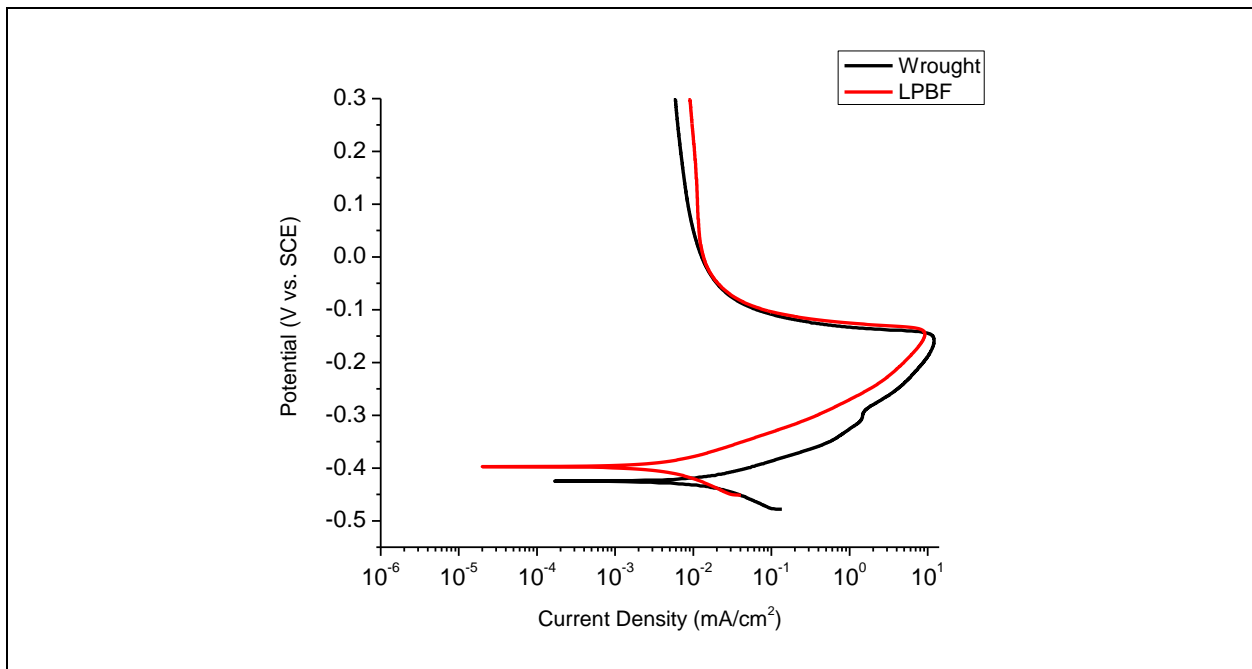
Fig. 3.1. Polarization scan of wrought and LPBF 316L in 1 M H_2SO_4 and 0.01 M KSCN.

Fig. 3.2 shows post-test micrographs of wrought and LPBF 316L after potentiodynamic testing in 1 M H_2SO_4 and 0.01 M KSCN. Crystallographic attack is seen to be taking place for the wrought material. In the case of the LPBF material, its honeycomb-like structures are seen which show the preferential dissolution of the interior of cellular dendritic structures.

27

(a)   (b)
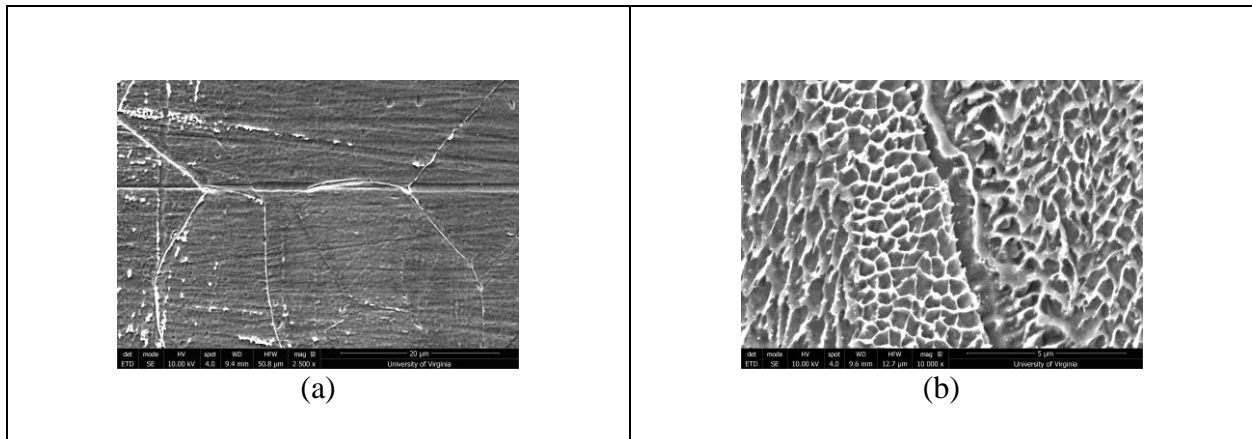
Fig. 3.2. Surface of wrought (a) and LPBF (b) 316L after potentiodynamic scanning in 1 M H_2SO_4 and 0.01 m KSCN for 24 hours. There is a difference in scale to highlight the cellular structures in the LPBF material.

Fig. 3.3 shows crystallographic attack in wrought material (Fig. 3.3a) and cellular core attack in LPBF 316L material (Fig. 3.3b) after full immersion in 1 M H_2SO_4 and 0.01 M KSCN for 24 hours under open circuit conditions.

(a)   (b)
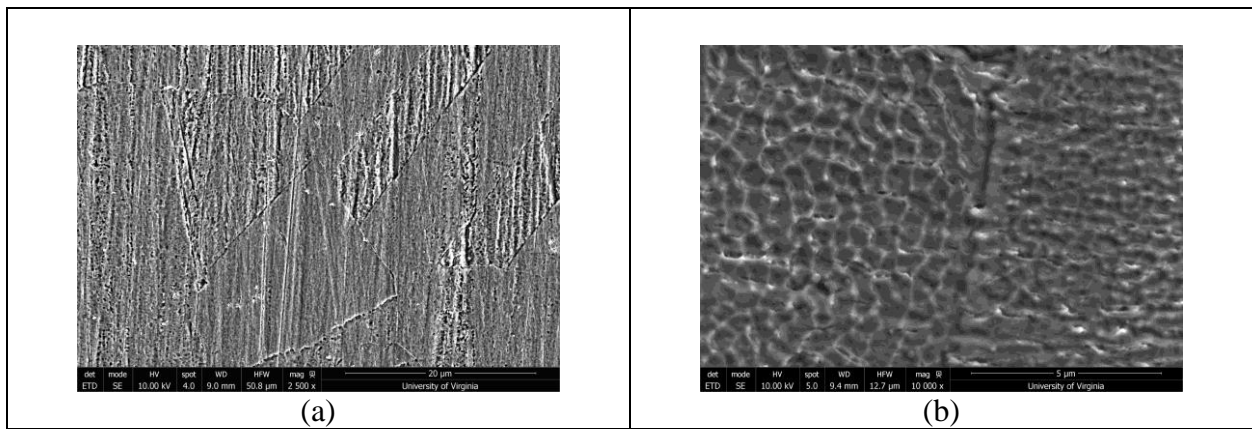
Fig. 3.3. Surface of wrought (a) and LPBF (b) 316L after full immersion in 1 M H_2SO_4 and 0.01 m KSCN for 24 hours. There is a difference in scale to highlight the cellular structures in the LPBF material.

Fig. 3.4. shows polarization scans of wrought and LPBF 316L in 1 M H_2SO_4. Differences in behavior are seen near the open circuit potential as there appears to be small active nose in the case of the wrought material. Nevertheless, there is great similarity in the passive current densities

for both materials. At approximately 900 mV vs. SCE, there is an increase in the measured current though the two currents remain nearly the same with an increase in potential. At approximately 1 V vs. SCE, the currents diverge from each other and the current of the LPBF material is seen to be higher.
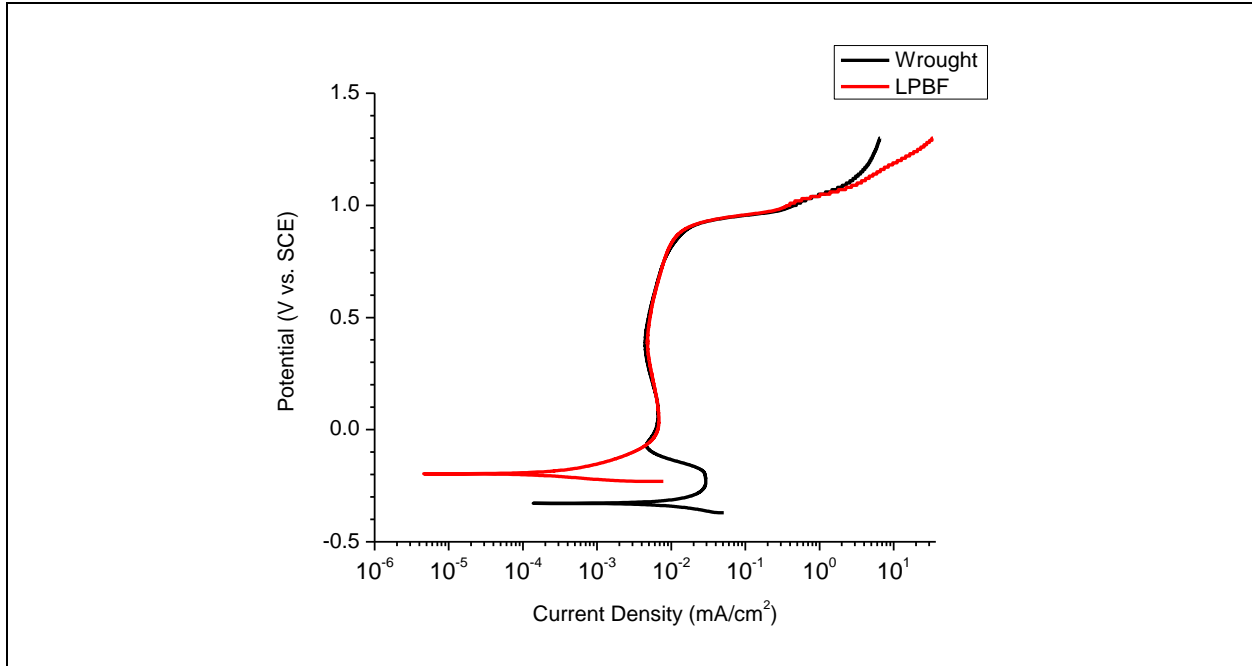
Fig. 3.4. Potentiodynamic scan of wrought and LPBF 316L in 1 M H_2SO_4.

Fig. 3.5 shows the post-test micrographs for wrought (Fig. 3.5a) and LPBF 316L (Fig. 3.5b.) after testing in 1 M H_2SO_4. For the wrought material, the dissolution is relatively uniform although there is some localized attack that takes place along a grain boundary. For the LPBF material, straw-like structures are observed signifying preferential attack of cellular dendritic walls.

(a)

(b)
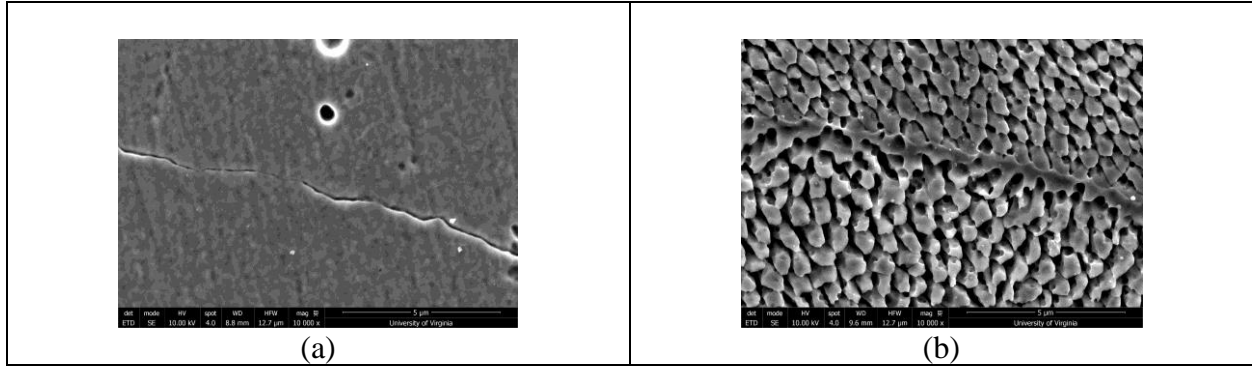
Fig. 3.5. Scanning electron micrograph of wrought (a) and LPBF (b) 316L after potentiodynamic testing in 1 M H_2SO_4.

3.4.2 Characterization of LPBF Material

Fig. 3.6 shows the grain and phase maps for LPBF 316L. The grain map (Fig. 3.6a) shows the grain structure of the LPBF material and shows elongated grains along the build direction. In the case of the phase map (Fig. 3.6b), it is seen that there is very little to no ferrite in the material indicating that the material is indeed nominally austenitic.

(a)

(b)
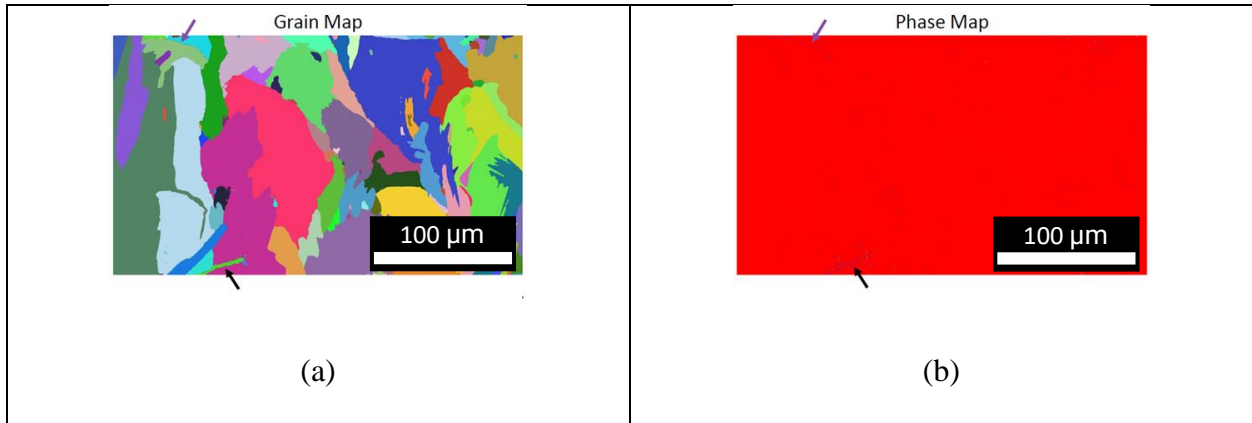
Fig. 3.6. Grain map (a) and phase map (b) of LPBF 316L obtained through electron backscatter diffraction. Black arrows point to areas of the ferritic phase.

Fig. 3.7 shows STEM micrographs of cellular structures of LPBF 316L through high-angular annular dark-field imaging. HAADF imaging shows that there is a higher dislocation density at the cellular boundary im comparison to the interior. Energy dispersive spectroscopy shows depletion of iron and enhancement of chromium along cellular boundaries. Fig. 3.7b -3.7f are plots composition as a function of position along the red arrow drawn. At approximately 250 nm, it is seen that there is clear depletion of iron along the cellular boundaries. It is also seen that there is an enrichment of chromium, molybdenum, and nickel along the cellular boundaries.
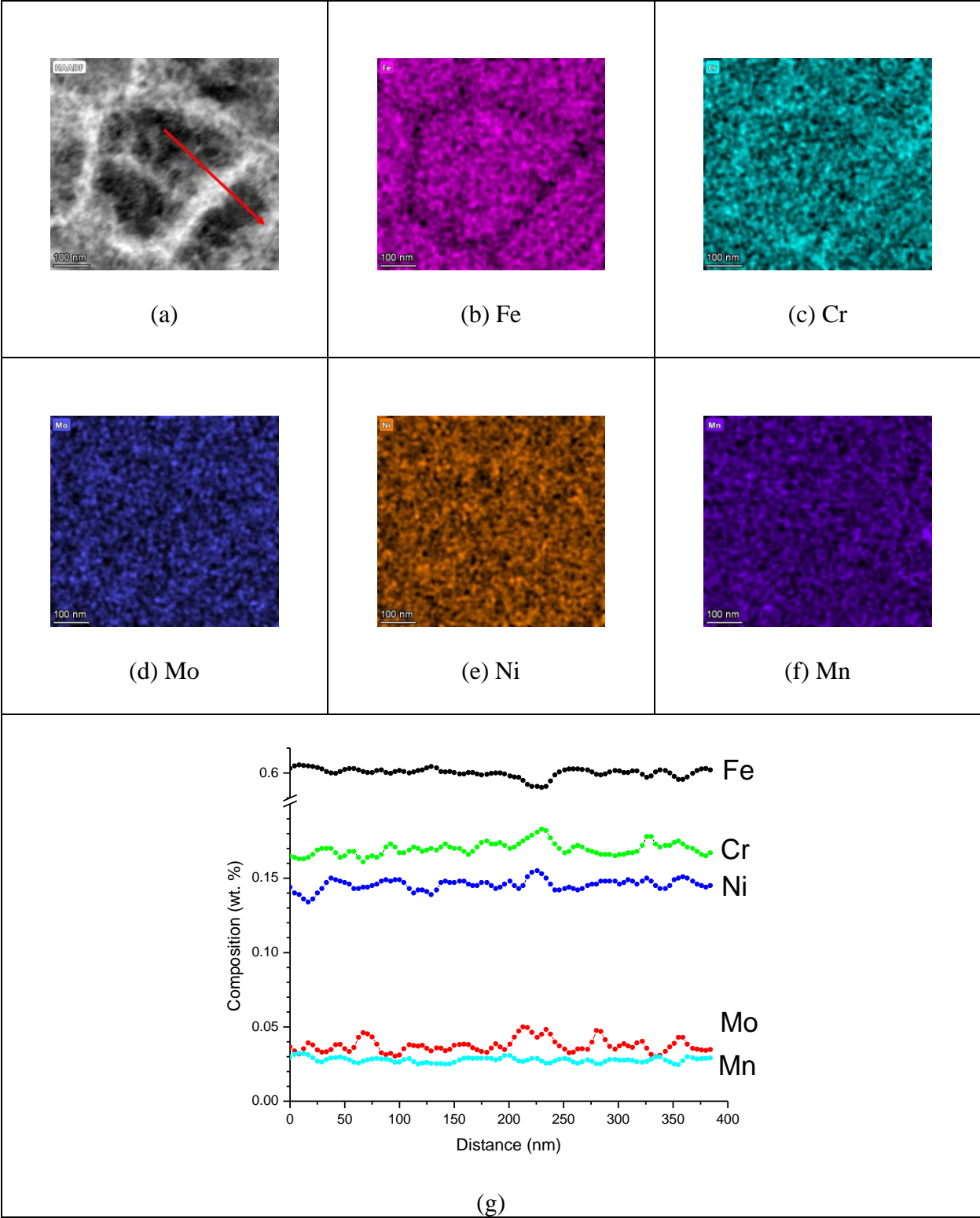
Fig. 3.7. HAADF image (a) of cellular structure in LPBF 316L. EDS maps of (b) Fe, (c) Cr, (d) Mo, (e) Ni, and (f) Mn are also shown. The compositional profile (g) is shown for the line represented in the HAADF image.

3.4.3 The Effects of Compositional Variations on Stainless Steel Electrochemical Behavior

Fig. 3.8 shows potentiodynamic scans for wrought 316L and 317L in 1 M H_2SO_4 and 0.01 M KSCN. Active dissolution can be observed of at a range -0.4 to -0.2 V vs. SCE. The current in the active range is consistently higher for the 316L variant. It is also seen that the passive current densities are nearly equivalent for the two materials.
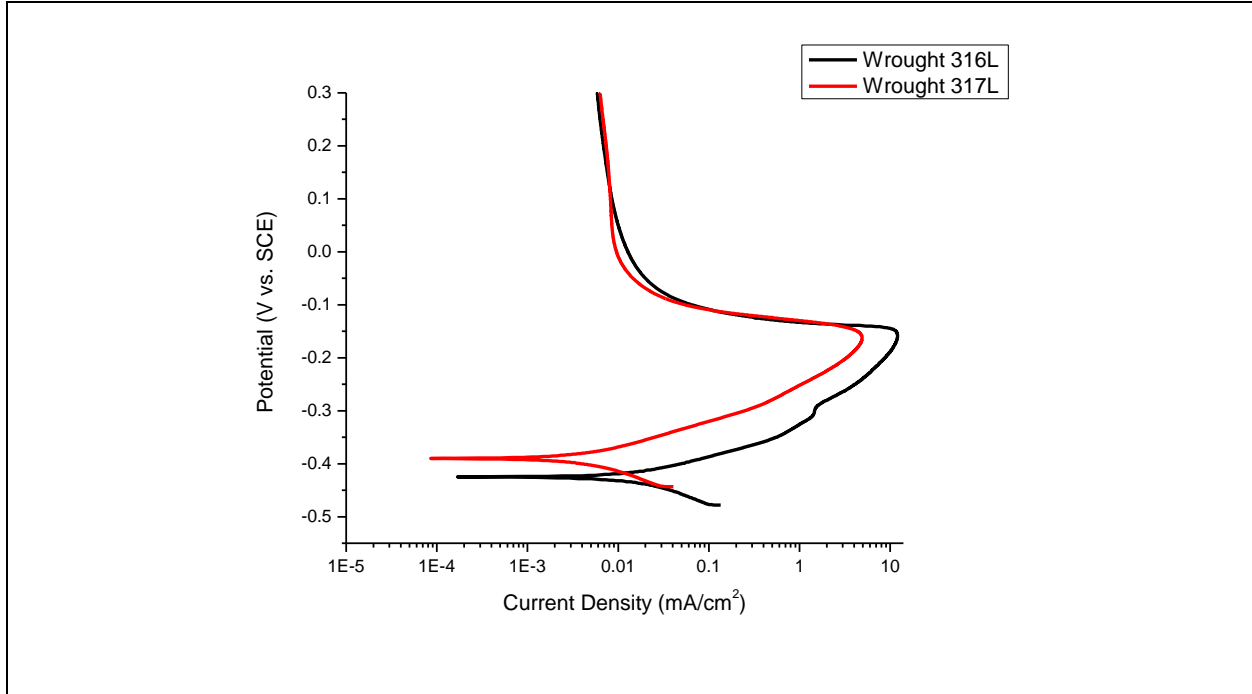
Fig. 3.8. Polarization scan of wrought 316L and 317L in 1 M H_2SO_4 and 0.01 M KSCN.

Fig. 3.9 shows the zero resistance ammeter results in testing the galvanic interaction between wrought 316L and 317L. In this experimental set up, the 316L was set up to be the working electrode. In Fig. 3.9a, current is reported to be positive for the entire 24-hour hold, showing that the 316L is anodic with respect to the 317L. Fig. 3.9b shows the evolution of the coupling potential and how it rises steadily with time.

33

(a)

(b)

Fig. 3.9. Coupling current between 316L and 317L after zero resistance ammeter for 24 hours.
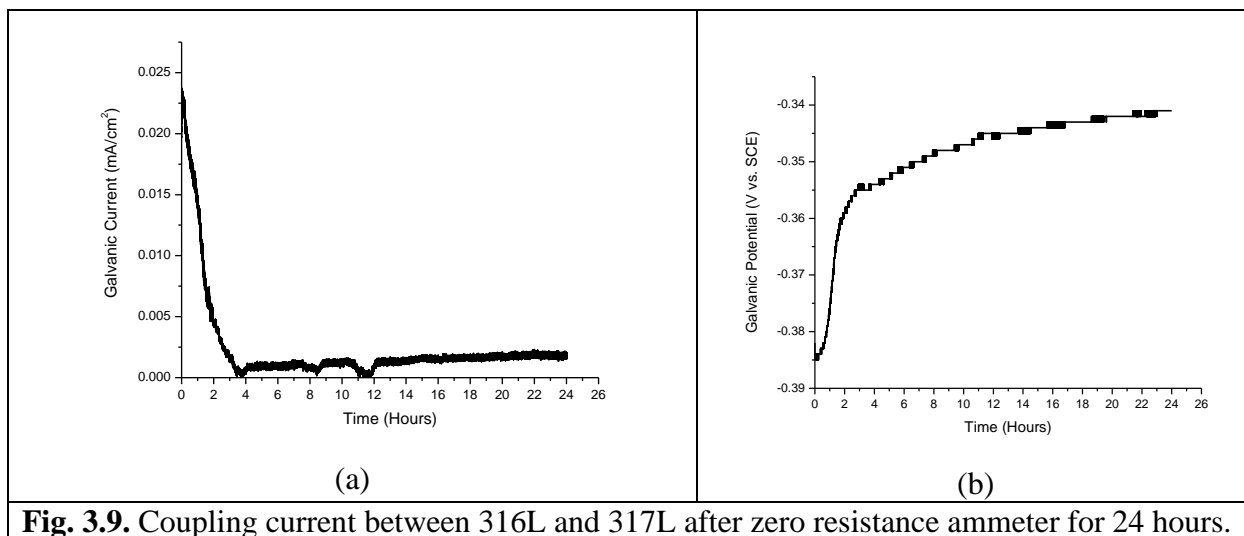
Experiments were performed comparing on 317L in comparison to 316L to rationalize the effect of the observed compositional differences on selective corrosion in AM materials. Fig. 3.10 shows potentiodynamic scans for wrought 316L and 317L in 1 M H_2SO_4. Anodic dissolution can be observed of in the range from -0.4 to -0.2 V vs. SCE. The maximum current density is higher for 316L. At an approximate range -0.2 V to 1.0 V vs. SCE, the currents nearly converge with each other through the passive range and the early stages of transpassive dissolution. Above a potential of 1 V vs. SCE, the electrochemical behaviors diverge, and the current for 317L is higher than that observed in 316L.
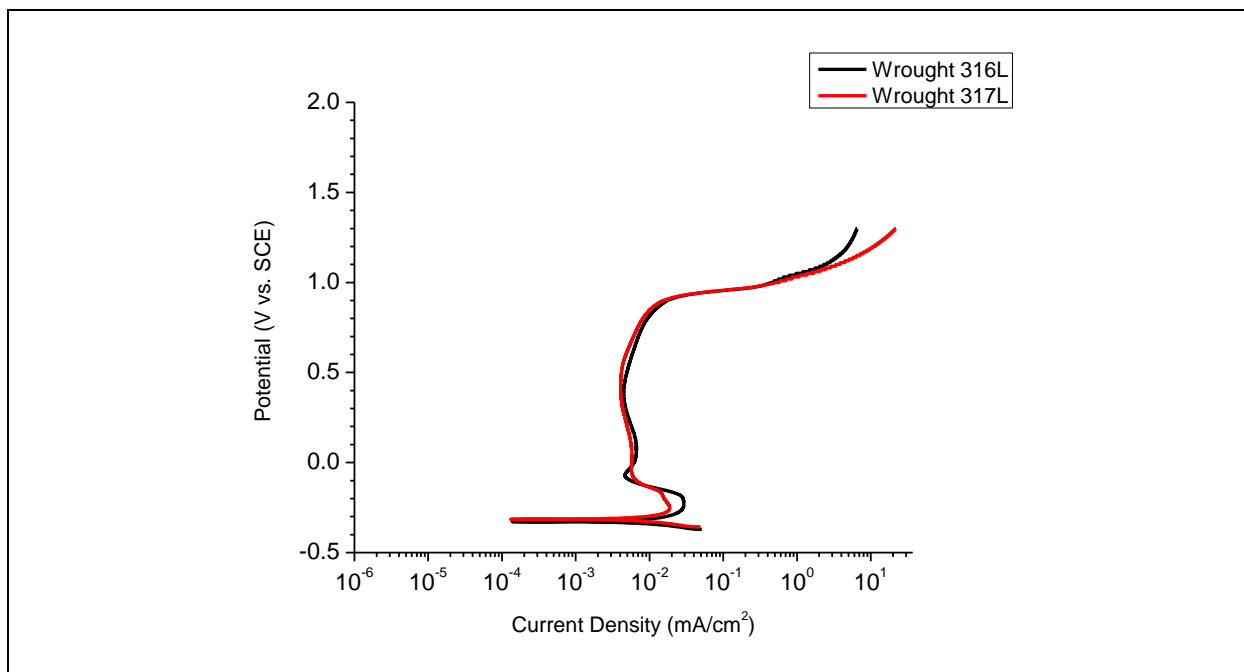
Fig. 3.10. Polarization scan of wrought 316L and 317L in 1 M H_2SO_4.

3.4.4 The Effects of Residual Stress on Electrochemical Behavior

Fig. 3. 11 shows polarization scans of as-received and annealed wrought 316L in 1 M H_2SO_4 + 0.01 M KSCN. The two polarization scans show that there is very little difference in potentiodynamic behavior between the two wrought variants. This observation is consistent in both the approximate range of active dissolution (-400 to -150 mV vs. SCE) and the passive region (-150 to 300 mV vs. SCE). It is also noted that the as-received wrought material was cold worked.
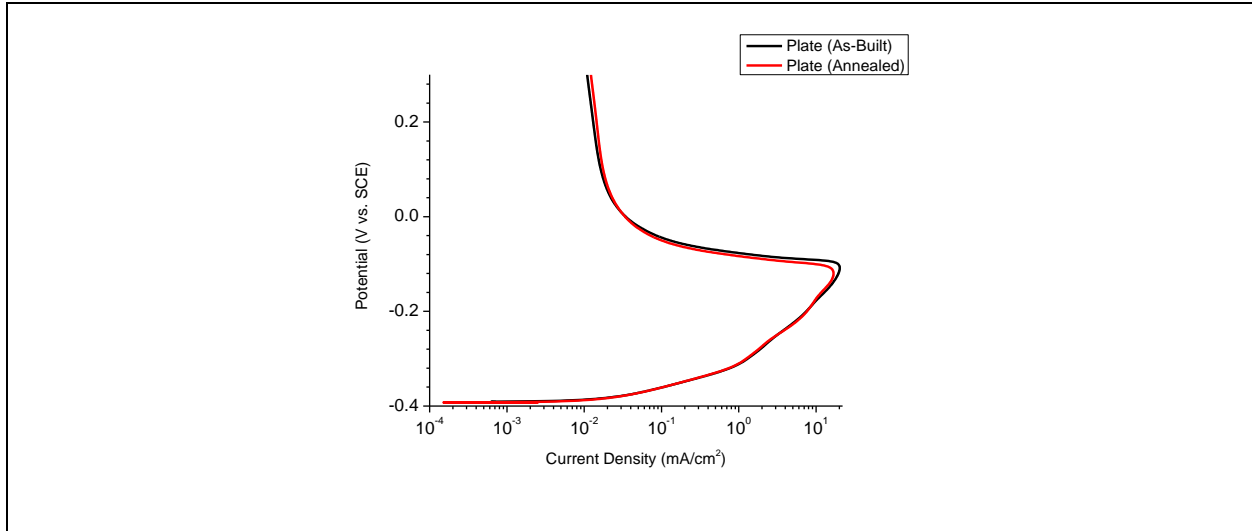
Fig. 3.11. Polarization scan of wrought 316L in the as-built and annealed state in 1 M H$_2$SO$_4$ and 0.01 M KSCN.

3.4.5 Electrochemical Behavior of DED 316L

Fig. 3.12 shows the microstructure for DED material on a polished surface. The surface is parallel to the build direction. EBSD imaging (Fig. 3.12b) shows the presence of both ferritic and austenitic phases. EDS compositional analysis shows how the austenitic phase is rich in nickel while the ferritic phase is enriched in chromium and molybdenum.
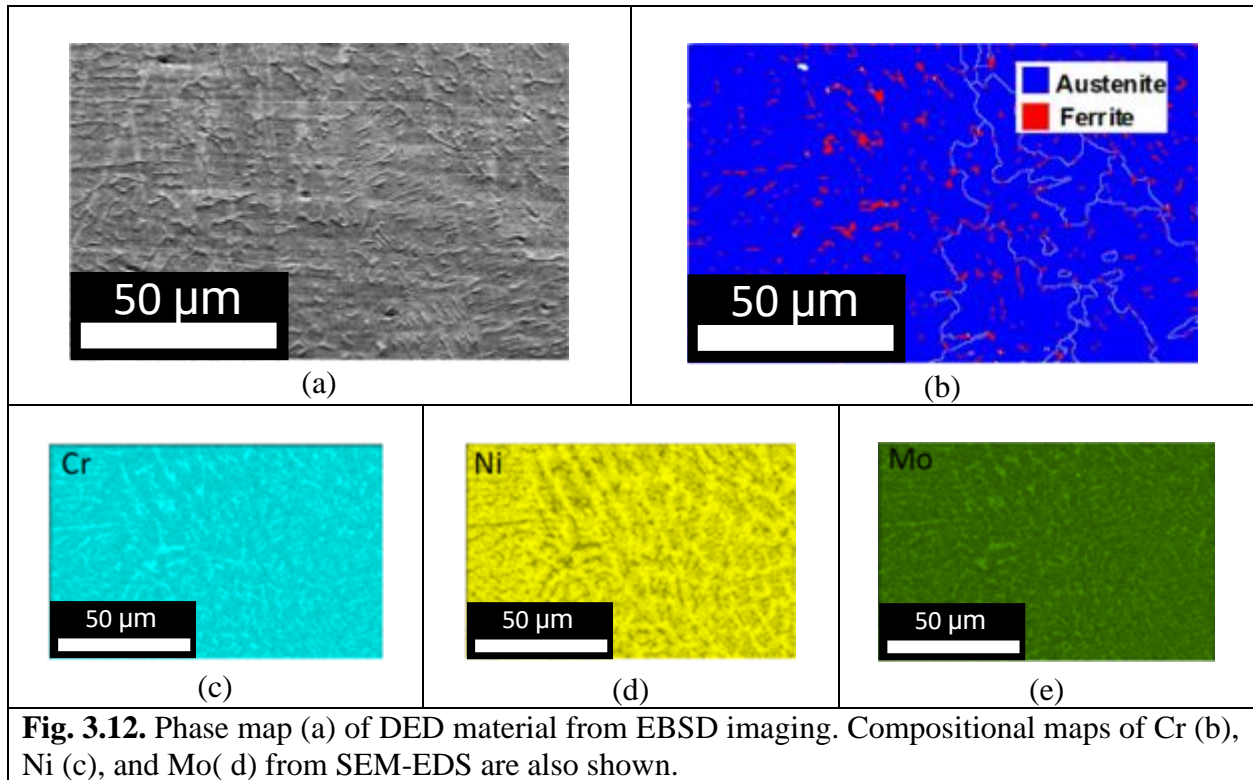
Fig. 3.12. Phase map (a) of DED material from EBSD imaging. Compositional maps of Cr (b), Ni (c), and Mo(d) from SEM-EDS are also shown.

Fig. 3.13 shows the polarization behavior of wrought and DED 316L in 1 M H_2SO_4 and 0.01 M KSCN. Although there are great similarities in the active behavior, it seen that the passive current in the DED material is initially lower than that of the wrought material and then increases to and becomes higher than that of the wrought in the passive regime.
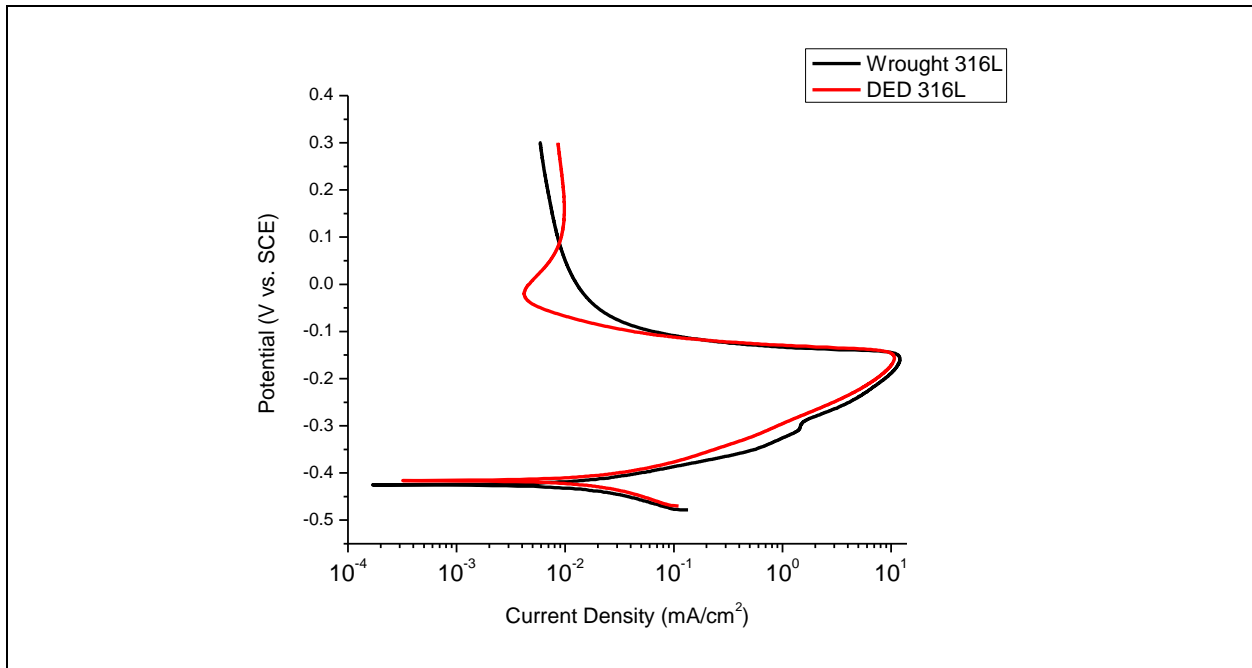
Fig. 3.13. Polarization scan of wrought and DED 316L in 1 M H_2SO_4 and 0.01 M KSCN.

Fig. 3.14 shows post-test micrographs of DED 316L after potentiodynamic testing in 1 M H_2SO_4 and 0.01 M KSCN. It is seen that the austenitic matrix undergoes preferential dissolution in comparison to the skeletal-like ferrite in the material.

(a)　　　　　　　　　　　　　　　　(b)
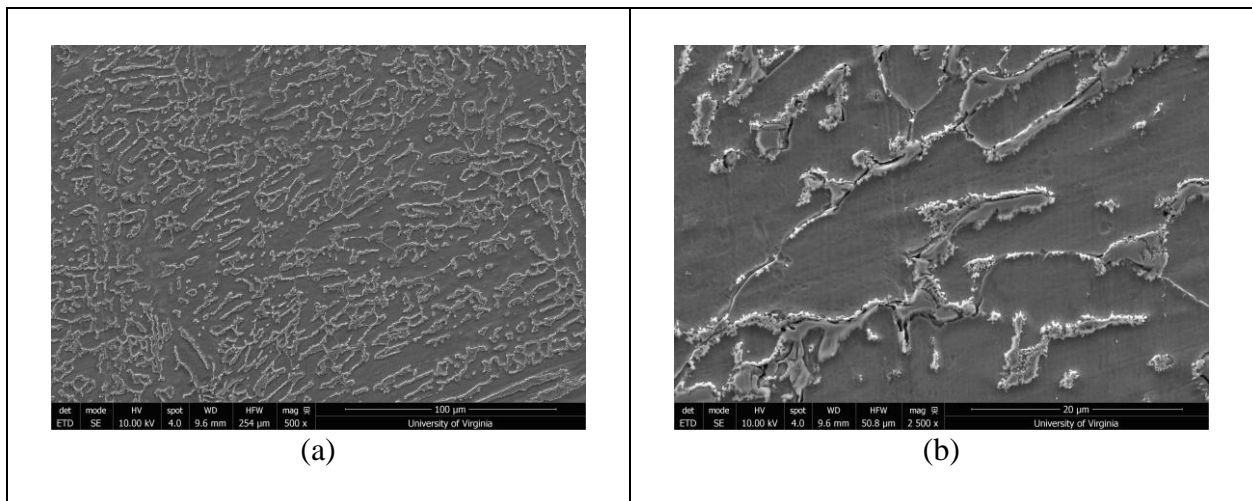
Fig. 3.14. Surface of DED 316L at (a) 500X and (b) 2500X magnification after potentiodynamic scanning in 1 M H_2SO_4 and 0.01 m KSCN.

Fig. 3.15 shows the EDS maps for this corroded surface and further confirms that the matrix undergoes preferential corrosion and is lower in chromium (Fig. 3.15c) and molybdenum (Fig. 3.15d) while being rich in iron (Fig. 3.15b) and nickel (Fig. 3.15e) relative to the ferrite islands. The manganese signal (Fig. 3.15f) is relatively constant throughout the map.

Fig. 3.15. Corresponding SEM micrograph (a) and compositional SEM-EDS maps for (b) Fe, (c) Cr, (d) Mo, (e) Ni, and (f) Mn after potentiodynamic testing in 1 M H_2SO_4 and 0.01 M KSCN.
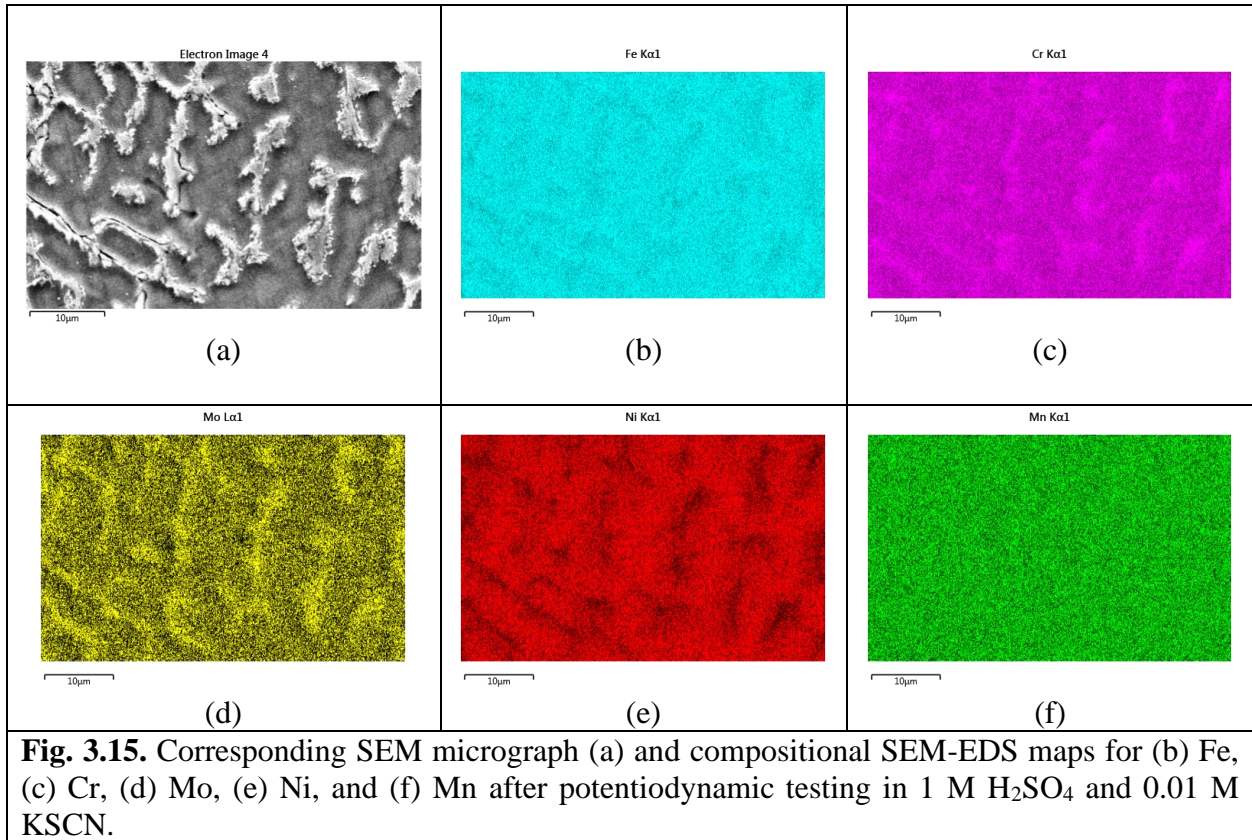
Fig. 3.16 shows the polarization behavior of wrought and DED 316L in 1 M H_2SO_4. The open circuit potential of the DED material is higher than that of the wrought counterpart. Although the passive behavior is similar for both the wrought and DED material, the current density of the DED material exceeds that of the wrought material in the transpassive regime.
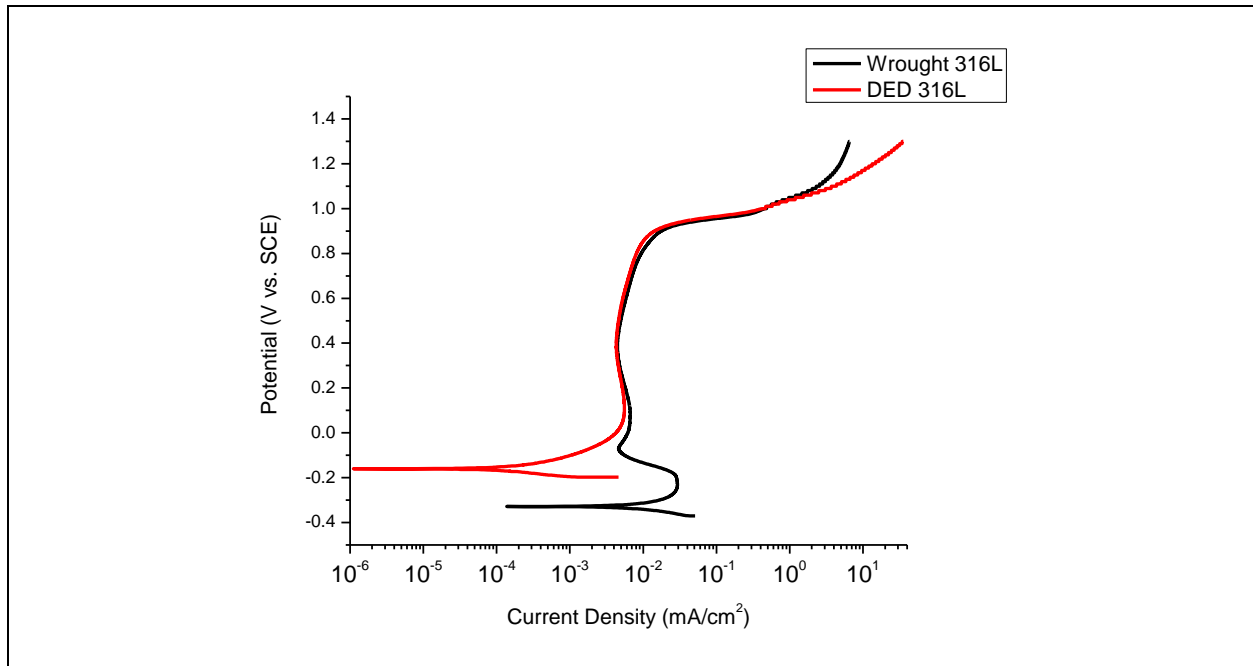
Fig. 3.16. Polarization scan of wrought and DED 316L in 1 M H_2SO_4.

Fig. 3.17 shows post-test micrographs of DED 316L after potentiodynamic scanning in 1 M H_2SO_4 and reveals that unlike the situation in sulfuric acid and thiocyanate, the skeletal-like ferritic features undergo preferential attack.

(a)

(b)
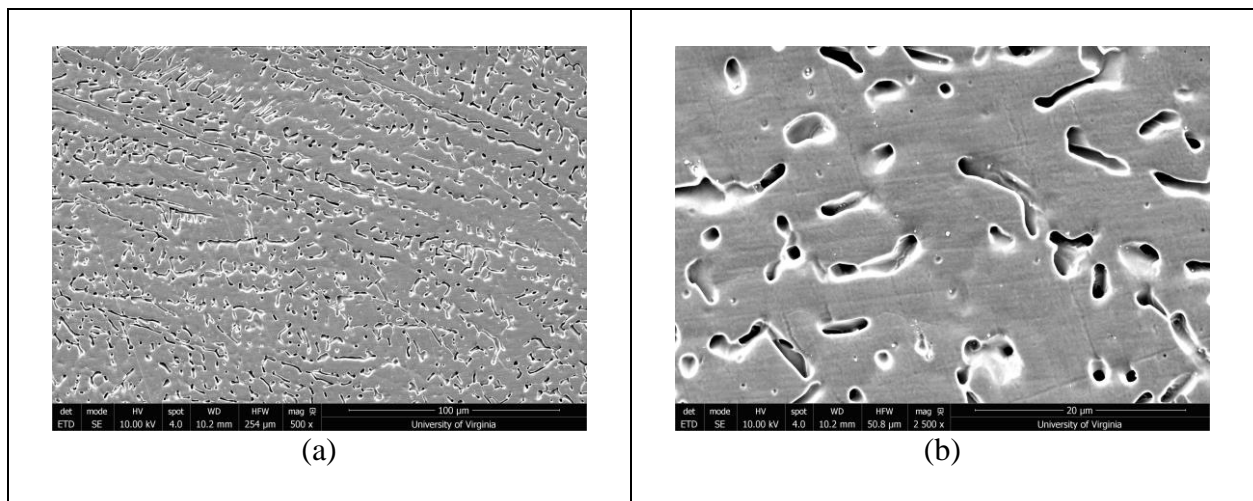
Fig. 3.17. Surface of DED 316L at (a) 500X and (b) 2500X magnification after potentiodynamic scanning in 1 M H_2SO_4.

Fig. 3.18. shows the EDS maps of the surface of the DED 316L material after polarization in 1 M H_2SO_4. While the features that underwent preferential corrosion have lower x-ray signals in iron (Fig. 3.19b), molybdenum (Fig. 3.19d), and nickel (Fig. 3.19e), there is little to no decrease in the chromium (Fig. 3.19c) and manganese (Fig. 3.19g) signals.

Fig 3.18. Corresponding SEM micrograph (a) and compositional SEM-EDS maps for (b) Fe, (c) Cr, (d) Mo, (e) Ni, and (f) Mn after potentiodynamic testing in 1 M H_2SO_4.
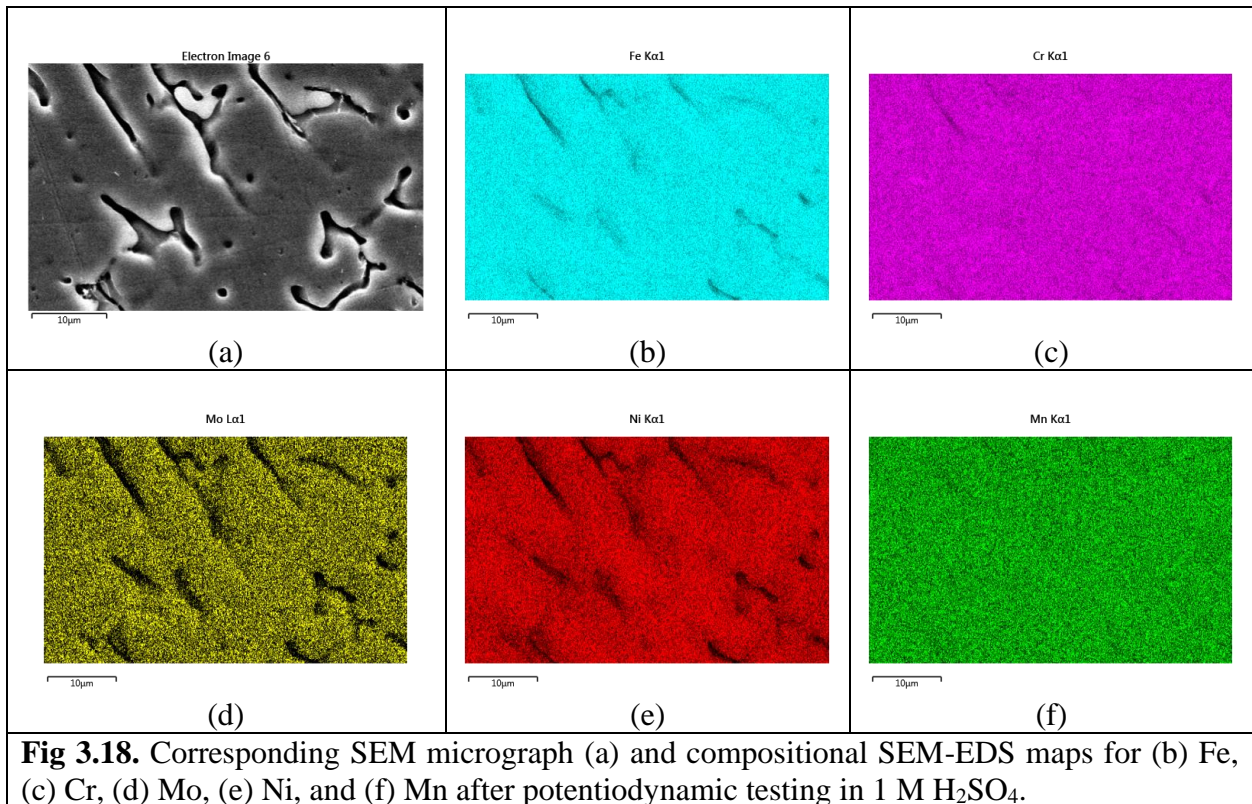
3.4.6 Boiling Acid Mass Loss Test Results for LPBF 316L

Fig. 3.19 shows the mass loss results after testing wrought and LPBF 316L in boiling sulfuric acid and ferric sulfate for 48 hours. It is seen that the corrosion rate for the wrought material is higher than that of the LPBF material by approximately a factor of two.
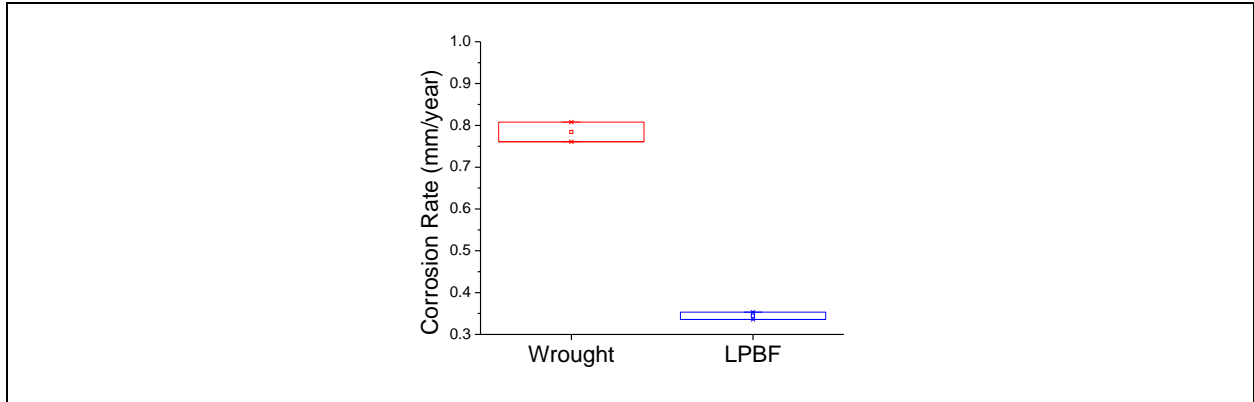
Fig. 3.19. Mass loss results for wrought and LPBF 316L after testing in boiling sulfuric acid and ferric sulfate for 48 hours.

Fig. 3.20 shows the micrographs of wrought (Fig. 3.20a and Fig. 3.20b) and LPBF 316L (Fig. 3.20c and Fig. 3.20d) surfaces after testing in boiling sulfuric acid and ferric sulfate for 48 hours. The corrosion morphology of the wrought material is uniform and this was additionally confirmed with white light interferometry. In the case of the LPBF material, preferential dissolution takes place in the core of the cellular structures.

Fig. 3.20. Post-test micrographs for wrought 316L at (a) lower and (b) higher magnfication after testing in boiling sulfuric acid and ferric sulfate for 48 hours. Micrographs for LPBF 316L at (c) lower and (d) higher magnification are also shown.
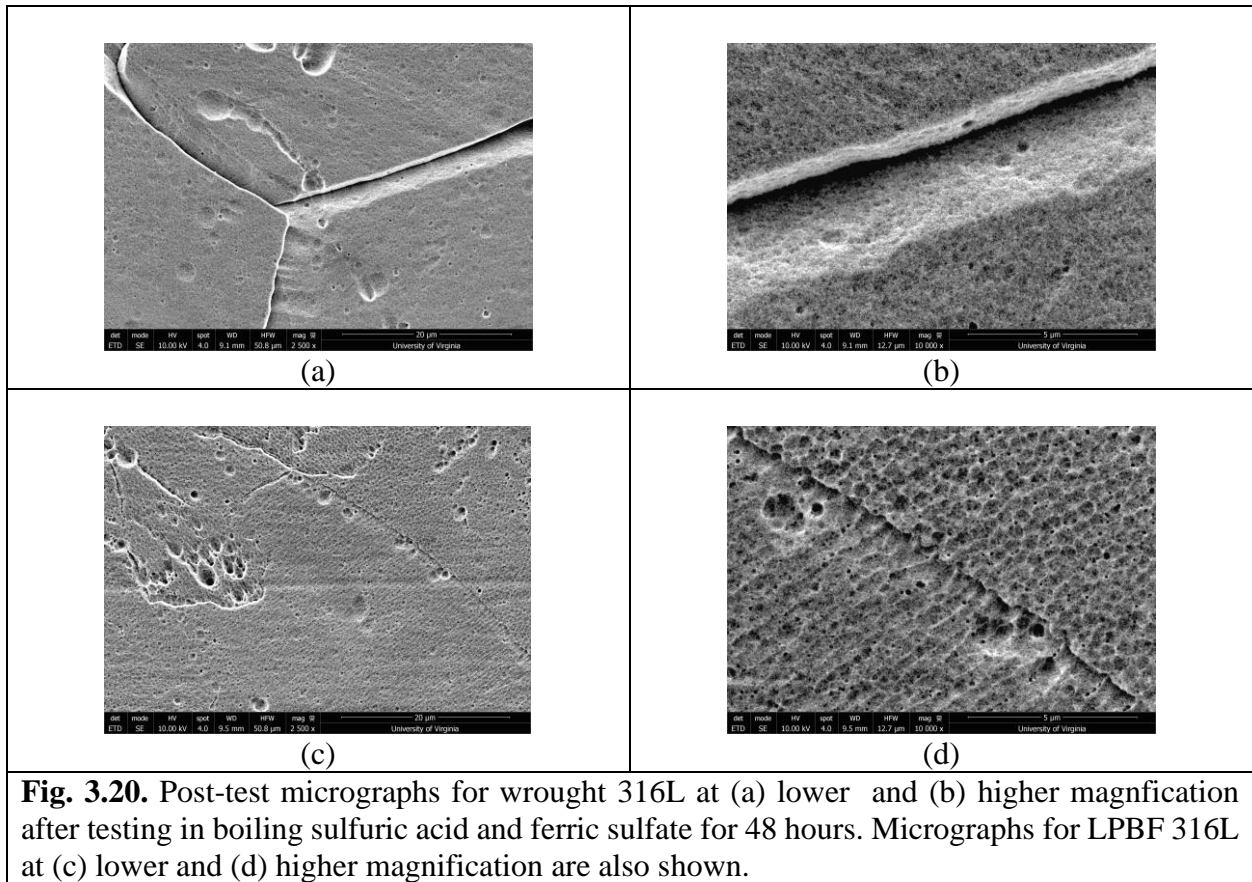
Fig. 3.21 shows the mass loss results after testing wrought and LPBF 316L in boiling 65 wt.% HNO_3 for 48 hours. It is seen that the corrosion rate for the wrought material is higher than that of the LPBF material.

Fig. 3.21. Mass loss results for wrought and LPBF 316L after testing in boiling nitric acid for 48 hours.
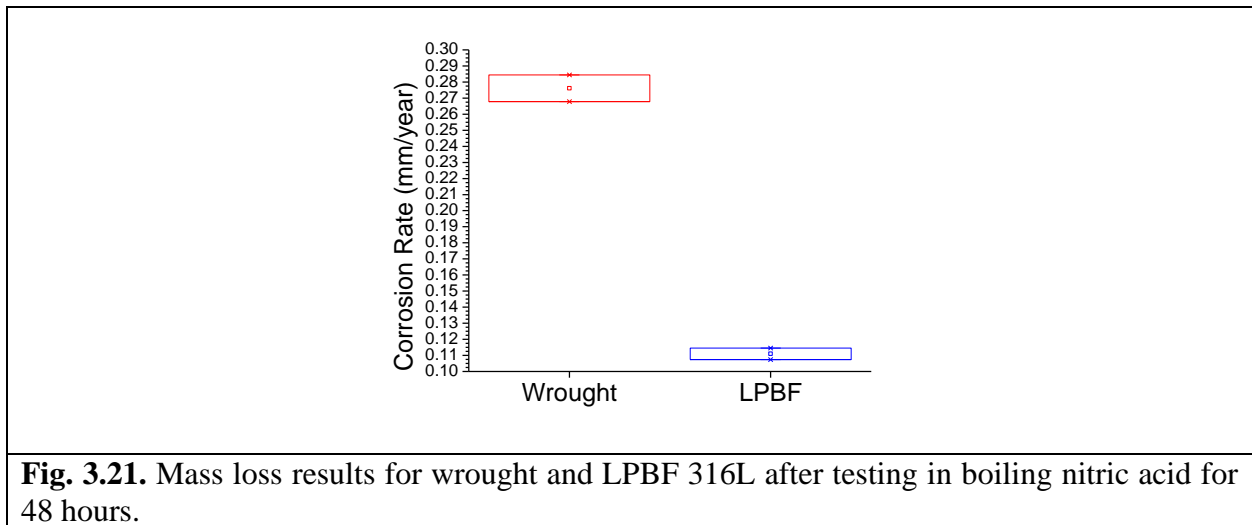
Fig. 3.22 shows the micrographs testing wrought and LPBF 316L surfaces after testing in boiling nitric acid for 48 hours. For the wrought material (Fig. 3.22a and Fig. 3.22b), while there are some pit-like structures within the grains, the attack is mostly uniform. In the case of the LPBF material (Fig. 3.22c and Fig. 3.22d), straw-like structures are seen suggesting the corrosion of cellular dendritic walls.

(a)

(b)

(c)

(d)
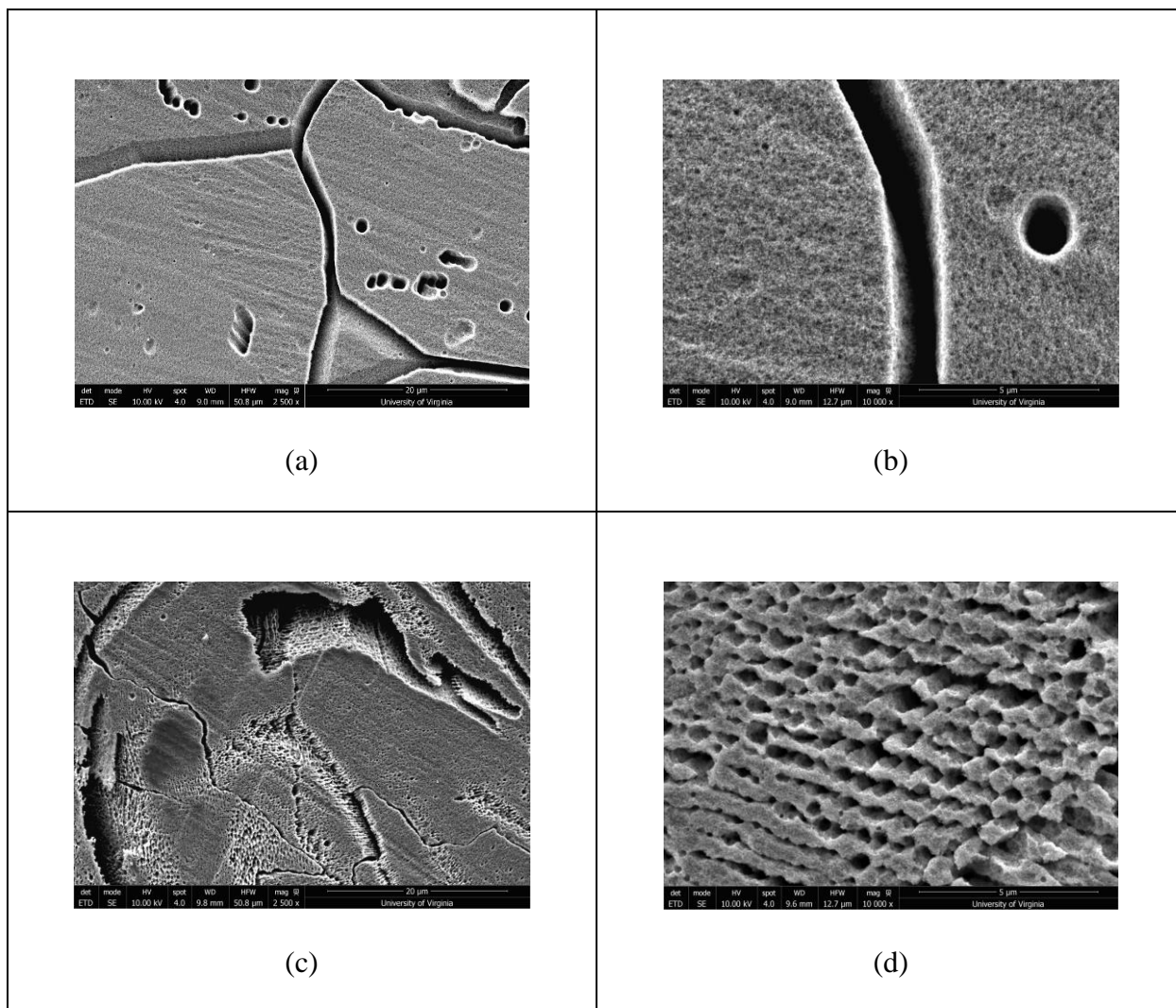
Fig. 3.22. Post-test micrographs for wrought 316L after testing in boiling 65 wt.% HNO_3 for 48 hours. Micrographs are shown for the wrought material at (a) lower and (b) higher magnification. Micrographs are also shown for LPBF material at (c)lower and (d) higher magnification.

Fig. 3.23 shows mass loss data for wrought and LPBF 316L after immersion in 6 wt.% FeCl3 for 72 hours. Mass loss values are seen to be higher in the wrought counterpart by greater than an order of magnitude.

Fig. 3.23. Mass loss for wrought and LPBF 316L after testing in 6 wt.% FeCl$_3$ for 72 hours.
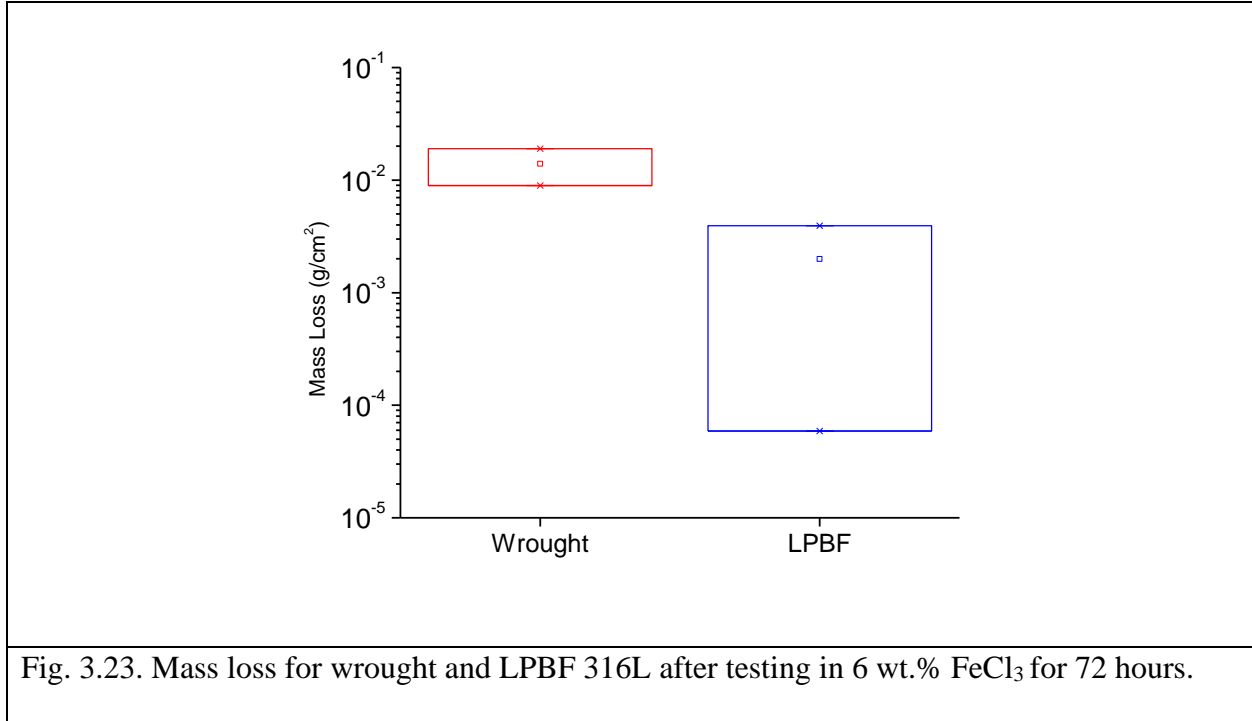
3.4.7 Behavior of LPBF 316L in Chloride Environments

Fig. 3.24 shows post-test micrographs for wrought and LPBF 316L after testing in 6 wt.% FeCl3 solution. Fig. 3.24a shows the pits in the wrought material, and Fig. 24b shows the morphology of the pit circled in Fig. 3.24b and crystallographic dissolution is observed. Fig. 3.24c shows the pits in the LPBF material, and from Fig. 3.24d, cellular structures can be seen to be experience preferential in the interior.

Fig. 3.24. Scanning electron micrograph of (a) surface and (b) pit interior of wrought 316L after immersion in 6 wt.% FeCl$_3$ for 72 hours. Micrographs for (c) surface and (d) pit interior are also shown for the LPBF material. Black circles are drawn on surface micrographs to highlight the pit being further imaged.
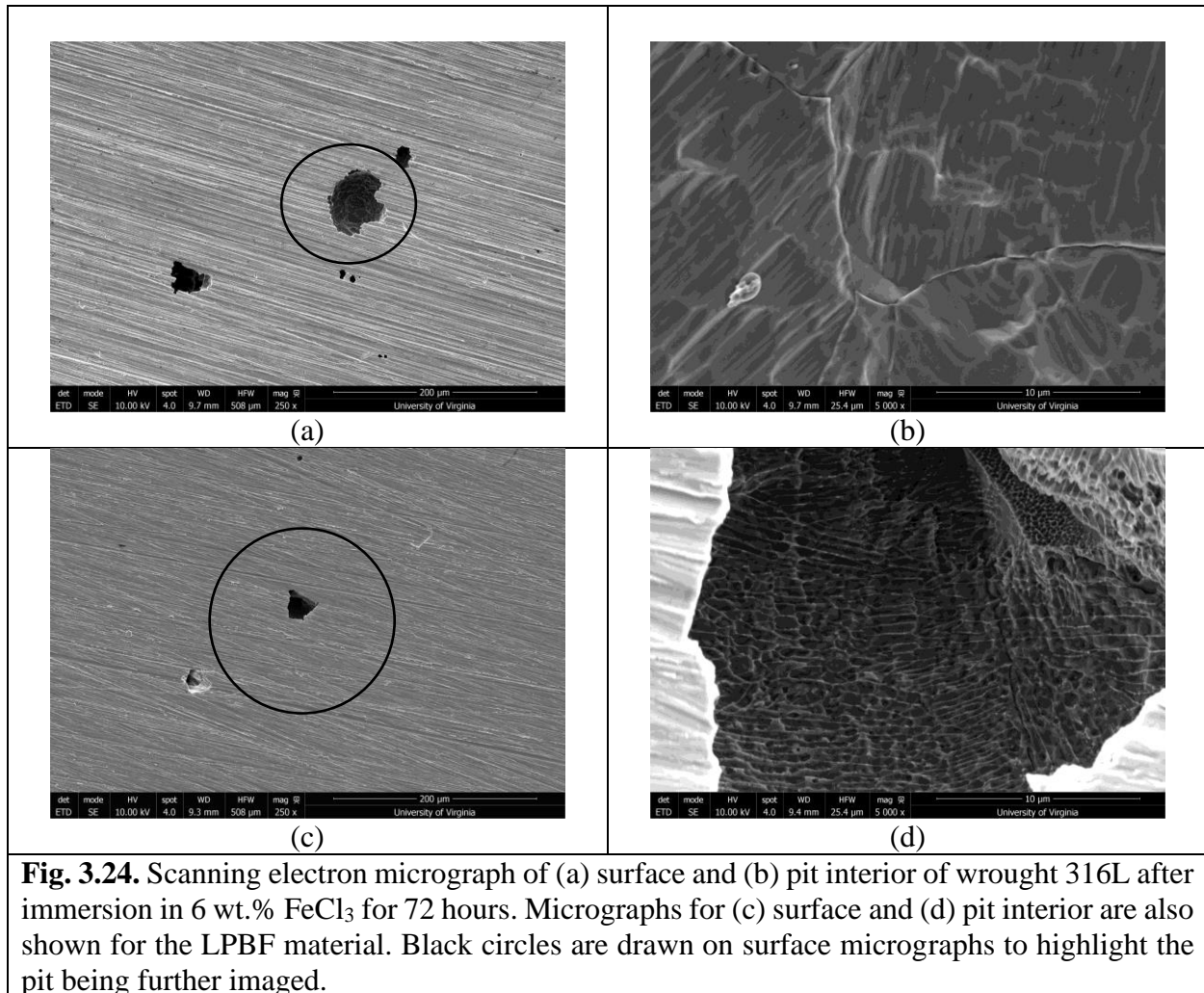
Fig. 3.25 shows micrographs of wrought (Fig. 3.25a) and LPBF (Fig. 3.25b) 316L after a potentiostatic hold at +0.6V vs. SCE in 0.6 M NaCl for 12 minutes. In comparing the two micrographs, there are more pits that formed on the wrought material.
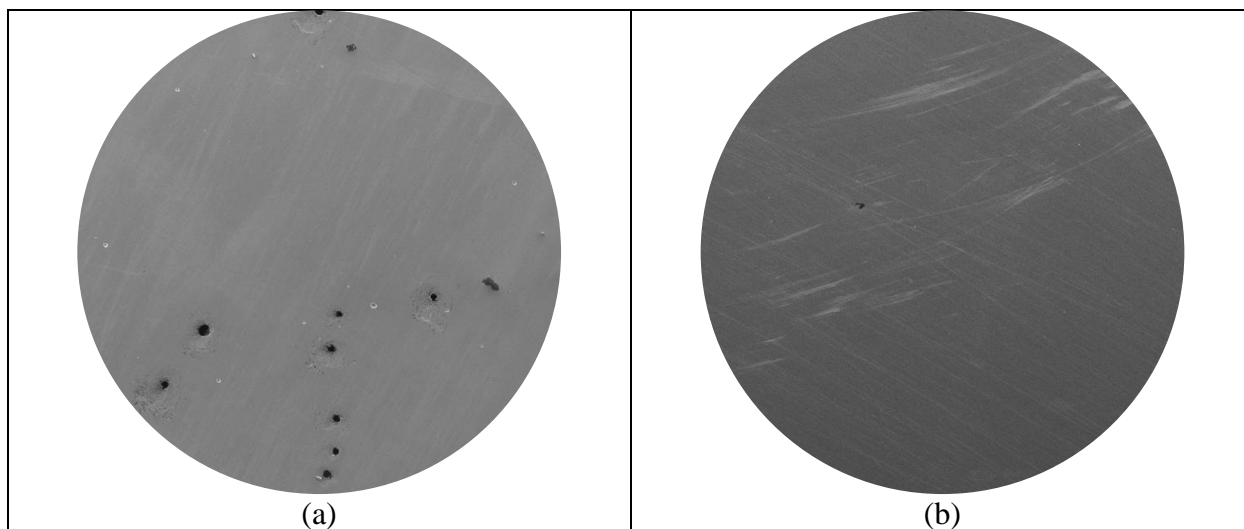
Fig. 3.25. Post-test micrograph of (a) wrought and (b) LPBF 316L after performing a potentiodynamic hold at 600 mV vs. SCE for 10 minutes. Each circular view has a diameter of 1 mm.

Fig. 3.26 shows morphologies of the surfaces inside the pits for wrought and LPBF 316L after a potentiostatic of 0.6 V vs. SCE in 0.6 M NaCl. The wrought material exhibits crystallographic dissolution while the interior of the cellular structures experience preferential dissolution.
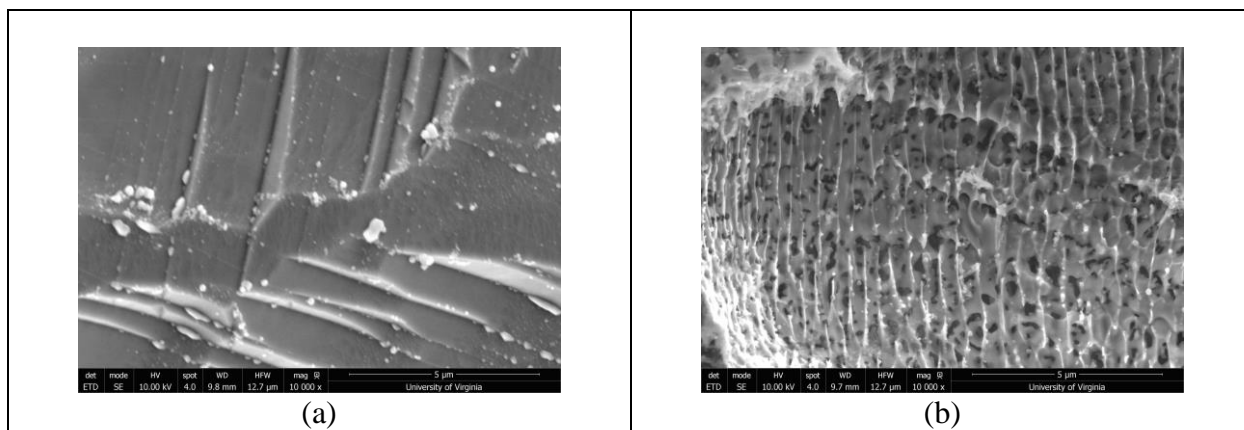
Fig. 3.26. Post-test micrograph of within a pit of (a) wrought and (b) LPBF 316L after performing a potentiodynamic hold at 600 mV vs. SCE for 12 minutes.
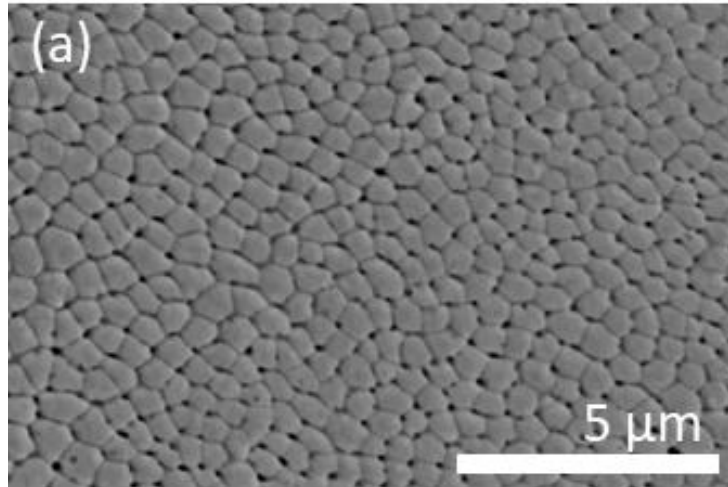
Figure 3.27. Post-test micrograph of LPBF 316L after potentiostatic hold (1.65 V vs. SCE) for 10 minutes in 0.6 M NaCl. Figure is adapted from [25].

3.5 Discussion

The discussion is set up in a way that initially discusses the behavior of LPBF and DED material at both high and low potentials. Hypotheses involving local differences in composition are validated by both compositional mapping and supplemental electrochemical behavior. Finally, the behavior in boiling acid environments and chloride environments are described in a way that further makes distinctions between active and transpassive behavior in LPBF material.

3.5.1 Behavior of LPBF 316L in Sulfuric Acid Environments

The potassium thiocyanate and sulfuric acid environment is known to provide an environment for austenitic stainless steel grades like 316 and 304 that induces active corrosion due to the depassivating characteristics of the thiocyanate ion [34,35]. This environment was ultimately

chosen due to its use in the double-loop potentiokinetic reactivation test [36–39]. Upon polarization, active dissolution (i.e., film-free) occurs with exponentially increasing current density with increased potential until a transition potential in which the oxidation behavior transitions due to the formation of a stable passive film. Although performed on LPBF material, Fig. 3.1. reflects this well-known behavior of austenitic steel in sulfuric acid and thiocyanate. From Fig. 3.2b, it is seen that there is preferential attack that takes place along the internal cores of cellular structures and nearly uniform dissolution is observed in the wrought material. Under open circuit conditions, while uniform corrosion along grain faces (Fig. 3.3a) takes place in wrought material, preferential corrosion along the cores of cellular structures is observed in the LPBF material (Fig. 3.3b). The use of thiocyanate in acidic environments (whether under open circuit conditions or polarized) ultimately shows that the core of cellular structures is susceptible to preferential attack relative to the cellular walls during active dissolution. This qualitative result is consistent with DL-EPR experiments performed on LPBF materials printed with different processing conditions [21].

When LPBF 316L is polarized to high potentials in sulfuric acid, transpassive dissolution is observed due to the rapid increase in current at approximately 1 V. vs. SCE as shown by Fig. 3.4. From the post-test micrograph from Fig. 3.5a, it is seen that wrought material exhibits nearly uniform attack with some preferential corrosion along grain boundaries. In the case of the LPBF materials (Fig. 3.6b), straw-like structures are seen in which preferential corrosion has taken place along boundaries of the cellular structures. Although the images are not reported in this study, this type of corrosion morphology was seen in the case in which LPBF 316L was potentiodynamically scanned from 0.1 V vs. SCE (where the formation of a passive film is observed) to 1.3 V vs. SCE (where transpassive dissolution takes place) in 1 M H_2SO_4 and 0.01 M KSCN.

These results show the effect of applied potential and the potential range on the resulting corrosion morphology. It seems that under active conditions/more relatively reducing potentials, preferential corrosion of cellular core takes place. Under transpassive conditions, a transition takes place and preferential corrosion takes place along the cellular walls. These phenomenological results are consistent with reports in multiple works of chromium and molybdenum enrichment at the cellular boundaries [10,45,46]. Studies have shown that increased chromium and molybdenum levels lead to lower rates of anodic dissolution in acidic solutions under reducing conditions (i.e., in the absence of a passive film). At the same time, preferential attack along cellular boundaries under transpassive conditions may be explained by higher chromium content due to the tendency of chromium to experience oxidation to the hexavalent state [29,30]. Additionally, this may be due to the oxidation of molybdenum into the molybdate ion which has been observed in Fe-Ni-Cr alloys in nitric acid conditions [44,47].

3.5.2 Evaluating the Effect of Microstructural Features on LPBF 316L Corrosion

Fig. 3.6 shows the underlying microstructure LPBF 316L. Whereas conventionally wrought austentic stainless steel typically have equiaxed grains, the LPBF material shows elongated grains [5,8,9]. It is observed that the LPBF material is nominally austenitic with traces of delta ferrite. Alloys such as 316L undergoes FA solidification in which ferrite may form due to its stability at high temperatures [19,48–50]. The observed microstructure with small traces of ferrite, however, may be due to the limited amount of time in which ferrite could have formed from the liquid state due to a high cooling rate from the LPBF process.

Whereas a single phase predominantly exists in the LPBF material, TEM images confirm the existence of cellular structures as well as the compositional heterogeneities that exist along these boundaries from STEM-EDS. Higher brightness at the cellular boundaries from HAADF

50

imaging (Fig. 3.7a) indicate that these boundaries have higher dislocation densities compared to the cores and the presence of dislocation walls and compositional heterogeneities have also been reported in other studies [10,45,46]. While the LPBF material seems to be nominally austenitic, the development of these non-equilibrium cellular structures stem from the rapid solidification process. Studies on solidification show that high solidification rates favor the formation of protrusions along the solid-liquid interface. Solute rejection from the solid phase then leads to the formation of structures such as cellular dendrites [48–51].

STEM-EDS maps and line scans show that there is a depletion of iron at the cellular boundaries. At the same time, it is seen that there is an enrichment of elements such as chromium, molybdenum, and nickel at the cellular boundaries. Multiple studies highlight the beneficial effect of these elements on the corrosion resistance on stainless iron-based alloys [40,42,43,52].

The effect of this compositional difference on LPBF corrosion was further investigated by performing supplemental tests on 317L stainless steel. Corresponding to the higher chromium, molybdenum, and nickel at LPBF cellular boundaries, 317L was used as a basis of comparison of electrochemical behavior to 316L. The relative behavior of 316L and 317L under both active and transpassive conditions are consistent with observations of LPBF behavior. Under active conditions in sulfuric acid and thiocyanate (Fig. 3.8), the current for 316L is consistently higher than that of 317L. Zero resistance ammetry further confirms that 316L is anodic with respect to 317L in the active state. This observation further confirms how alloy compositions of higher chromium, molybdenum, and nickel levels are less prone to rapid dissolution in acidic and active environments. At the same time, potentiodynamic scanning in sulfuric acid that induces transpassive dissolution shows higher current for 317L compared to 316L highlighting the change

in relative susceptibility at higher applied potentials. This result is consistent with work that reports

higher transpassive dissolution rates and is associated with chromium oxidation [53].

The observation of dislocation cell walls from HAADF imaging provides motivation to

study local strain distributions on observed selective corrosion. Multiple studies have shown the

detrimental of residual stress on corrosion properties [54]. However, it is noted that while higher

residual stresses increase corrosion susceptibility and the cell walls do experience preferential

corrosion at high potentials, the cell boundaries undergo less dissolution when tested under

conditions of active dissolution (i.e., in sulfuric acid with potassium thiocyanate). When annealing

was performed on wrought material to relieve the material of dislocations, it is observed that there

is little change in electrochemical behavior compared to the as-built wrought material. While these

results do not necessarily signify that these dislocation structures have no impact on the resulting

corrosion morphology, it seems that differences in composition have a more dominant effect on

selective corrosion.

3.5.3 Electrochemical Behavior of DED 316L

A major difference between the LPBF and DED microstructures is the greater observable

amountof ferrite in the DED material (Fig. 3.12). This distinct difference is likely due to the DED

process resulting in cooling rates that are 1-2 orders of magnitude lower than that of the LPBF

process [17–19]. Ferrite forms at higher temperatures for 316L and the greater presence of ferrite

may be due to lower cooling rates resulting in longer time periods where the material is at a

temperature range where formation of the ferritic phase is thermodynamically favorable

[19,49,50]. Multiple works have shown the presence of the ferrite phase in DED processing of

austenitic grades such as 304L and 316L [22]. From the EDS results, it is to be noted that the ferrite

phase has a higher content of chromium and molybdenum while having a lower content of nickel,

52

as would be expected. Nickel with its face centered cubic structure is known to be an austenitic stabilizer (and would thus partition to the austenite phase), whereas chromium and molybdenum (both of which have a body centered cubic structure) are ferritic stabilizers [19,48–50].

In viewing the corrosion morphology of the DED material after testing in sulfuric acid and potassium thiocyanate, it seen that there is preferential corrosion of the chromium and molybdenum depleted austenite matrix (Fig. 3.15a – 3.15f). Although multiple works have shown that nickel has beneficial effects on passivation, it seems that effects from chromium and molybdenum dominate, suppressing the dissolution of the ferrite phase [35]. Under transpassive conditions, the phase that preferentially dissolves switches to the skeletal-like ferritic phase. These observations in electrochemical behavior and corrosion morphology are consistent with results obtained from the duplex stainless steel 2205 which is known to have both austenitic and ferritic phases with the same relative differences in phase composition. The appendix shows supplemental work performed on 2205 and is consistent with that observed in the DED material particularly in the behavior of the austenitic and ferritic phases. Other works performed on duplex stainless steel have also reported the preferential transpassive dissolution of the ferrite phase and have connected it to the oxidation of chromium[53]. Although LPBF and DED 316L have dramatic differences in microstructure, great similarities exist between the two in how preferential corrosion is dictated by local differences in key alloying elements such as chromium and molybdenum.

3.5.4 Behavior of LPBF 316L in Boiling Acid Environments

The boiling acid experiments from conventional ASTM testing for intergranular corrosion susceptibility are another way of testing the effect of oxidizing behavior on corrosion phenomenology. For the wrought counterparts, it is seen that there is grain face corrosion in the material exposed to the boiling ferric sulfate/sulfuric acid solution (Fig. 3.20a and Fig. 3.20b)

while there is some attack along grain boundaries in the case of the boiling nitric acid environment (Fig 3.22a. and Fig. 3.22b.). For the wrought material, pits can also be seen within the grain face after exposure to boiling nitric acid and has been associated with MnS inclusions. This phenomenology has been documented in other works on the corrosion of wrought steels [55,56]. Although potential measurements of the working electrode were not made during these tests to avoid test solution contamination, it is well known in the literature that the open circuit potential of stainless steel in the boiling ferric sulfate/sulfuric acid test (where the Fe^{3+} ion is the oxidizer) is nearly 0.6 V vs. SCE [57,58]. The open circuit potential of austenitic stainless steels in the boiling nitric acid solution used is on the order of 0.75 – 1 V vs. SCE [57,58]. It can then be predicted that nitric acid has stronger oxidizing tendency compared to the solution of ferric sulfate and sulfuric acid. In observing the post-test micrographs, one must take note of the dramatic difference in corrosion morphology between the two environments. Whereas cellular boundary attack is observed in the nitric acid environment, preferential cellular core dissolution is observed in the ferric sulfate/sulfuric acid environment.

In sulfuric acid solution that contains ferric ions, the behavior of stainless steel consists of the continuous dissolution and re-formation of a protective film between the metal surface and the solution [57–59]. This formation of a chromium-rich passive film is coupled to the reduction of ferric (Fe^{3+}) ions [57,58]. In the case there is chromium depletion (such as observed in sensitized alloys), the corrosion current required to keep the film in repair is higher [57,58]. This higher current density leads to the observation of intergranular attack in grain boundary sensitized alloys [57,58]. Although there is no observation of intergranular attack in the LPBF material, it is observed that there is preferential corrosion along the interior of the cellular structure, and this result is consistent with observations of increased chromium level at the cellular boundaries as

shown in Fig. 3.20c and Fig. 3.20d. Like the rapid corrosion of chromium-depleted areas in sensitized alloys, this observed phenomenology agrees with predictions of chromium depletion along cellular cores of cellular dendritic structures.

Under boiling conditions in nitric acid, it has been shown that passivity is lost due to how reduction of the nitrate ion promotes the oxidation of chromium to the hexavalent state [47,55,57,58,60]. This accumulation of hexavalent chromium has also been shown to result in an increase in corrosion rate due to its reducing tendencies which is why testing solution is typically changed at 48-hour intervals [47,57,58]. In considering the effect of molybdenum on corrosion rates in nitric acid, it has been shown that a higher molybdenum level is detrimental to the corrosion behavior of austenitic stainless steel [44,47,57,58]. For example, in comparing the corrosion rate of 316 steel to that of 304 (which contains no molybdenum) in fuming nitric acid, the corrosion rate in the 316 variant was nearly twice the corrosion rate of 304 [57]. The preferential attack along cell boundaries under these highly oxidizing conditions agrees with the known enhancement of Mo and Cr along cellular dendritic boundaries.

It is interesting to compare the corrosion rates of LPBF alloys to that of the wrought counterpart in these key standardized tests. Fig. 3.19 and Fig. 3.21 show that the corrosion rates of the LPBF materials are less than that of the wrought material. This notable difference may be attributed to microstructural features in the wrought material that are not typically found in the LPBF material such as MnS inclusions [55,56]. Additionally, end grain corrosion due to the presence of non-metallic constituents along the rolling direction has been shown to be detrimental to the behavior of conventionally wrought steel in boiling nitric acid environments [55,56]. While the elimination of these inclusions in the additive process has been associated with observations

of increasing pitting resistance, the lower corrosion rate of LPBF 316L in nitric acid may also be due to this microstructural feature [15].

The ferric sulfate test was originally developed due to the labor involved with performing the boiling nitric acid test in determining susceptibility to intergranular corrosion as well as the concern of increased oxidizing behavior from Cr^{6+} formation [47,57,58]. Although results from either of these two tests provide insight into the IGC susceptibility of conventionally wrought austenitic stainless steel, the non-equilibrium microstructure of LPBF 316L results in two different corrosion morphologies between these two testing environments. In predicting behavior in terms of selective/non-uniform corrosion, these tests show how differences in oxidizing behavior and local differences in composition can dramatically alter corrosion morphology.

3.5.5 Behavior of LPBF 316L in Chloride Environments

The contrast of behavior at low and high potential has also been extended to chloride environments in acidic to near neutral pH. Chloride favors the formation of corrosion pits due to localized breakdown of the passive film and this is seen from micrographs of wrought (Fig, 3.24a) and LPBF 316L (Fig. 3.24c) after testing in ferric chloride solution. In the case of the wrought material (Fig. 3.24b), uniform crystallographic dissolution is observed within the pits. For the LPBF material, the cellular structures are highlighted, and it seen that there is preferential attack along the cores of cellular structures (Fig. 3.24d). These observed pit morphologies are also observed after potentiostatic holds in 0.6 M NaCl (Fig. 3.26a and Fig. 3.26b)

In chloride environments, pits form due to localized breakdown of passive film. Localized galvanic coupling takes place due to diffusion limitations that lead to difference in oxidizer (i.e., oxygen or ferric ions) concentration in which areas of higher oxidizer concentration are more cathodic [61–63]. The interior of a pit becomes depleted of oxidizer and effectively becomes

anodic. The accumulation of metal ions promotes hydrolysis which results in the formation of metal hydroxide and H^+ effectively acidifying the interior of a corrosion pit [61-63].

The mechanism of pitting corrosion shows that local activation takes place due to the development of an acidic environment. Therefore, it is logical to see corrosion morphology consistent with mechanisms of active dissolution within the interior of a pit. Observations of preferential cellular core attack within corrosion pits in both sodium chloride and ferric chloride environments are consistent with increased chromium and molybdenum at the cell boundaries as well as what has been observed for LPBF behavior in sulfuric acid and thiocyanate.

0.6 M NaCl experiments at 1.65 V vs. SCE again shows a fundamental difference in corrosion behavior regarding the cellular structures and high applied potentials that induce transpassive dissolution. Fig. 3.27 reveals that at this high potential, the walls of the cellular structures undergo preferential attack. Similar to the other environments explored in this study, this behavior is associated with high chromium content at the cellular boundaries.

These series of experiments show the interplay between compositional heterogeneities and electrochemical environment. Whether it is through the DED or LPBF process, the solidification process leads to heterogenous microstructures that drive selective corrosion. From the presence of ferrite in DED to the formation of cellular dendritic structures in LPBF, these corrosion tests show the impact of chromium and molybdenum segregation on the corrosion of additively manufactured 316L stainless steel. These tests show a dramatic difference in corrosion morphology at high potential ranges and low potential ranges for various environments and ultimately provide motivation in transferring information from standardized tests to in-service performance.

Although these studies highlighted the impact of local alloy chemistry on electrochemical behavior, additively manufactured alloys whether through LPBF or DED have complex

57

microstructures. Examples include lack-of-fusion pores, oxide inclusions, and melt pool boundaries. Other studies have highlighted the impact of these features on corrosion behavior [15,20–22,25,64]. While these experiments showed the impact that elemental segregation plays in the selective corrosion of additively manufactured stainless steel, it is important to take a holistic view that incorporates AM defects across all length scales to more fully understand AM corrosion.

3.6 Conclusions

- Transpassive dissolution promotes the dissolution of cellular boundaries in LPBF 316L, whether it is through potentiodynamic scans in 1 M H_2SO_4, exposure to boiling 65 wt.% nitric acid, or a 1.3 V vs. SCE potentiostatic hold in 0.6 NaCl.

- Transpassive dissolution also promotes dissolution of the ferritic phase in DED 316L

- Active dissolution preferentially takes place at the core of cellular structures, whether it is through potentiodynamic scans in sulfuric acid/thiocyanate environments or pitting in chloride solutions.

- In the case of DED 316L, active dissolution preferentially takes place along the austenitic phase over the ferritic phase.

- Chemical heterogeneities from EDS techniques suggest the significant impact of elements such as chromium and molybdenum on preferential corrosion at high and low potentials.

3.7 Appendix

Supplemental experiments were performed on 2205 stainless steel to emphasize the difference in behavior between the austenitic and ferritic phases in a stainless steel alloy containing both phases.

The transpassive behavior of 2205 in 1 M H_2SO_4 was investigated through potentiodynamic scanning. Samples were ground to 1200 grit. After an open circuit potential hold

for 30 minutes, the working electrode was scanned from 0.05 V below the open circuit potential to 1.2 V vs. SCE. The active behavior of 2205 in 1 M H_2SO_4 was investigated with the addition of 0.01 M KSCN. Scanning electron microscopy was performed to assess corrosion morphology in both cases.

Potentiodynamic scanning in sulfuric acid and thiocyanate (Fig. 3.28) shows active dissolution in the 2205 material. In investigating the post test micrographs (Fig. 3.29a), it is seen that certain microstructural features undergo a greater amount of dissolution. EDS maps (Fig. 3.29b – Fig. 29f.) reveal that the phase that undergoes preferential corrosion (most likely the austenitic phase) is depleted in chromium and molybdenum while being rich in nickel. The phase that undergoes less corrosion (most likely the ferritic phase) is enriched with chromium and molybdenum while being depleted of nickel.
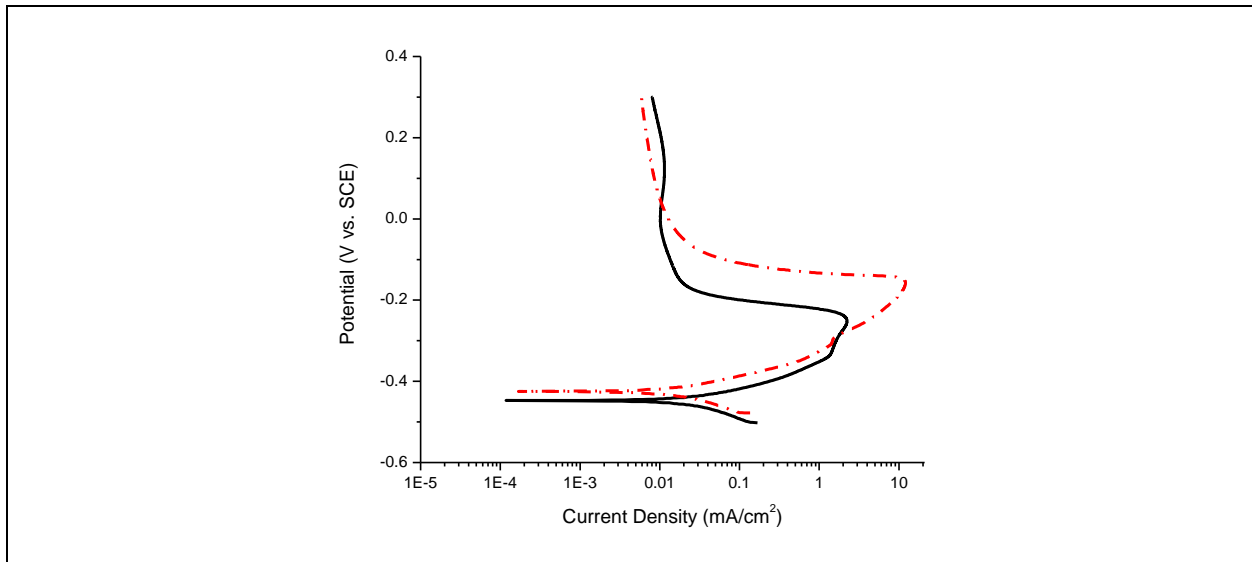
Fig. 3.28. Polarization scan of wrought 316L and 2205 in 1 M H_2SO_4 and 0.01 M KSCN.
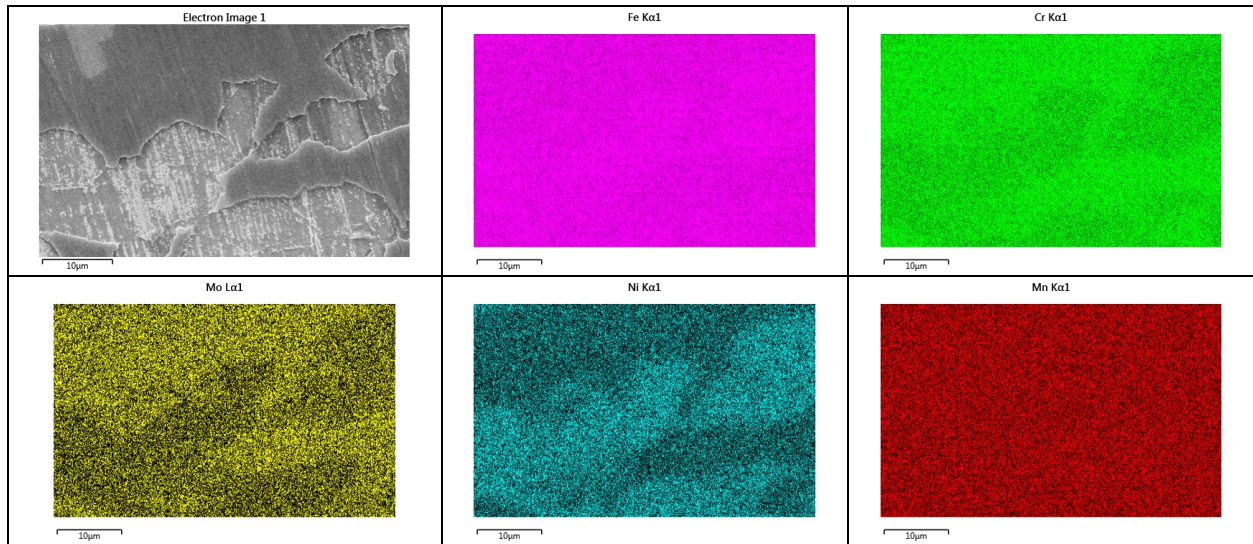
Fig. 3.29. (a) Scanning electron micrograph 2205 after testing in 1 M H_2SO_4 and 0.01 M KSCN. EDS compositional maps of (b) iron, (c) chromium, (d) molybdenum, (e) nickel, and (f) manganese are shown.

Potentiodynamic scanning in sulfuric acid (Fig. 3.30) reveals transpassive dissolution in the 2205 material above 1 V vs. SCE. In investigating the post test micrographs (Fig. 3.31a), it is seen that certain microstructural features undergo more dissolution. EDS maps (Fig. 3.31b – Fig. 3.31f) reveal that the phase that undergoes preferential corrosion (most likely the ferritic phase) is rich in chromium and molybdenum while the phase that undergoes less corrosion (most likely the austenitic phase) is enriched in nickel.
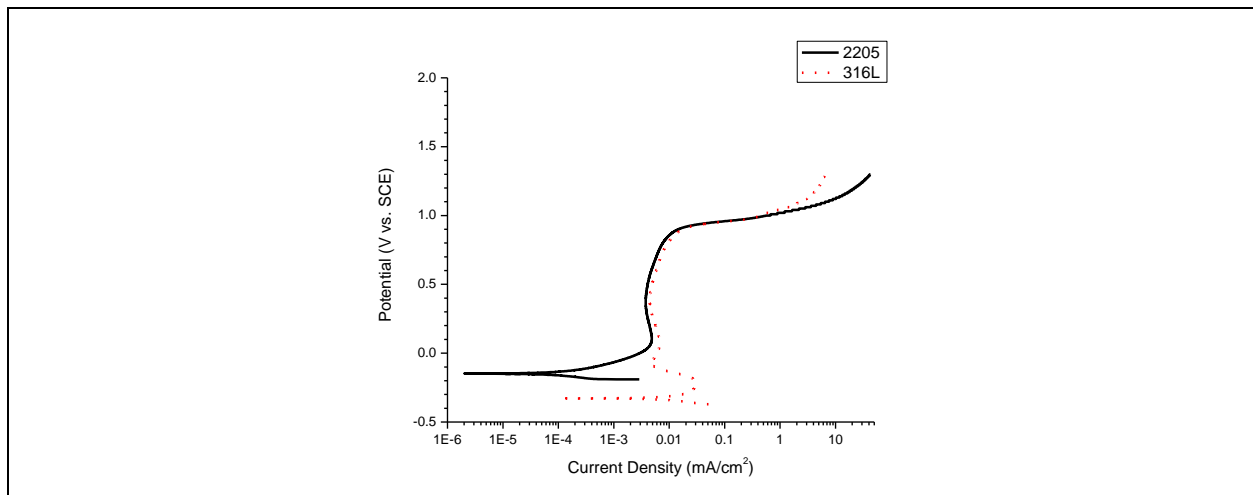
Fig. 3.30. Polarization scan of wrought 316L and 2205 in 1 M H_2SO_4.
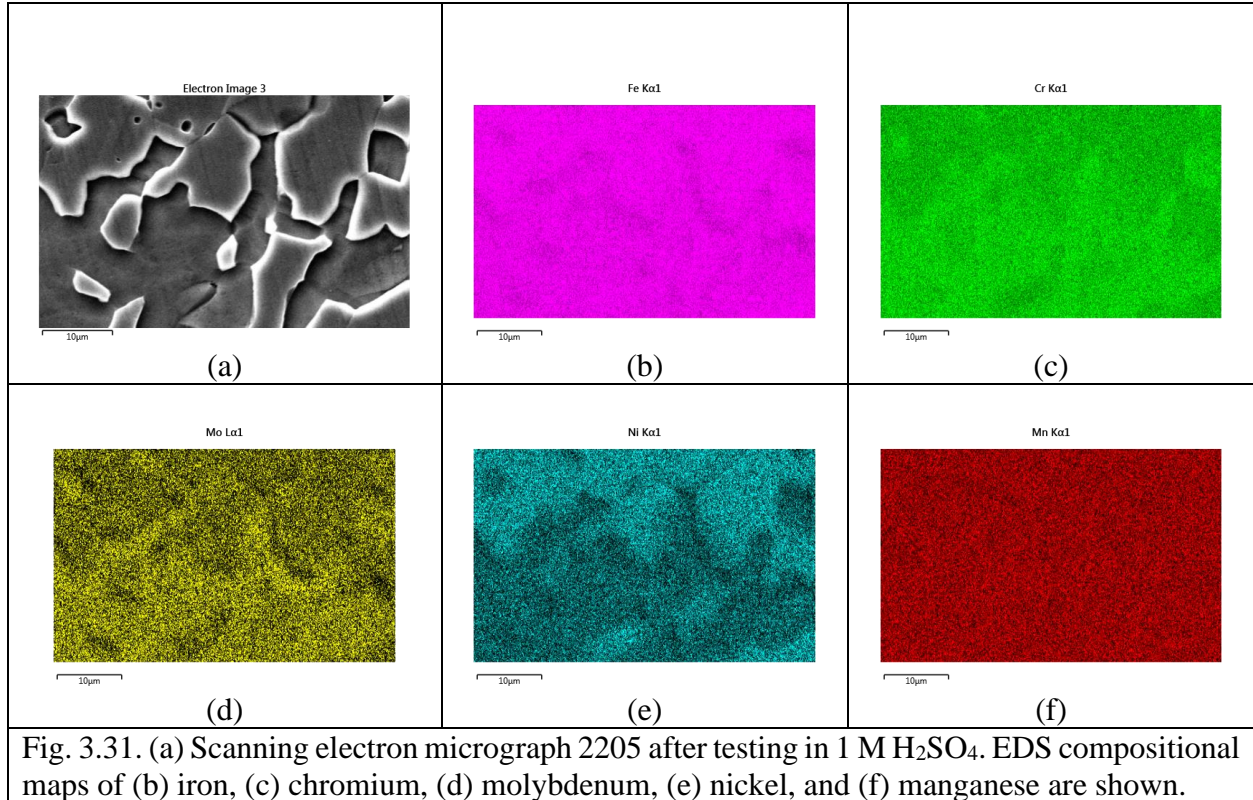
Fig. 3.31. (a) Scanning electron micrograph 2205 after testing in 1 M H_2SO_4. EDS compositional maps of (b) iron, (c) chromium, (d) molybdenum, (e) nickel, and (f) manganese are shown.

3.8 Acknowledgements

3.9 Citations

1. D. Herzog, V. Seyda, E. Wycisk, and C. Emmelmann, Acta Materialia **117**, 371 (2016).
2. H. Hack, R. Link, E. Knudsen, B. Baker, and S. Olig, Additive Manufacturing **14**, 105 (2017).
3. H. Sahasrabudhe, S. Bose, and A. Bandyopadhyay, in *Advances in Laser Materials Processing* (2018), pp. 507–539.
4. T. M. Mower and M. J. Long, Materials Science and Engineering A **651**, 198 (2016).
5. K. M. Mantrala, M. Das, V. K. Balla, Ch. S. Rao, and V. V. S. Kesava Rao, Front Mech Eng **1**, 1 (2015).
6. F. Bartolomeu, M. Buciumeanu, E. Pinto, N. Alves, O. Carvalho, F. S. Silva, and G. Miranda, Additive Manufacturing **16**, 81 (2017).
7. D. D. Gu, W. Meiners, K. Wissenbach, and R. Poprawe, **57**, 133 (2013).

8. M. Ziętala, T. Durejko, M. Polański, I. Kunce, T. Płociński, W. Zieliński, M. Łazińska, W. Stępniowski, T. Czujko, K. J. Kurzydłowski, and Z. Bojar, Materials Science and Engineering A **677**, 1 (2016).

9. E. Yasa and J. P. Kruth, Procedia Engineering **19**, 389 (2011).

10. U. S. Bertoli, B. E. Macdonald, and J. M. Schoenung, Materials Science & Engineering A **739**, 109 (2019).

11. P. Hanzl, M. Zetek, T. Bakša, and T. Kroupa, Procedia Engineering **100**, 1405 (2015).

12. K. N. Amato, S. M. Gaytan, L. E. Murr, E. Martinez, P. W. Shindo, J. Hernandez, S. Collins, and F. Medina, Acta Materialia **60**, 2229 (2012).

13. E. Liverani, S. Toschi, L. Ceschini, and A. Fortunato, Journal of Materials Processing Technology **249**, 255 (2017).

14. T. Simson, A. Emmel, A. Dwars, and J. Böhm, Additive Manufacturing **17**, 183 (2017).

15. X. Lou, P. L. Andresen, and R. B. Rebak, Journal of Nuclear Materials **499**, 182 (2018).

16. G. Sander, J. Tan, P. Balan, O. Gharbi, D. R. Feenstra, L. Singer, S. Thomas, R. G. Kelly, J. R. Scully, and N. Birbilis, Corrosion **74**, 1318 (2018).

17. G. T. Gray, V. Livescu, P. A. Rigg, C. P. Trujillo, C. M. Cady, S.-R. Chen, J. S. Carpenter, T. J. Lienert, S. J. Fensin, C. M. Knapp, R. A. Beal, B. Morrow, O. F. Dippo, D. R. Jones, D. T. Martinez, and J. A. Valdez, *L2 Milestone 5433: Characterization of Dynamic Behavior of AM and Conventionally Processed Stainless Steel (316L and 304L)* (Los Alamos, NM (United States), 2016).

18. G. R. Mirshekari, E. Tavakoli, M. Atapour, and B. Sadeghian, Materials & Design **55**, 905 (2014).

19. J. W. Elmer, S. M. Allen, and T. W. Eagar, Metallurgical Transactions A **20**, 2117 (1989).

20. D. A. Macatangay, S. Thomas, N. Birbilis, and R. G. Kelly, **74**, 153 (2018).

21. D. A. T. Macatangay, J. M. Conrades, K. L. Brunner, and R. G. Kelly, Corrosion **78**, 13 (2022).

22. M. A. Melia, H.-D. A. Nguyen, J. M. Rodelas, and E. J. Schindelholz, Corrosion Science **152**, 20 (2019).

23. J. R. Trelewicz, G. P. Halada, O. K. Donaldson, and G. Manogharan, Jom **68**, 850 (2016).

24. M. Laleh, A. E. Hughes, W. Xu, N. Haghdadi, K. Wang, P. Cizek, I. Gibson, and M. Y. Tan, Corrosion Science **161**, 108189 (2019).

25. J. J. Sopcisak, M. Ouyang, D. A. Macatangay, B. P. Croom, T. J. Montalbano, D. J. Sprouster, R. G. Kelly, J. R. Trelewicz, R. Srinivasan, and S. M. Storck, JOM **74**, 1719 (2022).

26. G. W. Kubacki, J. P. Brownhill, and R. G. Kelly, Corrosion **75**, 1527 (2019).

27. G. N. Nigon, O. B. Isgor, and S. Pasebani, Journal of The Electrochemical Society **167**, 141508 (2020).

28. G. Song, Corrosion Science **47**, 1953 (2005).

29. A. Fattah-Alhosseini and N. Attarzadeh, International Journal of Electrochemistry **2011**, 521384 (2011).

30. S. Khan, V. Kain, and A. V. R. Reddy, Corrosion **70**, 19 (2014).

31. A. S. A262, ASTM International, West Conshohocken, PS **01**, 1 (2014).

32. S. S. Parts, S. Surfaces, E. Corro-, C. C. Resis-, and F. C. Solution, 1 (2016).

33. (n.d.).

34. W. Li, Carnegie Mellon University (2012).

35. W. Li and P. C. Pistorius, Journal of The Electrochemical Society **159**, C513 (2012).

36. M. Momeni, M. H. Moayed, and A. Davoodi, Corrosion Science **52**, 2653 (2010).

37. A. P. Majidi and M. A. Streicher, CORROSION **40**, 584 (1984).
38. T. Amadou, H. Sidhom, and C. Braham, Metallurgical and Materials Transactions A **35**, 3499 (2004).
39. R. B. Rebak and S. W. Dean, Corrosion **76**, 742 (2020).
40. S. J. Kropschot and J. Doebrich, Usgs 1 (2010).
41. B. Stypula and J. Banaś, Electrochimica Acta **38**, 2309 (1993).
42. Y. H. Yau and M. A. Streicher, Corrosion **47**, 352 (1991).
43. H.-Y. Ha, T.-H. Lee, J.-H. Bae, and D. Chun, Metals (Basel) **8**, 653 (2018).
44. A. H. Seikh, H. Halfa, and M. S. Soliman, Metals (Basel) **11**, 852 (2021).
45. Y. Zhong, L. Liu, S. Wikman, D. Cui, and Z. Shen, Journal of Nuclear Materials **470**, 170 (2016).
46. P. Deng, H. Yin, M. Song, D. Li, Y. Zheng, B. C. Prorok, and X. Lou, JOM **72**, 4232 (2020).
47. F. Balbaud-Célérier, N. Gruet, B. Gwinner, and P. Laghoutaris, in *Nuclear Corrosion* (Elsevier, 2020), pp. 301–340.
48. H. Inoue, T. Koseki, S. Okita, and M. Fuji, Welding International **11**, 876 (1997).
49. H. INOUE and T. KOSEKI, Nippon Steel Technical Report (2007).
50. H. Inoue and T. Koseki, Acta Materialia **124**, 430 (2017).
51. M. Roussel, X. Sauvage, M. Perez, D. Magné, A. Hauet, A. Steckmeyer, and M. Vermont, Materialia (Oxf) **4**, 331 (2018).
52. G. O. Ilevbare and G. T. Burstein, Corrosion Science **43**, 485 (2001).
53. M. Långberg, C. Örnek, J. Evertsson, G. S. Harlow, W. Linpé, L. Rullik, F. Carlà, R. Felici, E. Bettini, U. Kivisäkk, E. Lundgren, and J. Pan, Npj Materials Degradation **3**, 1 (2019).
54. O. Takakuwa and H. Soyama, Advances in Chemical Engineering and Science **05**, 62 (2015).
55. M. KANEKO and S. ABE, Tetsu-to-Hagane **81**, 857 (1995).
56. M. TAKEUCHI and G. O. H. WHILLOCK, Journal of Nuclear Science and Technology **41**, 702 (2004).
57. In *Corrosion of Weldments* (ASM International, 2006), pp. 203–216.
58. In *Corrosion: Fundamentals, Testing, and Protection* (ASM International, 2003), pp. 568–571.
59. (n.d.).
60. B. Laurent, N. Gruet, B. Gwinner, F. Miserque, K. Rousseau, and K. Ogle, Electrochimica Acta **258**, 653 (2017).
61. N. U. Obeyesekere, Trends in Oil and Gas Corrosion Research and Technologies 215 (2017).
62. A. Pardo, M. C. Merino, A. E. Coy, F. Viejo, R. Arrabal, and E. Matykina, Corrosion Science **50**, 1796 (2008).
63. H. Li, Z. Jiang, Y. Yang, Y. Cao, and Z. Zhang, International Journal of Minerals, Metallurgy and Materials **16**, 517 (2009).
64. D. A. Macatangay, G. W. Kubacki, and R. G. Kelly, JOM (2022).

4 The Effect of Processing on LPBF 316L Selective Corrosion

4.1 Abstract

Progress in additive manufacturing technology such as laser powder bed fusion (LPBF) has allowed for the use of processing parameters to ultimately control material features such as microstructure and mechanical properties. However, limited studies have related corrosion properties to processing. In this study, the double loop potentiokinetic reactivation (DLEPR) test was used construct trends between LPBF processing and surface reactivation. Volumetric energy density (VED) was used as a guide for testing a broad array of materials. Though limitations in the utility of VED discussed, it was found that LPBF material printed at lower VED generally have a greater propensity for reactivation. The reactivation behavior is further discussed in the context of the complex LPBF microstructure.

4.2 Introduction

Laser powder bed fusion (LBPF) is an additive manufacturing technique that uses a high-energy laser to melt powder on a build plate which undergoes rapid solidification on a layer-by-layer basis [1–3]. The application of the LPBF process to austenitic stainless steels such as 316L presents opportunities in microstructure control and the refinement of mechanical properties like strength and ductility [4–9]. Advances in additive manufacturing have allowed for the understanding of the association between processing parameters and material features such as the presence of lack of fusion (LOF) defects and grain refinement [10,11].

The volumetric energy density (VED) is a value that describes the energy input during a LPBF build and is related to processing parameters such as power (P), scan speed (v), hatch spacing (h), and layer thickness (t) by the Equation 1[12,13].

$$VED = \frac{P}{vht}$$

Equation 2

Studies have shown how low VED input tends to lead to the formation of defects such as unmelted powder and porosity due to incomplete fusion of material during the solidification process [10,12,14–16]. High VED tends to lead to the formation of keyholing. Rapid solidification from the LPBF process leads to the formation of cellular dendritic structures with boundaries that are enriched in critical alloying elements such as chromium and molybdenum [17–20]. Works have also shown how there is greater depletion of these elements under conditions that promote more rapid solidification such as higher scan speed and is associated to be due to less diffusional mixing in the liquid state [21]. While VED may be interpreted as a thermodynamic value, it should not be interpreted as a kinetic input value and multiple studies have criticized the blind use of VED in predicting microstructure and mechanical properties of LPBF alloys. The dramatic impact that processing parameters have on microstructure provides motivation to study and draw generalizations on the effect of LPBF processing on corrosion behavior.

This manuscript is focused on the selective corrosion behavior of LPBF 316L specifically in terms of active behavior. The dependence of propensity for surface reactivation on processing parameters is assessed through the double loop potentiokinetic reactivation test. Post-test microscopy as well as modifications to the traditional EPR test are employed to validate the results from the DL-EPR test in predicting susceptibility to localized reactivation along a surface. Volumetric energy density is used as a guide for testing a broad array of LPBF materials printed at varying parameters to create connections between conditions of rapid solidification during the AM process to depassivation behavior.

4.3 Experimental

4.3.1 Material Information

AISI 316L stainless steel powder manufactured by EOS (EOS GmbH -Electro Optical Systems, Krailing, Germany, EOS art.-no. 9011-0032) with a spherical particle size distribution of10-53 μm was used in this study; see Table 1 for the chemical composition. Square prism samples with dimensions 20 mm x 20 mm x 30 mm were manufactured using an EOS GmbH M290DMLS-SLM system, which utilizes a 1060-1100 nm, 200 W continuous Yb fiber laser with a fixed 100 μm spot size and an inert argon-purged atmosphere. Table 4.1 shows the composition of the powder used for the build. Table 4.2 shows the printing parameters used in this study.

Table 4.1. Composition of wrought 316L material and powder used for the LPBF 316L.

Element	Analysis Method	LPBF Powder Composition (Wt. %)
Fe	-	Balance
Cr	ICP	18.62
Ni	ICP	14.04
Cu	ICP	< 0.1
Mn	ICP	1.65
Si	ICP	0.37
Mo	ICP	2.77
C	Combustion	0.007
S	Combustion	0.005
P	ICP	< 0.010
N	Fusion	0.07

Table 4.2. Printing parameters for LPBF 316L Samples

Identification	A1	A2	A3	A4	A5	A6	A7	A8	A9	A10	A11
Power (W)	182.5	205	95	105	155	134	110	195	220	199	255
Velocity (mm/s)	960	960	1510	953	1280	700	1400	1083	755	2286	880
Hatch (mm)	0.11	0.11	0.06	0.08	0.09	0.12	0.05	0.09	0.11	0.03	0.09
Layer Thickness (mm)	0.04	0.04	0.02	0.02	0.02	0.02	0.02	0.02	0.02	0.02	0.02
Volumetric Energy Density (J/mm³)	42	48	52	67	67	77	77	100	132	132	161

4.3.2 Double Loop Potentiokinetic Reactivation (DL-EPR) test

The DL-EPR test was performed to determine the susceptibility of the passive film on LPBF to reactivation. All exposed surfaces were ground to 1200 grit in the direction that is perpendicular to the build direction. The sample was exposed under open circuit conditions for 30 minutes. A potentiodynamic scan was performed starting at the open circuit potential before scanning to 0.3 V vs. SCE at a scan rate of 1.67 mV/s. Upon reaching a value of 0.3 V vs. SCE, the potential was scanned in the reverse direction to the original open circuit potential. The scan strategy is schematically depicted in Fig. 4.1a. A degree of reactivation (DOR) is expressed as the ratio of the peak reactivation current during the reverse scan to the peak activation current from the forward scan as schematically expressed in Fig. 4.1b. The DOR value is used to quantify susceptibility to passive film under activation conditions.
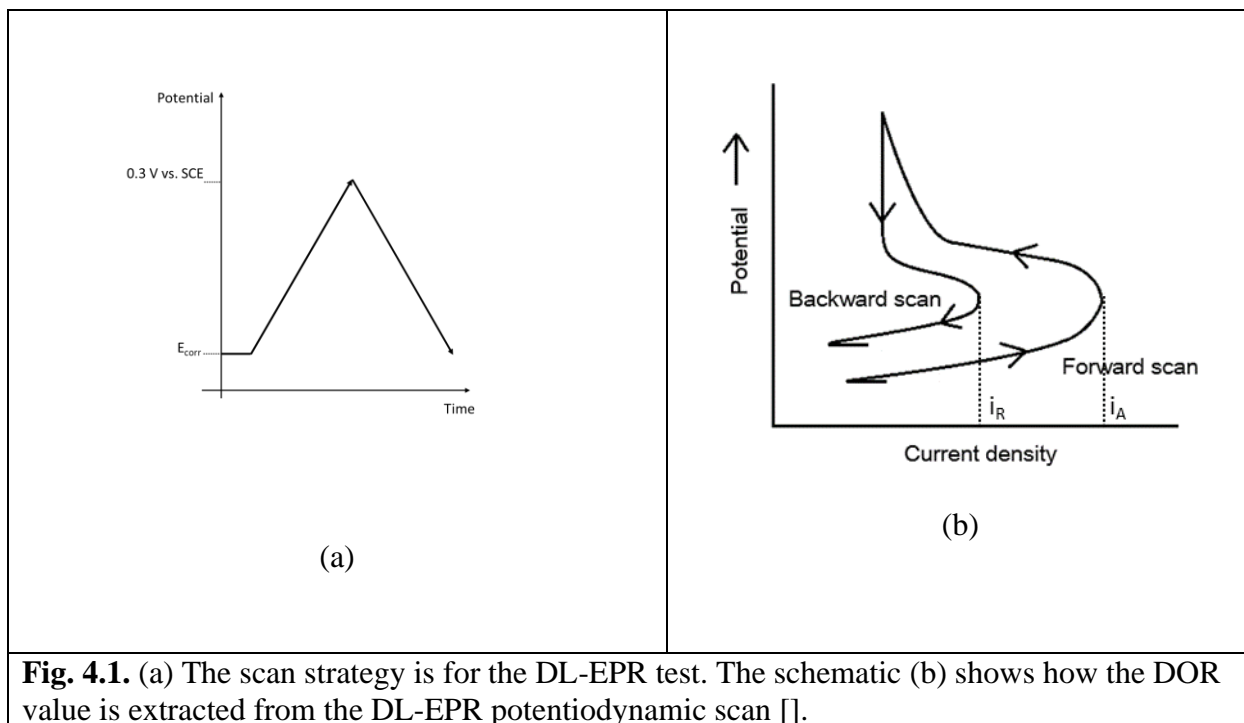
Fig. 4.1. (a) The scan strategy is for the DL-EPR test. The schematic (b) shows how the DOR value is extracted from the DL-EPR potentiodynamic scan [].

4.3.3 Modified Single Loop Potentiokinetic Reactivation Test

Due to how active corrosion takes place during the forward scan of the DL-EPR test, additional experiments were performed to validate the use of the DL-EPR test in assessing reactivation and show microstructural features that were more prone to depassivation. Sample AX and AY were each exposed to a 30-miute and 2-hour hold under open circuit conditions. A potentiodynamic scan was initiated from +0.1 V vs. SCE and scanned down to the original open circuit potential at a rate of 1.67 mV/s. Surfaces were characterized with scanning electron microscopy. For the rest of this study, this method will be referred to as the SL-EPR test.
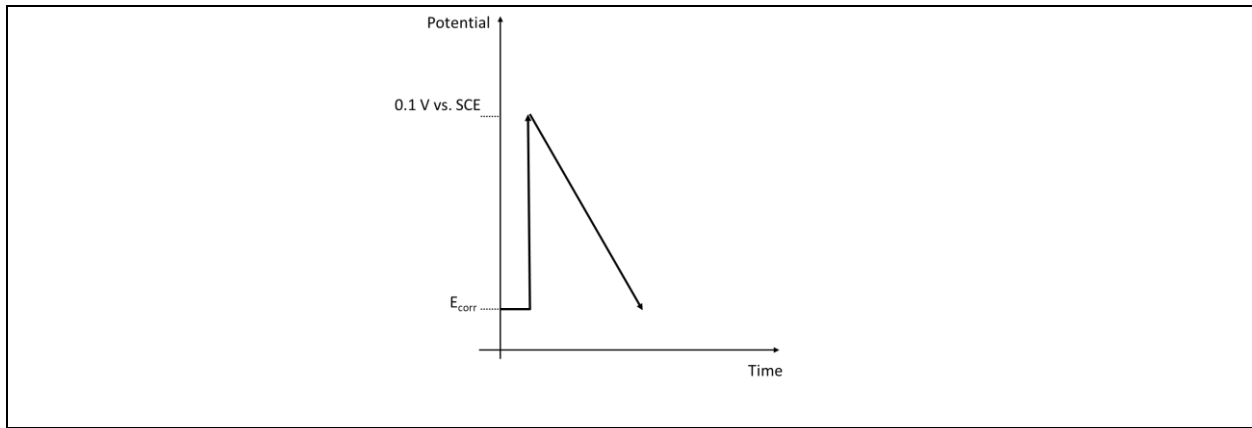
Fig. 4.2. Schematic showing scan strategy for modified SL-EPR test.

4.3.4 Potentiostatic Active Behavior of Passivated LPBF 316L

Using sample A4 and A5, another experiment in which the samples were exposed under open circuit conditionsfor 30 min. Starting from a potential of +0.1 V vs. SCE, the surfaces were then potentiodynamically scanned in the cathodic direction and terminated at a potential of -0.3 vs. SCE. The surfaces were then held at -0.3 V vs. SCE for 12 minutes and the current was measured. The current during this 12-minute period is reported. Scanning electron microscopy was performed to characterize corrosion surfaces. Fig. 4.3 schematically depicts how the applied potential changes with time from this experimental setup.
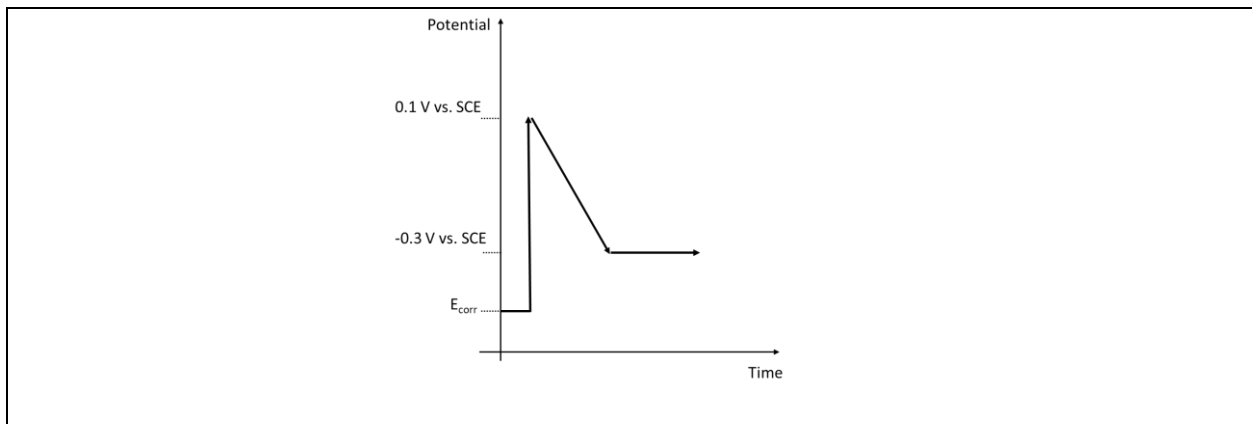
Fig. 4.3. Schematic showing scan strategy for studying potentiostatic active behavior of passivated LPBF 316L material.

4.3.5 TEM Characterization

A Themis 60-300 kV transmission electron microscope was used to characterize the cellular structures in samples A1 and A8. STEM-EDS was used to perform line scans and construct compositional profiles. These samples were chosen due to the great differences in DOR values from the DL-EPR testing as will be shown in the results section.

4.4 Results

The results section is organized in a way that first shows DOR values as a function of processing parameters. Comparisons of polarization behavior and post-test surface morphology are connected to the processing parameters. Modifications of the DL-EPR test are also presented to further validate results from the DL-EPR test.

4.4.1 DL-EPR Results

Fig. 4.4 shows the degree of reactivation (DOR) for the LPBF materials that were used in this study and the relationship between DOR and VED is shown. The y-axis in Fig. 4.4a extends to a value of 0.0020 to highlight the relatively high DOR value for sample A3. Fig. 4.4b highlights trends in other LPBF materials. It is seen that at lower values of VED, there is a tendency for the DOR value to be greater than zero. It is also to be noted that for two materials with equal values in volumetric energy density, differences in behavior may be observed. This is seen in the DOR values for materials with a VED of 67 J/mm^3 (A4 and A5) as well as materials with a value of 78 J/mm^3 (A6 and A7).
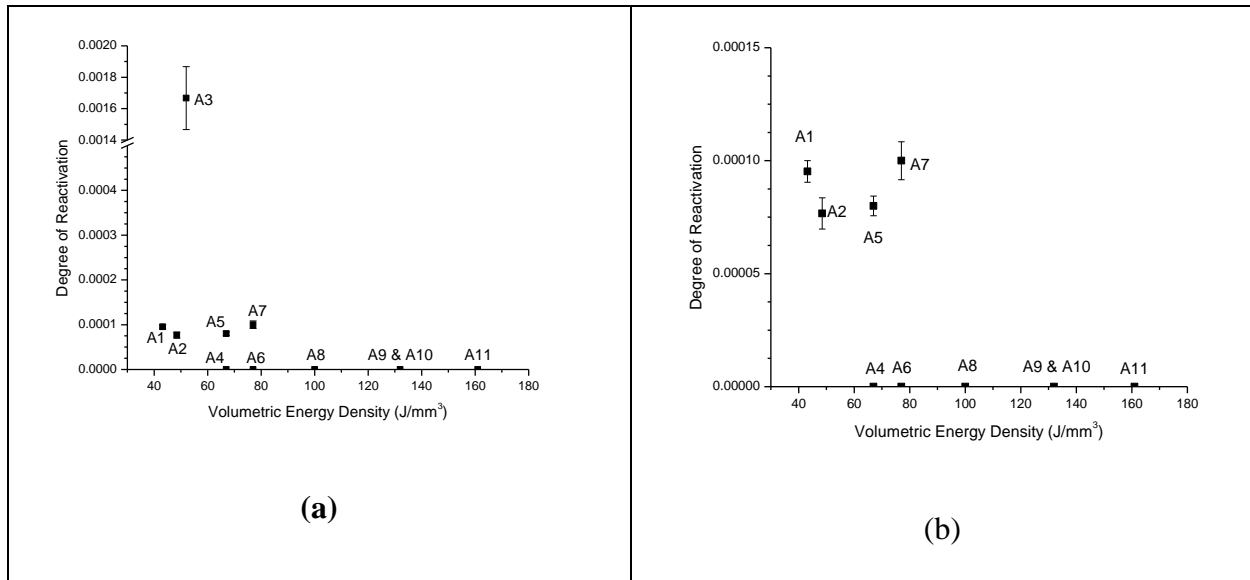
Fig. 4.4. The relationship between DOR and VED are depicted in the following graphs. One of the graphs (a) has a maximum DOR value of 0.002 while the other (b) has a maximum DOR value of 0.00015 to highlight the range and trends in DOR values for as-built LPBF materials.

Fig. 4.5 shows DL-EPR scans for select LPBF materials to highlight the difference potentiodynamic behavior for materials that have varying susceptibilities to reactivation. Fig. 4.5a shows behavior for materials with VED values of 67 J/mm^3 while Fig. 4.5b shows behavior for materials with VED values of 78 J/mm^3. In the case of materials with VED values of 67 J/mm^3, sample A5 is shown to have greater propensity for reactivation due to an increase in anodic current density within the reverse scan at approximately -0.15 V vs. SCE. Meanwhile, sample A4 does not show this increase in anodic current showing that this material is less susceptible to passive film breakdown. In comparing the behavior between sample A6 and A7 in Fig. 4.5b, sample A7 is shown to be more susceptible to reactivation due to the same type of increase in anodic current while sample A8 does not have this signature increase in anodic current.

(a)

(b)
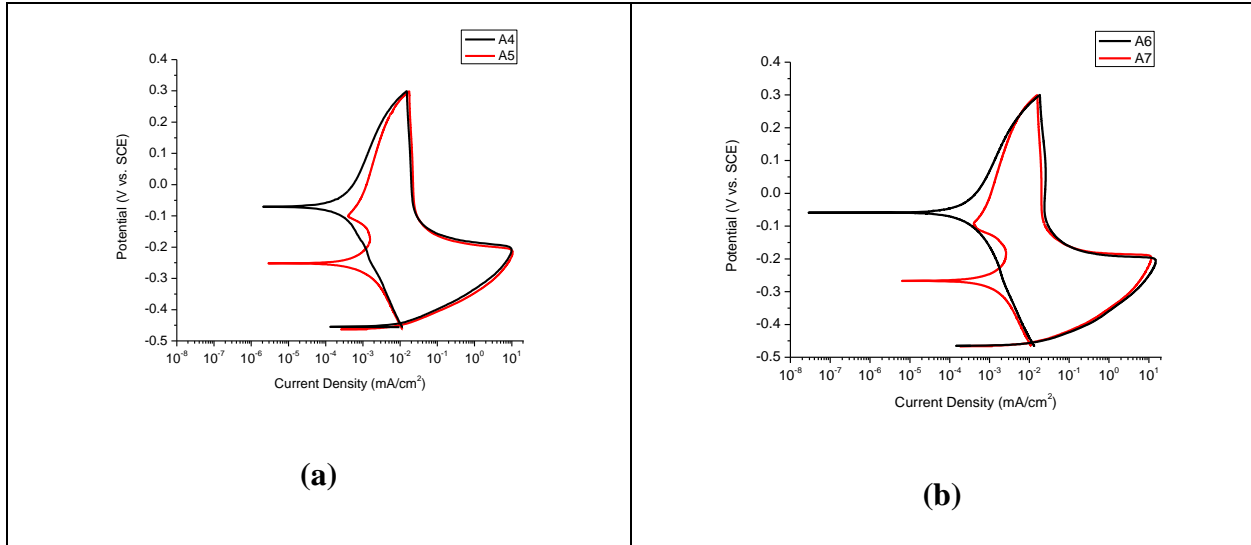
Fig. 4.5. DL-EPR Curves for LPBF Material with printed with parameters that resulted in VED values of (a) 67 J/mm^3 and (b) 78 J/mm^3.

Fig. 4.6 shows surface of LPBF 316L materials A4 and A5 after the DL-EPR test. In both cases, attack is seen to be taking place along the cellular interiors as seen from the honeycomb-like structures on the surface. In the case of material A4, an additional spiral morphology is observed. While only of these two samples (A4) had a DOR value greater than zero, it is to be noted that both materials still exhibit preferential cellular interior dissolution.

(a)   (b)
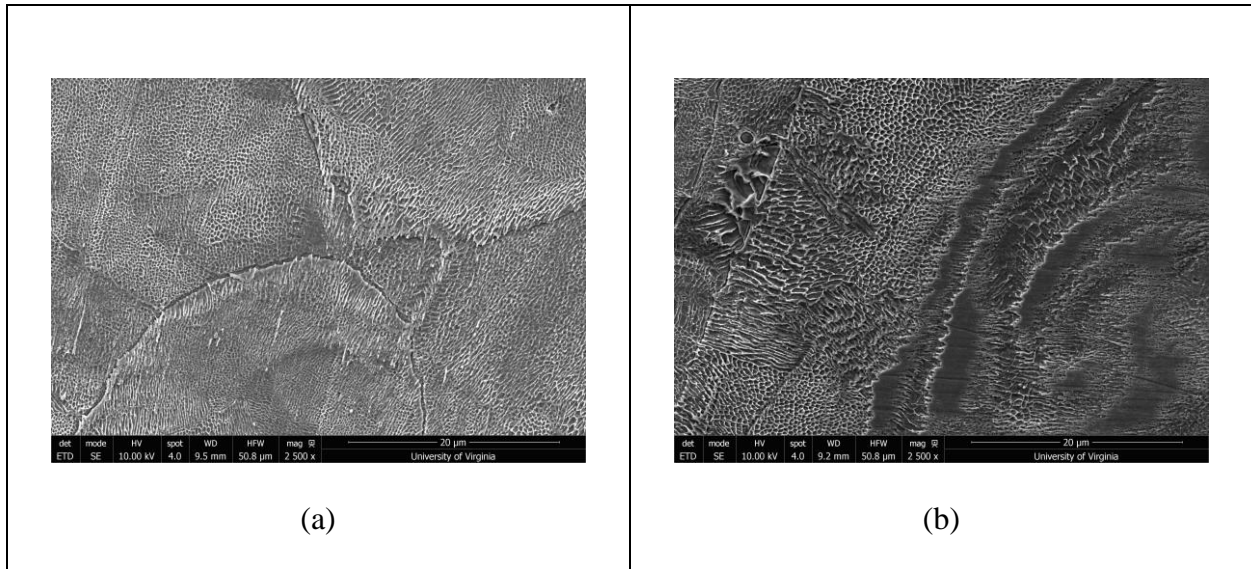
Fig. 4.6. Post-test micorgraphs of materials (A) A4 and (B) A5 after the double-loop potentiokinetic reactivation test. Both materials have VED values of 67 J/mm^3. Both surfaces are oriented perpendicular to the build direction.

Fig. 4.7 shows the behavior of LPBF sample A4 after immersion in the DL-EPR solution for 2 and 24 hours. At an exposure time of 2 hours (Fig. 4.7a), it seen that there is little to no corrosion damage. However, in the case of the 24-hour exposure (Fig. 4.7b), attack along the cellular interiors are seen similar to that observed in Fig. 4.6. These results highlight the depassivation of LPBF 316L under open circuit conditions in 1 M sulfuric acid and 0.01 M potassium thiocyanate.

| (a) | (b) |
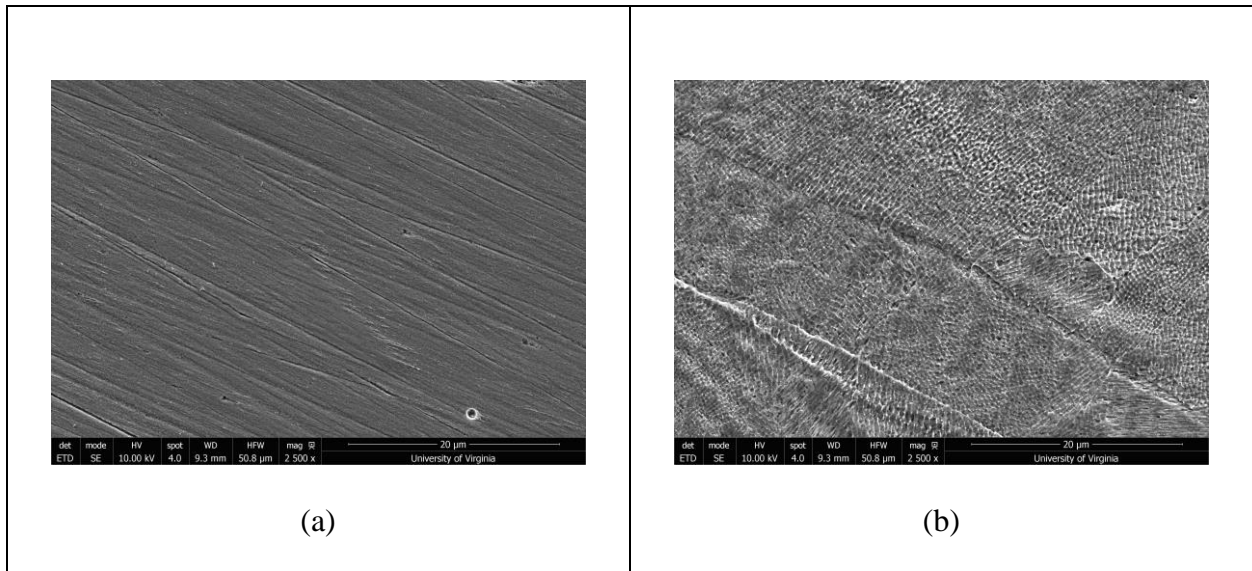
Fig. 4.7. Surface of LPBF Material A4 after immersion in 1 M H_2SO_4 and 0.01 M KSCN after (a) 2 hours and (b) 24 hours.

Fig. 4.8 shows the SL-EPR scan performed on sample A4 for varying pre-test holds under open circuit conditions. In the case of the 30 minute pre-test hold, there is an increase in the cathodic current from approximately -0.1 V vs. SCE to -0.5. However, in the case of the 2-hour pre-test OCP hold, a subtle decrease is seen in the cathodic current at approximately -0.275 V – 0.3 V vs. SCE as shown by the black arrow.

4.4.2 SL-EPR Experiments
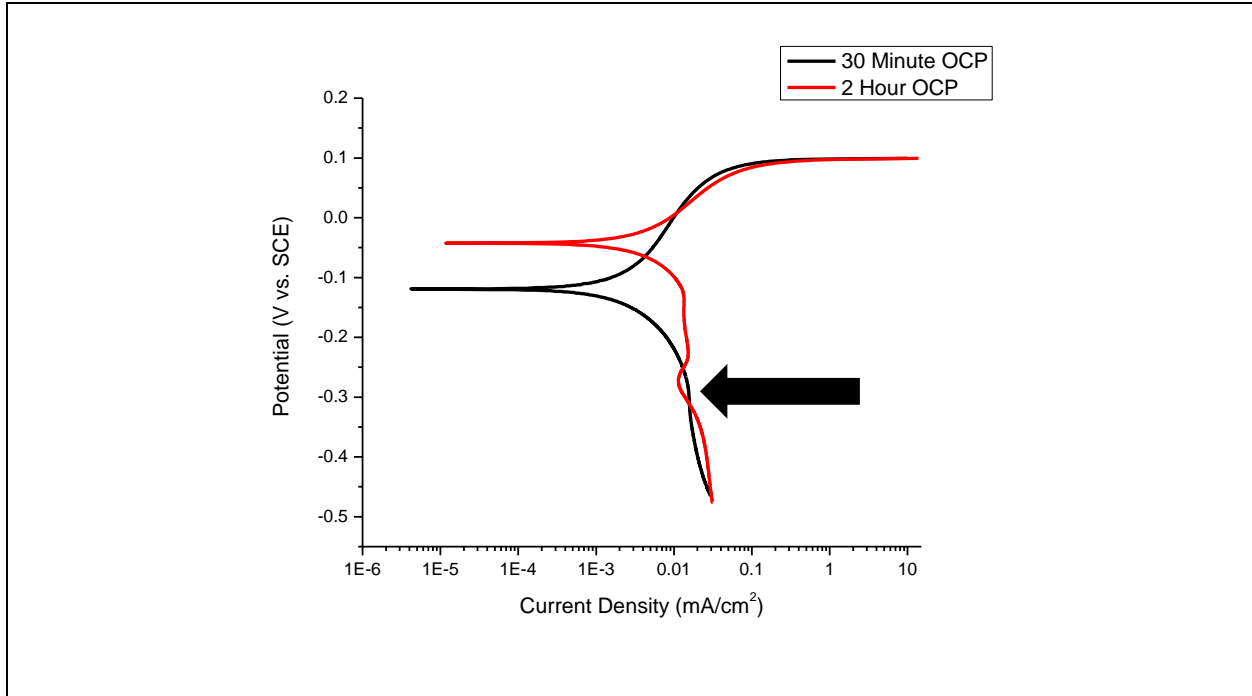
Fig. 4.8. Potentiodynamic scan of LPBF 316L material A4 after open circuit holds for 30 minutes and 2 minutes. Each scan started at a potential of 0.1 V vs. SCE and terminated at the original open circuit potential. A black arrow points to a region of diminished cathodic current.

Fig. 4.9 shows the post-test micrographs for these two SL-EPR scans. In the case of the material with a 30-minute pre-test OCP hold (Fig. 4.9a), little attack is seen through in what appears to be a porous network throughout the surface. In the case of the 2-hour hold however (Fig. 4.9b), greater corrosion is damage is seen through the increased melt pool boundary attack as well as the cellular dendritic structures that experience interior preferential dissolution.
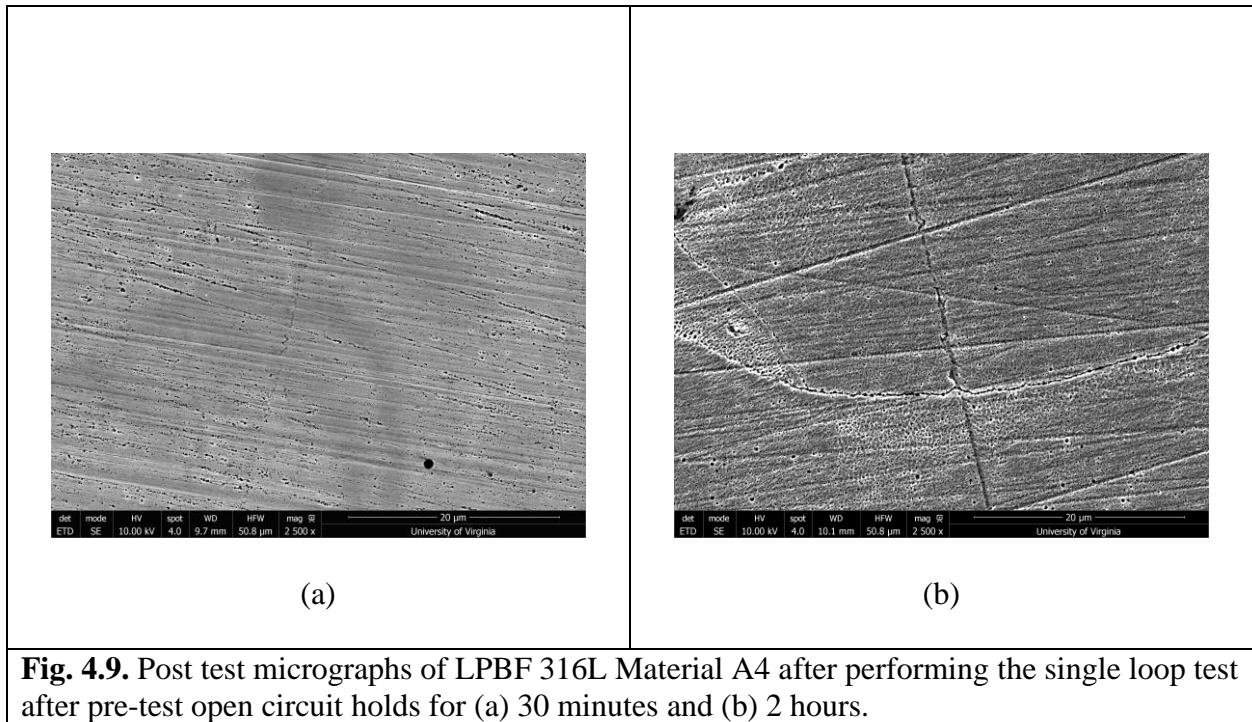
Fig. 4.9. Post test micrographs of LPBF 316L Material A4 after performing the single loop test after pre-test open circuit holds for (a) 30 minutes and (b) 2 hours.

Fig. 4.10a shows the SL-EPR potentiodynamic scan for materials A4 and A5. For both materials, the measured currents are similar during the anodic portion of the scan, it should be noted that when the DL-EPR scan was performed for both materials, A4 had a DOR value that non-zero while A5 did not. While there is little increase in the cathodic current in the case of sample A5, a decrease cathodic current is observed in sample A4 at a range of -0.2 to -0.3 V vs. SCE. From the post test micrographs, it is qualitatively seen that there is greater cellular interior and melt pool boundary damage in sample A4 (Fig. 4.10b) compared to sample A5 (Fig. 4.10c).

(a)

(b)   (c)
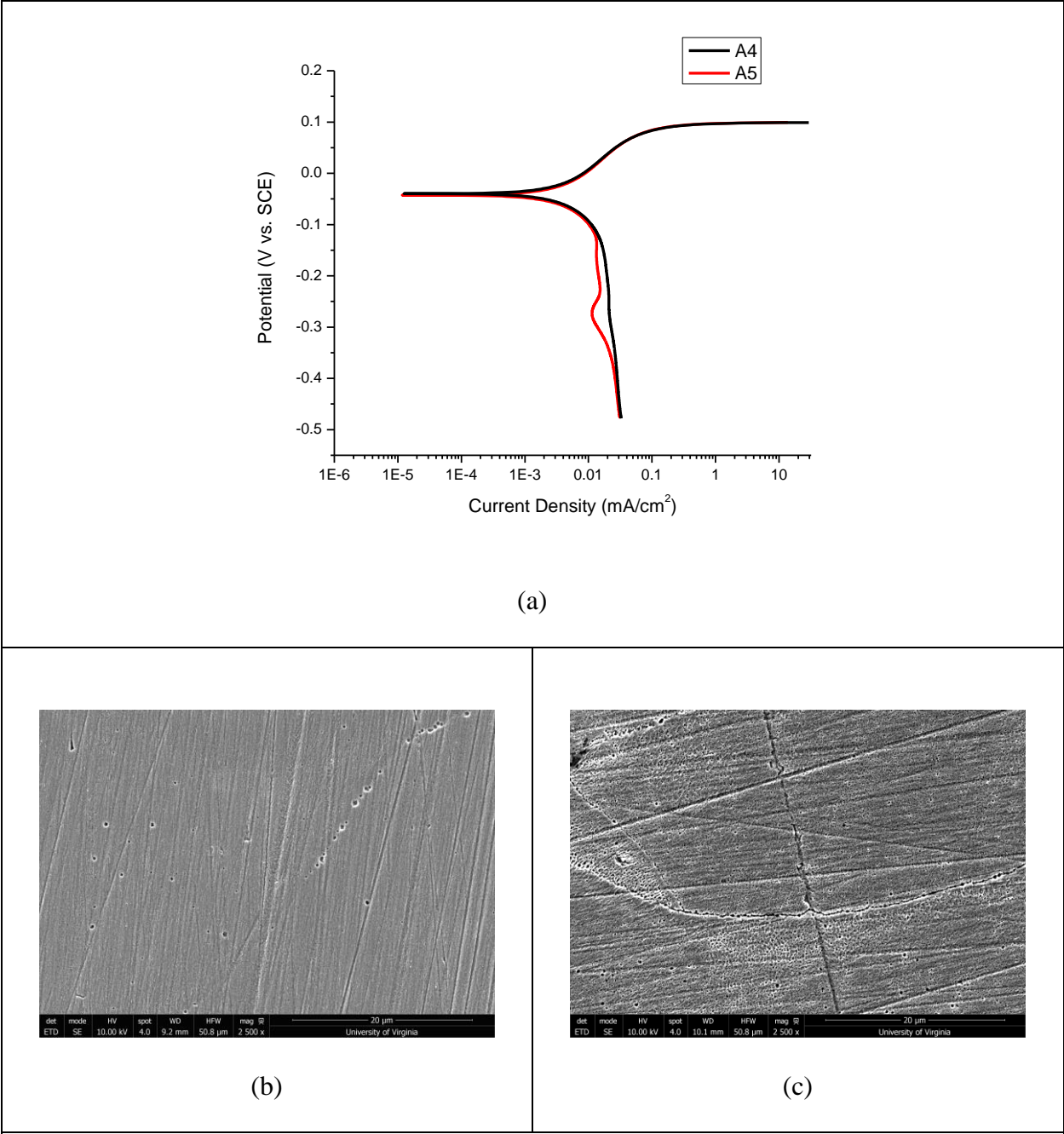
Fig. 4.10. Potentiodynamic scans for LPBF samples A4 and A5. Samples were held under open circuit conditions for 2 hours and scanned cathodically from 0.1 V vs. SCE to the open circuit potential. Post-test scanning electromicrographs for (b) A4 and (c) A5 are also shown.

4.4.3 Potentiostatic Active Behavior

Fig. 4.11 shows the current profiles for samples A4 and A5 at a potentiostatic hold of -0.3 V vs. SCE. This potentiostatic hold took place after a potentiodynamic scan from -0.1 V vs. SCE

to -0.3 V vs. SCE as was previously schematically demonstrated by Fig. 4.3. It is seen that while there is initially little difference in the current between the two materials, the current for the A4 material is slightly higher than that of the A5 material. It is to be noted that the material with the higher current (A4) also had a DOR value that was non-zero in the DL-EPR test.

Fig. 4.11. Potentiostatic behavior of LPBF 36L Material AX and AY at -0.3 V vs. SCE after polarizing from 0.1 V vs SCE to -0.3 V vs. SCE.
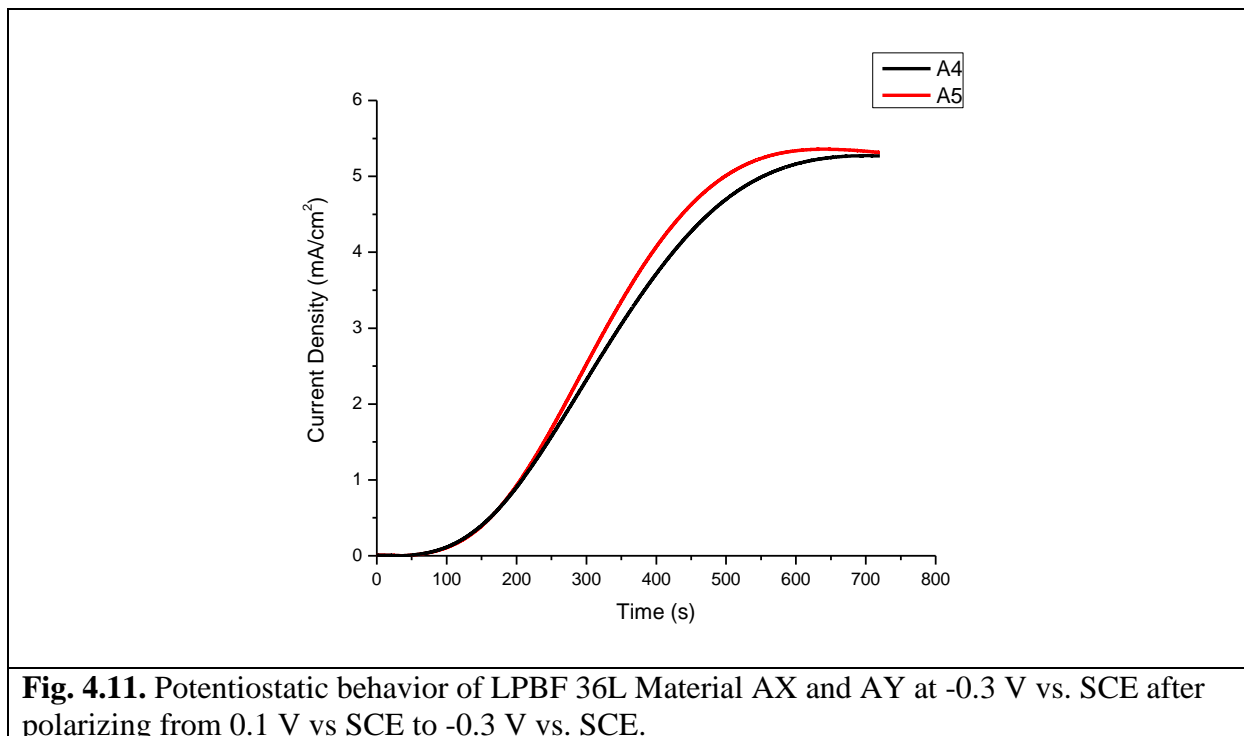
4.4.4 Transmission Electron Microscopy

Fig. 4.12 shows TEM micrographs of cellular structures in LPBF materials A1 and A7 to compare the difference between the cellular dendrites in a material that exhibited a non-zero and a zero DOR value from the DL-EPR test.
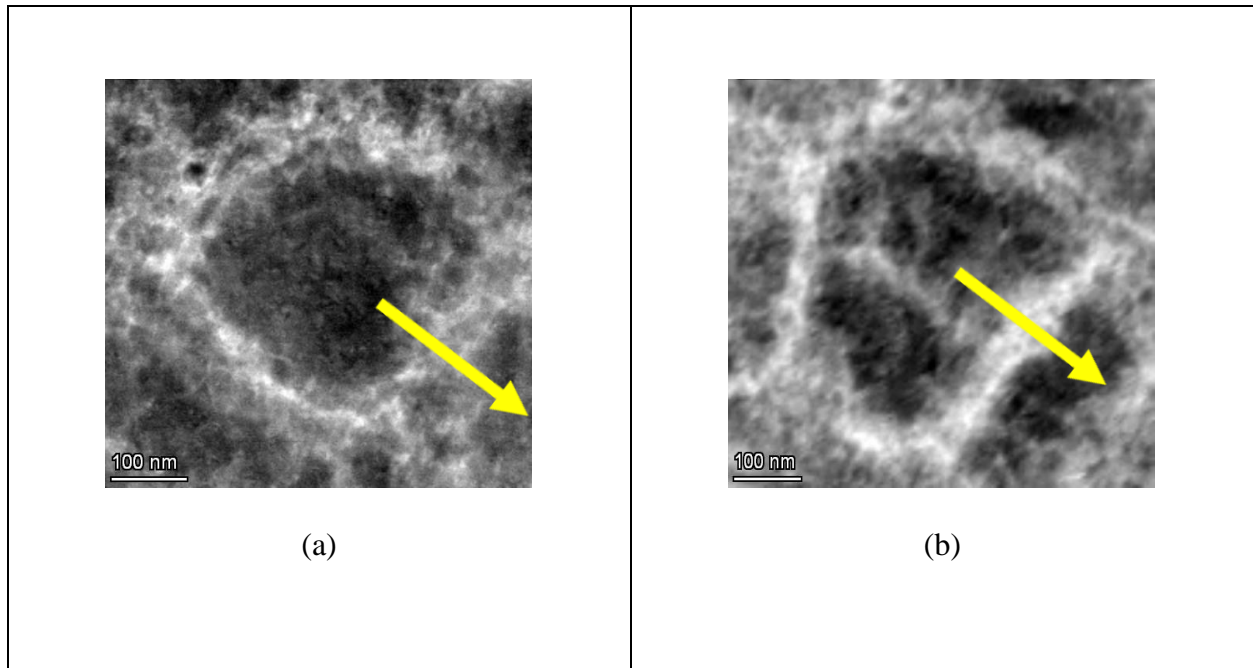
Fig. 4.12. HAADF TEM micrographs for LPBF Materials (a) A1 and (b) A6.

Fig. 4.13 shows compositional mapping for the LPBF samples and the profiles are correspond to the yellow arrows shown in Fig. 12. In the case of material A1, it is seen that there are generally higher levels in chromium, nickel, and molybdenum while having lower levels of iron. The position center of the cellular boundary lies at approximately 100 nm. and it is seen that there is a depletion in iron while there is an enrichment of chromium and nickel.
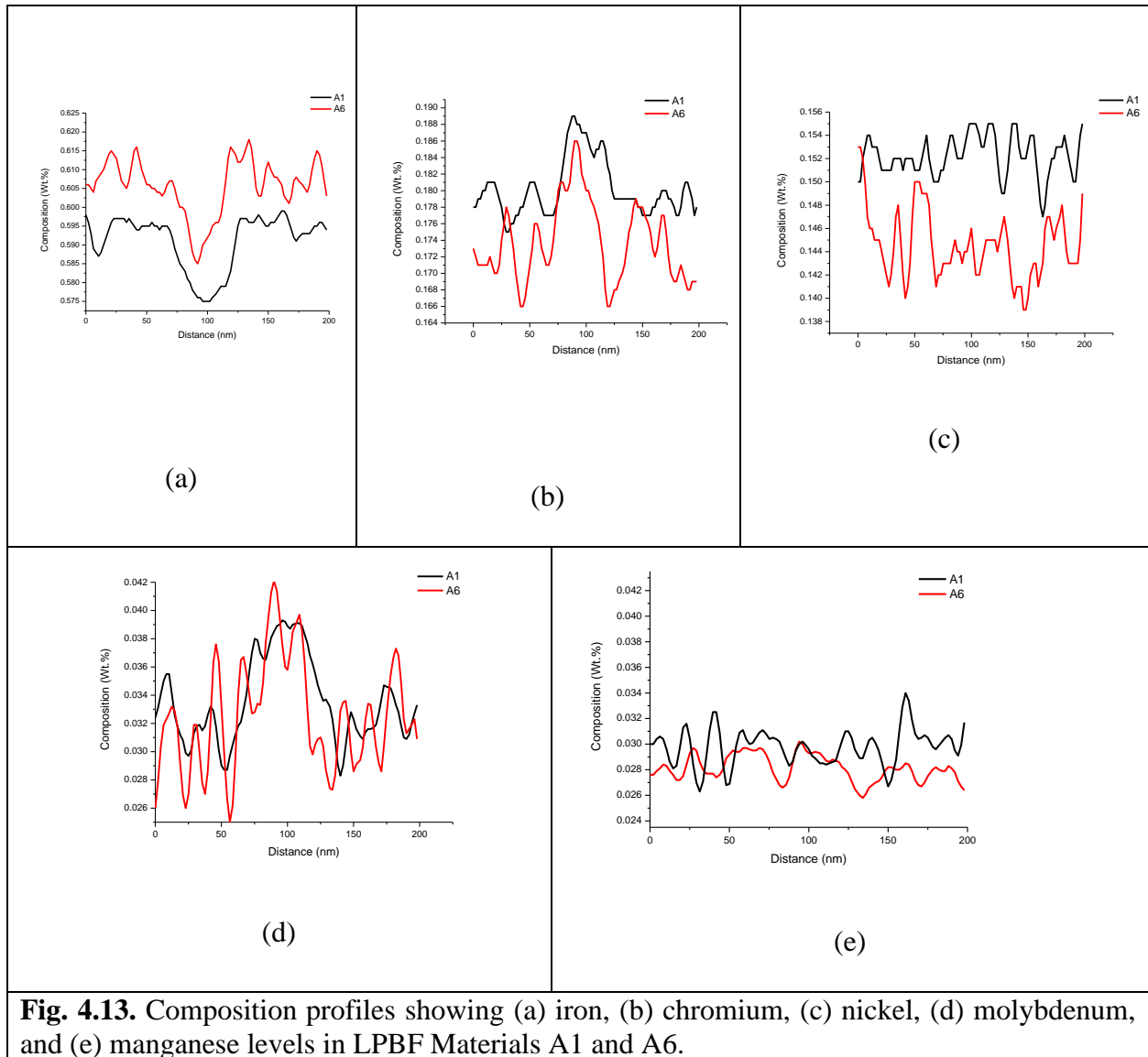
Fig. 4.13. Composition profiles showing (a) iron, (b) chromium, (c) nickel, (d) molybdenum, and (e) manganese levels in LPBF Materials A1 and A6.

4.5 Discussion

The discussion first investigates the effect of volumetric energy density on the resulting DOR results from the DL-EPR. Post-test micrographs are also discussed so that the DOR value may be related to the relative reactivation of LPBF microstructural features. The DL-EPR was originally developed to investigate the behavior of wrought materials so additional modifications to the EPR experiments were performed to further validate results from the EPR test as well as to further clarify on which microstructural features are more prone to reactivation.

4.5.1 DL-EPR Behavior of As-Built LPBF 316L

The SL-EPR and DL-EPR tests were developed as non-destructive methods to investigate the susceptibility of wrought austenitic stainless steel to grain boundary sensitization [22–25]. Nevertheless, previous works have utilized this test to detect the susceptibility of as-built LPBF materials to global surface reactivation and corrosion morphologies have been observed that show preferential dissolution of cellular dendritic interiors [26–35]. Testing of LPBF materials of varying process parameters has shown that materials that are printed with lower volumetric energy density tend to be more susceptible to global reactivation as seen from the results of Fig. 4.4. Beyond a volumetric energy density of 100 J/mm^3, materials seem to have a zero DOR value indicating lower susceptibility to passive film breakdown. These observed trends may be due to lower energy densities resulting in faster cooling rates that leading to lower times in the liquid phase and a more compositionally heterogenous cellular dendritic structures [21]. The existence of LOF defects are typically associated with materials printed at lower VED and may also be contributing factors to the observed DOR values.[10,14,36]

Multiple studies have criticized the use of the volumetric energy density as a tool for optimization and the sole predictor of features such as alloy microstructure, LOF defect density, and even mechanical properties [15,16,37,38]. Fig. 4.5 demonstrates that materials printed with similar VED values may exhibit dramatically different potentiodynamic behavior. For VED values of 67 J/mm^3 (Fig. 4.5a) and 78 J/mm^3 (Fig. 4.5b), it is seen that the variation printed with the higher velocity had a non-zero DOR value. In the case of the materials with a VED of 67 J/mm^3, the material with higher power (A5) showed greater susceptibility to reactivation than the lower power variant (A4). In the case of the materials printed with a VED of 78 J/mm^3, the opposite is observed: the material printed with lower power (A6) showed greater susceptibility to reactivation

compared to the other material with the same VED but printed at a higher power (A6). Other works have shown how lower laser speed leads to lower cooling rates and leads to lower degrees of elemental microsegregation [21,39]. Previous work has also shown how higher scan speeds at constant volumetric energy density led to lessened susceptibility to pitting corrosion [40].

From Fig. 4.6, subtle differences in the corrosion morphology are observed between the two materials printed at the same volumetric energy density of 67 J/mm^3. In the case of the variant printed at lower speed (A4), attack along cellular structures and melt pool boundaries are observed while a swirl-like pattern is observed in the variant printed a higher speed (A5). The swirl-like pattern may have developed due to local convection in the liquid state [41]. These experiments show the limits in using volumetric energy density and shows that speed may be a significant contributing factor in dictating corrosion morphology and the propensity for reactivation in materials printed at a constant VED.

4.5.2 Validating DL-EPR Scan Use in Assessing LPBF Depassivation Behavior

Although the post-test electron microscopy of LPBF materials after the DL-EPR test show preferential dissolution of the interior cellular structures, the majority of dissolution took place during the upward scan. This observation provides motivation in validating the phenomenology that takes place during the reactivation of a surface that has experienced passivation during the potentiodynamic scan. This was the motivation in performing a series of SL-EPR scans to further validate the results from the DL-EPR scans especially in making a phenomenological distinction between a material with and without a non-zero DOR value.

Studies of the behavior of austenitic stainless steels in sulfuric acid and thiocyanate have shown that the thiocyanate acts as a depassivator and promotes activation of the surface[42,43]. From Fig. 4.7, it is made how longer exposure time in sulfuric acid and thiocyanate promotes

81

active corrosion. After performing the SL-EPR scan at varying (Fig. 4.8) pre-test open circuit holds, it is seen that there is a brief decrease in cathodic current at -0.3 mV vs. SCE for the LPBF sample that had a longer pre-test hold. This is predicted to be due to a higher reactivation current as a result of a surface that was rid of more oxide as a result of exposure to the depassivating thiocyanate under acidic conditions. Post-test micrographs further qualitatively validate this hypothesis and shows that there is greater corrosion of cellular dendritic interiors in the case of the surface that had a longer pre-test open circuit potential hold. Due to the use of the DL-EPR method in testing susceptibility to intergranular corrosion, it is important to clarify that grain boundary corrosion is not observed and that any indication of reactivation should not be automatically associated with IGC when studying LPBF alloys [26].

SL-EPR tests for materials printed with a VED value of 67 J/mm^3 further validate results from the DL-EPR testing. Fig. 4.10 Shows SL-EPR for these two materials: A4 (which had a DOR of zero) and A5 (which had a non-zero DOR value). The SL-EPR for A5 shows a decrease in the cathodic current at approximately – 0.3 V vs. SCE while no decrease is observed in the cathodic current for the A4 SL-EPR scan. Fig. 4.14 graphically depicts a mechanism through Evans diagrams that would indicate more rapid anodic reactivation that would lead to an observable decrease in cathodic current. All measured electrochemical currents are net currents, that is the difference between the cathodic current and the anodic current. In the case of A4, it is likely that the reactivation current is negligibly small with respect to the cathodic current that the net current is effectively representative of the cathodic kinetics. In the case of A5, although the anodic dissolution current is still lower than the cathodic current, its magnitude of the current is just high enough that a substantial decrease from the current in the cathodic branch of the scan is observed.
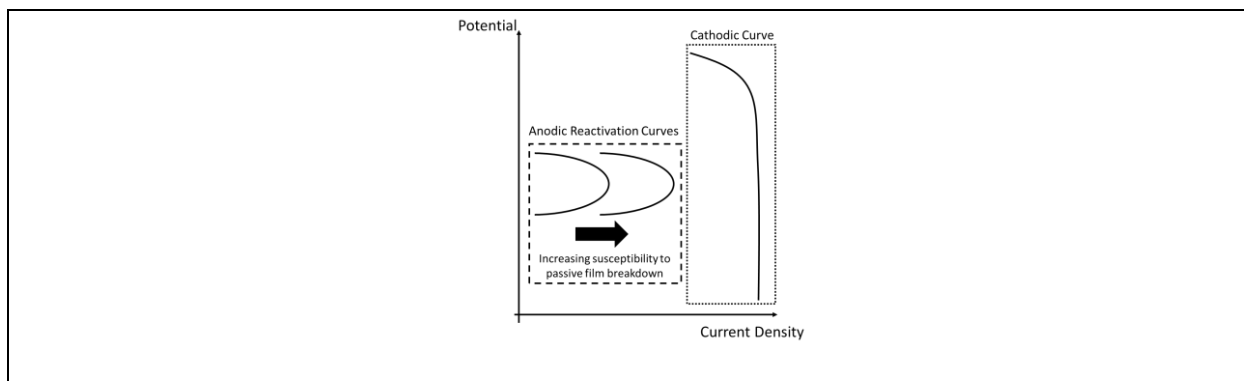
Fig. 4.14. Schematic depicting proposed anodic kinetics for LPBF materials relative to the cathodic kinetics for the SL-EPR scan.

Overall, it is suggested that in comparing the activation behavior of electrochemically passivated LPBF materials A4 and A5, the A5 variant is more prone to passive film breakdown leading to metal active dissolution. SL-EPR post test micrographs validate this hypothesis and it is seen in both variants that this depassivation takes place through the preferential dissolution of melt pool boundaries and the interiors of cellular dendrites. However, it is observed that the A5 variant (Fig. 4.10c.) has qualitatively a greater degree of localized corrosion in comparison to the A4 variant (Fig. 4.10b.). This suggests that the origin of greater propensity for reactivation in the A5 material compared to the A4 material may be due to the compositional character of the cellular structures.

These results are further validated by the potentiostatic holds of passivated A4 and A5 at an active potential of -0.3 V vs. SCE and it is observed that the anodic current (and therefore overall charge) for the A5 variant is higher than that of the A4 variant. The results indicate that the cellular cores in the A5 materials are more prone to passive film breakdown.

Transmission electron microscopy was performed as an additional tool of validation for the DL-EPR test and to test the hypothesis that there is greater local depletion of critical elements such as chromium and molybdenum from cellular interiors in materials with higher DOR values.

The TEM was performed for the A1 material, a material with non-zero DOR, and the A7 material, a material with zero DOR. Discrepancies, however, are observed between the compositional profiles as well as the DL-EPR scans. For example, in looking at the chromium profiles (Fig. 4.13b), the A1 material has a higher overall chromium level as well as a lower difference in chromium content between the boundaries and the cells. Nickel, which is known to improve corrosion resistance[44], is also shown to be higher in the material that has non-zero DOR. Despite this discrepancy, this TEM work only assessed the compositional features of a single cellular structure in these LPBF materials. The LPBF process is dynamic and the laser processing has been shown to demonstrate spatial differences in temperature gradient and solidification velocity [35,44,45]. Studies have also shown that there are variations in the character of cellular structures within a single build [28]. For example, within single LPBF builds, dislocation cells have been observed to have compositional heterogeneities while other dislocation cells did not contain these heterogeneities [46]. The DL-EPR test screens the overall susceptibility of material to reactivation and must be treated as a representation of all microstructural features that would lead to reactivation.

The DL-EPR testing in this study has shown that higher scan speed leads to greater tendency for reactivation under constant volumetric energy density. Although these results have allowed for the construction of generalizations about susceptibility to depassivation in terms of LPBF processing, one of the limitations of the DL-EPR test is the potential to distinguish behavior between two materials that have DOR values that are equal to zero. DOR values being equal to zero (such as in the case of materials A9 and A10) only signify that reactivation currents are significantly smaller than the cathodic current. The DL-EPR test was originally developed to test for intergranular corrosion susceptibility, but not necessarily other microstructural features in

austentic stainless steels that may lead to selective corrosion. This provides further work to optimize the DL-EPR testing conditions in such a way that allows for greater discrimination particularly in studying the behavior of materials printed with higher volumetric energy densities.

4.6 Conclusion

- Results from DL-EPR testing suggest that LPBF materials printed with lower VED tend to be more susceptible to reactivation.

- VED is not alone in predicting susceptibility to reactivation and under constant VED values, it was found that materials printed at higher speeds displayed greater reactivation susceptibility.

- Post-test modified EPR testing displayed that cellular interiors are more prone to depassivation.

- Results from modified EPR testing such as SL-EPR results and potentiostatic holding at active potentials are consistent with DL-EPR results.

- In comparing the behavior between two materials printed at the same VED, SL-EPR post-test microscopy further confirmed that the material printed at a higher velocity qualitatively displayed more corrosion damage.

4.7 Acknowledgements

4.8 Citations

1. A. Vafadar, F. Guzzomi, A. Rassau, and K. Hayward, Applied Sciences (Switzerland) **11**, 1 (2021).
2. D. D. Gu, W. Meiners, K. Wissenbach, and R. Poprawe, **57**, 133 (2013).
3. H. Sahasrabudhe, S. Bose, and A. Bandyopadhyay, in *Advances in Laser Materials Processing* (2018), pp. 507–539.
4. H. Hack, R. Link, E. Knudsen, B. Baker, and S. Olig, Additive Manufacturing **14**, 105 (2017).

5. P. Hanzl, M. Zetek, T. Bakša, and T. Kroupa, Procedia Engineering **100**, 1405 (2015).
6. T. M. Mower and M. J. Long, Materials Science and Engineering A **651**, 198 (2016).
7. K. N. Amato, S. M. Gaytan, L. E. Murr, E. Martinez, P. W. Shindo, J. Hernandez, S. Collins, and F. Medina, Acta Materialia **60**, 2229 (2012).
8. K. Kunze, T. Etter, J. Grässlin, and V. Shklover, Materials Science and Engineering A **620**, 213 (2014).
9. F. Bartolomeu, M. Buciumeanu, E. Pinto, N. Alves, O. Carvalho, F. S. Silva, and G. Miranda, Additive Manufacturing **16**, 81 (2017).
10. J. v. Gordon, S. P. Narra, R. W. Cunningham, H. Liu, H. Chen, R. M. Suter, J. L. Beuth, and A. D. Rollett, Additive Manufacturing **36**, 101552 (2020).
11. Z. Hu, B. Nagarajan, X. Song, R. Huang, W. Zhai, and J. Wei, **2019**, (2019).
12. M. Guo, D. Gu, L. Xi, H. Zhang, J. Zhang, J. Yang, and R. Wang, International Journal of Refractory Metals and Hard Materials **84**, 105025 (2019).
13. D. Herzog, V. Seyda, E. Wycisk, and C. Emmelmann, Acta Materialia **117**, 371 (2016).
14. D. R. Clymer, J. Cagan, and J. Beuth, Journal of Mechanical Design **139**, (2017).
15. P. Ferro, R. Meneghello, G. Savio, and F. Berto, The International Journal of Advanced Manufacturing Technology **110**, 1911 (2020).
16. M. Ghayoor, K. Lee, Y. He, C. Chang, B. K. Paul, and S. Pasebani, Additive Manufacturing **32**, 101011 (2020).
17. J. W. Elmer, S. M. Allen, and T. W. Eagar, Metallurgical Transactions A **20**, 2117 (1989).
18. H. INOUE and T. KOSEKI, Nippon Steel Technical Report (2007).
19. H. Inoue, T. Koseki, S. Okita, and M. Fuji, Welding International **11**, 876 (1997).
20. U. S. Bertoli, B. E. Macdonald, and J. M. Schoenung, Materials Science & Engineering A **739**, 109 (2019).
21. Q. Shi, D. Gu, M. Xia, S. Cao, and T. Rong, Optics & Laser Technology **84**, 9 (2016).
22. M. Momeni, M. H. Moayed, and A. Davoodi, Corrosion Science **52**, 2653 (2010).
23. A. P. Majidi and M. A. Streicher, CORROSION **40**, 584 (1984).
24. T. Amadou, H. Sidhom, and C. Braham, Metallurgical and Materials Transactions A **35**, 3499 (2004).
25. R. B. Rebak and S. W. Dean, Corrosion **76**, 742 (2020).
26. D. A. T. Macatangay, J. M. Conrades, K. L. Brunner, and R. G. Kelly, Corrosion **78**, 13 (2022).
27. D. A. Macatangay, S. Thomas, N. Birbilis, and R. G. Kelly, **74**, 153 (2018).
28. D. A. Macatangay, G. W. Kubacki, and R. G. Kelly, JOM (2022).
29. G. Sander, J. Tan, P. Balan, O. Gharbi, D. R. Feenstra, L. Singer, S. Thomas, R. G. Kelly, J. R. Scully, and N. Birbilis, Corrosion **74**, 1318 (2018).
30. D. Kong, C. Dong, X. Ni, and X. Li, Npj Materials Degradation **3**, (2019).
31. M. A. Melia, H.-D. A. Nguyen, J. M. Rodelas, and E. J. Schindelholz, Corrosion Science **152**, 20 (2019).
32. J. R. Trelewicz, G. P. Halada, O. K. Donaldson, and G. Manogharan, Jom **68**, 850 (2016).
33. S. F. Yang, C. W. Li, A. Y. Chen, B. Gan, and J. F. Gu, Journal of Manufacturing Processes **65**, 418 (2021).
34. M. Laleh, A. E. Hughes, W. Xu, N. Haghdadi, K. Wang, P. Cizek, I. Gibson, and M. Y. Tan, Corrosion Science **161**, 108189 (2019).
35. G. R. Mirshekari, E. Tavakoli, M. Atapour, and B. Sadeghian, Materials & Design **55**, 905 (2014).

36. K. Moussaoui, W. Rubio, M. Mousseigne, T. Sultan, and F. Rezai, Materials Science and Engineering: A **735**, 182 (2018).

37. F. Caiazzo, V. Alfieri, and G. Casalino, Materials **13**, 538 (2020).

38. K. G. Prashanth, S. Scudino, T. Maity, J. Das, and J. Eckert, Materials Research Letters **5**, 386 (2017).

39. S. Gao, Z. Hu, M. Duchamp, P. S. S. R. Krishnan, S. Tekumalla, X. Song, and M. Seita, Acta Materialia **200**, 366 (2020).

40. J. J. Sopcisak, M. Ouyang, D. A. Macatangay, B. P. Croom, T. J. Montalbano, D. J. Sprouster, R. G. Kelly, J. R. Trelewicz, R. Srinivasan, and S. M. Storck, JOM **74**, 1719 (2022).

41. Y. Hwa, C. S. Kumai, N. Yang, J. K. Yee, and T. M. Devine, Corrosion **77**, 1014 (2021).

42. W. Li, Carnegie Mellon University (2012).

43. W. Li and P. C. Pistorius, Journal of The Electrochemical Society **159**, C513 (2012).

44. In *Corrosion of Weldments* (ASM International, 2006), pp. 203–216.

45. G. R. Mirshekari, E. Tavakoli, M. Atapour, and B. Sadeghian, Materials & Design **55**, 905 (2014).

46. P. Deng, H. Yin, M. Song, D. Li, Y. Zheng, B. C. Prorok, and X. Lou, JOM **72**, 4232 (2020).

5 Sensitization and Intergranular Corrosion of Thermally Treated LPBF 316L

5.1 Abstract

While an issue in stainless steel weldments, the topics of intergranular corrosion (IGC) and sensitization are not typically incorporated in the discussion of austenitic stainless such as 316L fabricated through laser powder bed fusion (LPBF). This study is focused on the corrosion of LPBF 316L alloys that have been exposed post-build to thermal conditions that are known to induce sensitization. Mass loss testing and potentiodynamic scanning are used to characterize IGC behavior. To study the effect of LPBF processing, volumetric energy density (VED) was used as a guide for testing a broad array of materials. It was found that LPBF materials printed at lower VED are more susceptible to intergranular corrosion and the discussion of observed behavior makes connections to grain refinement and LPBF porosity. Ultimately, the utility of classical standardized tests in determining IGC behavior of heat-treated LPBF alloys was able to be validated.

5.2 Introduction

In austenitic stainless steels such as the 316L and 304L grades, sensitization is the phenomena by which chromium carbides precipitate along grain boundaries [1–4]. This precipitation leads to the formation of a chromium-depleted zone adjacent to the boundaries and makes the material susceptible to intergranular corrosion [1,2]. Grain boundary sensitization typically takes place at a temperature range of $450^{\circ}C – 800^{\circ}$ C and is a potential issue in fabrication methods such as welding and casting [5,6]. In addition to increased preferential corrosion along grain boundaries leading to rapid loss of material through grain dropping, grain boundary sensitization has been shown to make stainless steel susceptible to intergranular stress corrosion cracking [4,7–11].

88

Although there is great motivation in being able to use laser powder bed fusion (LPBF) alloys in the as-printed state, defects such as lack-of-fusion porosity provide motivation to take advantage of post-processing techniques such as hot isotactic pressing (HIP) and friction stir welding [12–14]. These post-processing techniques are performed at elevated temperatures and promote conditions that may induce grain boundary sensitization. Observations of IGC, for example, have been exhibited in LPBF 316L that underwent the HIP process [15]. Although previous work has anticipated the effects of grain size on the IGC susceptibility of sensitized LPBF 316, trends in processing and susceptibility to IGC and sensitization are not clearly established [16]. Whereas most work on corrosion of additively manufactured austenitic stainless steels tend to be focused on pitting as well selective corrosion in the as-printed state, attention must also be paid to the corrosion properties of heat-treated LPBF alloys particularly in the area of grain boundary sensitization and intergranular corrosion [12,17–19].

This manuscript is focused on the grain boundary sensitization and intergranular corrosion of heat treated LPBF 316L. Materials printed at varying volumetric energy density (VED) are tested and trends in microstructural features such as grain refinement, porosity and corrosion behavior points of focus for these varying printing conditions. Equation 1 gives the relationship between VED and processing parameters such as power (P), velocity (v), hatch spacing (h), and layer thickness[13,20,21].

$$VED = \frac{P}{vht} \qquad\qquad Equation\ 3$$

Lower VED tends to favor the formation of refined grains and porosity so it is hypothesized that there is a greater level of grain fall out and surface activation along grain boundaries under these conditions[20–25]. The double-loop potentiokinetic reactivation test (DL-EPR) is used to determine the propensity of sensitized LPBF surface to reactivation while mass-loss testing is used as another tool to determine propensity for grain dropping because of IGC susceptibility[6,26–30]. These experiments are performed with the motivation of understanding the link between AM processing and the susceptibility to intergranular corrosion and grain boundary sensitization.

5.3 Methodology

5.3.1 Material Information and Thermal Treatments

Conventionally wrought 316L plate from North American Stainless was used for this study. AISI 316L stainless steel powder manufactured by EOS (EOS GmbH – Electro Optical Systems, Krailing, Germany, EOS art.-no. 9011-0032) with a spherical particle size distribution of 10-53 µm was used in this study; see Table 1 for the chemical composition. Square prism samples with dimensions 20 mm x 20 mm x 30 mm were manufactured using an EOS GmbH M290 DMLS-SLM system, which utilizes a 1060-1100 nm, 200 W continuous Yb fiber laser with a fixed 100 µm spot size and an inert argon-purged atmosphere. Table 2 shows the parameters used in this study. The default vendor (EOS) parameters are given by the parameters for sample A7. Sensitization was induced in wrought and LPBF materials by treatment at 675°C for 24 hours. All heat treatments were conducted under atmospheric conditions.

Table 5.1. Composition of wrought 316L material and powder used for the LPBF 316L.

Element	Analysis Method	Wrought Composition (Wt. %)	LPBF Powder Composition (Wt. %)
Fe	-	Balance	Balance
Cr	ICP	16.7	18.62
Ni	ICP	10.2	14.04
Cu	ICP	<0.1	< 0.1
Mn	ICP	1.99	1.65
Si	ICP	0.86	0.37
Mo	ICP	1.99	2.77
C	Combustion	0.006	0.007
S	Combustion	0.006	0.005
P	ICP	< 0.010	< 0.010
N	Fusion	0.004	0.07

Table. 5.2. Processing parameters for LPBF 316L material

Identification	A1	A2	A3	A4	A5	A6	A7	A8	A9
Power (W)	182.5	205	95	134	110	146	195	220	199
Velocity (mm/s)	960	960	1510	700	1400	1939	1083	755	2286
Hatch (mm)	0.11	0.11	0.06	0.12	0.05	0.05	0.09	0.11	0.03
Layer Thickness (mm)	0.04	0.04	0.02	0.02	0.02	0.02	0.02	0.02	0.02
Volumetric Energy Density (J/mm^3)	42	48	52	77	77	77	100	132	132

5.3.2 Double Loop and Single Loop Potentiokinetic Reactivation Tests

The double-loop potentiokinetic reactivation (DL-EPR) and single-loop reactivation potentiokinetic reactivation (SL-EPR) tests have traditionally been used to detect the susceptibility of wrought austenitic stainless grades such as 304 and 316 to grain boundary sensitization [26–31]. For the DL-EPR scan in this study, a solution with 1 M H_2SO_4 and 0.01 M KSCN was used. A horizontal flat cell three-electrode set up was used for potentiodynamic scanning with a scanning calomel electrode. After holding under open conditions for 30 minutes, the working electrode was

polarized to 0.1 V vs. SCE and then scanned in the reverse direction back to the original open circuit potential. Fig. 5.1a. Shows the scan strategy used for the DL-EPR test. A degree of sensitization (DOS) is expressed as the ratio of the peak reactivation current during the reverse scan to the peak activation current from the forward scan as schematically expressed in Fig. 5.2.

To show the depassivation of sensitized grain boundaries, the SL-EPR test was performed on select samples. After holding under open circuit conditions for 30 minutes, the scan started at 0.1 V vs. SCE and the working electrode was scanned to the original open circuit potential at a scan rate of 1.67 mV/s. Fig. 5.1b shows the scan strategy for the SL-EPR test. While the SL-EPR potentiodynamic scans are not reported in this study, the post-test micrographs are shown to highlight intergranular corrosion that takes place during reactivation of a clean, passivated surface.
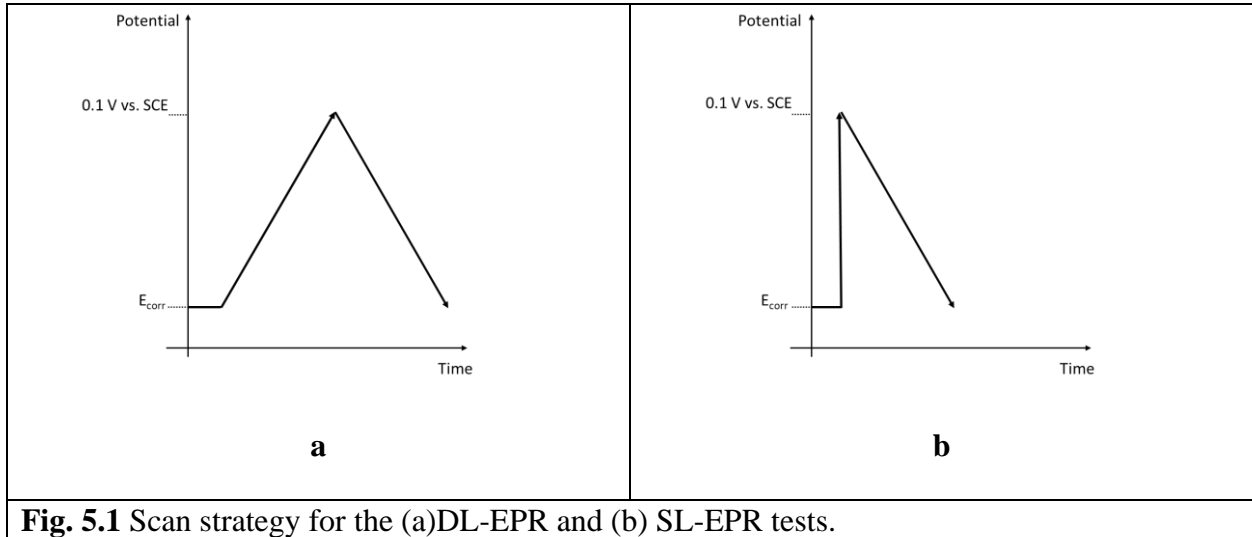
Fig. 5.1 Scan strategy for the (a)DL-EPR and (b) SL-EPR tests.
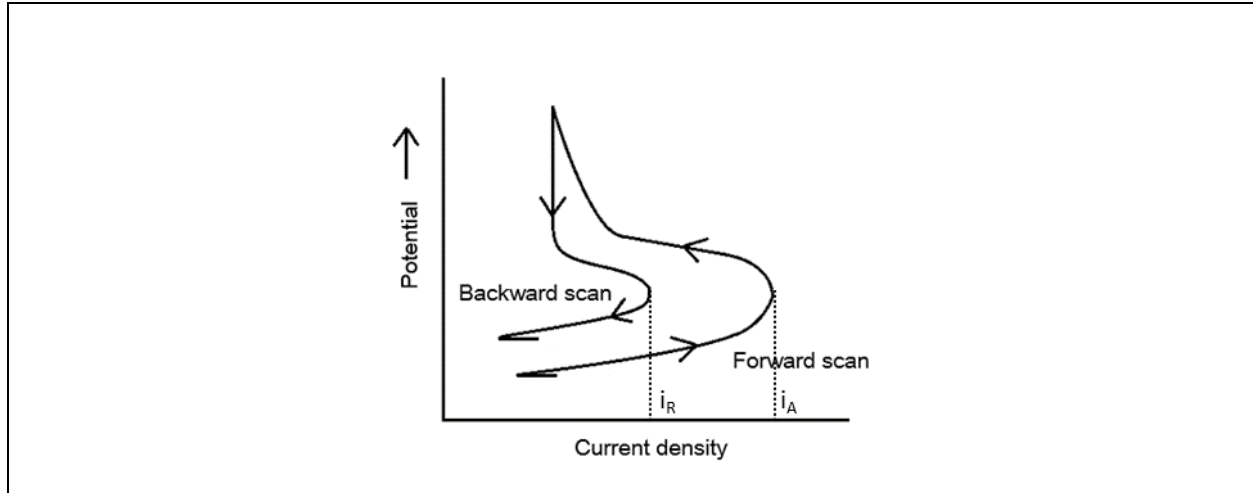
Fig. 5.2. Schematic of DL-EPR test. iR and iA respectively represent the reactivation and activation currents.

5.3.3 Boiling Ferric Sulfate and Sulfuric Acid Mass Loss Test

The boiling test provided by ASTM A-262 Practice B was utilized [32].An Erlenmeyer flask with solution was heated with a hot plate. Teflon tape and glass cradles were used to suspend the samples during the boiling test. Boiling chips were added to the solution to promote boiling. A reflux system was developed by using an Alihin condenser to promote the condensation of vapors back into the liquid phase. Teflon and vacuum grease were placed along the interface of the condenser and the neck of the flask to create a tight seal. In both testing environments, the hot plate was set to a temperature of 475 °C to promote boiling. Solution was checked to make sure there was little to no decrease in solution volume during the test. Table 3 shows the composition of each test solution in weight percent. Table 4 shows the amount of reagent used for each boiling test while table X shows the weight percent of reagent used in each boiling test.

Table 5.3. Amount of reagent used in boiling test solutions.

Reagent	Amount
Deionized Water (H2O)	472 mL
Concentrated Sulfuric Acid (H_2SO_4)	800 mL
Ferric Sulfate Hexahydrate ($Fe_2(SO_4)_3$ * $6H_2O$)	50.0 g

Table 5.4. Composition of boiling test solution in wt. %

	Composition (Wt. %)
Water (H_2O)	47.3
Sulfuric Acid (H_2SO_4)	50.4
Ferric Sulfate $Fe_2(SO_4)_3$	2.3

For all boiling tests, samples of approximate dimensions 20 mm x 20 mm x 2.5 mm were prepared. In the case of LPBF samples, the 20 mm x 20 mm square base is oriented perpendicular to the build direction. All faces were ground to a finish of 1200 grit with SiC paper Mass loss was recorded by measuring the mass before and after exposure to boiling acid solutions for 48 hours. Mass loss is expressed in units of mm/year and was calculated by the following formula [32].

$$Corrosion\ Rate = \frac{87660W}{Atd}$$

Corrosion rate is in units of mm/year, W is mass loss in grams, A is area in cm^2, t is exposure time in hours and d is the density of 316L in units of g/cm^3. In the case of chromium-nickel-molybdenum steels, a density value of 8 g/cm^3 was used.

A FEI Quanta 650 Scanning electron microscopy was used mass loss testing to assess corrosion morphology. Additionally, optical micrographs of cross sections of sensitized wrought and LPBF material to assess damage propagation. Samples were mounted in Buehler EpoThin epoxy resin and were allowed to cure at room temperature for 9 hours. Samples were ground with

SiC and rinsed with water to 1200 grit. Samples were polished to with 0.25 um diamond paste. Samples were sonicated in ethanol and air dried prior to characterization.

5.4 Results

5.4.1 EPR Experiments of Sensitized Material

Fig. 5.3 shows DL-EPR polarization curves to highlight the potentiodynamic behavior of sensitized wrought and LPBF 316L. For each material, reactivation is observed during the reverse scan as shown by an increase in anodic current. While the wrought and LPBF material A1 both have reactive current densities on the order of 10^{-2} mA/cm^2, it is interesting to note how material can be so prone to reactivation (as in the case of material A3) that the reactivation current density that it is nearly the same order of magnitude as the forward scan peak activation current density.
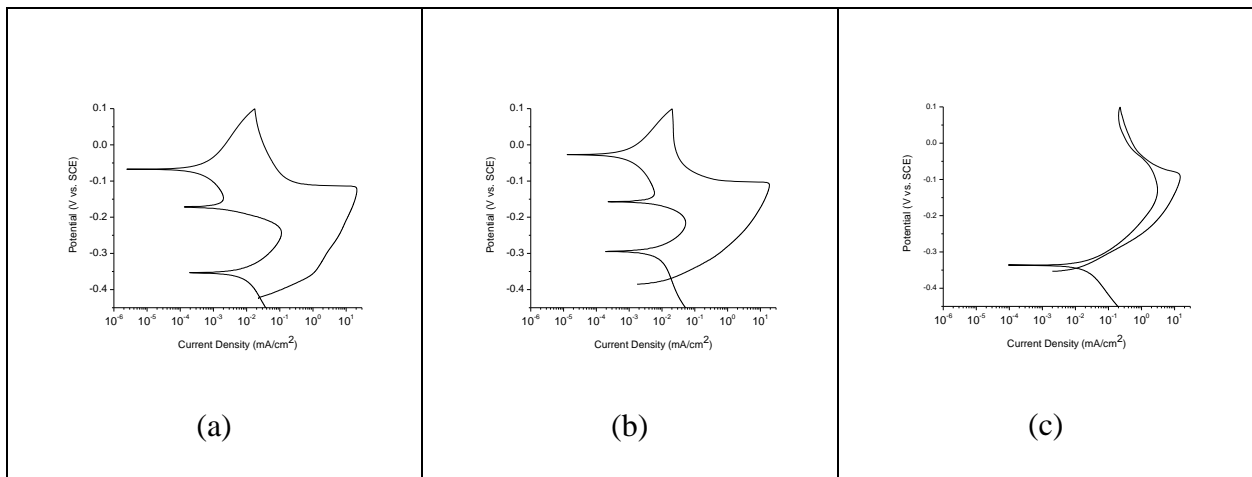
Fig. 5.3. DL-EPR potentiodynamic scans for sensitized (a) wrought, (b) LPBF Material A1, (c) LPBF Material A3. All materials were heat treated at 675°C for 24 hours.

Fig. 5.4 shows the post-test micrographs wrought and LPBF materials after the SL-EPR and DL-EPR tests. For each of the DL-EPR scans, it is seen that intergranular corrosion takes place although it is likely that a majority of this attack took place during the forward scan as the dissolution current is 2-3 orders of magnitude higher than that measured in the reactivation portion of the reverse scan. The SL-EPR post-test micrographs (Fig. 5.4b and 5.4d) show whether it is in

wrought or LPBF material, passivated surfaces will experience exhibit preferential reactivation at the grain boundaries.
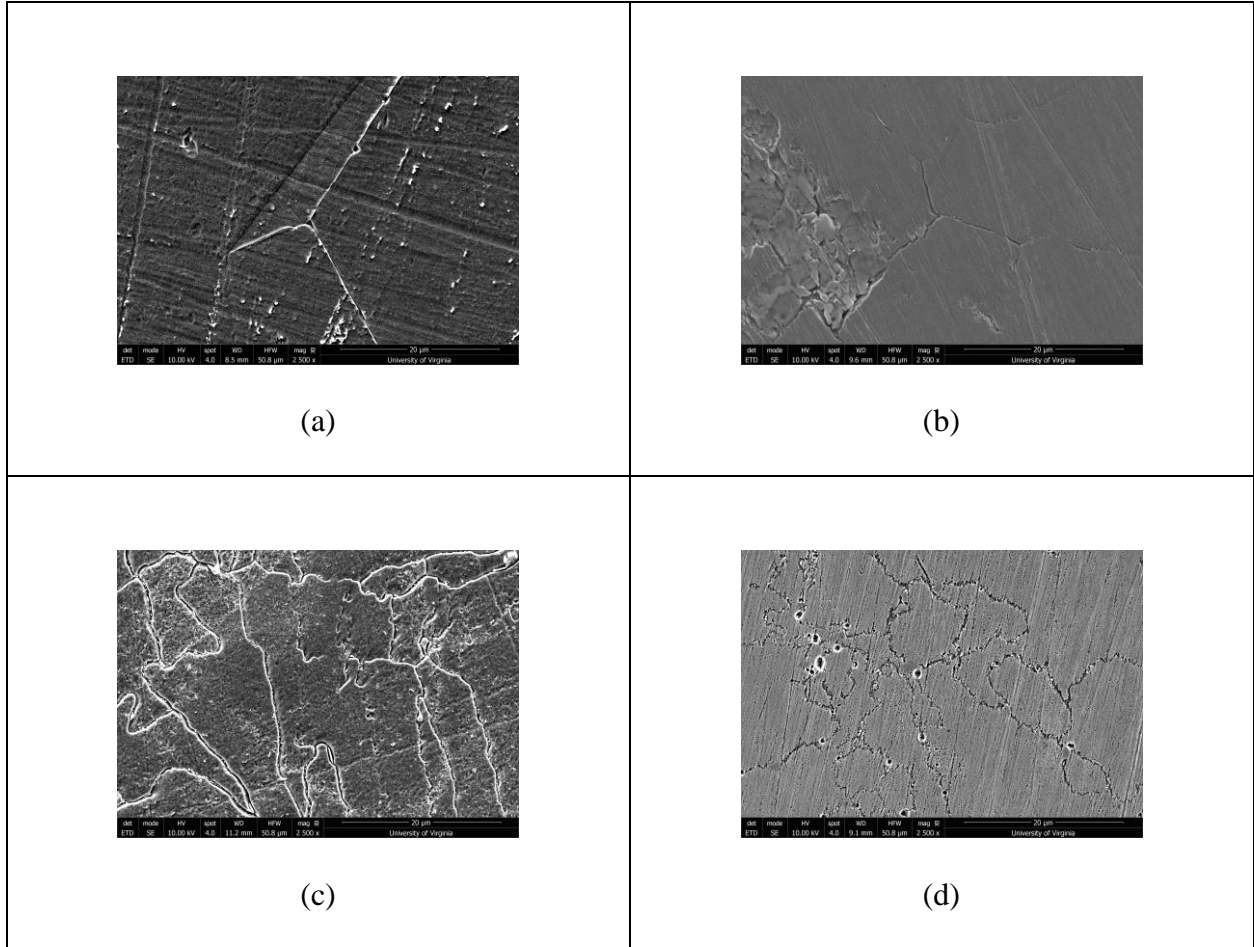
Fig. 5.4. Post-test micrographs of wrought surfaces after (a) DL-EPR and (b)SL-EPR testing. Post-test micrographs of LPBF Material A1 after (c) DL-EPR and (d) SL-EPR testing are also shown. The LPBF surfaces shown are oriented perpendicular to the build direction.

Fig. 5.5. shows the DOS values measured from performing the DL-EPR test on the wrought and LPBF materials listed on Table 2. The DOS values are shown as a function of volumetric energy density. The DOS values tend to be higher for materials with lower volumetric energy density. It is also shown how DOS values may differ between materials printed at the same volumetric energy density with different printing parameters. The difference in DOS values

between samples A4, A5, and A6 highlight this, but is also shown in the difference in DOS values

between samples A8 and A9.
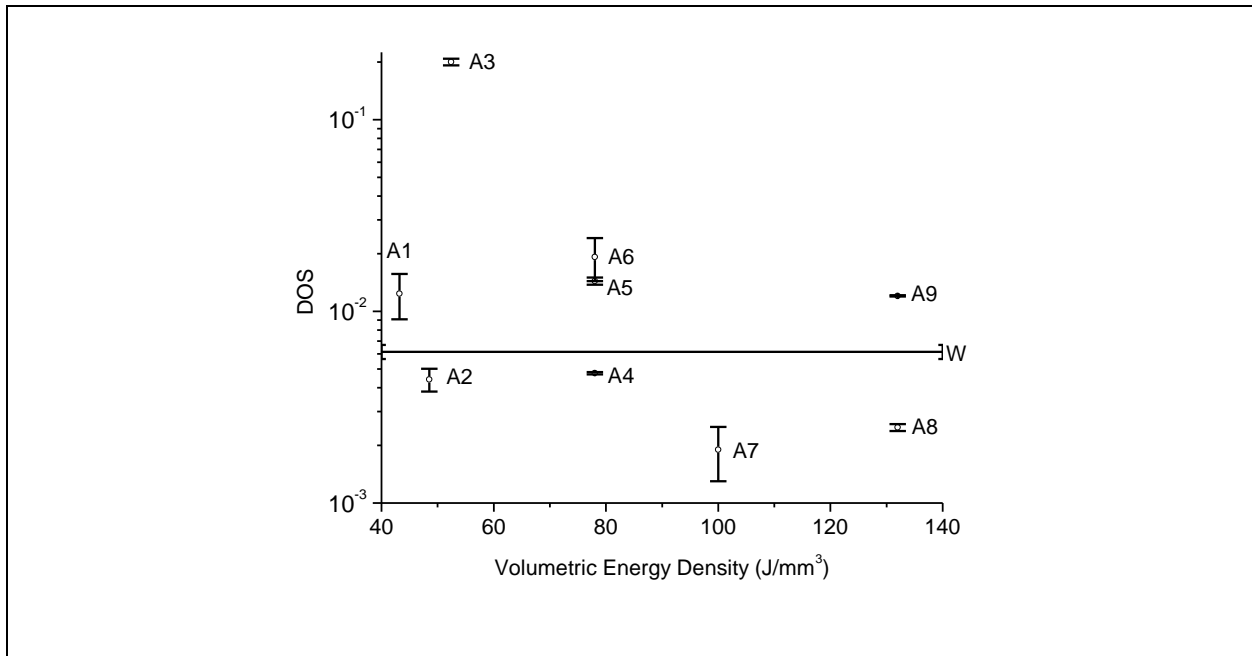
Fig. 5.5. Graph depicting DOS values from the DLEPR for sensitized LPBF materials as a function of volumetric energy density. Points represent mean DOS values and error bars represent the standard deviation. A black horizontal line labeled as "W" represents the DOS for sensitized wrought material.

Fig. 5.6 shows backscatter electron imaging for samples A4 (Fig. 5.6a and Fig. 5.6b) and

A6 (Fig. 5.6c and Fig. 5.6d). Both materials have a volumetric energy density of 78 J/mm^3). At

both magnifications, it is shown that material A6 has a greater amount of grain boundary per unit

area.

Fig. 5.6. Backscatter electron images of LPBF Material A4 are shown at (a) lower and (b) higher magnifications. Backscatter electron images of LPBF Material A6 are also shown at (a) lower and (b) higher magnification. The surfaces shown are oriented perpendicular to the build direction.
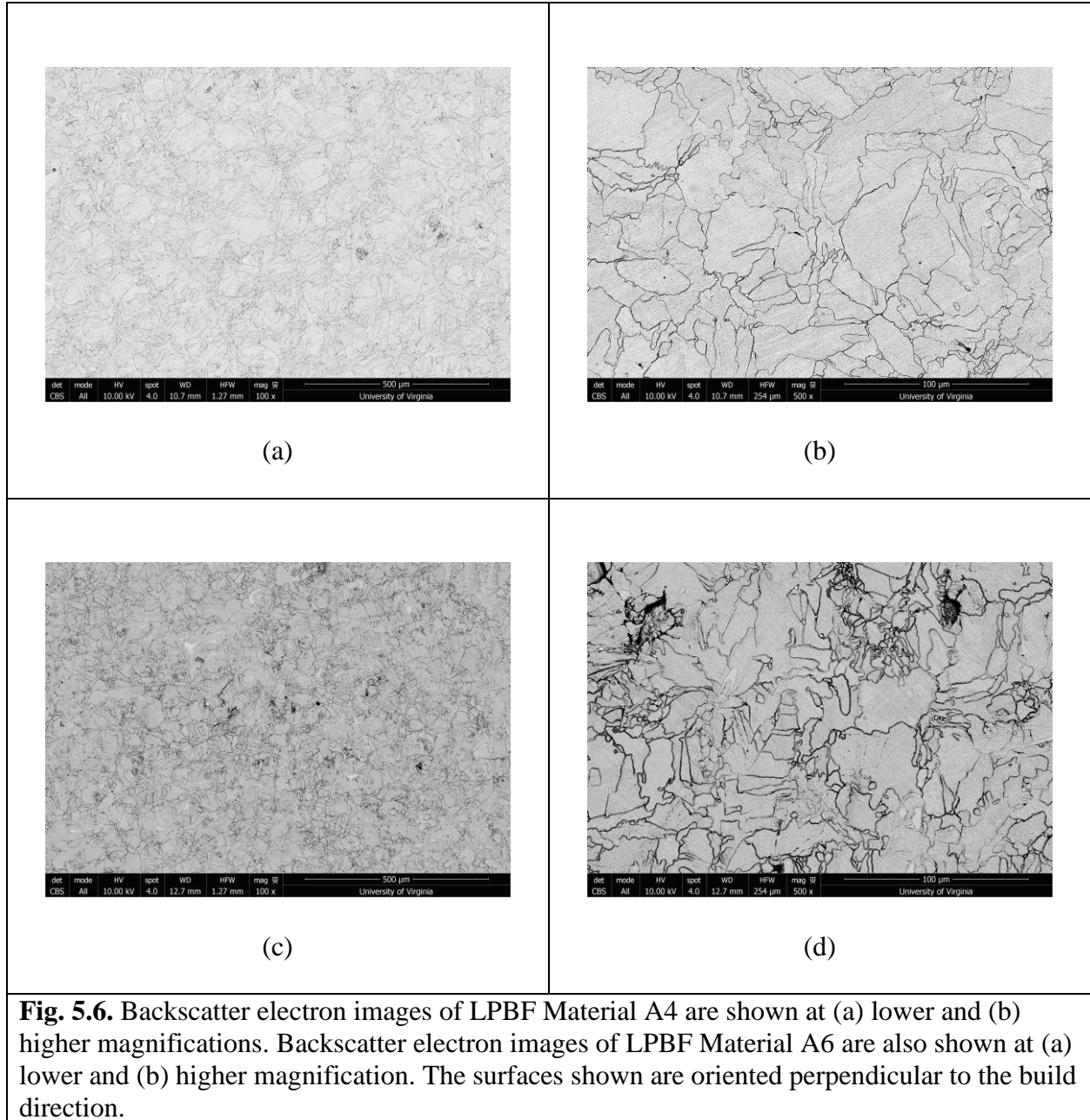
5.4.2 Mass Loss Testing of Sensitized Material in Ferric Sulfate and Sulfuric Acid

Fig. 5.7 shows corrosion rates for sensitized wrought and LPBF material after testing in boiling ferric sulfate and sulfuric acid. The materials printed at lower volumetric energy densities generally have higher corrosion rates. The corrosion rate for a majority of the sensitized LPBF materials are shown to be lower than that of the wrought counterpart. Similar to the trends in the

DL-EPR results, it is seen that there are differences in corrosion behavior between materials printed at constant VED with varying printing parameters. This effect is seen in comparing the behavior between samples with a VED of 78 J/mm^3 (A4, A5, and A6), but it is also shown in the difference between the corrosion rates of samples with a VED of 132 J/mm^3 (A8 and A9).
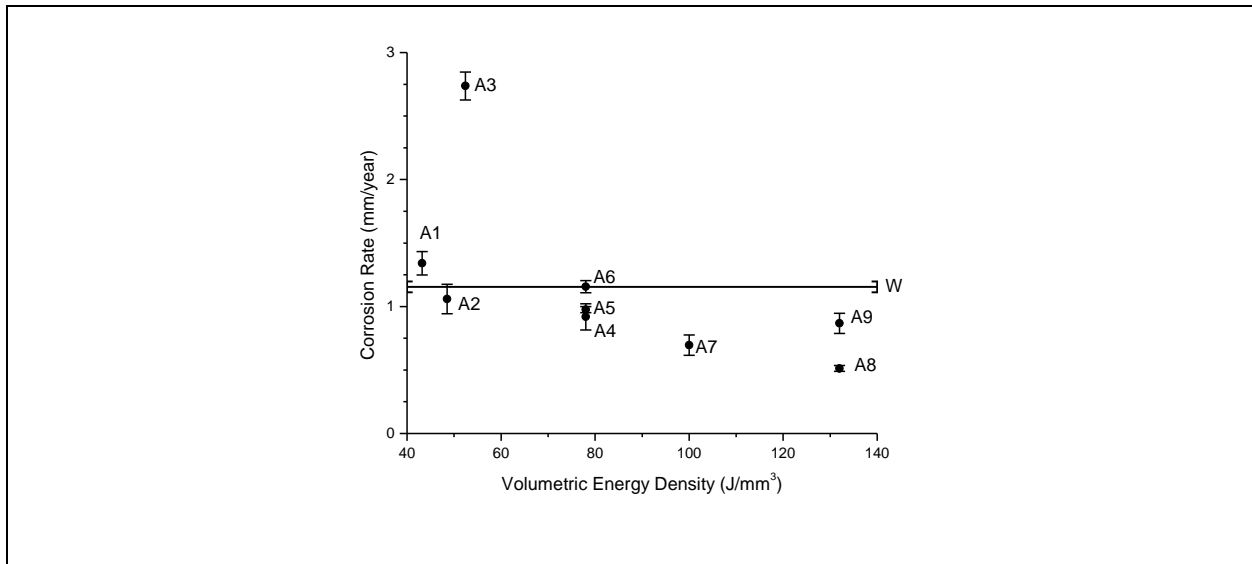
Fig. 5.7. Graph depicting corrosion rate values from the boiling sulfuric acid and ferric sulfate test for sensitized LPBF materials as a function of volumetric energy density. Points represent mean corrosion rate values and error bars represent the standard deviation. A black horizontal line labeled as "W" represents the corrosion rate for sensitized wrought material.

Fig. 5.8 shows scanning electron micrographs of sensitized wrought and select LPBF materials after exposure in boiling ferric sulfate and ferric sulfate. For each micrograph, damage is clearly observed along the grain boundaries. Greater amount of grain fall out is seen in samples A1 (Fig. 5.8b) and A3 (Fig. 5.8c), while little to no fallout is seen in samples A8 (Fig. 5.8d) and A9 (Fig. 5.8e). It is also to to be noted that samples A8 and A9 seem to have larger grains compared to A1 and A3.

Fig. 5.8. Scanning electron micrographs of sensitized (a) wrought, (b) LPBF A1, (c) LPBF A3 (d) LPBF A8 (e) LPBF A9 after testing in boiling sulfuric acid and ferric sulfate. The LPBF surfaces depicted are oriented perpendicular to the build direction. The surfaces shown are oriented perpendicular to the build direction.
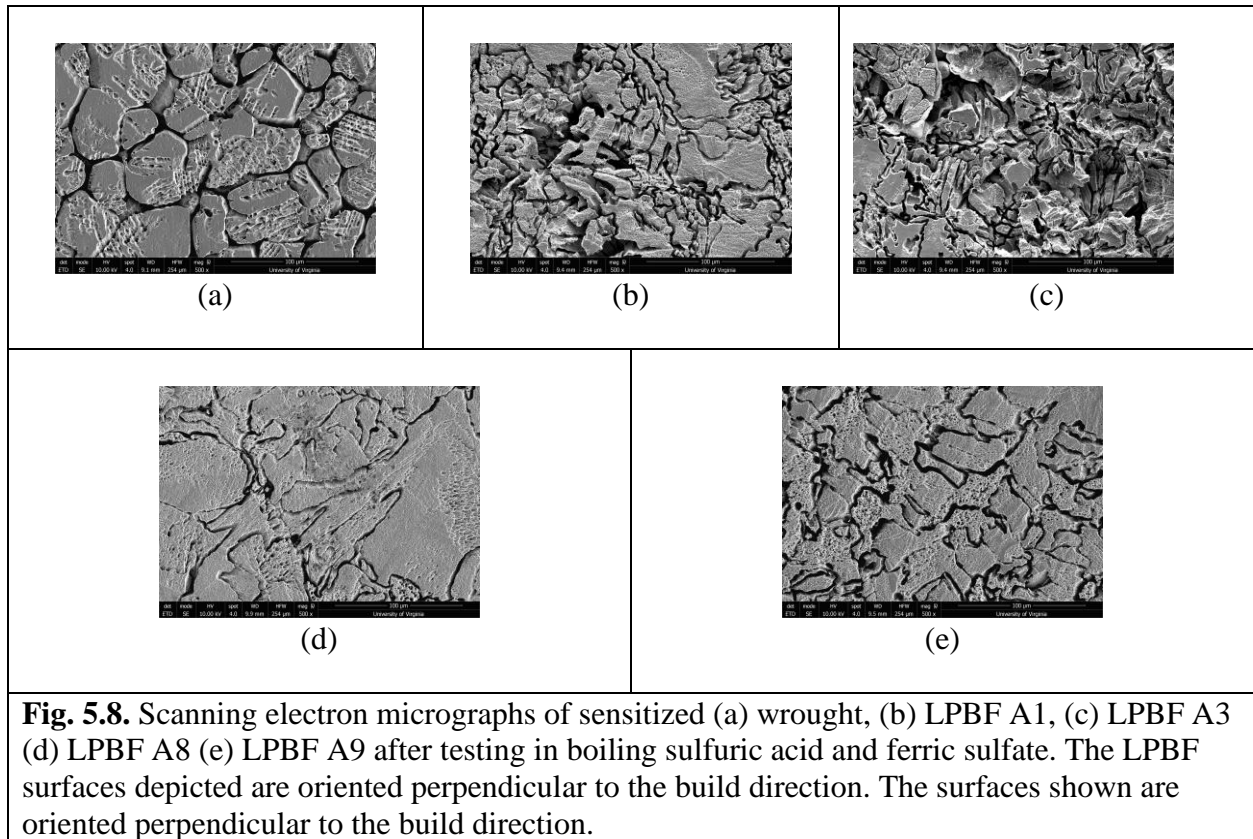
Fig. 5.9 shows cross sections of sensitized wrought material exposed to a boiling ferric sulfate and sulfuric acid environment before and after etching in Carpenter's etchant. Fig. 5.9a shows the equiaxed grains on the metal surface. From Fig. 5.9b, the etching highlights the grains and further confirms that the attack propagates along the grain boundaries. In the case of the normal-rolling surface, damage propagates along the equiaxed grains. However, for the normal-transverse direction (Fig. 5.9c), deeper fissures are observed and the etching (Fig. 5.9d) reveals that damage may propagate along inclusion stringers in the wrought material.
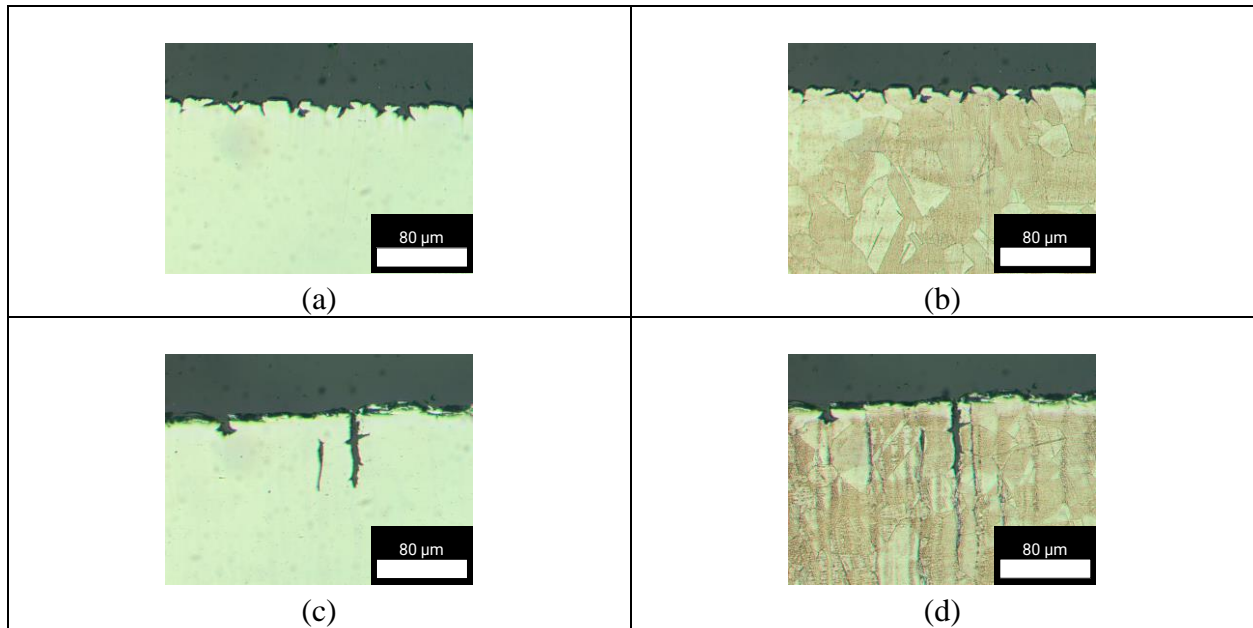
Fig. 5.9. Cross-sections of sensitized wrought material showing damange along the normal-rolling plane after testing in boiling sulfuric acid and ferric sulfate are shown (a) before and (b) after etching in Carpenter's etch. Cross sections for the transverse-rolling plane (c) before and (d) after etching are also shown.

Fig. 5.10 shows cross sections of sensitized LPBF material exposed to a boiling ferric sulfate and sulfuric acid environment before and after etching in Carpenter's etchant. For all LPBF materials, it is seen that damage takes place along the grain boundaries as confirmed by metallographic etching. In the case of materials A1 (Fig. 5.10a and Fig. 5.10b) and A3 (Fig. 5.10c and Fig. 5.10d), deeper propagation of damage is observed not only through grain boundaries but also through what appears to be lack-of-fusion pores. These pores are not observed in LPBF materials A8 (Fig. 5.10e and Fig. 5.10f) and A9 (Fig. 5.10g. and Fig. 5.10h.), and fissures that are not as a deep are qualitatively observed.
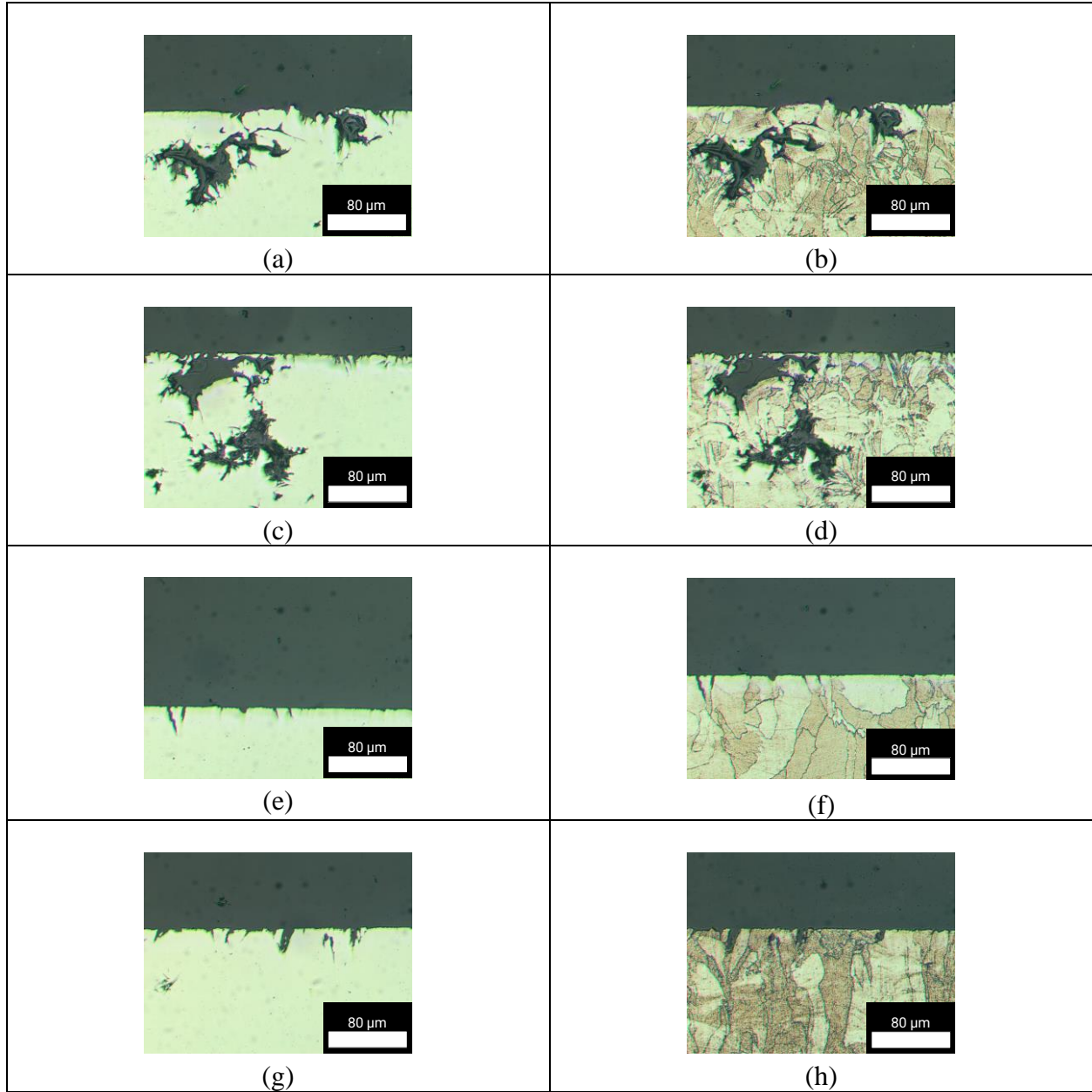
Fig. 5.10. Cross-sections of sensitized LPBF material showing damage along the orientation perpendicular to the build direction after testing in boiling sulfuric acid and ferric sulfate for LPBF materials A1 (a) before and (b) after etching, A3 (c) before and (d) after etching, A8 (e) and (f) before and after etching, and A9 (g) before and (h) after etching.

Fig. 5.11 shows damage depth as a function of average measured corrosion rate in the boiling ferric sulfate and sulfuric acid test for LPBF and wrought materials. It is seen generally

102

that larger measured damage depths acre associated with higher measured corrosion rates. It is also interesting to take note of how the standard deviation is higher for LPBF materials A1 and A3. Finally, in the case of the wrought material, damage propagation is reported for two orientations and greater differences in damage depth is observed.
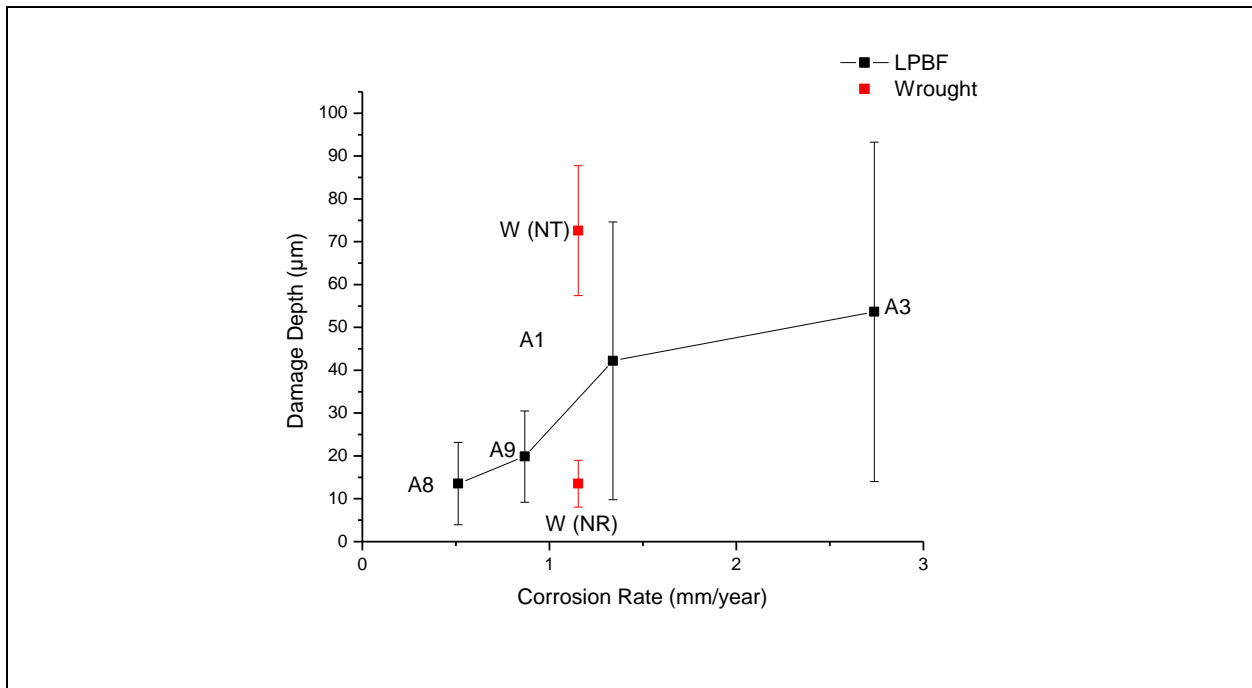
Fig. 5.11. Graph depicting damage depth along the surface perpendicular to the build direction from cross sectional analysis as a function of measured of corrosion rate from the boiling sulfuric acid and ferric sulfate test for select LPBF materials. Damage depths are shown for the wrought material in the NT and NR plane.

Fig. 5.12 combines the results from the DL-EPR potentiodynamic test as well as the boiling ferric sulfate and sulfuric acid mass loss test. This graph plots corrosion rate from the mass loss test as a function of measured DOS from the DL-EPR test. The DOS values are reported on a logarithmic scale. Higher mass loss rates are generally associated with higher DOS values.
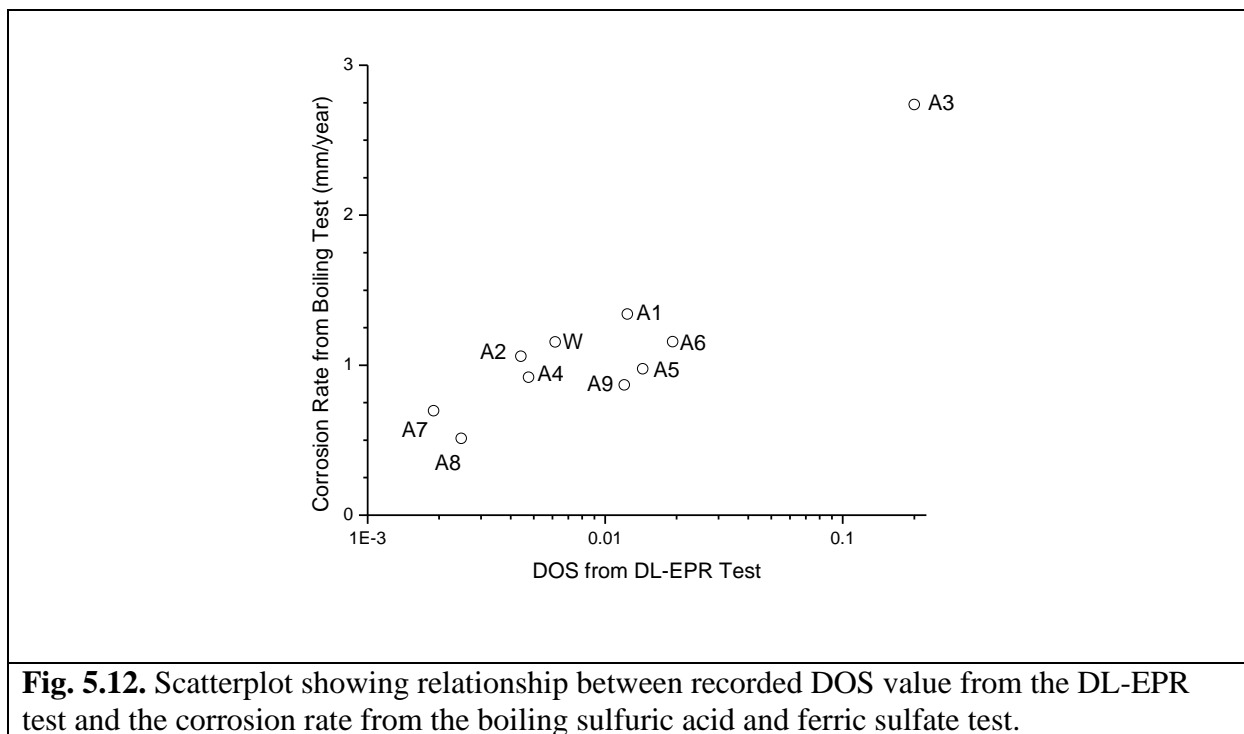
Fig. 5.12. Scatterplot showing relationship between recorded DOS value from the DL-EPR test and the corrosion rate from the boiling sulfuric acid and ferric sulfate test.

5.5 Discussion

The discussion section is set up in a way that first discusses results from the EPR experiments followed by the mass loss test. The impact of processing parameters is discussed in discussed with respect to the volumetric energy density value. Finally, the concurrent validity of each test in IGC testing of sensitized LPBF alloys is discussed.

5.5.1 EPR Experiments

The DL-EPR scan is a test that is traditionally used to detect the susceptibility of wrought austenitic steels to intergranular corrosion [26–29]. The DL-EPR test was originally developed for 304 stainless steel and is usually performed with 0.5 M H_2SO_4 and is scanned to a maximum potential of 0.3 V vs. SCE. This modified DL-EPR test is relatively more aggressive due to higher acid concentration and lower maximum potential as the 316 grades contain Mo and typically have passive films that are more resistant to breakdown [33–37]. From the scans shown in Fig. 5.3,

reactivation in the reverse scan is clearly observed in both wrought and LPBF samples that have been held at 675°C for 24 hours. In the case of LPBF Material A3, the scan behavior differs greatly from that of the wrought and LPBF Material A1. This major difference in scan behavior may be due to reactivation current densities that greatly exceed the cathodic current density in that potential range so that a cathodic loop is not observed in the scan.

Post-test micrographs further highlight that the reactivation is mainly attributed to grain boundary depassivation. For the wrought (Fig. 5.4a) and the LPBF material (Fig. 5.4c), preferential corrosion of the grain boundaries is observed. In the case of the LPBF material, small pit-like structures are observed within the grains, but the damage is mainly seen at the grain boundaries. Other works have shown that this temperature range does not necessarily anneal away the cellular structures [15,38,39]. While this grain boundary corrosion is clearly observed, most of this dissolution most likely took place during the forward scan of the DL-EPR scan due to how the activation currents are 2-3 orders of magnitude higher than the reactivation currents measured during the reverse portion of the EPR scan . SL-EPR scans were ultimately performed to confirm that electrochemically passivated as-ground wrought and LPBF material would exhibit grain boundary corrosion when polarized to potentials that induce active corrosion. These characterization experiments further highlight the use of the DL-EPR in testing susceptibility to intergranular corrosion. While this manuscript is not focused on the corrosion properties of as-built LPBF material, it is important to note that this type of intergranular behavior is not typically observed in as-built LPBF material [12,15,16,18,19,40,41].

DOS calculations show that material printed at lower volumetric energy density values are generally more susceptible to intergranular attack. While it is seen that the DOS value is higher for materials printed at lower VED values, the results also indicate that the VED value alone is not

sufficient in describing susceptibility to intergranular corrosion. This effect is evident in comparing DOS values of materials printed with VED values of 78 J/mm^3 (A4, A5, and A6) as well as materials printed with a VED of 132 J/mm^3 (A8 and A9). In discussing the materials printed with a volumetric energy of 78 J/mm^3, it is observed that while there is an overlap between the DOS values for sensitized A5 and A6, A4, the material from this trio with the lowest scan speed is shown to demonstrate the lowest susceptibility to IGC. Similarly, in comparing the results of the two materials printed with a VED of 132 J/mm^3 (A8 and A9), the material with the lower scan speed (A8) has lower susceptibility compared to the material printed with a higher scan speed at the same VED (A9). Multiple studies in sensitized wrought austenitic steels have attributed higher DOS values to smaller grain sizes which effectively lead to a greater density of sensitized boundary prone to reactivation [42–46]. Post-DLEPR testing microscopy for select LPBF materials further justifies this in comparing the post-test micrographs of LPBF A4 and A6, materials printed with VED values of 78 J/mm^3. Material A4 was printed with a lower scan speed in comparison to A6 and a greater number of grain boundaries are observed in the A6 variant. This trend between microstructure and laser processing has been shown in various alloy systems and is likely due to how more rapid solidification conditions result in more refined grains [42–46]. From the DL-EPR results and post-test micrographs, it is therefore proposed that grain boundary density greatly dictates observed trends in DOS.

5.5.2 Mass Loss Testing

While the DL-EPR test investigates the tendency of grain boundaries for depassivation, boiling acid tests are another way that tests intergranular corrosion susceptibility through mass loss. In these tests, grain boundaries corrode in the case of sensitized alloys and mass loss takes place through the dislodging and dropping of entire grains [1,30] and this mechanism is clearly

seen in post-test micrographs (Fig. 5.8). The boiling test provided by ASTM A-262 Practice B uses ferric ions as an oxidizer and it has been shown that mass loss takes place due to the continuous formation and breakdown of a protective oxide [1,2,30,32]. This process occurs more rapidly in areas that are depleted of chromium such as areas adjacent to sensitized grain boundaries [1,30].

In observing trends between mass loss rate and VED, it is seen that mass loss is generally higher in the case of sensitized materials printed with lower VED values. It is seen that materials printed with lower VED (Fig. 5.8b and Fig. 5.8c) have smaller grains compared to those printed at higher VED (Fig. 5.8d and Fig. 5.8e). A higher density of grain boundaries more efficiently favors the ability of grains to dislodge due to the lower amount of grain boundary that needs to dissolve before an entire grain can dislodge [47,48]. This relationship between grain size and the mechanism of mass loss is consistent with trends between processing parameters and corrosion rates.

Cross-sectional analysis provides further insight into the mechanism of IGC in sensitized LPBF alloys. However, in observing the post-test cross sections for sensitized wrought material, it is seen that mass loss can take place through the dropping of individual grains (Fig. 5.9a and Fig. 5.9b) and penetration through what appear to be inclusions (Fig. 5.9c. and Fig. 5.9d.). These inclusions are anticipated to be manganese sulfide inclusions and have shown to lead to end-grain corrosion in environments such as boiling nitric acid. Studies have reported that these are typically eliminated during the LPBF process [12,17]. Therefore, it is not surprising that the wrought material has a higher mass loss rate than a majority of the LPBF materials.

Cross-sectional analysis of sensitized LPBF alloys after the boiling test reveals dramatic differences in how LPBF defects can dictate the propagation of damage. First, it is seen that the

lower VED materials (Fig. 5.10b.) have smaller grains than higher VED materials (Fig. 5.10f.) and further supports how a greater amount of grain boundary needs to dissolve in higher VED materials before individual grains can fallout. Outside of grain size, LOF porosity is seen in materials with lower VED such as A1 (Fig. 5.10a.) and A3 (Fig. 5.10c.). It is clear in the LPBF literature that lower VED tends to lead to defects due to incomplete melting of powder and/or fusion of liquid. While it is observed that LPBF materials A8 (Fig. 5.10e) and A9 (Fig. 5.10g) display penetration simply through the propagation of damage along grain boundaries, LOF defects in the lower VED materials seem to reinforce IGC propagation. IGC damage can be observed in the actual pores in the lower VED materials suggesting that the oxidizing solution was eventually able to enter these pores. The consequence of these processing conditions is also highlighted in measuring IGC damage depths (Fig. 5.11) and shows how higher corrosion rates are associated with a greater damage depth. These results further highlight the detrimental nature of these defects in promoting further IGC propagation in LPBF materials.

Although the DL-EPR potentiodynamic test and the mass loss test vary in how they detect IGC susceptibility, concurrence is observed between the two tests from Fig. 5.12. It was highlighted how grain refinement would lead to detrimental results for both tests so the trends in results between these two tests is logical. Whereas the discussion of relatively susceptibility was limited to the presence of LPBF defects and grain size, a more holistic consideration of microstructural features needs to be taken into account especially with respect to processing parameters. For example, multiple studies have cited the impact of boundaries such as twin boundaries and low angle grain boundaries that increase resistance to sensitization and intergranular corrosion [47,49]. Due to the relevance of IGC susceptibility in the area of stress corrosion cracking, these studies provide further motivation to study the behavior of sensitized

LPBF alloys from a fracture mechanics perspective [7–9,50,51]. These experiments, however, show the general relationship between processing parameters and IGC susceptibility as well as the applicability of using these tests as a tool for assessing IGC behavior in sensitized LPBF 316L.

5.6 Conclusions

- Testing of thermally treated wrought and LPBF 316L DL-EPR and ferric sulfate/sulfuric acid mass loss tests demonstrate susceptibility to sensitization and intergranular corrosion.

- In both tests, it was generally found that LPBF materials printed with lower VED values are more prone to IGC.

- VED simply cannot be used as a predictor for IGC susceptibility due to variations in IGC behavior printed at varying conditions at constant VED. Nevertheless, materials printed with higher scan speed at constant VED demonstrated greater susceptibility to IGC.

- Post-test characterization shows grain refinement and a higher amount of porosity in lower VED materials that may be key to increased IGC susceptibility.

- Under constant VED, material printed at higher scan speed have more refined grains which may lead to greater IGC susceptibility.

5.7 Acknowledgements

5.8 Citations

1. In *Corrosion: Fundamentals, Testing, and Protection* (ASM International, 2003), pp. 568–571.
2. U. Ultrasonic and N. S. Modification, (2015).
3. M. Terada, M. Saiki, I. Costa, and A. F. Padilha, Journal of Nuclear Materials **358**, 40 (2006).

4. A. King, G. Johnson, D. Engelberg, W. Ludwig, and J. Marrow, Science (1979) **321**, 382 (2008).

5. H. Inoue and T. Koseki, Nippon Steel Technical Report 62 (2007).

6. K. Weman, in *Welding Processes Handbook (Second Edition)*, edited by K. Weman, Second Edi (Woodhead Publishing, 2012), pp. 191–206.

7. S. Ahmad, M. L. Mehta, S. K. Saraf, and I. P. Saraswat, Corrosion **38**, 347 (1982).

8. V. Kain, in *Stress Corrosion Cracking*, edited by V. S. Raja and T. Shoji (Woodhead Publishing, 2011), pp. 199–244.

9. S. Ahmad, M. L. Mehta, S. K. Saraf, and P. Saraswat, 3 (1981).

10. T. J. Marrow, L. Babout, A. P. Jivkov, P. Wood, D. Engelberg, N. Stevens, P. J. Withers, and R. C. Newman, Journal of Nuclear Materials **352**, 62 (2006).

11. D. B. Wells, J. Stewart, A. W. Herbert, P. M. Scott, and D. E. Williams, Corrosion **45**, 649 (1989).

12. G. Sander, J. Tan, P. Balan, O. Gharbi, D. R. Feenstra, L. Singer, S. Thomas, R. G. Kelly, J. R. Scully, and N. Birbilis, Corrosion **74**, 1318 (2018).

13. D. Herzog, V. Seyda, E. Wycisk, and C. Emmelmann, Acta Materialia **117**, 371 (2016).

14. D. D. Gu, W. Meiners, K. Wissenbach, and R. Poprawe, **57**, 133 (2013).

15. D. A. Macatangay, G. W. Kubacki, and R. G. Kelly, JOM (2022).

16. D. A. T. Macatangay, J. M. Conrades, K. L. Brunner, and R. G. Kelly, Corrosion **78**, 13 (2022).

17. G. Sander, S. Thomas, V. Cruz, M. Jurg, N. Birbilis, X. Gao, M. Brameld, and C. R. Hutchinson, Journal of The Electrochemical Society **164**, C250 (2017).

18. J. J. Sopcisak, M. Ouyang, D. A. Macatangay, B. P. Croom, T. J. Montalbano, D. J. Sprouster, R. G. Kelly, J. R. Trelewicz, R. Srinivasan, and S. M. Storck, JOM **74**, 1719 (2022).

19. M. A. Melia, H.-D. A. Nguyen, J. M. Rodelas, and E. J. Schindelholz, Corrosion Science **152**, 20 (2019).

20. F. Caiazzo, V. Alfieri, and G. Casalino, Materials **13**, 538 (2020).

21. M. Guo, D. Gu, L. Xi, H. Zhang, J. Zhang, J. Yang, and R. Wang, International Journal of Refractory Metals and Hard Materials **84**, 105025 (2019).

22. P. Ferro, R. Meneghello, G. Savio, and F. Berto, The International Journal of Advanced Manufacturing Technology **110**, 1911 (2020).

23. K. G. Prashanth, S. Scudino, T. Maity, J. Das, and J. Eckert, Materials Research Letters **5**, 386 (2017).

24. M. Ghayoor, K. Lee, Y. He, C. Chang, B. K. Paul, and S. Pasebani, Additive Manufacturing **32**, 101011 (2020).

25. H. R. Javidrad, M. Ghanbari, and F. Javidrad, Journal of Materials Research and Technology **12**, 989 (2021).

26. M. Momeni, M. H. Moayed, and A. Davoodi, Corrosion Science **52**, 2653 (2010).

27. A. P. Majidi and M. A. Streicher, CORROSION **40**, 584 (1984).

28. T. Amadou, H. Sidhom, and C. Braham, Metallurgical and Materials Transactions A **35**, 3499 (2004).

29. R. B. Rebak and S. W. Dean, Corrosion **76**, 742 (2020).

30. In *Corrosion of Weldments* (ASM International, 2006), pp. 203–216.

31. G. R. Mirshekari, E. Tavakoli, M. Atapour, and B. Sadeghian, Materials & Design **55**, 905 (2014).

32. A. S. A262, ASTM International, West Conshohocken, PS **01**, 1 (2014).

33. S. J. Kropschot and J. Doebrich, Usgs 1 (2010).
34. W. Li and P. C. Pistorius, Journal of The Electrochemical Society **159**, C513 (2012).
35. B. Stypula and J. Banaś, Electrochimica Acta **38**, 2309 (1993).
36. A. H. Seikh, H. Halfa, and M. S. Soliman, Metals (Basel) **11**, 852 (2021).
37. H.-Y. Ha, T.-H. Lee, J.-H. Bae, and D. Chun, Metals (Basel) **8**, 653 (2018).
38. G. N. Nigon, O. B. Isgor, and S. Pasebani, Journal of The Electrochemical Society **167**, 141508 (2020).
39. P. Deng, H. Yin, M. Song, D. Li, Y. Zheng, B. C. Prorok, and X. Lou, JOM **72**, 4232 (2020).
40. D. A. Macatangay, S. Thomas, N. Birbilis, and R. G. Kelly, **74**, 153 (2018).
41. D. Kong, C. Dong, X. Ni, and X. Li, Npj Materials Degradation **3**, (2019).
42. K. Moussaoui, W. Rubio, M. Mousseigne, T. Sultan, and F. Rezai, Materials Science and Engineering: A **735**, 182 (2018).
43. E. Liverani, S. Toschi, L. Ceschini, and A. Fortunato, Journal of Materials Processing Technology **249**, 255 (2017).
44. Q. Shi, D. Gu, M. Xia, S. Cao, and T. Rong, Optics & Laser Technology **84**, 9 (2016).
45. A. Ahmadi, R. Mirzaeifar, N. S. Moghaddam, A. S. Turabi, H. E. Karaca, and M. Elahinia, Materials and Design **112**, 328 (2016).
46. T. Kurzynowski, K. Gruber, W. Stopyra, and E. Chlebus, **718**, 64 (2018).
47. R. Singh, S. G. Chowdhury, B. Ravi Kumar, S. K. Das, P. K. De, and I. Chattoraj, Scripta Materialia **57**, 185 (2007).
48. R. v. Taiwade, R. Shukla, H. Vashishtha, A. v. Ingle, and R. K. Dayal, ISIJ International **53**, 2206 (2013).
49. A. Y. Chen, W. F. Hu, D. Wang, Y. K. Zhu, P. Wang, J. H. Yang, X. Y. Wang, J. F. Gu, and J. Lu, Scripta Materialia **130**, 264 (2017).
50. T. Simson, A. Emmel, A. Dwars, and J. Böhm, Additive Manufacturing **17**, 183 (2017).
51. O. Takakuwa and H. Soyama, Advances in Chemical Engineering and Science **05**, 62 (2015).

6 Conclusions

6.1 Chapter 3: Overview of Corrosion Phenomenology in Additively Manufactured 316L

(1) The work identified and described selective corrosion in phenomenology in AM 316L produced by both LPBF and DED.

(2) Under conditions that promote active dissolution, microstructural features that had higher chromium and molybdenum experienced less dissolution compared to areas poor of these elements.

    a. For LPBF 316L, cellular dendritic boundaries had higher chromium and molybdenum.

        i. Under active dissolution in potassium thiocyante and sulfuric acid, cellular dendritic interiors underwent preferential corrosion.

        ii. Under active dissolution in ferric chloride and sodium chloride environments, pit interiors exhibited preferential corrosion at the cellular interiors.

    b. For DED 316L, the ferritic phase had higher chromium and molybdenum.

        i. Under active dissolution in potassium thiocyante and sulfuric acid, the austenitic phase demonstrated preferential corrosion.

(3) Under conditions that promote transpassive dissolution, microstructural features that had higher chromium and molybdenum experienced preferential dissolution compared to areas poor of these elements.

    a. For LPBF 316L, cellular dendritic boundaries had higher chromium and molybdenum.

        i. Under transpassive dissolution in sulfuric acid, cellular dendritic boundaries underwent preferential corrosion.

  ii. Cellular boundaries experienced preferential corrosion in boiling nitric

    acid due to chromium oxidation to the hexavalent state.

 b. For DED 316L, the ferritic phase had higher chromium and molybdenum.

  i. Under transpassive dissolution in sulfuric acid, the ferritic phase

    demonstrated preferential corrosion.

6.2 Chapter 4: The Effect of Processing on LPBF 316L Selective Corrosion

(1) This work is focused on the relationship between reactivation behavior and LPBF

  processing parameters.

(2) Using the DLEPR test as a tool for determining susceptibility to reactivation, it was

  determined that LPBF materials printed at lower volumetric energy density tend to

  demonstrate greater propensity for surface reactivation.

 a. The limits of using volumetric energy density have also been shown. At constant

   VED, it was demonstrated how there is greater propensity for reactivation for

   materials printed with higher scan speed

(3) Modified SLEPR and DLEPR tests further validate the results from the DLEPR scan.

 a. The SLEPR scan shows how a passivated surface will demonstrate reactivation

   through preferential dissolution of the cellular dendritic interiors due to lower

   chromium and molybdenum at the interiors.

 b. When comparing the SLEPR behavior between material with zero and non-zero

   DOR values, the material with a non-zero DOR value demonstrated a higher

   degree of corrosion shown through dissolution of cellular dendritic interiors.

 c. Under active conditions, potentiostatic holds of passivated material that had zero

   and non-zero DOR values from the DLEPR scan showed that the material with

the non-zero value had higher anodic dissolution currents compared to the

material that demonstrated zero DOR.

    d. These tests further validate the use of the DL-EPR method in detecting

susceptibility to surface reactivation as well as the role of the cellular dendritic

structures in observed electrochemical behavior.

6.3 Chapter 5: Sensitization and Intergranular Corrosion of Thermally Treated LPBF 316L

(1) This work describes IGC phenomenology in sensitized LPBF 316L and the role of

processing parameters on susceptibility to IGC and sensitization.

(2) IGC testing through the DLEPR technique and mass loss testing in boiling ferric sulfate

and sulfuric acid showed that material printed with lower VED values had greater

susceptibility to intergranular corrosion.

    a. Post-test characterization showed that susceptibility may be to greater grain

refinement at lower VED and a higher level of porosity.

    b. VED alone is not sufficient in predicting IGC susceptibility and it was found that

constant VED, material printed at higher scan velocity had greater susceptibility.

(3) The consistency between DLEPR testing and the boiling acid mass loss test as well as

post-test characterization validate the use of these techniques in assessing IGC

susceptibility for heat treated LPBF 316L.

7. Appendix: Supplemental Publications

The appendix highlights manuscripts that have been approved for publication. The manuscript "Unexpected Interface Corrosion and Sensitization Susceptibility in Additively Manufactured Austenitic Stainless Steel" briefly discusses observations of melt pool boundary dissolution in LPBF 316L. It also shows observations of intergranular corrosion in sensitized LPBF 316L. The manuscript "Applications of Wrought Austenitic Stainless Steel Corrosion Testing to Laser Powder Bed Fusion 316L" applies standardized tests to a multitude of LPBF 316L printed with difference parameters and machines. Like the body of the dissertation, this publication focuses on localized corrosion in LPBF alloys and is a critique on the applicability of conventional testing on LPBF alloys. The manuscript "Localized Corrosion in Additively Manufactured Stainless Steel and Aluminum Alloys" is a brief discussion of corrosion in additively manufactured stainless steel and aluminum alloys. In relation to the material in the dissertation, this manuscript talks about melt pool and cellular interior dissolution. It also discusses the corrosion of LPBF 316L after hot isotactic pressing.

Unexpected Interface Corrosion and Sensitization Susceptibility in Additively Manufactured Austenitic Stainless Steel

D.A. Macatangay,* S. Thomas,** N. Birbilis,** and R.G. Kelly‡,*

ABSTRACT

This communication describes observations of unexpected microstructural interface susceptibility to accelerated dissolution in additively manufactured (AM) Type 316L stainless steel prepared by selective laser melting. Observations include accelerated microstructural interface dissolution in the as-built condition, as well as more rapid sensitization of grain boundaries upon exposure to elevated temperature. Electrolytic etching in persulfate solution was used to evaluate the susceptibility of microstructural interfaces to accelerated dissolution in both wrought and AM 316L. Post-test optical microscopy and profilometry on AM 316L revealed that the melt pool boundaries in the as-built condition were susceptible to accelerated attack, although the small grains within the prior melt pools were not. Furthermore, short, elevated temperature exposure (1 h at 675°C) also induced sensitization of the grain boundaries. Identical testing on as-manufactured wrought 316L confirmed that no microstructural interfaces showed susceptibility to accelerated dissolution, and grain boundaries could be sensitized only by extended periods (24 h) at elevated temperature (675°C). Annealing was capable of removing sensitization in wrought 316L, but activated the surface of the AM 316L, leading to widespread, uniform dissolution.

INTRODUCTION

Currently there is an intense interest in the use of additive manufacturing (AM) methods for a range of materials.[1] Opportunities are abundant for component complexity and design,[2] material (and multi-material) control,[2] and repair of existing structures.[2] The study of additively manufactured materials (namely metallic materials) to date has principally focused on mechanical properties, often with the goal of generating strength and ductility at least equivalent to that of wrought counterpart alloys.[3] Corrosion studies have been limited, with several focusing on the role of manufacturing defects as precursor sites for localized corrosion initiation.[4-7]

Additive manufacturing of metallic alloys nominally commenced with high-value alloys (on the basis of cost savings from the additive nature of manufacturing and component complexity in the aerospace industry) such as nickel and titanium alloys, which are nominally corrosion resistant.[8-10] However, most recently, stainless steels are becoming increasingly explored in the context of AM on the basis of the ability to rapidly and economically deploy so-called corrosion resistant alloys in a range of industries, including replacement components. Austenitic stainless steels such as Type 316L (UNS S31603[(1)]) are nominally single-phase microstructures, but are inherently susceptible to intergranular corrosion when second

TABLE 1
Chemical Composition of Wrought and AM 316L[(A)]

	Fe	Cr	Ni	Mo	Mn	S	Cu	C	N	O
Wrought	Bal.	16.7	10.2	1.99	1.48	0.0011	0.350	0.023	0.029	0.0028
AM	Bal.	18.1	10.8	2.51	1.42	0.0086	0.029	0.014	0.048	0.0510

[(A)] Fe, Cr, Mn, Mo, and Ni content were determined through inductively coupled plasma optical emission spectrometry. S and Cu content were determined through glow discharge mass spectrometry. C, N, and O content were determined by instrumental gas analysis.

phases form at grain boundaries, which cause a local depletion of chromium (Cr) in the areas adjacent to the grain boundaries.[11-12] This grain boundary sensitization occurs as a result of elevated temperature exposure (~550°C to 800°C) for periods of time that depend on the alloy carbon content.[12] Local microstructural regions denuded of chromium no longer have the local composition to remain "stainless" and thus undergo rapid dissolution in many environments.[12] Susceptibility to intergranular corrosion also can represent susceptibility to intergranular stress corrosion cracking.[13] This communication describes observations of unexpected microstructural interface susceptibility to accelerated dissolution in AM 316L in the as-built condition, as well as more rapid sensitization of grain boundaries upon exposure to elevated temperature. The discovery of degradation phenomena unique to AM is an area of significant and timely relevance.

EXPERIMENTAL PROCEDURES

AM 316L specimens of 60 mm × 20 mm × 20 mm were produced by selective laser melting (SLM) using an EOS M280[†] instrument. The 316L powder was supplied by Sandvik Osprey,[†,(2)] and melted using the following parameters: laser scanning speed of 960 m/s, laser power of 205 W, and hatch distance of 0.11 mm. The wrought 316L sheet (12.7 mm thick) used was obtained from North American Stainless[†] and its composition was also within specifications. Chemical analyses of both the wrought and AM 316L were performed at EAG Laboratories (Liverpool, New York) and the results are shown in Table 1.

Etching for grain boundary and interface sensitization was performed according to ASTM A262 Practice A,[7] applying 1 A/cm^2 for 5 min to a previously ground (to 1200 grit) surface exposed to 10 wt% solution of ammonium persulfate ((NH$_4$)$_2$S$_2$O$_8$), as recommended for Type 316L stainless steel. Following etching, samples were rinsed and sonicated in ethanol and examined with both optical microscopy and white light interferometry (Zygo NewView 7300 Optical Surface Profiler[†]). Mountain Maps[†] software (version 6, Digital Surf) was utilized to obtain topographical

profiles from interferometry data. Representative line scans were extracted to confirm the nature of the etching structures observed. Scanning electron microscopy (ThermoFischer Quanta LV 200[†]) was implemented to obtain higher resolution images of the etched structures. All AM 316L images were performed on cross sections perpendicular to the build direction.

RESULTS AND DISCUSSION

The persulfate etching of wrought 316L (in the as-received condition) reveals a classic "step" etch structure in which grains dissolve uniformly (Figure 1[a]). The etching of unique grains in persulfate solution occurs at different rates as a result of the crystallographic dependence of dissolution rate in acid under oxidizing conditions in the absence of chloride.[14] The deliberate sensitization of wrought 316L (by 24 h exposure at 675°C) led to a "ditch" etch structure (Figure 1[b]) in which the grain boundaries, depleted in chromium, dissolve at significantly higher rates than grain interiors. Shorter time exposure at 675°C did not result in grain boundary sensitization detectable with persulfate etching. It was also revealed that annealing (1 h exposure at 1,100°C) homogenizes the chromium concentration,[12] leading back to a step etch structure (Figure 1[c]).

In contrast to the behavior of wrought 316L, the etching of as-built AM 316L revealed extensive melt pool boundary attack (Figure 1[d]). Essentially, the entire boundary was dissolved around each melt pool during etching, while the interiors (to the melt pool boundaries) appeared to dissolve uniformly. Interestingly, it was determined that only ~1 h of exposure to 675°C was required to cause sensitization of grains inside the melt pools for the AM 316L (Figure 1[e]). In addition, the melt pool boundaries were still active, with grains extending across the melt pool boundaries. Even more curiously, the annealing of AM 316L (1 h exposure at 1,100°C) led to both the formation of pores (of the order of 30 μm to 50 μm in diameter) and a generalized activation/uniform dissolution of the surface (Figure 1[f]), rather than the formation of a step structure, as one would expect. This set of phenomena has not been previously reported or documented in the context of AM prepared fully austenitic stainless steels.

The differences in the etching structures obtained are confirmed by optical profilometry to be a

---

[†] Trade name.
[(2)] The 316L powder had the following composition in weight percent: 17.0% Cr, 10.6% Ni, 2.1% Mo, 1.32% Mn, 0.66% Si, 0.03% P, 0.02% S, 0.01% C.
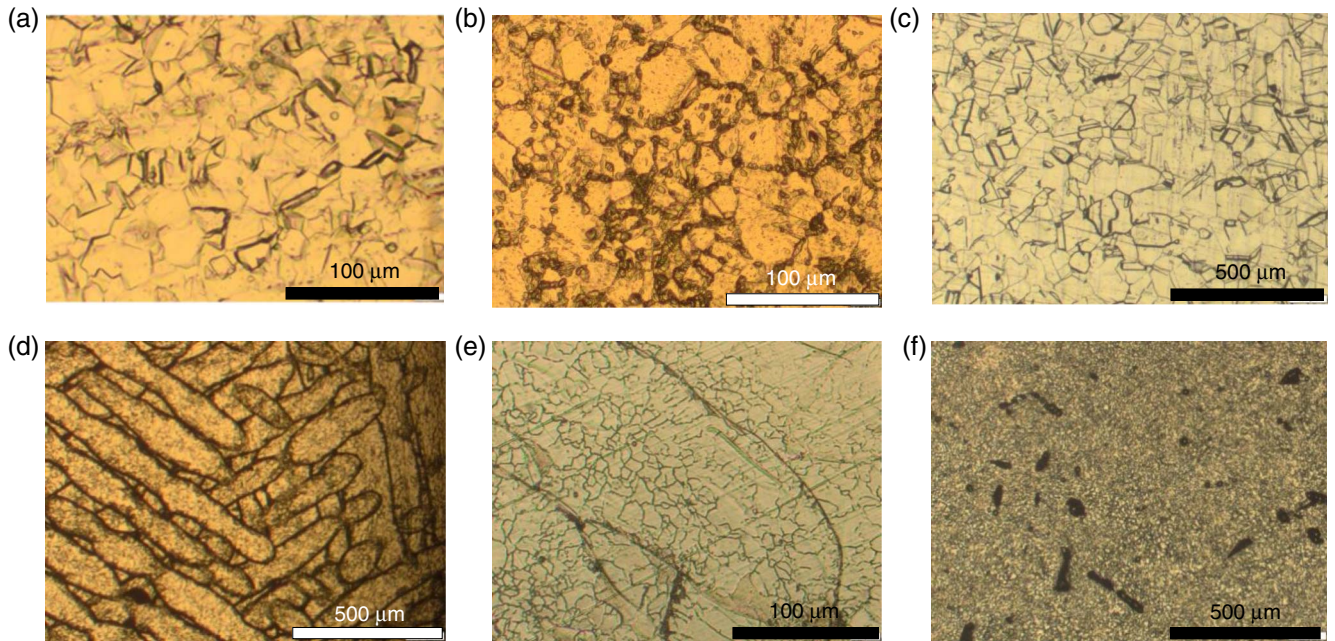
FIGURE 1. *Optical micrographs following persulfate etching of: (a) wrought 316L, unsensitized, (b) wrought 316L, sensitized at 675°C for 24 h, (c) wrought 316L, sensitized then annealed at 1,100°C for 1 h, (d) AM 316L, unsensitized, (e) AM 316L, sensitized at 675°C for 1 h, and (f) AM 316L, sensitized and annealed. Note: different magnifications used to highlight etching structures.*

result of crystallographically-controlled dissolution for step structures (Figure 2[a] corresponding to Figure 1[c]), and interface attack (Figure 2[b] corresponding to Figure 1[d]). The depths of the attack in the as-received AM 316L were notably deeper (ca. 4 μm) than that those observed on what is considered to be heavily sensitized (24 h at 675°C) wrought 316L (ca. 2 μm).
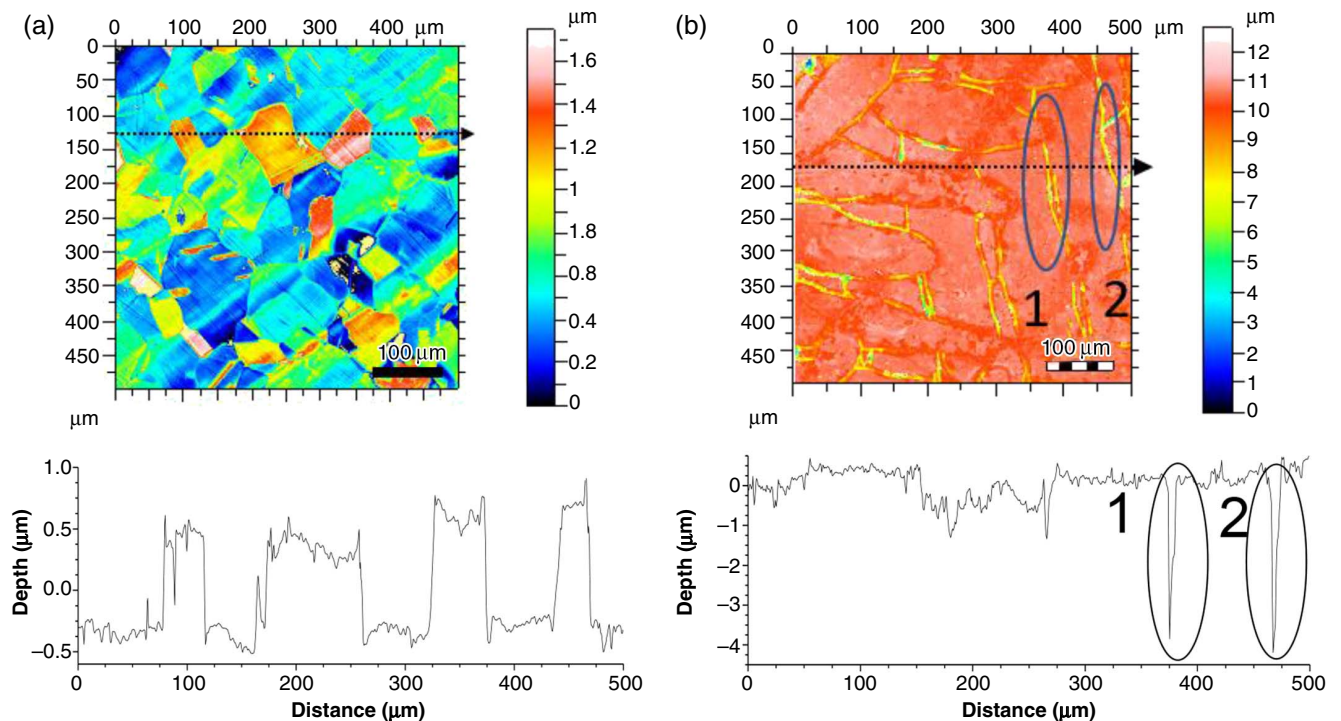
FIGURE 2. *Optical profilometry of (a) step structure from wrought 316L after sensitization and subsequent annealing, and (b) as-received AM 316L.*

Scanning electron microscopy using secondary electron imaging highlights the inner melt pool microstructure after etching. Although melt pool boundaries underwent rapid attack, the melt pool interiors exhibited almost uniform dissolution in the as-built sample (Figure 3[a]), which is very curious as preliminary electron backscatter diffraction (EBSD) work confirms a distribution of grains with different orientations within the melt pools. After undergoing heat treatment for 1 h, step-like attack was observed within the melt pools revealing the grains (Figure 3[b]). Even more surprisingly, exposure to at 675°C for 9 h resulted in the sensitization of the grain boundaries within the melt pools, although 24 h at 675°C is required to observe sensitization in the wrought material. As the grain sizes in the wrought 316L are marginally higher than those of AM 316L, this observation is in contrast with work that showed an inverse relationship between degree of sensitization and grain boundary area in austenitic stainless steels.[15] These observations provide even further motivation to investigate the sensitization mechanism in AM 316L.

The details regarding the source of the sensitization are under current study. It seems unlikely that the initial observed corrosion susceptibility phenomenon is the same as traditional chromium depletion at grain boundaries via formation of $Cr_{23}C_6$, as the depth of attack at the melt pool boundaries does not become more severe with the 1 h (or longer) sensitization treatment at 675°C. X-ray diffraction (not reported herein) showed no indication of the formation of other phases (such as ferrite). One possibility is the formation of sigma phase (σ)[16-18] resulting from extended times at elevated temperatures during the build. A second possibility is that the higher nitrogen content of the AM material, along with its rapid solidification from the melt, could have led to the formation of Cr_2N at the melt pool boundaries, which would lead to increased susceptibility to dissolution, as is the case for their formation in duplex stainless steels.[19] Transmission electron microscopy studies will be required

to assess these hypotheses and are planned. The transition in behavior for AM-prepared 316L upon annealing is particularly curious and merits reporting. The nominally hemispherical pores that form were not present in the as-received or any of the sensitized AM 316L. The higher annealing temperature may give sufficient vacancy mobility to allow coalescence into pores.[19] The generalized activation/uniform dissolution of the surface and widespread pitting (~5 μm diameter) remains unexplained.

AM 316L has been demonstrated to be more resistant to pit initiation compared to wrought 316L.[5,7] The improved pitting resistance in AM 316L was attributed to the absence of detrimental MnS inclusions, which were annihilated during the SLM process.[7] However, the pit initiation sites and pitting mechanisms in AM 316L are yet to be clarified, although some researchers have hypothesized that the pit initiation sites may actually be related to pores on the AM alloy surfaces.[6] In regard to the influence of porosity, Sander, et al.,[5] observed that the repassivation potentials for AM specimens decrease with increasing specimen porosity. Herein, it was observed that AM 316L was more prone to sensitization, and thus intergranular corrosion, compared to wrought 316L. Also, it has been identified that annealing of AM 316L will have a profound influence on its corrosion characteristics, although the reason for this difference in behavior relative to wrought materials is unknown. These contrasting sets of results for the two materials, in terms of pitting and intergranular corrosion, provide motivation for the investigation of similar microstructural interfacial sensitization in other AM materials, as well as the effects of powder characteristics, processing parameters, and post-build heat treatments. Such studies are particularly relevant for materials that have issues with traditional welding or exposure to elevated temperatures. For example, wrought 316L has been shown to form phases including σ and carbides ($M_{23}C_6$) upon extended aging[15-17] in the temperature range of 600°C to 900°C, which may also be
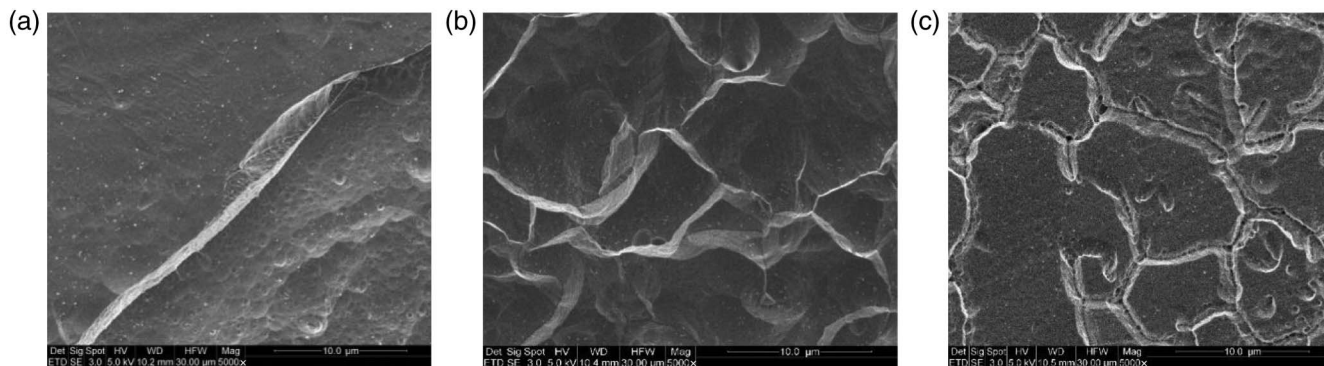
FIGURE 3. *Secondary electron images of persulfate etching of (a) as-received AM 316L, (b) AM 316L sensitized at 675°C for 1 h, and (c) AM 316L sensitized at 675°C for 9 h.*

influenced by cold work; however, such phase formation (and kinetics) in AM 316L have not been explored to date.

ACKNOWLEDGMENTS

REFERENCES

1. D. Bourell, J.P. Kruth, M. Leu, G. Levy, D. Rosen, A.M. Beese, A. Clare, *CIRP Ann.* 66, 2 (2017): p. 659-681.
2. X. Guo, J. Zhou, W. Zhang, Z. Du, C. Liu, Y. Liu, *Comput. Methods Appl. Mech. Eng.* 323 (2017): p. 27-63.
3. M. Ziętala, T. Durejko, M. Polański, I. Kunce, T. Płociński, W. Zieliński, M. Łazińska, W. Stępniowski, T. Czujko, K.J. Kurzydłowski, Z. Bojar, *Mater. Sci. Eng. A* 677 (2016): p. 1-10.
4. K.M. Mantrala, M. Das, V.K. Balla, C.S. Rao, V.S.S. Kesava Rao, *Front. Mech. Eng.* 1, 2 (2015): https://doi.org/10.3389/fmech.2015.00002.
5. G. Sander, S. Thomas, V. Cruz, M. Jurg, N. Birbilis, X. Gao, M. Brameld, C.R. Hutchinson, *J. Electrochem. Soc.* 164, 6 (2017): p. C250-C257.
6. R.F. Schaller, J. Taylor, J. Rodelas, E. Schindelholz, *Corrosion* 73, 7 (2017): p. 796-807.
7. Q. Chao, V. Cruz, S. Thomas, N. Birbilis, P. Collins, A. Taylor, P.D. Hodgson, D. Fabijanic, *Scrip. Mater.* 141 (2017): p. 94-98.
8. Q. Jia, D. Gu, *Opt. Laser Technol.* 62 (2014): p. 161-171.
9. H.S. Klapper, M. Burns, N. Molodtsov, C. Wangenheim, "Critical Factors Affecting the Pitting Corrosion Resistance of Additively Manufactured Nickel Alloy in Chloride Containing Environments," CORROSION 2017, paper no. 9345 (Houston, TX: NACE International, 2017).
10. J. Yang, H. Yang, H. Yu, Z. Wang, X. Zeng, *Metall. Mater. Trans. A* 48 (2017): p. 3583-3593.
11. A.J. Sedriks, *Corrosion of Stainless Steels*, 2nd ed. (New York, NY: Wiley-Interscience, 1996).
12. M. Warikh Abd Rashid, M. Gakim, Z. Mohd Rosli, M.A. Azam, *Int. J. Electrochem. Sci.* 7 (2012): p. 9465-9477.
13. X. Guo, K. Chen, W. Gao, Z. Shen, P. Lai, L. Zhang, *Corros. Sci.* 127 (2017): p. 157-167.
14. ASTM A262-15, "Standard Practices for Detecting Susceptibility to Intergranular Attack in Austenitic Stainless Steels" (West Conshohocken, PA: ASTM International, 2015).
15. R. Singh, S.G. Chowdhury, B. Ravi Kumar, S.K. Das, P.K. De, I. Chattoraj, *Scrip. Mater.* 57, 3 (2007): p. 185-188.
16. B. Weiss, R. Stickler, *Metall. Trans.* 3, 4 (1972): p. 851-866.
17. M. Matula, L. Hyspecka, M. Svoboda, V. Vodarek, C. Dagbert, J. Galland, Z. Stonawska, L. Tuma, *Mater. Charact.* 46 (2001): p. 203-210.
18. A. Ben Rhouma, T. Amadou, H. Sidhom, C. Braham, *J. Alloys Compd.* 708 (2017): p. 871-886.
19. O. Conejero, M. Palacios, S. Rivera, *Eng. Fail. Anal.* 16 (2009): p. 699-704.

Applications of Wrought Austenitic Stainless Steel Corrosion Testing to Laser Powder Bed Fusion 316L

Duane Armell T. Macatangay,[‡,] Jenna M. Conrades,* Keegan L. Brunner,* and Robert G. Kelly**

Recent developments in the 3D printing of austenitic stainless steels have led to the need for standardization of electrochemical techniques used to assess the corrosion performance of these alloys. Currently, ASTM standards for austenitic stainless focus on assessing their resistance to different modes of corrosion such as pitting, crevice, and intergranular corrosion. Due to the complexity of the additive process, selective corrosion occurs in microstructural features such as cellular structures and melt pool boundaries. Standardized corrosion testing needs to incorporate these microstructural features. This study characterizes the corrosion behavior of laser powder bed fusion stainless steel in a variety of ASTM standards with special attention to melt pool boundary dissolution, cellular structures, and intergranular corrosion.

KEY WORDS: additive manufacturing, intergranular corrosion, laser powder bed fusion, localized corrosion, sensitization, solidification

INTRODUCTION

Laser powder bed fusion (LPBF) is a form of additive manufacturing that builds material on a layer-by-layer basis through laser melting of powder and rapid solidification.[1-3] Research in LPBF has shown great control over the refinement of mechanical properties such as strength and ductility.[2,4-5] Due to conditions of rapid solidification, metal alloys made through LPBF have unique microstructural features such as melt pool boundaries, cellular structures, and melt pool boundaries.[3,6-9] The effect of processing parameters, such as scan speed and laser power, on the nature of these microstructural features has also been thoroughly investigated.[1] Due to the inevitable formation of a nonequilibrium microstructure in LPBF alloys, questions and concerns of selective corrosion validly arise.

The issue of corrosion is gaining attention in informing the longevity and performance of these alloys.[10-14] Multiple works have acknowledged the effects of porosity from the lack of fusion or keyholing as problematic from the perspective of pitting corrosion.[7,15-17] In oxidizing environments such as ferric chloride and ammonium persulfate, works have shown the susceptibility of melt-pool boundary attack in different alloy systems.[10,18] Due to observations of elemental segregation from rapid solidification and the formation of cellular structures, localized corrosion is observed across different alloy systems.[10,13,15,18] Other work has also shown how LPBF alloys may be more susceptible to sensitization upon exposure to elevated temperatures.[10,19] Despite the great advance in investigating the implications of these microstructural features on corrosion, standardized testing does not exist in specifically addressing localized corrosion susceptibility in these alloys in a way that acknowledges the unique and complex LPBF microstructure.

Currently, standards exist in determining the susceptibility of stainless steel grades such as 304 (UNS S30400[(1)]) and 316 (UNS S31600) to different forms of selective and localized corrosion.[20-24] Grades such as 304 and 316 have a nominally homogenous and single-phase microstructure.[25] Susceptibility to pitting corrosion is dictated by the presence of manganese-sulfide inclusions and can be determined by standards such as ASTM G-48.[26-28] Additionally, intergranular corrosion is an issue with steel exposed to elevated temperatures due to grain boundary precipitation of carbides and tests have been determined to test the susceptibility of these alloys to this form of selective corrosion from galvanostatic etching to mass loss testing.[29] However, these standards are catered more toward the microstructural features of conventionally wrought stainless steel. Thus, there is a need to determine if these tests are representative of localized corrosion that take place in LPBF alloys such as 316L (UNS S31603).

The primary goal of this work is to determine if current standardized tests are appropriate in capturing the tendency for localized corrosion in these alloys. In this study, ASTM standards specific to determining the susceptibility to intergranular corrosion in LPBF 316L of various printing parameters are utilized. ASTM A262 describes a qualitative test through galvanostatic etching and a quantitative test through mass loss testing in boiling nitric acid.[24,29] An electrochemical technique known as the double-loop electrochemical potentiokinetic test is also assessed.[30-32] The quantitative tests were supplemented with post-test microscopy to determine if the tests capture observations of localized corrosion in these alloys. These tests

were performed on as-built LPBF 316L, but they were also applied to LPBF 316L that have been exposed to elevated temperatures that would lead to sensitization. This study is designed to be critical of the application of conventional tests in determining corrosion behavior for both as-built and sensitized LPBF 316L. In order to broadly capture corrosion phenomena in LPBF 316L, builds from various processing methodologies were utilized.

EXPERIMENTAL PROCEDURES

Conventionally wrought 316L plate from North American Stainless[†] was used as a basis for comparison. In this study, three LPBF materials were tested. In addition to varying scan parameters, different machines were used for each part that was printed. Table 1 identifies these three samples and lists scanning parameters such as laser power, scan speed, hatch distance, and layer thickness. The machine that was used to print each sample and volumetric energy density are also indicated in Table 1. For all testing performed in this study, LPBF samples were cut from parts that were originally printed with dimensions of 20 mm × 20 mm × 60 mm. Post processing methods such as hot isotactic pressing or stress relieving were not performed. In each case, powder was not reused from previous builds. Due to previous printing of other alloys in these machines, the machines were made sure to be cleaned prior to the printing of materials for this study. In the case of LPBF materials 1, powder from Sandvik Osprey[†] was used with a nominal particle size distribution of –53 μm to 15 μm. In the case of LPBF materials 2 and 3, powder from Oerlikon[†] was used with a nominal particle size distribution of –45 μm to 15 μm.

Table 2 shows the composition of wrought and LPBF materials. Inductively coupled plasma atomic emission spectroscopy was used to obtain the composition of iron, nickel, molybdenum, chromium, and manganese. Instrumental gas analysis was used to determine the levels of carbon, nitrogen, and oxygen. Glow discharge mass spectrometry was used to determine the composition of silicon, phosphorus, sulfur, and copper.

2.1 | Sensitization

In addition to the performance of corrosion testing on as-built LPBF and as-is wrought 316L, testing was also performed on sensitized samples. Sensitization was achieved by exposing each sample to a temperature of 675°C for 24 h under ambient atmospheric conditions. A water bath was then used to quench each sample.

2.2 | Galvanostatic Etching

Galvanostatic etching was performed for all as-built (wrought and LPBF) and sensitized samples (wrought and LPBF) as detailed by ASTM-A262 practice A and is traditionally used to screen the susceptibility of stainless steel to intergranular corrosion.[24] All materials were ground to a 1200 grit finish. The surface tested was perpendicular to the build direction. A solution of 10 wt% ammonium persulfate was used as the electrolyte for etching. A constant current density of 1 A/cm^2 was applied. Micrographs were obtained through scanning electron microscopy (FEI Quanta 650[†]). It is to be noted that while oxalic acid is the common etchant given by this standard, ammonium persulfate is the etchant to be used for molybdenum-bearing steels.[24]

† Trade name.

Table 1. *Processing Parameters of LPBF Materials*

	LPBF Material 1	LPBF Material 2	LPBF Material 3
Laser Power (W)	205	235	220
Scan Speed (mm/s)	960	700	755.5
Hatch spacing (mm)	0.11	0.11	0.11
Layer thickness (mm)	0.04	0.05	0.02
Volumetric energy density (J/mm^3)	48.53	61.04	132.36
Machine	EOS M280[†]	SLM 125[†]	EOS M290[†]
Shielding gas	Nitrogen	Argon	Argon

Table 2. *Composition of Wrought and LPBF Materials in wt%*

	Wrought	LPBF Material 1	LPBF Material 2	LPBF Material 3
Iron	Balance	Balance	Balance	Balance
Chromium	16.7	18.1	17.1	17.9
Manganese	1.48	1.42	0.68	1.50
Molybdenum	1.99	2.51	2.32	2.40
Nickel	10.2	10.8	12.7	10.7
Copper	0.35	0.029	0.061	0.025
Silicon	0.27	0.86	0.61	0.060
Carbon	0.023	0.014	0.013	0.016
Nitrogen	0.029	0.048	0.071	0.020
Oxygen	0.028	0.051	0.048	0.060

2.3 | Double-Loop Potentiokinetic Reactivation Test

The double-loop potentiokinetic reactivation (DL-EPR) test is a cyclic potentiodynamic method for quantifying the degree of sensitization (DOS) in stainless steel. The electrolyte used for these scans contained 1 M H_2SO_4 and 0.01 M KSCN. The reference electrode used was a standard calomel electrode (SCE). All samples were ground to a 1200 grit finish and were tested in the orientation perpendicular to the build direction. Prior to the DL-EPR scan, the material was under open-circuit conditions for 30 min. Starting from the open-circuit potential (typically ~–0.4 V_{SCE}), the working electrode was scanned to a potential of 300 mV_{SCE} at a rate of 1.67 mV/s. Upon reaching this maximum potential, the working electrode was scanned in the reverse direction back to the open-circuit potential at the beginning of the test. Post-test micrographs were obtained through scanning electron microscopy. The degree of sensitization is expressed as the ratio of the peak current in the reverse scan and the peak current in the forward scan. A horizontal flat cell setup was used in testing and the solutions were not deaerated. Potentiodynamic tests were repeated twice to ensure precision.

2.4 | Huey Test

The Huey test is a mass loss test that is used to determine the susceptibility of stainless steel to intergranular corrosion and is described in by ASTM A262 Practice C.[24] LPBF materials were ground to a 1200 grit finish. Cut samples had

dimensions of 20 mm × 20 mm × 3 mm. In the case of LPBF materials, the surface perpendicular to the build direction made up the 20 mm × 20 mm square base. Materials were tested in boiling 65 wt% HNO_3 solution. Five 48 h tests were run. The mass was measured between each consecutive run and the solution was freshly prepared for each of the five tests. Scanning electron microscopy was implemented after the test to characterize the corrosion morphology.

RESULTS

Figure 1 shows scanning electron micrographs from galvanostatic etching with 10 wt% ammonium persulfate in conventionally wrought stainless steels. In the case of as-is wrought material, crystallographic stepping is seen. In contrast, sensitized wrought material shows ditching along grain boundaries.

Figure 2 shows scanning electron micrographs from the galvanostatic etching of LPBF materials 1, 2, and 3 (as indicated in the experimental). Figures 2(a) through (c) are images taken at magnification 500×. From these micrographs, localized ditching can be seen at the melt pool boundaries. Crystallographic stepping is also seen for the different grains within the melt pools. Figures 2(d) through (f) are micrographs that were acquired at 5,000×. At this level of magnification, cellular structures can be seen. Selective attack of the interior of these cellular structures are observed.

Figure 3 shows scanning electron micrographs of sensitized LPBF materials 1, 2, and 3, taken at a magnification of 500×
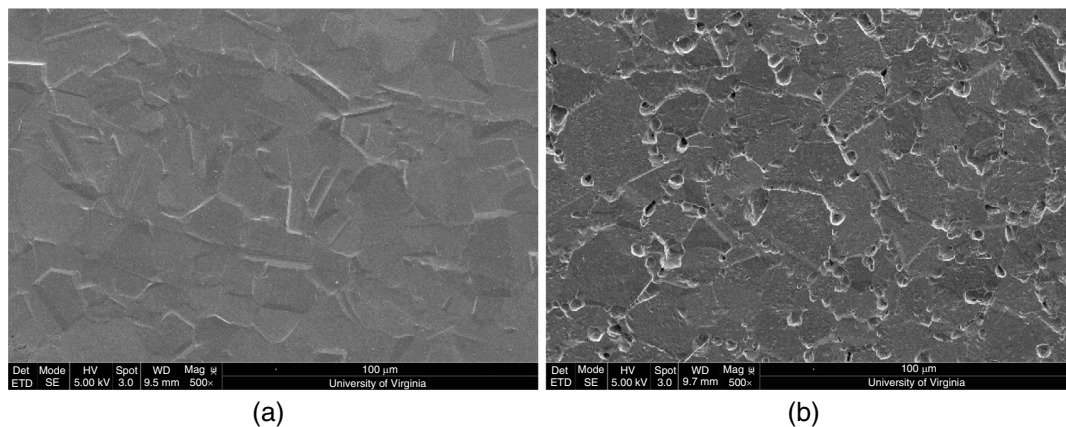
FIGURE 1. *Scanning electron micrographs of (a) as-is and (b) sensitized wrought 316L material. Micrographs were taken after galvanostatic etching of material in 10 wt% ammonium persulfate.*
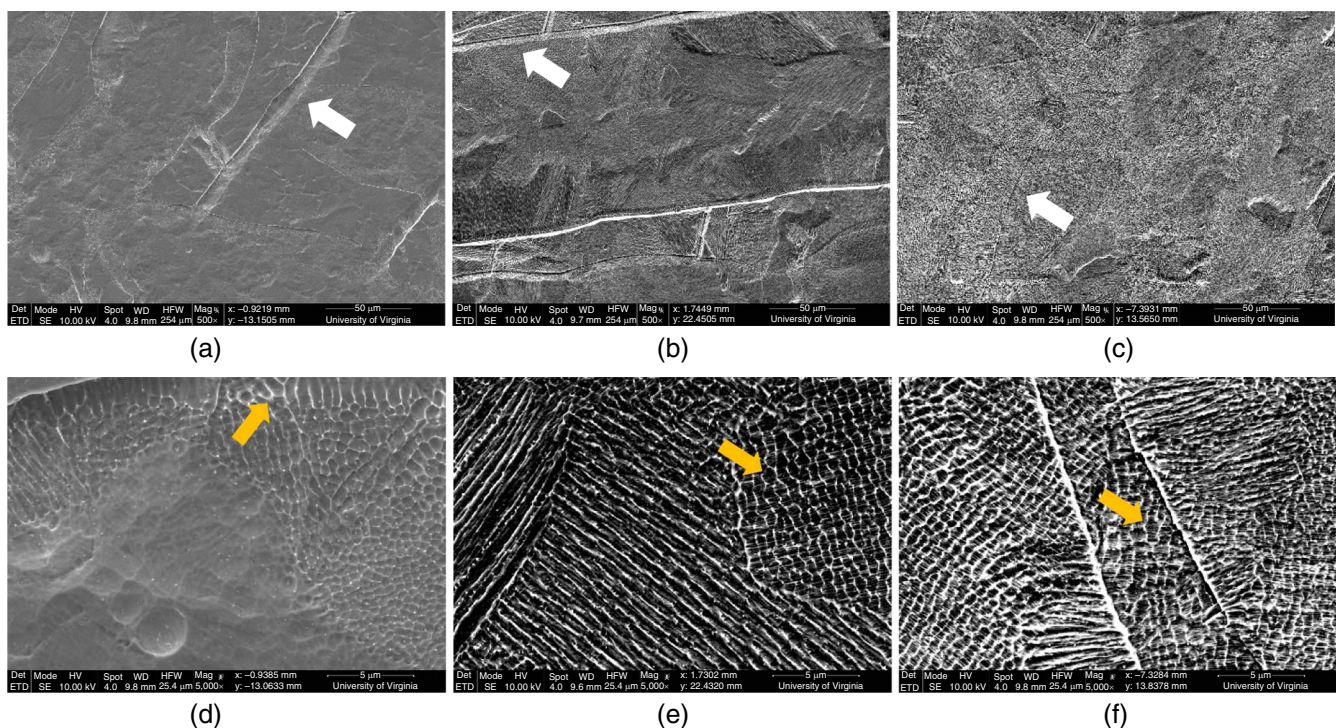
FIGURE 2. *Scanning electron micrographs of as-built (a) LPBF material 1, (b) material 2, and (c) material 3 at a magnification of 500×. These micrographs were taken after galvanostatic etching of each material in the as-built state. Scanning electron micrographs of (d) LPBF material 1, (e) material 2, and (f) material 3 at a magnification of 5,000×. White arrows show areas of localized melt pool boundary attack. Orange arrows point to areas of cellular attack.*
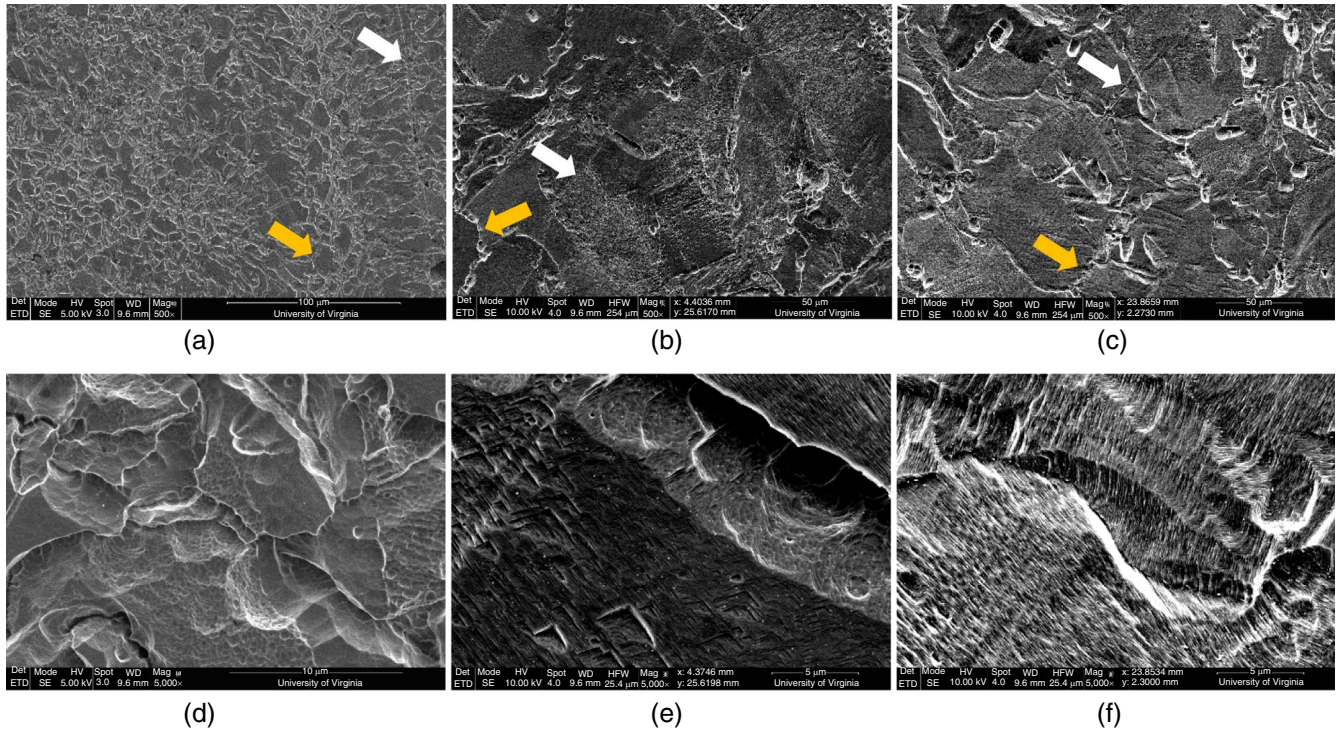
FIGURE 3. *Scanning electron micrographs of sensitized (a) LPBF material 1, (b) material 2, and (c) material 3 at a magnification of 500×. These micrographs were taken after galvanostatic etching of each material in the sensitized state. Scanning electron micrographs of (d) LPBF material 1, (e) material 2, and (f) material 3 at a magnification of 5,000×. White arrows show areas of localized melt pool boundary attack. Orange arrows point to areas of intergranular attack.*

and LPBF materials 1, 2, and 3 at 5,000×. Areas of localized melt pool boundary attack and intergranular attack can be seen.

Figure 4 shows mass loss profiles for as-is wrought materials and LPBF materials 1 and 2 under the Huey test. While the mass loss for that of material 1 is greater than that of material 2, there is no great difference between the two profiles for the LBPF materials.

Figure 5 shows the post-test micrographs from the Huey testing of as-is wrought and LPBF 316L. In every case, it seen

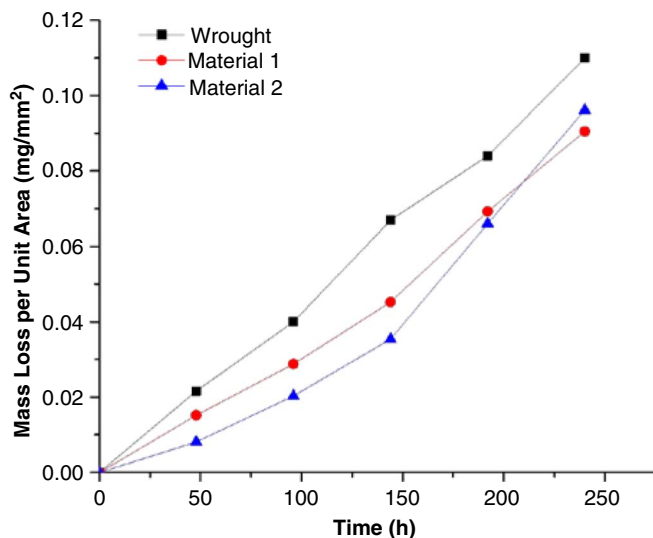that there is attack along the grain boundaries. In every case, little to no grain dislodgement is observed.

Figure 6 shows the mass loss profile for wrought and LPBF materials 1 and 2 that have been sensitized under the Huey test. While the mass loss for sensitized material 1 is greater than that of the wrought material, it is seen that the mass loss profile for sensitized material 2 is less than that of the wrought material.

Figure 7 shows the post-test micrographs for sensitized wrought and LPBF materials. In the case of the sensitized wrought material, it is seen that there is clearly greater grain fallout than in that of the as-received wrought material (shown in Figure 5). In the case of the sensitized LPBF materials, grain fallout is also seen. A greater amount of grain dislodgement is seen in the post-test micrograph for material 1 compared to material 2.

Figure 8 shows polarization curves described by the DL-EPR procedure for both as-is (a) and sensitized wrought 316L (b). In the curve for the as-is material, it is seen that there is no reactivation in the reverse scan corresponding to a DOS value of zero. In the sensitized wrought material, reactivation is observed in the reverse scan, which would lead to the calculation of a DOS value that is greater than zero.

Figure 9 shows the scanning electron micrographs of the surfaces of (a) as-received and (b) sensitized wrought 316L after the DL-EPR test. In the case of the sensitized wrought material, localized ditching (analogous to that seen in the results of galvanostatic etching) is observed.

Figure 10 depicts the polarization curves of as-built LPBF 316L (a) material 1, (b) material 2, and (c) material 3 in 1 M H_2SO_4 and 0.01 M KSCN as described by the DL-EPR procedure. It is to be noted that the polarization scan for material 1

FIGURE 4. *Huey test mass loss profile for as-is wrought material and as-built LPBF materials 1 and 2.*
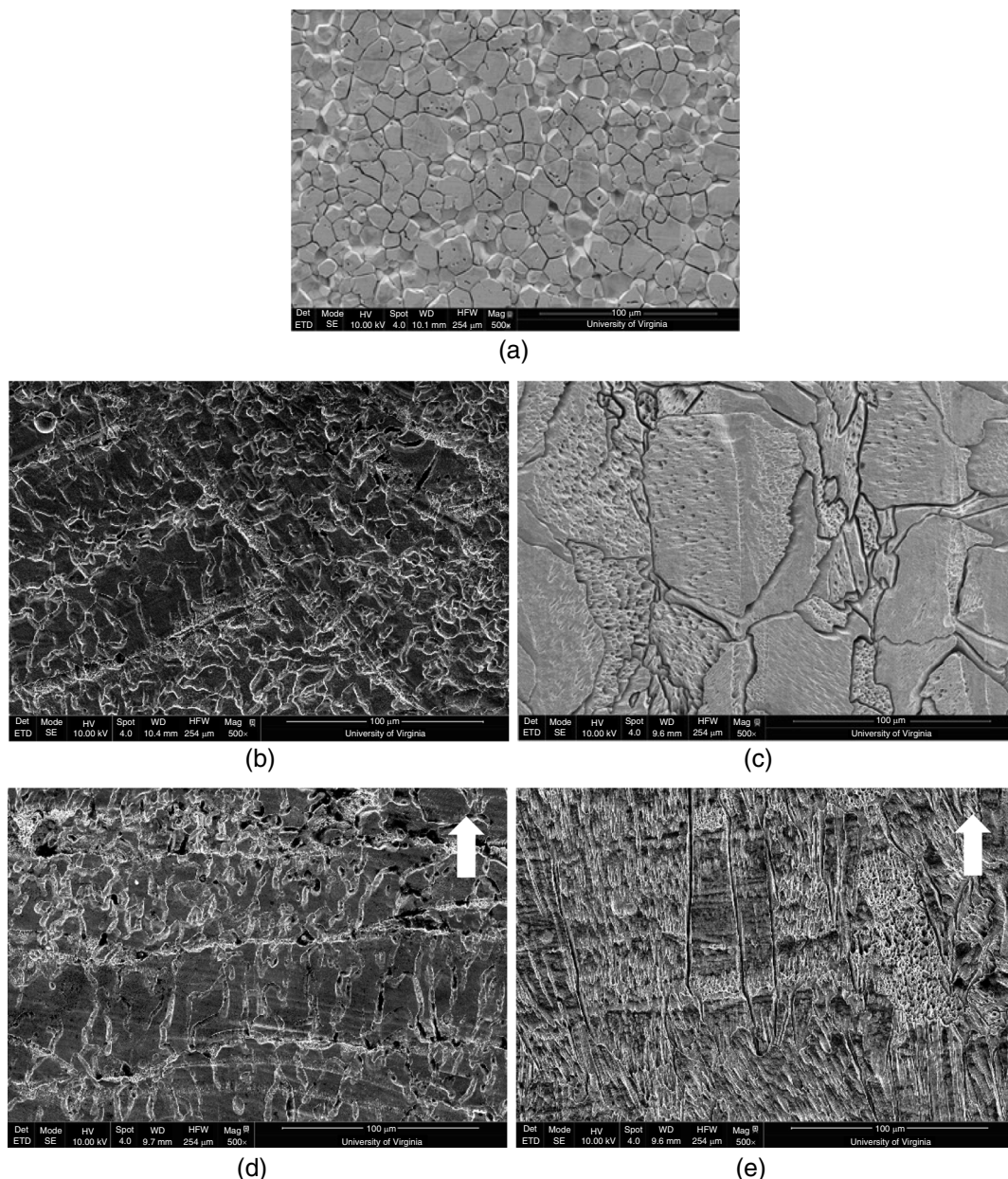
FIGURE 5. *(a) Post-test scanning electron micrographs of as-built wrought material. The images of (b) LPBF material 1 and (c) material 2 are of the surfaces oriented perpendicular to the build direction. The images of (d) LPBF material 1 and (e) material 2 are oriented parallel to the build direction. These micrographs correspond to samples that have been tested through the Huey test. White arrows were added to indicate the build direction.*

displays a reactivation current in the reverse scan with a DOS value of 3.30×10^{-4}. The polarization scans for materials 2 and 3 do not displays this behavior. Table 3 shows the characteristic reverse current densities, forward peak current densities, and the ratio of the reverse current to the forward current.

Figure 11 shows post-test micrographs after the DL-EPR scans for the as-built LPBF materials. Figures 11(a) through (c) show micrographs taken at 500× for LPBF materials and it is seen that melt pool boundaries are highlighted from the electrochemical test. Images taken at higher magnification (Figures 11[d] through [f]) show that for all as-built LPBF materials, there is preferential attack along the interiors of the cellular structures and the melt pool boundaries.

Figure 12 depicts the polarization curves of sensitized LPBF 316L (a) material 1, (b) material 2, and (c) material 3 in 1 M H_2SO_4 and 0.01 M KSCN as described by the DL-EPR procedure. In each case, a reactivation current is observed in the reverse scan. Table 4 shows the characteristic reverse current densities, forward peak current densities, and the ratio of the reverse current to the forward current.

Figure 13 shows post-test micrographs accompanying the DL-EPR scans for the sensitized LPBF materials. Figures 13(a) through (c) show micrographs taken at 500× for LPBF materials and the grain structure can be seen. Images taken at higher magnification (Figures 13[d] through [f]) show that in addition to intergranular ditching, pore-like attack is seen in the interior of these grains.
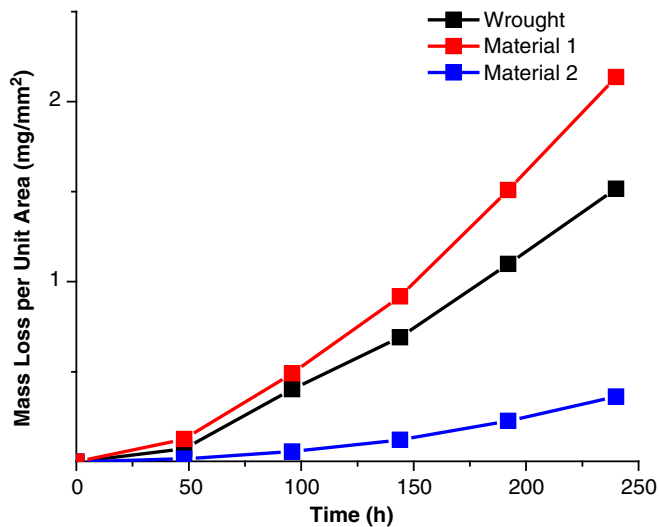
FIGURE 6. *Huey test mass loss profile of sensitized wrought material and LPBF material 1 and 2.*

DISCUSSION

In the spirit of ASTM A262, this discussion is organized by first discussing galvanostatic etching in ammonium persulfate due to its historical use as a screening tool, followed by results from the nitric acid mass loss test. Although not currently an ASTM standard, the results from the DL-EPR are then discussed. A discussion of the use of these tests in determining the susceptibility of conventionally wrought stainless steels to intergranular corrosion, as well as an assessment of the applicability and shortcomings of these tests are discussed for LPBF 316L in the as-built and sensitized state. Emphasis is given toward the anticipated effect of LPBF microstructure on the observations recorded.

4.1 | Ammonium Persulfate Etching

ASTM A262 practice A is a qualitative way of determining the susceptibility to intergranular corrosion of stainless steels such as 304L (UNS S30403) and 316L. The galvanostatic etching process takes advantage of selectivity to identify this susceptibility. In the case of conventionally wrought stainless steels that do not have any sensitization issues, a classic crystallographic stepping behavior is seen. This appearance results from the different rates of uniform dissolution of different crystallographic facets. In the case of steels that have been sensitized (e.g., Figure 1[b]), ditching is observed along the grain boundaries. This localized attack is due to presence of a chromium-depleted region that developed from the formation of chromium carbides ($Cr_{23}C_6$) along grain boundaries.[24,26] A dual structure is also reported in which stepping and ditching are simultaneously observed. It is to be mentioned that as a prescreening tool, if a ditch or dual structure are observed by this qualitative method, it is suggested that other methods that measure susceptibility to intergranular corrosion such as the Huey test or the Streicher test be implemented.[29]

In the case of as built LPBF 316L, mild crystallographic stepping is seen within the melt pools. It is also observed that there is no ditching along the grain boundaries in any of the as-built materials. This observation would suggest that there is little to no chromium carbide precipitation that would lead to selective corrosion from the formation of a chromium-depleted area adjacent to a grain boundary. Nevertheless, different

microstructural features experience selective corrosion that is not observed in the wrought counterpart.

As confirmed by white light profilometry from previous work, preferential ditching around melt pool boundaries is observed.[10] It is interesting to note the difference in the attack morphology between the three different LPBF materials. In the case of materials 1 and 2, localized ditching is seen between two adjacent melt pools, analogous to the ditching seen in stainless steels prone to intergranular corrosion due to sensitization. In the case of material 3, there is more uniformity in attack, although there is a step morphology between two adjacent melt pools. The greater level of uniformity may be attributed to the solidification conditions. The higher volumetric energy density in material 3 may lead to a microstructure that is more uniform, leading to the observed etching behavior. Other work has discussed the presence of residual stresses and porosity at the melt-pool boundaries.[16,33] The mechanism behind this selective attack is still unclear and this drives the use of methods such as transmission electron microscopy to determine if there is a degree of chemical heterogeneity that dictates this behavior. Preferential attack along the interior of the honeycomb-like cellular structures are observed across the three printed materials at a smaller length scale. Cellular structures, which have been shown to grow preferentially in the <100> direction, grow normal to the build direction and an elongated straw-like structure is observed.[3,8,34-35] These cellular structures develop due to the development of protrusions in the solid/liquid interface during rapid solidification and are favored by conditions of low-temperature gradients and fast solidification velocities.[36] Solute rejection takes place and leads to the formation of cellular walls enriched in chromium and molybdenum and is most likely the reason as to why preferential attack is observed along the interior of the cellular structures.[34,37]

In the case of sensitized LPBF material, the galvanostatic etching provides information that matches its traditional use in informing an alloy's susceptibility to intergranular corrosion. In the case of material 1 (Figure 3[a]), it is seen that grain fallout has occurred. This loss of material may be due to the small size of the grains that allowed for greater dislodgement of grains.[38] Although fallout is not something conventionally reported during etching of sensitized materials, it is a phenomenon that has been observed in the sensitization of stainless steels with grain sizes in the submicrometer range. The smaller volumetric energy density and faster scan velocity that were involved in the synthesis of material 1 led to conditions that allowed for the generation of smaller grains than those of materials 2 and 3.[1,14,39-40] In contrast, sensitization of materials 2 and 3 had etching morphologies that exhibited traditional grain boundary ditching one would associate with chromium carbide precipitation in wrought material. In addition to grain boundary ditching, attack along the melt pool boundaries is still seen. Work has shown that a temperature of 675°C is within a range of temperatures that would not necessarily rid the material of these melt pool boundaries.[5,34]

Despite the simplicity in the use of this method in assessing the susceptibility of wrought stainless steel to intergranular corrosion, these results show that the conditions of rapid solidification from the LPBF process introduce additional microstructural features that are highlighted through preferential etching. In addition to grain boundaries, one needs to consider attack along melt pool boundaries and cellular structures from the solidification process and the classification of a material becomes more complex than the discrete
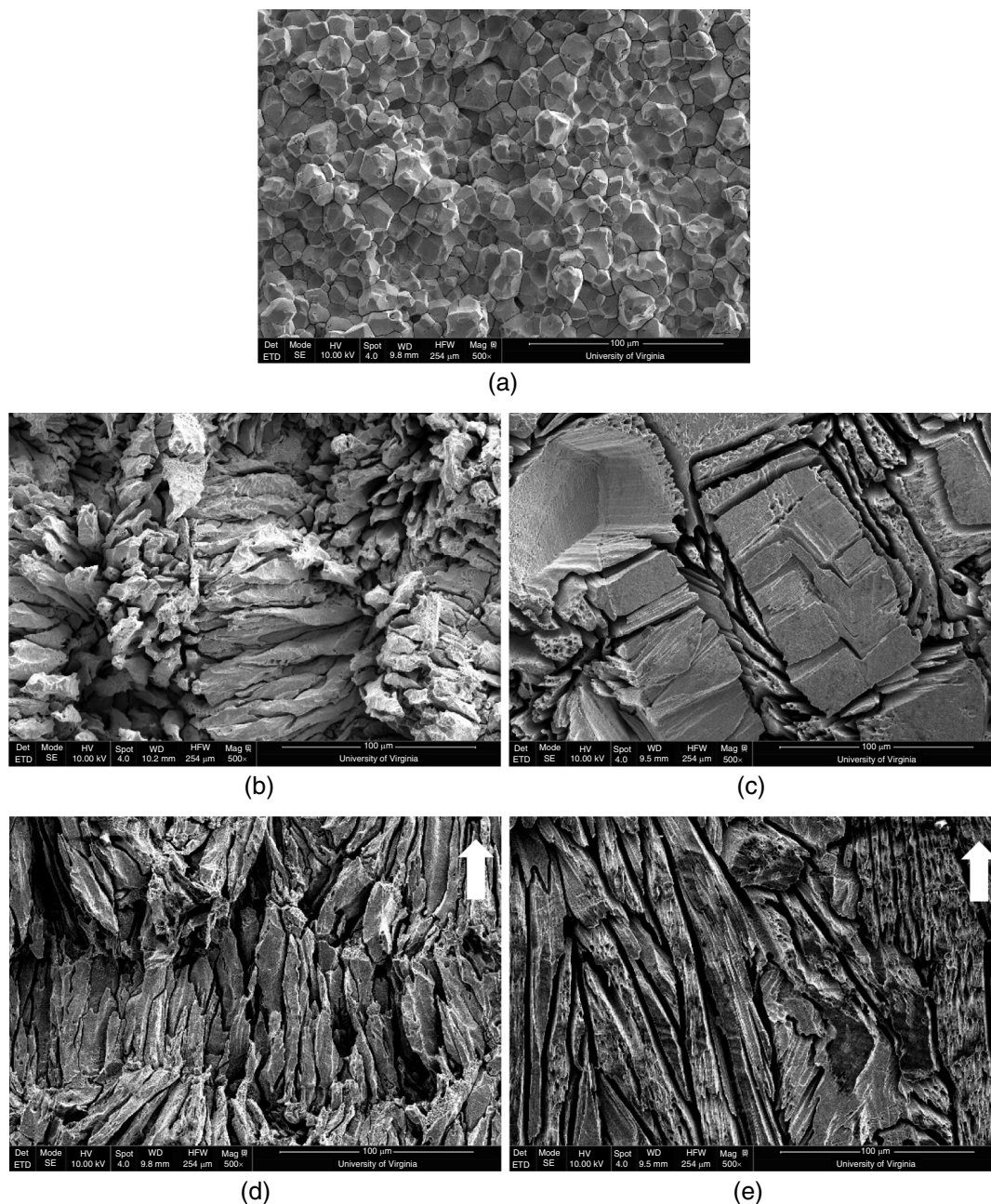
FIGURE 7. *(a) Post-test scanning electron micrographs of sensitized wrought material. The images of (b) LPBF material 1 and (c) material 2 are of the surfaces oriented perpendicular to the build direction. The images of (d) LPBF material 1 and (e) material 2 are oriented parallel to the build direction. These micrographs correspond to samples that have been tested through the Huey test. White arrows were added to indicate build direction.*

archetypes "step," "dual," or "ditched." In the spirit of using ASTM A262 practice A as a tool for lot acceptance, categorizations of etching behavior must be generated in the case of as-printed LPBF materials that appropriately incorporate these different microstructural features and their correlation to susceptibility to intergranular corrosion in service.

4.2 | Huey Test

Figure 4 shows the difference in mass loss profile between wrought stainless steel and sensitized stainless steel. In the case of solution-annealed stainless steel, there is a linear mass profile. The corrosion rate is constant and it is assumed that grain-

face corrosion is the dominant mechanism form mass loss.[29,38] Although intergranular corrosion is seen, the attack does not occur such that there would be grain dislodgement. In the case of sensitized wrought stainless steels, preferential corrosion takes place along the grain boundaries to the degree that grain dislodgement can occur and a sharp increase in mass loss is seen. This explains the parabolic behavior in the mass loss profile. A mechanism has been proposed that suggests the acceleration of grain fallout is due to the accumulation of oxidizing cations such as hexavalent chromium in the grooves from intergranular attack.[38] This type of mass loss profile may also be observed in annealed wrought stainless steel with small grains.[38]
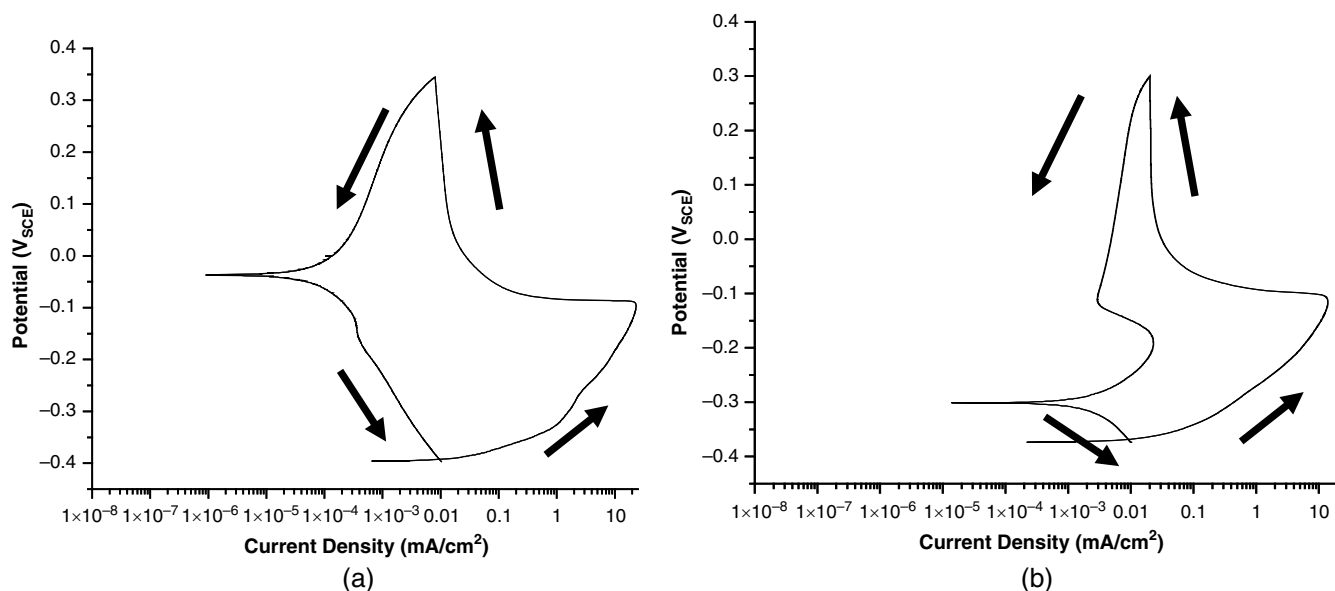
FIGURE 8. *Polarization curves of as-is and sensitized wrought 316L in 1 M H₂SO4 and 0.01 M KSCN as provided by the DL-EPR technique. Arrows were added to indicate the direction of the scan.*
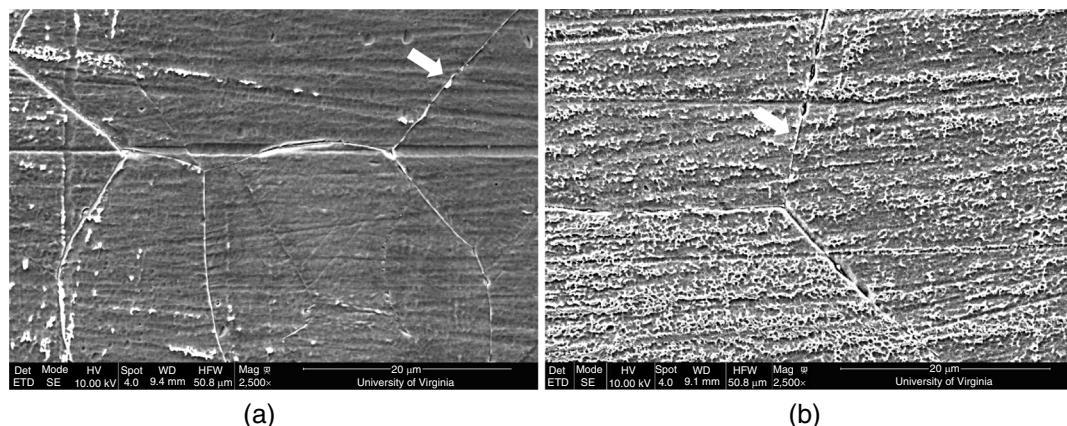
FIGURE 9. *Scanning electron micrographs of (a) as-is and (b) sensitized wrought 316L following electrochemical testing by the DL-EPR method. White arrows were drawn to highlight a grain boundary.*
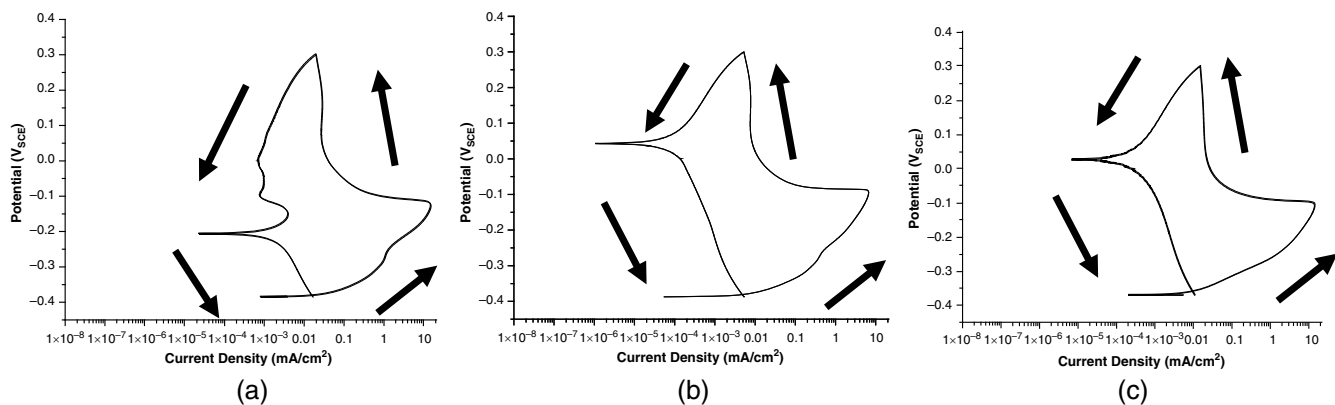
FIGURE 10. *Polarization scans of as-built LPBF 316L (a) material 1, (b) material 2, and (c) material 3 in 1 M H₂SO₄ and 0.01 M KSCN as provided by the DL-EPR technique. Arrows were added to indicate the direction of the scan.*

Consistent with micrographs from the ammonium persulfate etching, Figure 5 shows attack along the grain boundaries in both as-built LPBF materials. This attack, however, was insufficient to cause grain fallout. With observations of melt-pool boundary attack in both materials, it is interesting to observe a linear mass loss profile for both LPBF materials in the as-built state. In the same way that localized attack along grain boundaries does not lead to fallout in annealed austenitic

Table 3. *DL-EPR Values of As-Is Wrought and LPBF Materials in the As-Built State*

	Wrought	LPBF Material 1	LPBF Material 2	LPBF Material 3
Reverse Peak Current (mA/cm²)	0	4.52×10^{-3}	0	0
Forward Peak Current (mA/cm²)	2.00×10^1	1.53×10^1	1.4×10^1	2.01×10^1
Ratio	0	3.3×10^{-4}	0	0

stainless steels, the reasons for this observation may be because the localized attack along melt pools is not sufficient in creating conditions such as a groove accumulated with oxidizing ions in the 48 h time frame of each consecutive test. Despite material 1 having small equiaxed grains, it is interesting to note how the mass loss profile still demonstrated a constant mass loss. Grain face corrosion dominates in the as-built LPBF materials and demonstrates constant rate mass loss profiles in the Huey test as one would observe in the testing of annealed 316L.

In the case of the sensitized materials, the mass loss profiles of LPBF materials demonstrate parabolic behavior that is signature of accelerated attack due to rapid intergranular corrosion. This is consistent with observations of grain fallout in the post test micrographs provided by Figure 7. Both LPBF materials demonstrate grain fallout as a result of intergranular

corrosion. LPBF material 1 shows greater mass loss than LPBF material 2 and this may be due to the presence of smaller grains in material 1. Less intergranular attack is required for grain dislodgement to occur with materials with smaller grains and the smaller grains in material 1 may be the reason for this observed trend. These results are also consistent with the fact that materials undergoing more rapid solidification conditions such as being printed with a higher speed and lower volumetric energy density have smaller grains.[1,6]

Another trend to acknowledge from the post-test micrographs are the grains that do not undergo grain fallout after the Huey test. Figure 7 shows post-test micrographs taken in the orientation perpendicular to the build direction and it is seen that grains that are parallel to the build direction are retained for both LPBF materials. It is to be noted that in the case of LPBF materials, grains tend to be elongated along to the build direction. In the case of grains that penetrate deeper into the surface, more intergranular attack must take place for the dislodgement of these grains to occur. Despite the retainment of these elongated grains, the fallout of smaller and equiaxed grains still lead to mass loss rates that increase with time.

The Huey test was originally developed as a tool to quantitatively measure the susceptibility of wrought stainless steel to intergranular corrosion.[24,29,38] The mass loss data from LPBF materials showed a linear mass loss rate which would indicate the dominance of grain-face corrosion. A shortcoming of this is that mathematically, this does not capture tendencies of localized corrosion along melt pool boundaries and cellular interiors. In the context of sensitized LPBF stainless steels, the mass loss results demonstrate susceptibility to intergranular corrosion. However, it must be remembered that conventionally wrought stainless steels typically have an equiaxed grain
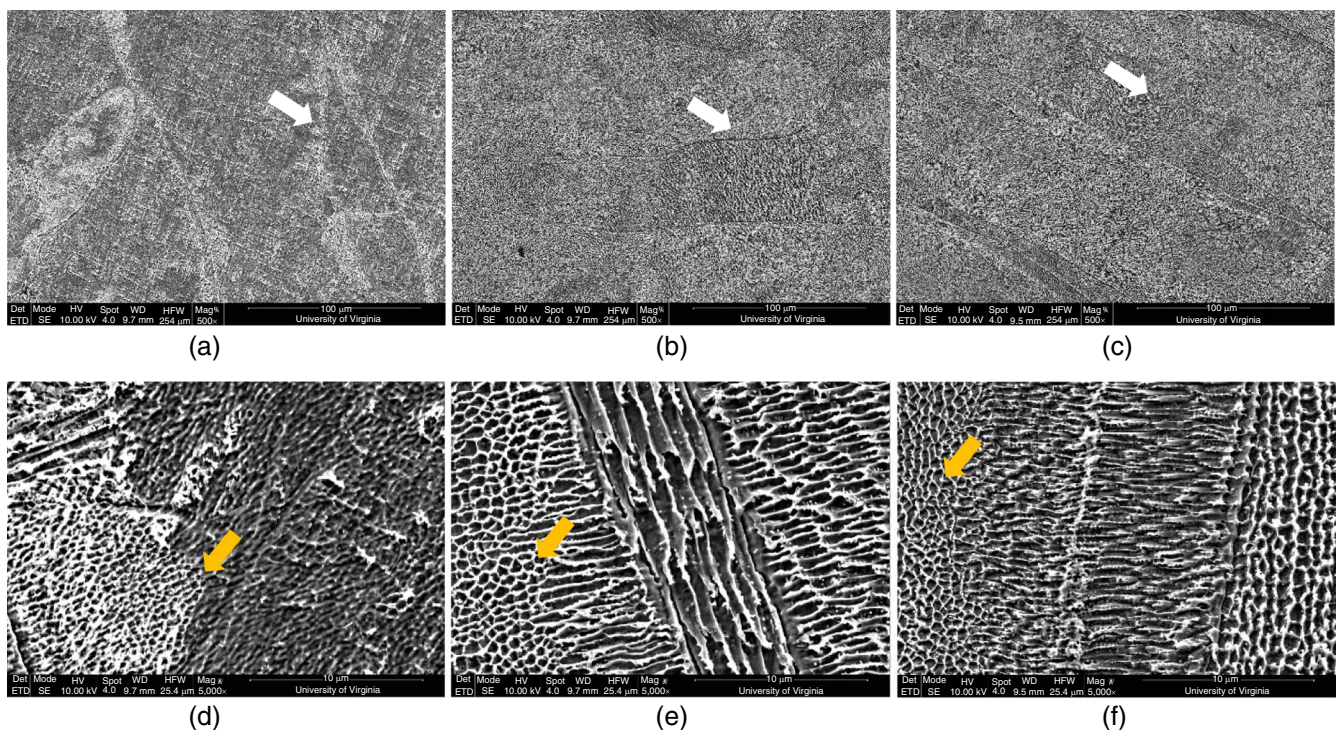
FIGURE 11. *Scanning electron micrographs of as-built LPBF 316L materials (a) 1, (b) 2, and (c) 3 following electrochemical testing by the DL-EPR method at a magnification of 500×. Scanning electron micrographs of LPBF 316L materials (d) 1, (e) 2, and (f) 3 following electrochemical testing by the DL-EPR method at a magnification of 5,000×. White arrows show areas of localized melt pool boundary attack. Orange arrows point to areas of cellular attack.*
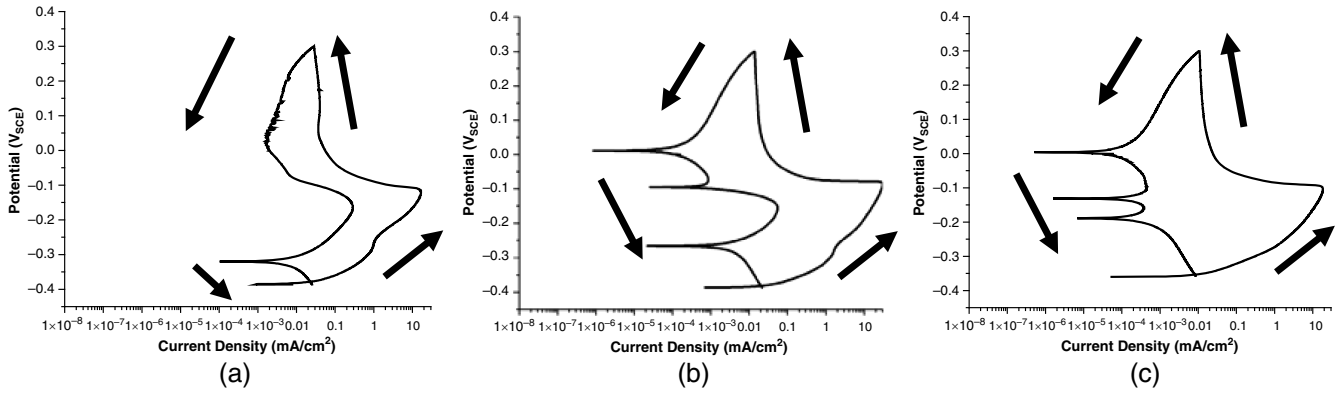
FIGURE 12. *Polarization scans of sensitized LPBF 316L (a) material 1, (b) material 2, and (c) material 3 in 1 M H$_2$SO$_4$ and 0.01 M KSCN as provided by the DL-EPR technique. Arrows were added to indicate the direction of the scan.*

Table 4. *DL-EPR Values of Wrought and LPBF Materials in the Sensitized State*

	Wrought	LPBF Material 1	LPBF Material 2	LPBF Material 3
Reverse Peak Current (mA/cm^2)	6.41×10^{-2}	2.86×10^{-1}	5.52×10^{-2}	1.32×10^{-3}
Forward Peak Current (mA/cm^2)	2.00×10^{1}	1.67×10^{1}	3.00×10^{1}	1.84×10^{1}
Ratio	3.20×10^{-3}	1.72×10^{-2}	1.84×10^{-3}	7.20×10^{-5}
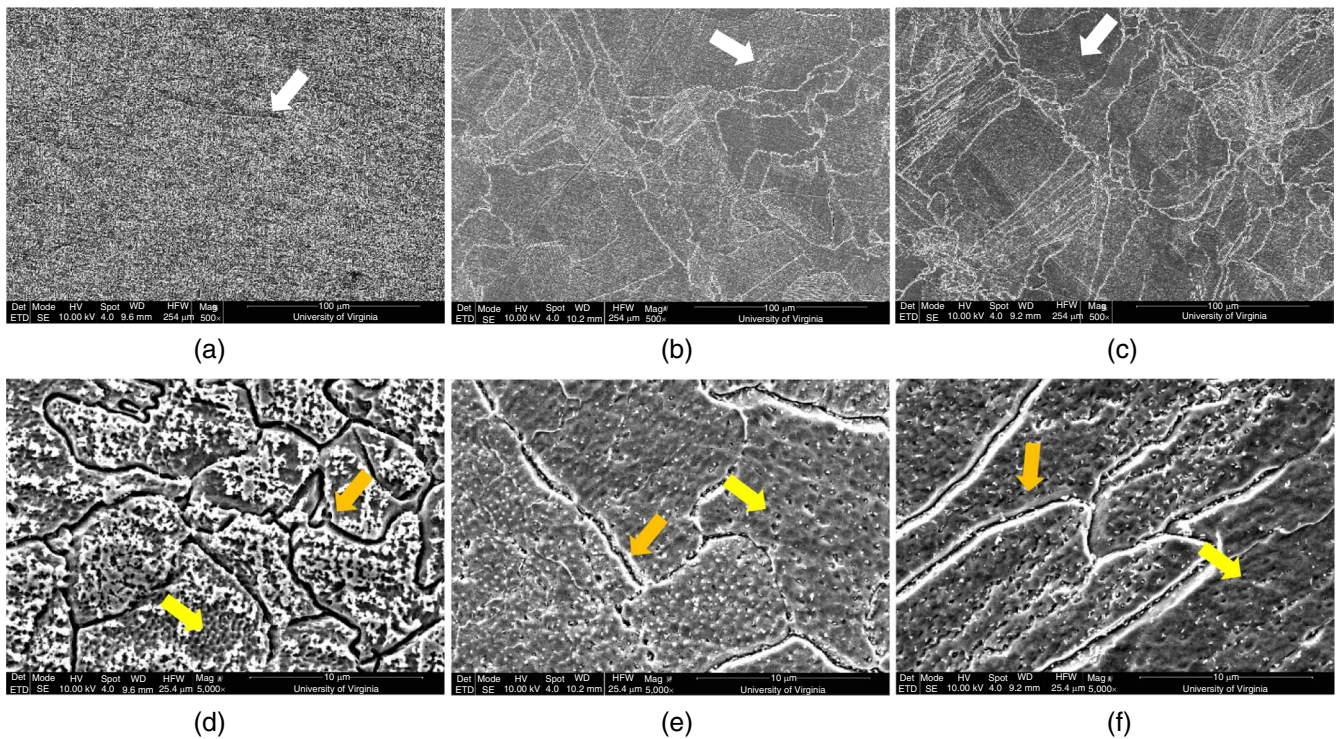
FIGURE 13. *Scanning electron micrographs of sensitized LPBF 316L materials (a) 1, (b) 2, and (c) 3 following electrochemical testing by the DL-EPR method at a magnification of 500×. Scanning electron micrographs of LPBF 316L materials (d) 1, (e) 2, and (f) 3 following electrochemical testing by the DL-EPR method at a magnification of 5,000×. White arrows show areas of localized melt pool boundary attack. Yellow arrows point to areas of cellular attack. Orange arrows point to areas of intergranular attack.*

structure. A mass loss profile without any post-test microscopy does not capture the resistance of elongated grains to grain fallout. In the case of LPBF alloys, these experiments show the value of accompanying mass loss tests via the Huey test with post-test microscopy.

4.3 | Double-Loop Electrochemical Potentiokinectic Reactivation

Unlike the Huey test which is run under essentially open-circuit conditions, the DL-EPR test is a potentiodynamic test. In the case of the conventionally wrought austenitic stainless

steels, it is assumed that uniform active corrosion occurs in the upward scan until a passive range is reached and there is a decrease in the anodic current due to the formation of a protective film.[31-32,41] The susceptibility to intergranular corrosion is measured by the activity that takes place in the reverse scan from 300 mV$_{SCE}$ to the original open-circuit potential. In wrought stainless steel without sensitization (as seen in Figure 8[a]), active behavior is not detected in the reverse scan due to an anodic current that is less than the cathodic current. In the case of sensitized material, an increase in current is detected in the range of −150 mV$_{SCE}$ to −200 mV$_{SCE}$ due to depassivation of areas adjacent to grain boundaries depleted of chromium. The peak anodic current in the reverse scan from reactivation leads to a DOS calculation that is greater than zero. It is also appropriate for one to classify a material with a nonzero DOS value as one that is susceptible to intergranular corrosion. This classification is further justified from Figure 9(b) in which grain boundary attack is seen in the post-test micrographs of the wrought materials that have been sensitized.

In the case of the tested LPBF materials, it is to be noted that one of these materials (material 1) demonstrates reactivation in the reverse scan, while two materials (materials 2 and 3) do not demonstrate reactivation from the DL-EPR polarization scans (Figure 8). By the conventional application of the DL-EPR scan, one would think that material 1 is susceptible to intergranular corrosion, while materials 2 and 3 are not prone to any kind of intergranular or selective corrosion. These assumptions are then inconsistent with the post-test microscopy. Despite the scans for materials 2 and 3 not demonstrating reactivation in the reverse scan, post-test microscopy shows that preferential attack still occurs within the interior of the cellular structures and the melt pool boundaries. It should also be pointed out that there is no intergranular attack seen in the post-test micrographs. These discrepancies may be reconciled by the fact that the net anodic current that is representative of reactivation of cellular interiors and melt pool boundaries is less than the total cathodic current. As the net current (the difference between the cathodic and anodic current) is recorded in these tests, the reverse scan does not represent the observed preferential attack.

Nevertheless, it is interesting to note how the scan provided by material 1 demonstrates reactivation in the reverse scan. Like the post-test micrographs shown by materials 2 and 3, attack can be seen in the in the interior of the cells and the melt pool boundaries. This morphology may be mechanistically explained by the character of the cellular structures in material 1. Studies have found that in parts that have been printed at higher speeds and low volumetric energy densities, there is greater depletion of critical elements such as molybdenum and chromium in the core of these cellular structures due to faster solidification velocities.[34] Material 1 was printed under parameters of higher velocity and a lower heat input compared to materials 2 and 3. Material 1 is also expected to have lower levels of prior layer remelting due to the parameters chosen.[42] These solidification conditions favor a less compositionally homogenous material and result in a DL-EPR scan that displays reactivation. It is also to be noted that after performing these potentiodynamic scans without the reverse component, the same type of cellular attack is still observed.

The polarization scans shown by Figure 12 show that in the case of LPBF alloys that are sensitized, the DL-EPR scan is an appropriate tool to use in measuring susceptibility to intergranular corrosion. For the scans that were performed on all three LPBF materials, reactivation was observed in the return

scan as one would observe in wrought material that has been sensitized. The results from the polarization scan are further validated by the post-test micrographs from Figure 13 due to the observation of intergranular attack. It is also important to take note of the localized pore-like attack happening in the grain faces due to the presence of the cellular structures. This observation is relevant because it shows how the reactivation observed in the reverse scan cannot be singularly attributed to grain boundary depassivation. As the heat treatment at 675°C did not homogenize the cellular structures, these contribute partially to the observed electrochemical behavior. It is also relevant to note that when comparing the polarization behavior of the as-built material to the sensitized material, the DOS value in the sensitized material is higher than that of the as-built material.

Another point of discussion is the relative orders of magnitude of DOS for the three sensitized LPBF materials due to the fact that three orders of magnitude are spanned. With smaller grains, there are more sites for grain boundary depassivation which may lead to a larger net reactivation current. Material 1 is seen to have smaller and more equiaxed grains than materials 2 and 3 and this may lead to its largest DOS value. In addition to smaller grains, the compositional differences induced by rapid solidification may be maintained and because a nonzero DOS was calculated in the case of LPBF material 1 in the as-received state, the cellular structures may also have a greater contribution to the calculated DOS value in the sensitized state.

Traditionally, the DL-EPR technique has been used to determine relative susceptibility of wrought austenitic stainless steels to intergranular corrosion through the DOS value. In the case of sensitized LPBF stainless steel, these results demonstrate that this test is likely an appropriate way to determine susceptibility to intergranular corrosion. The trends seen with grain size also agree with work that has been performed on wrought steels.[43-44] Nevertheless, the results provided show how the lack of a nonzero DOS value may misrepresent the tendency for selective and localized corrosion to take place through microstructural features from the rapid solidification process. As with most testing, caution must be taken in the interpretation of these polarization curves. Alternative solution compositions or scan strategies must also be considered in order to more accurately capture the tendency of LPBF alloys to experience selective corrosion through melt pool boundaries and the interiors of cellular dendritic structures.

CONCLUSIONS

➢ Galvanostatic etching by ammonium persulfate revealed attack along melt pool boundaries and the interior of cellular structures. It also revealed intergranular attack in sensitized LPBF 316L.
➢ In the Huey test, a constant mass loss rate is observed in as-built LPBF materials, but attack along melt pool boundaries was still observed.
➢ An increasing mass loss rate is seen in sensitized LPBF materials and greater rates are observed in LBPF material with small grains.
➢ In testing with the DL-EPR, it was found that localized attack is observed along melt pool boundaries and cellular structure.
➢ The DL-EPR technique showed signs of susceptibility to intergranular corrosion in the case of sensitized LPBF materials and was validated by observations of intergranular attack in post-test microscopy.
➢ While the tests demonstrate behaviors of intergranular corrosion in sensitized LPBF material, caution must be taken in the

interpretation of results from the Huey test and the DL-EPR test as the numerical behavior of the results may not be signature of the tendency for selective corrosion through melt pool boundaries and cellular structures that can take place in LPBF alloys.

References

1. A. Ahmadi, R. Mirzaeifar, N. Shayesteh Moghaddam, A. Sadi Turabi, H.E. Karaca, M. Elahinia, *Mater. Des.* 112 (2016): p. 328-338.
2. F. Bartolomeu, M. Buciumeanu, E. Pinto, N. Alves, O. Carvalho, F.S. Silva, G. Miranda, *Addit. Manuf.* 16 (2017): p. 81-89.
3. Y. Zhong, L.-E. Rännar, L. Liu, A. Koptyug, S. Wikman, J. Olsen, D. Cui, Z. Shen, *J. Nucl. Mater.* 486 (2017): p. 234-245.
4. K. Kunze, T. Etter, J. Grässlin, V. Shklover, *Mater. Sci. Eng. A* 620 (2014): p. 213-222.
5. M.L. Montero Sistiaga, S. Nardone, C. Hautfenne, J. Van Humbeeck, "Effect of Heat Treatment Of 316L Stainless Steel Produced by Selective Laser Melting (SLM)," 27th Annual International Solid Freeform Fabrication Symposium – An Additive Manufacturing Conference (Austin, TX: SSF Symposium, 2016), p. 558-565.
6. E. Yasa, J.P. Kruth, *Proc. Eng.* 19 (2011): p. 389-395.
7. J.R. Trelewicz, G.P. Halada, O.K. Donaldson, G. Manogharan, *JOM* 68 (2016): p. 850-859.
8. U.S. Bertoli, B.E. Macdonald, J.M. Schoenung, *Mater. Sci. Eng. A* 739 (2019): p. 109-117.
9. H. Inoue, T. Koseki, *Acta Mater.* 124 (2017): p. 430-436.
10. D.A. Macatangay, S. Thomas, N. Birbilis, R.G. Kelly, *Corrosion* 74 (2018): p. 153-157.
11. T.M. Mower, M.J. Long, *Mater. Sci. Eng. A* 651 (2016): p. 198-213.
12. H. Li, Z. Jiang, Y. Yang, Y. Cao, Z. Zhang, *Int. J. Miner. Metall. Mater.* 16 (2009): p. 517-524.
13. X.Z. Xin, N. Xiang, J. Chen, D. Xu, B. Wei, *J. Mater. Sci.* 47 (2012): p. 4813-4820.
14. X. Liu, C. Zhao, X. Zhou, Z. Shen, W. Liu, *Mater. Des.* 168 (2019): p. 107677.
15. G. Sander, S. Thomas, V. Cruz, M. Jurg, N. Birbilis, X. Gao, M. Brameld, C.R. Hutchinson, *J. Electrochem. Soc.* 164 (2017): p. C250-C257.
16. T. Simson, A. Emmel, A. Dwars, J. Böhm, *Addit. Manuf.* 17 (2017): p. 183-189.
17. G.N. Nigon, O.B. Isgor, S. Pasebani, *J. Electrochem. Soc.* 167 (2020): p. 141508.
18. D. Kong, C. Dong, X. Ni, X. Li, *npj Mater. Degrad.* 3 (2019): article 24.
19. M. Laleh, A.E. Hughes, W. Xu, N. Haghdadi, K. Wang, P. Cizek, I. Gibson, M.Y. Tan, *Corros. Sci.* 161 (2019): article 108189.
20. W.B. James, L.F. Pease, "Salt Spray and Immersion Corrosion Testing of PM Stainless Steel Materials," 2017.
21. ASTM G31-72, "Standard Practice for Laboratory Immersion Corrosion Testing of Metals" (West Conshohocken, PA: ASTM International, 2004).
22. N. Parvathavarthini, R.K. Dayal, H.S. Khatak, V. Shankar, V. Shan-mugam, *J. Nucl. Mater.* 355 (2006): p. 68-82.
23. ASTM B117-18, "Standard Practice for Operating Salt Spray (FOG) Apparatus" (West Conshohocken, PA: ASTM International, 2003).
24. ASTM A262, "Standard Practices for Detecting Susceptibility to Intergranular Attack in Austenitic Stainless Steels" (West Conshohocken, PA: ASTM International, 2014).
25. M. Terada, M. Saiki, I. Costa, A.F. Padilha, *J. Nucl. Mater.* 358 (2006): p. 40-46.
26. ASTM B895-16, "Standard Test Methods for Evaluating the Corrosion Resistance of Stainless Steel Powder Metallurgy (PM) Parts/Specimens by Immersion in a Sodium Chloride Solution" (West Conshohocken, PA: ASTM International, 2016).
27. V. Kain, "Stress Corrosion Cracking (SCC) in Stainless Steels," in *Stress Corrosion Cracking*, eds. V.S. Raja, T. Shoji (Cambridge, United Kingdom: Woodhead Publishing, 2011), p. 199-244.
28. N.U. Obeyesekere, "Pitting Corrosion," in *Trends in Oil and Gas Corrosion Research and Technologies*, ed. A.M. El-Sherik (Cambridge, United Kingdom: Woodhead Publishing, 2017), p. 215-248.
29. ASTM G28, "Standard Test Methods of Detecting Susceptibility to Intergranular Corrosion in Wrought, Nickel-Rich, Chromium-Bearing Alloys" (West Conshohocken, PA: ASTM International, 2003).
30. T. Amadou, H. Sidhom, C. Braham, *Metall. Mater. Trans. A* 35 (2004): p. 3499-3513.
31. M. Momeni, M.H. Moayed, A. Davoodi, *Corros. Sci.* 52 (2010): p. 2653-2660.
32. A.P. Majidi, M.A. Streicher, *Corrosion* 40 (1984): p. 393-408.
33. G. Sander, J. Tan, P. Balan, O. Gharbi, D.R. Feenstra, L. Singer, S. Thomas, R.G. Kelly, J.R. Scully, N. Birbilis, *Corrosion* 74 (2018): p. 1318-1350.
34. S. Gao, Z. Hu, M. Duchamp, P.S. Sankara Rama Krishnan, S. Tekumalla, X. Song, M. Seita, *Acta Mater.* 200 (2020): p. 366-377.
35. H. Inoue, T. Koseki, S. Okita, M. Fuji, *Weld. Int.* 11 (1997): p. 876-887.
36. H. Inoue, T. Koseki, "Clarification of Solidification Behaviors in Austenitic Stainless Steels Based on Welding Proces," Nippon Steel Technical Report 95, 2007, p. 62-70.
37. M.A. Jaafar, D.R. Rousse, S. Gibout, J.P. Bédécarrats, *Renew. Sustain. Energy Rev.* 74 (2017): p. 1064-1079.
38. R. Wellard, B. Shehan, D. Craik, W. Adam, *J. Magn. Reson. Ser. B* 104 (1994): p. 276-279.
39. P. Hanzl, M. Zetek, T. Bakša, T. Kroupa, *Proc. Eng.* 100 (2015): p. 1405-1413.
40. E. Liverani, S. Toschi, L. Ceschini, A. Fortunato, *J. Mater. Process. Technol.* 249 (2017): p. 255-263.
41. M.X. Zhang, B. Yang, S.L. Wang, H.C. Wu, Y.Z. Shi, *Mater. Corros.* 67 (2016): p. 271-276.
42. A. Yadollahi, N. Shamsaei, S.M. Thompson, D.W. Seely, *Mater. Sci. Eng. A* 644 (2015): p. 171-183.
43. R. Singh, S. Ghosh Chowdhury, B. Ravi Kumar, S.K. Das, P.K. De, I. Chattoraj, *Scr. Mater.* 57 (2007): p. 185-188.
44. R.V. Taiwade, R. Shukla, H. Vashishtha, A.V. Ingle, R.K. Dayal, *ISIJ Int.* 53 (2013): p. 2206-2212.

Localized Corrosion in Additively Manufactured Stainless Steel and Aluminum Alloys

D.A. MACATANGAY,[1] G.W. KUBACKI,[2] and R.G. KELLY [1,3]

1.—Center for Electrochemical Science and Engineering, Department of Materials Science and Engineering, University of Virginia, Charlottesville, VA 22901, USA. 2.—Department of Metallurgical and Materials Engineering, University of Alabama, Tuscaloosa, Al 35487-0200, USA. 3.—e-mail: rgk6y@virginia.edu

Localized corrosion susceptibility represents a risk to the long-term performance of all materials, additively manufactured (AM) alloys included. Understanding the impact of AM on localized corrosion resistance is at an early stage, but the unique microstructures that result from AM can have a dramatic impact on corrosion susceptibility and morphology. These microstructures also impact the response of AM alloys to standardized testing. AM 316L is shown to respond very differently to ASTM tests for intergranular corrosion susceptibility that were developed for and used to assess wrought austenitic stainless steels. The damage morphology and the impact of heat treatments are shown to vary significantly between cast A360 aluminum alloy and AM Al-10Si-Mg upon exposure to ASTM standard G85, a workhorse of aluminum alloy corrosion testing. AM build parameters can have dramatic effects on the susceptibility, likely through their impact on the lifetime of the liquid phase during manufacture.

INTRODUCTION

The explosion in interest in additive manufacturing (AM) is understandable based on the many advantages this type of production has in terms of allowable geometries.[1–3] Not surprisingly, the focus of most studies of AM metallic materials has been on mechanical properties such as strength and toughness.[3–7] The maintenance or, in some cases, improvement[7–9] in these properties has been encouraging for wider applications of components made in this way. Considerably less attention has been focused on other performance properties such as fatigue and corrosion resistance.[10] The use of stainless steel and aluminum alloys in engineering applications such as aerospace and naval motivate the investigation of AM corrosion. Nonetheless, the changes in the material microstructure that occurs in AM as compared to traditional manufacturing (e.g., casting, wrought material processing) could be expected to impact corrosion resistance. AM can improve corrosion resistance to the extent that deleterious second phase particles are evaporated (e.g., MnS inclusions[10]), but could degrade the corrosion resistance if its rapid solidification either exacerbates elemental heterogeneities or creates other deleterious phases.[11]

The vast majority of the corrosion studies of AM materials has focused on pitting resistance as manifested in potentiodynamic polarization curves in sodium chloride solutions.[12–15] Other corrosion testing aimed at other forms of corrosion such as intergranular corrosion, crevice corrosion, or environmentally assisted cracking are far less frequently reported.[11,16–18] The objective of this paper was to provide some highlights of recent work in the area of microstructurally controlled, interfacial corrosion of AM alloys.

There has been a great deal of interest in the additive manufacturing of AISI 316L (UNS 31603) due to the widespread use of wrought 316L selected for its combination of strength, toughness, and corrosion resistance. The susceptibility of AM 316L to pitting has been somewhat controversial, although on balance, pitting potentials seem to be somewhat higher in chloride solutions than their

wrought counterparts. Little attention has been paid to other forms of localized corrosion that can affect 316L such as intergranular corrosion or crevice corrosion.[10] While rapid solidification leads to the generation of structures such as cellular dendrites that could lead to compositional heterogeneities, it is also interesting to note that the AM process can lead to porosity.[10,17,19] For example, under printing parameters of low volumetric energy, lack of fusion porosity can be found, whereas at high volumetric energy keyhole porosity can form. The topic of grain boundary sensitization is also significant due to the complex thermal histories that can be generated from processing methods such as hot isostatic pressing. The effect of processing on these structural features are key in understanding localized corrosion in AM alloys.

The highest-performance of aluminum alloys are precipitation hardened (e.g., AA2024-T3, AA7075-T6). These materials are notoriously difficult to weld while maintaining their mechanical properties and corrosion resistance. The nature of the AM process thus presents a major challenge to its application to aluminum alloys. In addition to the welding issues, availability, and flowability of aluminum alloy powders have also presented limitations. Thus, Al10SiMg has been the focus of the majority of AM material studies due to the flowability of its powders and the success of the cast counterpart (A360) in many applications.

PROCESS-PARAMETER EFFECTS ON LASER POWDER BED FUSION (LPBF) 316L

As part of a program aimed at a more comprehensive evaluation of the corrosion behavior of AM alloys, we have focused on the impact of processing parameters and resulting microstructure on the corrosion of AM 316L at interfaces, including melt pool boundaries (MPB) and grain boundaries before and after exposure at 675°C where 316L is susceptible to grain boundary sensitization. Our first observations of a possible issue with AM 316L in this regard was the observation of grooves at MPB after standard etching for sensitization compared with the step-like attack in wrought 316L as shown in Fig. 1.

The wrought 316L surface undergoes dissolution at different rates for the different grains due to their different crystallographic orientation[20] which results in the step structure revealed by the profilometry (Fig. 1b). In contrast, the etched surface of the as-printed AM 316L shows more uniform corrosion within the very small grains, but accelerated attack at the MPB (Fig. 1b) with grooves several microns deep observed. Microstructural features such as cellular dendrites are a signature of rapid solidification, and it is interesting to note the effects of these features from a localized corrosion perspective. As these features exist at the micron to submicron range, electron microscopy must be used.

Figure 1c shows a scanning electron micrograph of LPBF 316L that has been etched under galvanostatic conditions as per ASTM A262 Practice A.[20] It is seen that analogous to how ditching occurs along grain boundaries in sensitized wrought 316L, preferential etching takes place in the core of these cellular structures. It should also be noted that multiple authors have reported that the core of these cellular structures can be depleted of elements such as molybdenum and chromium.[21,22] Due to the complex microstructure of LPBF alloys, micrographs from ASTM A262 Practice A cannot be simply labeled as "step" or "ditched" and more complex categorizations must be considered to properly capture the localized corrosion of AM stainless austenitic steel alloys.

The Double-Loop Potentiokinetic Reactivation (DL-EPR) is a potentiodynamic test that is traditionally used to determine the susceptibility of stainless steel to grain boundary sensitization.[23–26] This test begins by immersing a polished surface in a solution of sulfuric acid with potassium thiocyanate added as a depassivator.[25] Upon immersion, the air-formed oxide on the surface dissolves. Anodic polarization results in an active-passive transition. After reaching a prescribed potential in the passive region, the direction of polarization is reversed. Stainless steel that has been sensitized, i.e., chromium carbides ($Cr_{23}C_6$) have precipitated at the grain boundaries, exhibits a reactivation current density in the same potential range as the active-passive transition observed during the positive-going scan, whereas unsensitized material shows no such reactivation. The ratio of the peak current densities in the reverse and forward directions represents the degree of sensitization (DOS), a quantitative measure of the severity of the grain boundary depletion of chromium.

Application of the DL-EPR method to as-printed AM316L has shown reactivation after passivation (Fig. 2b), unlike the as-received, unsensitized wrought 316L as shown in Fig. 2a. Studies of the microstructure of etched, as-printed AM 316L showed no $Cr_{23}C_6$ precipitates at the grain boundaries. Instead, the reactivation appears to be due to more global reactivation of the entire surface. The microstructural connection to this global reactivation is still under study, but its connection to the solidification conditions of the AM 316L is clear. Post-test micrographs of AM 316L (Fig. 2c) show that attack preferentially takes place along cellular structure interiors and melt pool boundaries via attack of the cellular structure. As other works have shown that cellular interiors can be depleted of chromium, these observations are not surprising. This distinction in comparison to conventionally wrought material clearly shows that different microstructural features are responsible for reactivation in the case of AM stainless steel and must be considered in the analysis of these polarization curves.
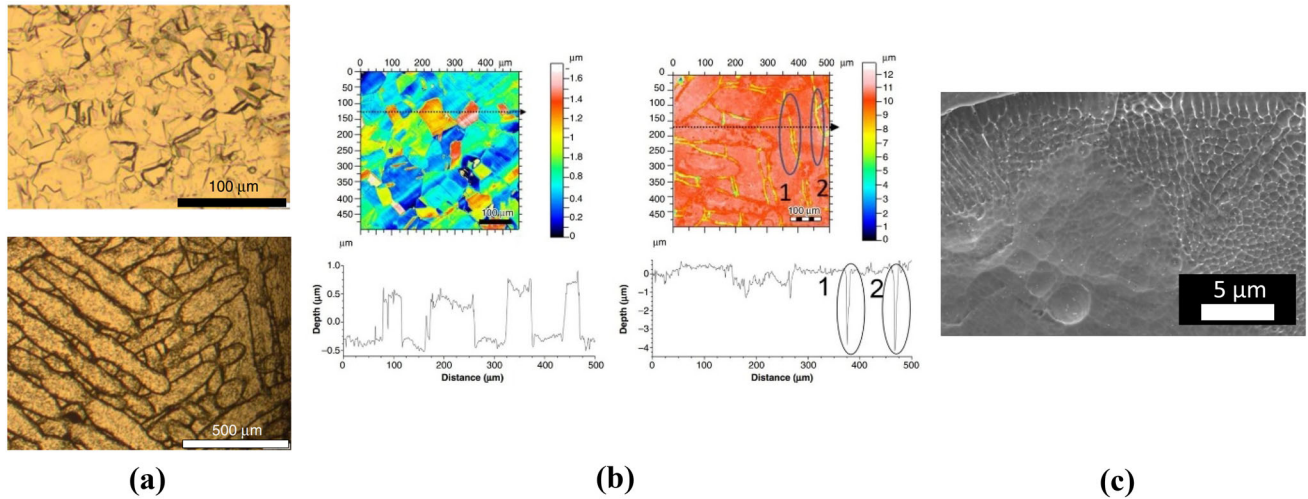
(a) **(b)** **(c)**

Fig. 1. (a) Optical micrograph of wrought (top) and LPBF (bottom) 316L after galvanostatic etching in 10 wt.% ammonium persulfate. (b) White light interferometry maps of wrought (left) and LPBF (right) 316L after galvanostatic etching in 10 wt.% ammonium persulfate. (c) Scanning electron micrograph of surface of LPBF 316L after galvanostatic etching in 10 wt.% ammonium persulfate. a. and b. were reprinted with permission from Ref 16.
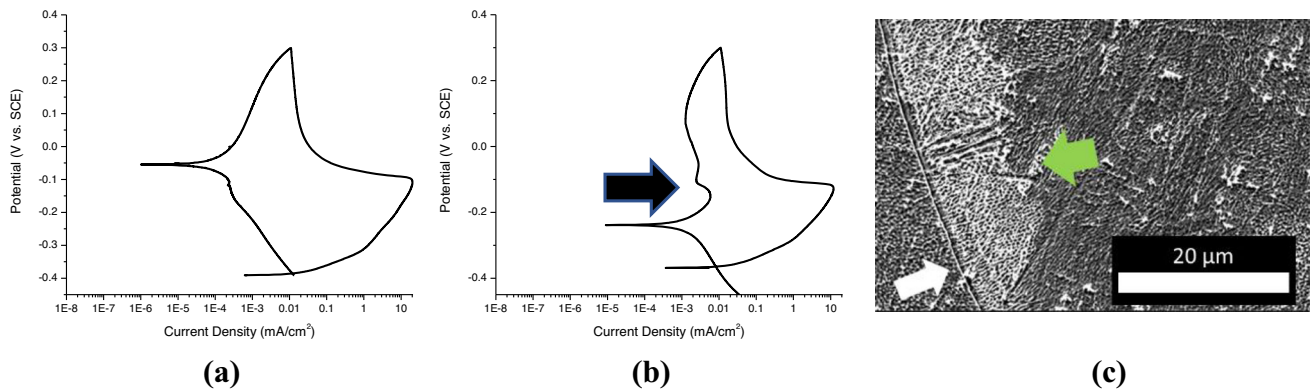

(a) **(b)** **(c)**

Fig. 2. Potentiodynamic scan of (a) wrought and (b) LPBF 316L in 1 M H_2SO_4 and 0.01 M KSCN. A black arrow shows anodic reactivation. (c) Post-test micrograph of LPBF material. A white arrow points to an area of melt pool boundary attack. A green arrow points to an area of cellular interior attack (Color figure online).

(a) **(b)**
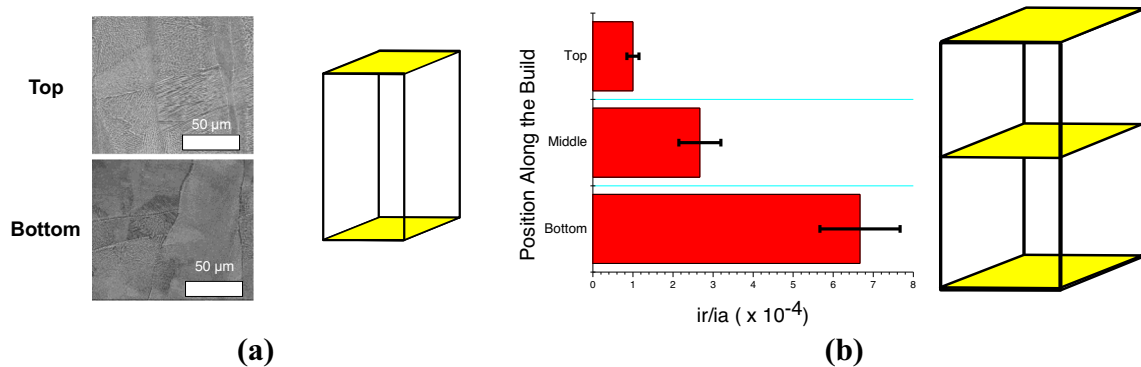
Fig. 3. (a) Galvanostatic etching of top and bottom surfaces of LPBF build. (b) DL-EPR i_r/i_a values for various positions along an LPBF build.

The reactivity of the microstructures formed during AM printing varies throughout the volume of a build. In Fig. 3, the microstructures revealed by etching of AM material show distinct differences in that near the top of the 60-mm-tall prismatic build and that near the bottom, with a concomitant difference in the level of reactivation measured by DL-EPR (Fig. 3b). Recent work has shown that the

extent of reactivation is not only a function of position in the build, but its presence is connected to the LPBF build parameters (power, scanning speed, hatch, thickness), with those that lead to keeping the solidifying melt pool in the liquid state longer acting to reduce the amount of measured reactivation, most likely due to the lower degree of elemental segregation, although proof of that speculation is currently being pursued.

Although the desire of the engineering community is to use AM materials in the as-printed condition, in some cases porosity needs to be removed, with the most popular way of removing porosity being hot isostatic pressing (HIP), a process widely used in powder metallurgy for densification. For 316L, the standard process for HIP involves heating to 675°C, holding there for 24 h, then cooling via a water quench. Limited studies to date show that standard HIP processing of AM 316L can create reactivation at the grain boundaries, as shown in Fig. 4a, akin to sensitization. In this AM material, reactivation is not observed in the as-printed condition, but after HIP processing, reactivation is observed that appears to be due to the formation of precipitates at the grain boundaries. Although the HIP process can lead to the elimination of pores that can be consequential from a pitting corrosion perspective, the DL-EPR and micrographs do raise concerns in terms of intergranular corrosion (Fig. 4a). Powder metallurgy 316L does not suffer this type of sensitization upon HIP processing, so there must be something inherent in the LBPF process that creates nucleation sites that grow during the HIP processing. Identification and characterization of the precipitates in Fig. 4a is currently underway.

Figure 4b shows that LPBF 316L can also be more susceptible to sensitization than wrought 316L after exposure to elevated temperatures, with higher values of DOS measured for the AM material at shorter times. Interestingly, other standard tests for intergranular corrosion that rely on mass loss (e.g., ASTM A262 Practice C, the Huey Test) have been found to be not appropriate for AM stainless steels due to the elongated, interlocking nature of the grains in these materials. That grain geometry greatly inhibits grain fallout after grain boundary corrosion has occurred, unlike more equiaxed wrought stainless steels whose mass loss is quite sensitive to grain boundary attack. This situation represents a challenge for the certification of AM stainless steels for service, as susceptibility to intergranular attack may not be detected using standard tests.

It should be noted that, as with the global reactivation, changes in process parameters can impact the extent of sensitization. In some cases, the AM 316L can be substantially more resistant to sensitization than the wrought material.[16] Metallurgical factors such as composition, grain size, and grain character have been shown to influence resistance to sensitization in wrought material.[24,27–30] Those observations provide guidance on aspects to investigate that influence of the AM process on sensitization resistance.

Further experiments have also shown that grain boundary corrosion is not the only mode of localized corrosion that should be considered in the case of LPBF 316L that has been exposed to sensitization conditions. Figure 5a shows the DL-EPR curve and post-test micrograph for LPBF 316L that has been exposed to 675°C for 24 h. This exposure is one that leads to grain boundary sensitization in wrought 316L. Not surprisingly, one finds reactivation in the reverse scan, indicating a non-zero DOS. However, the post-test micrograph of the surface (Fig. 5b) shows that intergranular corrosion is not the only form of localized corrosion that exists, unlike for wrought material. Accelerated attack within the core of cellular structures occurs in addition to intergranular corrosion. It seems that the cellular structures are retained after exposure to this temperature/time combination. The reactivation current is due to the combination of the attack at the grain boundaries due to the formation of the chromium carbides and the global reactivation

(a)   **(b)**

Fig. 4. (a) False-color profilometry and DL-EPR results for AM 316L as-printed and after HIP processing, (b) degree of sensitization via DL-EPR and micrographs of surfaces after attack for LPBF and wrought 316L as a function of time at 675°C.

Fig. 5. (a) DL-EPR curve for LPBF 316L that has been exposed to a temperature of 675°C for 24 h (a black arrow emphasizes anodic reactivation), and (b) the accompanying post-test scanning electron micrograph. A green arrow points to an area of intergranular attac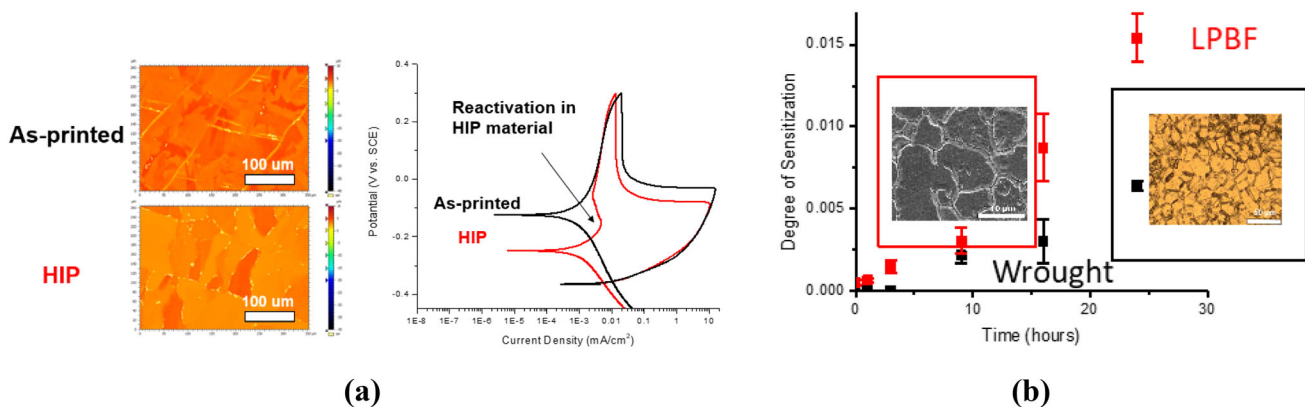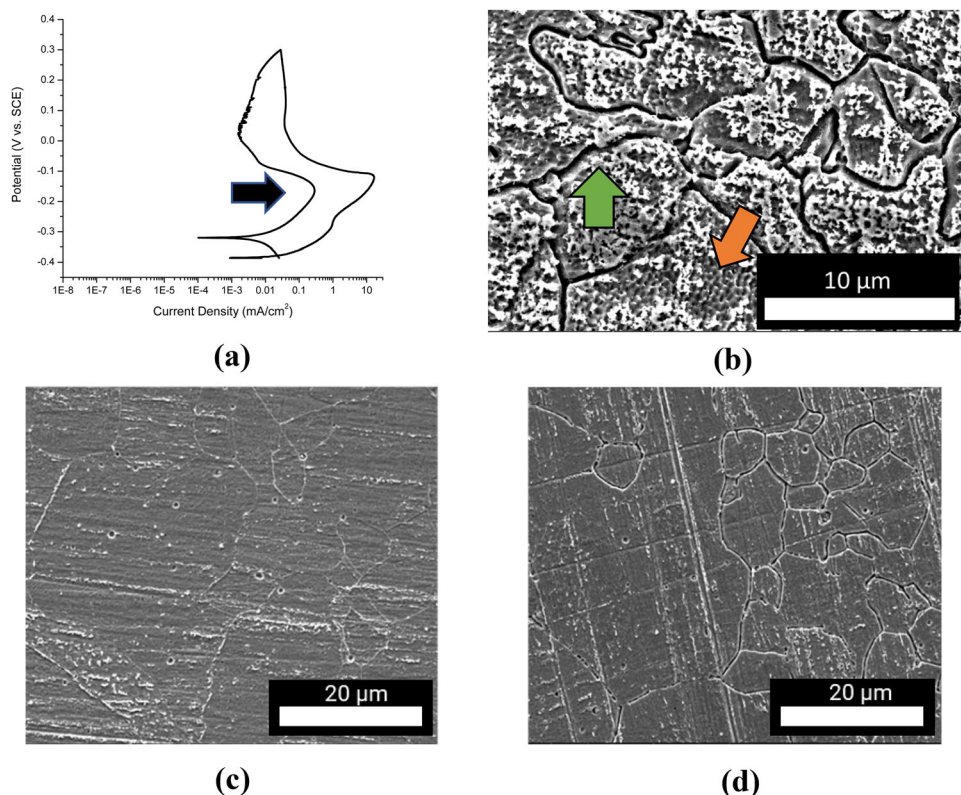k. An orange arrow points to an area of cellular attack. (c) Post-test scanning electron micrograph for LPBF material that has been solution annealed at 1100°C for 1 h, and (d) LPBF material that has been solution annealed at 1100°C for 1 h followed by an exposure at 675°C for 9 h (Color figure online).

described for the as-printed material above. Figure 5c shows the post-test micrograph of LPBF 316L that has been annealed at 1100°C. Although pores from the AM process can be seen, attack through cellular interiors is not seen due to the homogenization provided by the stress anneal. Instead, crystallographic attack is seen in the case of solution annealed material. Figure 5d shows that when solution annealed LPBF material has been exposed to 675°C for 9 h, classic intergranular attack is observed due to the sensitization process. In the case of the sensitized and non-sensitized annealed LPBF material, reactivation was not observed in the DL-EPR and the behavior matches that of Fig. 2a. Deconvolution of the relative contributions is challenging, if even possible, demonstrating that DOS from DL-EPR of AM materials needs to be interpreted with care whether in the as-printed state or after exposure to sensitizing conditions.

HEAT-TREATMENT EFFECTS ON AM VS CAST AL-10SI-MG

Whereas heat treatments are rarely applied to wrought austenitic stainless steels such as 316L, they are quite commonly applied to cast aluminum alloys such as A360. The heat treatments act to create the combination of mechanical properties and dimensional stability needed for the intended application. Due to its compatibility with the LPBF process requirements, such as flowability of the powder, Al-10Si-Mg has been the focus of a great deal of AM research.[31] AM processing has been shown to increase the yield and ultimate tensile strengths as well as the hardness relative to cast A360.[31] Corrosion studies of AM Al-10Si-Mg have come to mixed conclusions regarding its resistance to full immersion damage, with the observed selective attack of the primary alpha phase being attributed to the galvanic action of the Si network that forms. In practice, most components made from these alloys are more likely to be exposed to atmospheric conditions in which a thin film of electrolyte is present, or cyclic conditions of wetting and drying. ASTM G85-A2 has been widely used to assess the resistance of aluminum alloys to such exposures.

Figure 6. compares the corrosion damage produced by exposure to a modified G85-A2 test process for 31 days[31] of cast material and AM material under three heat treatments: as-produced, -T5, and -T6. Although A360 is not normally used in these tempers, the goal of this study was to scope the changes in microstructure and corrosion behavior that occur upon heat treatment. It is apparent that
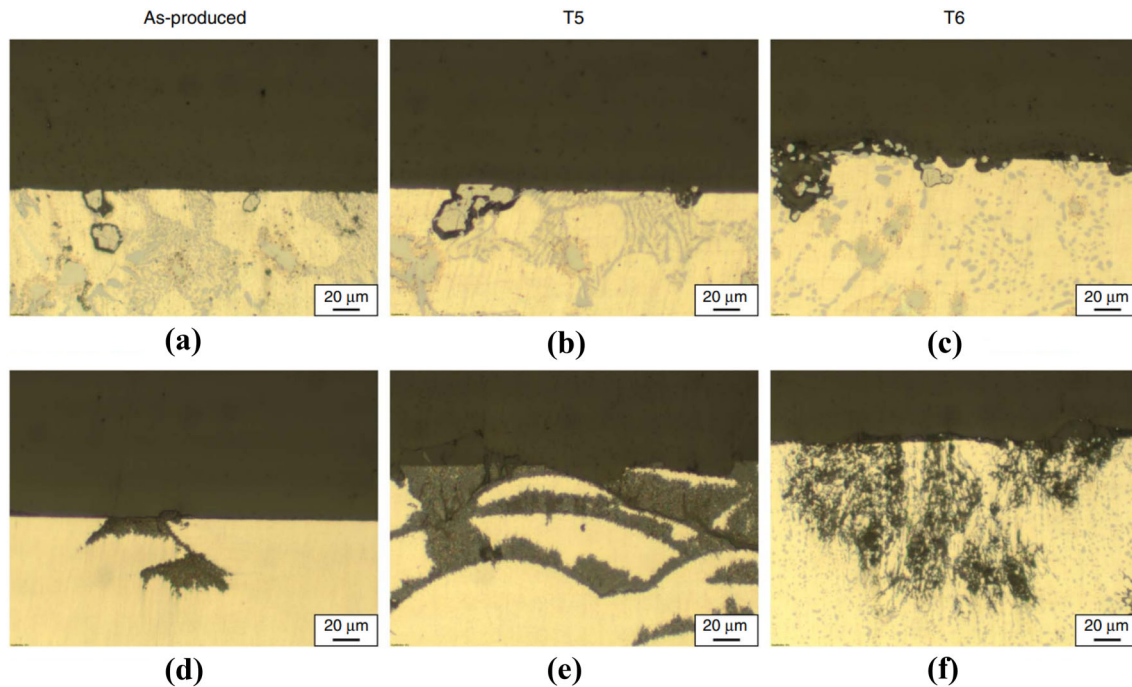
Fig. 6. Representative optical images of damage after exposure to modified ASTM G85-A2 testing for 31 days for cast A360 (a–c) and AM Al-10Si-Mg (d–f). Reprinted with permission from [31].

the cast microstructure is far coarser, with large grains of primary alpha aluminum surrounded by a eutectic structure of nearly pure silicon and alpha aluminum. The attack follows the outside of large silicon particles with limited propagation into the alpha-aluminum grains. In contrast, the AM materials damage follows the MPB with significant propagation into the interiors of the melt pool for the as-printed and -T5 temper materials, with more extensive attack in the -T6 temper as the MPBs have disappeared and a coarser microstructure has developed, more akin to the A360-T6 material. In the as-printed and -T5 temper, the AM Al10SiMg shows little second phase in the bulk of the melt pools at this magnification.

Higher magnification imaging of the as-printed and -T5 temper shows that there exists a fine-scale network of Si surrounding solid solution alpha interiors, as shown in Fig. 7. The attack from the G85 exposure is of the solid solution phase, with the Si network remaining, although the fineness of the Si network makes it susceptible to mechanical cracking and loss from the surface. Similar imaging on the AM-T6 material shows a similar attack morphology: dissolution of the alpha phase and retention of the Si, although the Si phase is now primarily fine particles.

Electrochemical testing has shown that the -T6 temper in the cast material increases its corrosion rate while lowering its corrosion potential, indicating an acceleration of the anodic kinetics, likely due to the substantial coarsening of the Si eutectic leading to larger areas of alpha phase as seen in Fig. 6c. In contrast, the -T6 temper for the AM
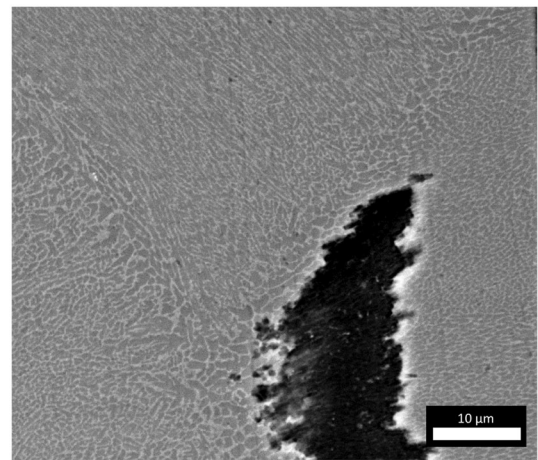

Fig. 7. High-magnification electron micrograph of propagation front of corrosion in AM Al-10Si-Mg-T5 after modified G85-A2 testing for 31 days. Note the lighter gray Si network defining the path of the corrosion of the darker gray alpha phase. Adapted with permission from [31].

material has a decrease in its corrosion rate, but an increase in corrosion potential, indicating that a decrease in anodic kinetics dominates. In addition, although there is little change in either the pitting potential or repassivation potential of the cast material upon application of the -T6 temper, there is a large decrease in the pitting potential for the AM material upon application of the -T6 temper, and a large increase in the repassivation potential.[31] Although the underlying microstructural reasons for these changes remain to be elucidated,

they starkly show that the corrosion behavior of AM materials can be dramatically different than their conventionally manufactured brethren.

It has been proposed that the corrosion behavior of these aluminum alloys is controlled by the galvanic couple formed between the alpha matrix and the Si second phase.[32,33] There is no doubt a large driving force in such a galvanic couple, with the open circuit potentials of the Si and actively corroding aluminum differing by more than 1 V in chloride solutions. Nonetheless, galvanic corrosion rates are determined by kinetics as well as driving forces. The polarization curves in Fig. 8. demonstrate that the nearly pure silicon of the cellular boundaries does not represent a kinetically strong cathode. The SiO_2 film on the silicon surface is a poor catalyst for either oxygen reduction or hydrogen evolution. Thus, although the aluminum is susceptible to high-rate corrosion upon polarization, the Si network simply cannot provide sufficient current. A cellular boundary to cellular interior area ratio would need to be $\sim$1000:1 to have a significant effect. From the microstructures shown in Fig. 6, it is obvious that the alpha phase of the interior of the cellular structures is actually larger in area than the surrounding Si. Thus, while attractive as an explanation, the galvanic argument previously suggested[31] cannot provide a reasonable rationalization. Instead, we believe[31] that the Si network actually serves to impede the dissolution of the aluminum. A more likely role for the Si network is its role as a barrier to corrosion propagation. Being inert, the more effectively it can segregate areas of alpha phase, the slower the propagation of the attack through the microstructure becomes. More open Si structures such as those that occur in the -
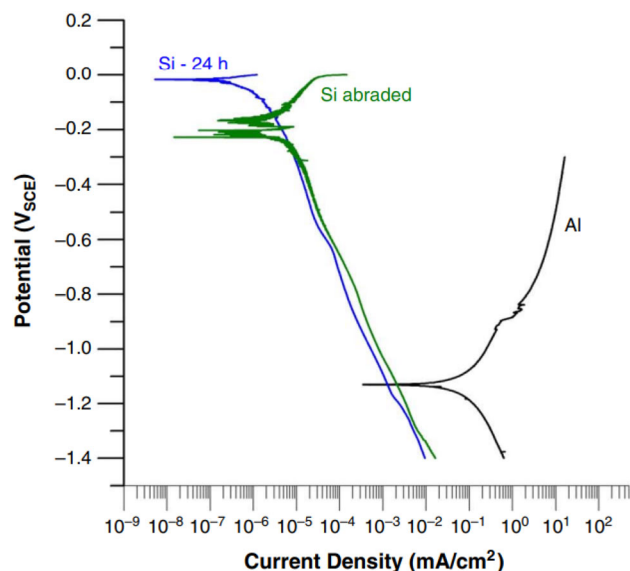

Fig. 8. Polarization curves for p-type Si, as-received and abraded, and Al activated by a potentiostatic hold at elevated potential before scanning in the negative direction in 5.4 M NaCl, pH 1.21 at 49°C, a solution composition expected for the G85-A2 test solution at 70% RH. Reprinted with permission from Ref. 30.

T6 temper would likely lead to higher corrosion rates as the dissolution of the alpha phase, as well as the transport of the dissolved ions from the interface, would be less impeded by the Si network.

CONCLUSION

With the increasing implementation of AM metallic materials into engineering structures, the need increases for a better understanding of the impact of AM processing and post-AM processing on the resistance of these alloys to corrosion when exposed to service atmospheres. Recent work comparing the response of AM 316L and wrought 316L to standard tests for intergranular corrosion shows that blind application of these tests can lead to either overestimation or underestimation of the susceptibility. The complicated nanostructures and microstructures created by the extremely rapid solidification that occurs during LPBF is at the root of these differences. Changes in processing parameters change the lifetime of the liquid state of the material as well as its local solidification rate, leading to changes in the spatial distribution of critical alloying elements. The results of both electrochemical tests such as DL-EPR and mass loss tests such as the Huey test for austenitic stainless steel sensitization require careful interpretation along with post-test examination of the damage morphology. Aluminum alloys based on A360 but manufactured via AM are also susceptible to different dependencies of corrosion rate on heat treatment due to differing morphologies of the Si second phase impacting its ability to shelter the more susceptible alpha phase from dissolution. Taken together, these results point to a glaring need for the development and validation of accelerated corrosion tests that are applicable to both AM metallic alloys and their conventionally manufactured counterparts.

CONFLICTS OF INTEREST

The authors declare that they have no conflicts of interest.

REFERENCES

1. H. Sahasrabudhe, S. Bose, and A. Bandyopadhyay, *Advances in Laser Materials Processing* (Second Edition), (Woodhead Publishing, Cambridge, 2018) pp. 507–539. https://doi.org/10.1016/B978-0-08-101252-9.00017-0.
2. D. Herzog, V. Seyda, and E. WyciskEmmelmann, *Acta Mater.* 371–392. https://doi.org/10.1016/j.actamat.2016.07.019 (2016).

3. P. Hanzl, M. Zetek, T. Bakša, and T. Kroupa, *Procedia Eng.* 1405–1513. https://doi.org/10.1016/j.proeng.2015.01.510 (2015).

4. D.D. Gu, W. Meiners, K. Wissenbach, and R. Poprawe, *Int. Mater. Rev.* 133–164. https://doi.org/10.1179/1743280411Y.0000000014 (2012).

5. K.M. Mantrala, M. Das, V.K. Balla, C.S. Rao, and V.V.S. KesavaRao, *Front. Mech. Eng.* https://doi.org/10.3389/fmech.2015.00002 (2015).

6. H. Hack, R. Link, E. Knudsen, B. Baker, and S. Olig, *Addit. Manuf.* 105–115. https://doi.org/10.1016/j.addma.2017.02.004 (2017).

7. E. Liverani, S. Toschi, L. Ceschini, and A. Fortunato, *J. Mater. Process. Technol.* 255–263. https://doi.org/10.1016/j.jmatprotec.2017.05.042 (2017).

8. F. Bartolomeu, M. Buciumeanu, E. Pinto, N. Alves, O. Carvalho, F.S. Silva, and G. Miranda, *Addit. Manuf.* https://doi.org/10.1016/j.addma.2017.05.007 (2017).

9. K.N. Amatoa, S.M. Gaytana, L.E. Murra, E. Martinez, P.W. Shindo, J. Hernandez, S. Collins, and F. Medina, *Acta Mater.* 2229–2239. https://doi.org/10.1016/j.actamat.2011.12.032 (2012).

10. G. Sander, J. Tan, P. Balan, O. Gharbi, D.R. Feenstra, L. Singer, S. Thomas, R.G. Kelly, J.R. Scully, and N. Birbilis, *Corrosion* 1318–1350. https://doi.org/10.5006/2926 (2018).

11. S. Cheruvathur, E.A. Lass, and C.E. Campbell, *JOM.* 930-942. https://doi.org/10.1007/s11837-015-1754-4 (2016).

12. G. Sander, S. Thomas, V. Cruz, M. Jurg, N. Birbilis, X. Gao, M. Brameld, and C.R. Hutchinson, *J. Electrochem. Soc.* C250. https://doi.org/10.1149/2.0551706jes (2017).

13. M. Ziętala, T. Durejko, M. Polański, I. Kunce, T. Płociński, W. Zieliński, M. Łazińska, W. Stępniowski, T. Czujko, K.J. Krzysztof, J. Kurzydłowski, and Z. Bojar, *Mater. Eng., A Sci.* 1–10. https://doi.org/10.1016/j.msea.2016.09.028 (2016).

14. X. Lou, P.L. Andresen, and R.B. Rebak, *J. Nucl. Mater.* 182–190. https://doi.org/10.1016/j.jnucmat.2017.11.036 (2018).

15. D. Kong, C. Dong, X. Ni, and X. Li, *npj Mater Degrad.* 24. https://doi.org/10.1038/s41529-019-0086-1 (2019).

16. D.A. Macatangay, S. Thomas, N. Birbilis, and R.G. Kelly, *Corrosion* 153–157. https://doi.org/10.5006/2723 (2018).

17. J.R. Trelewicz, G.P. Halada, O.K. Donaldson, and G. Manogharan, *JOM* 850–859. https://doi.org/10.1007/s11837-016-1822-4 (2016).

18. G.N. Nigon, O.B. Isgor, and S.J. Pasebani, *J. Electrochem. Soc.* 167. https://doi.org/10.1149/1945-7111/abc5dd (2020).

19 A. Yadollahi, N. Shamsaei, S.M. Thompson, and D.W. Seely, *Mater. Eng., A Sci.* 171–183. https://doi.org/10.1016/j.msea.2015.07.056 (2015).

20. A262, A. S. *Standard Practices for Detecting Susceptibility to Intergranular Attack in Austenitic Stainless Steels.* ASTM Int. West Conshohocken, PS 01, 1–17 (2014). https://doi.org/10.1520/A0262-02AE03.

21. Y. Zhong, L. Liu, S. Wikman, D. Cui, and Z. Shen, *J. Nucl. Mater.* 170–178. https://doi.org/10.1016/j.jnucmat.2015.12.034 (2016).

22 S. Gao, Z. Hu, M. Duchamp, P.S. Sankara Rama Krishnan, S. Tekumalla, X. Song, and M. Seita, *Acta Mater.* 366–377. https://doi.org/10.1016/j.actamat.2020.09.015 (2020).

23. M. Laleh, A.E. Hughes, W. Xu, N. Haghdadi, K. Wang, P. Cizek, I. Gibson, and M.Y. Tan, *Corros. Sci.* 108189. https://doi.org/10.1016/j.corsci.2019.108189 (2019).

24. M. Terada, M. Saiki, I. Costa, and A.F. Padilha, *J. Nucl. Mater.* 40–46. https://doi.org/10.1016/j.jnucmat.2006.06.010 (2006).

25. T. Amadou, H. Sidhom, and C. Braham, *Metall. Mater. Trans. A* 3499–3513. https://doi.org/10.1007/s11661-004-0187-4 (2004).

26. M. Momeni, M.H. Moayed, and A. Davoodi, *Corros. Sci.* 2653–2660. https://doi.org/10.1016/j.corsci.2010.04.015 (2010).

27. A.A. Pardo, M.C. Merino, A.E. Coy, F. Viejo, M. Carboneras, and R. Arrabal, *Acta Mater.* 2239–2251. https://doi.org/10.1016/j.actamat.2006.11.021 (2007).

28. A.Y. Chen, W.F. Hu, D. Wang, Y.K. Zhu, P. Wang, J.H. Yang, X.Y. Wang, J.F. Gu, and J. Lu, *Scr. Mater.* 264–268. https://doi.org/10.1016/j.scriptamat.2016.11.032 (2017).

29. A.S.M. Paroni, N. Alonso-Falleiros, and R. Magnabosco, *Corrosion* 1039–1046. https://doi.org/10.5006/1.3278231 (2006).

30. H. Sidhom, T. Amadou, H. Sahlaoui, and C. Braham, *Metall. Mater. Trans. A* 1269–1280. https://doi.org/10.1007/s11661-007-9114-9 (2007).

31. G.W. Kubacki, J.P. Brownhill, and R.G. Kelly, *Corrosion* 1527–1540. https://doi.org/10.5006/3318 (2019).

32. M. Cabrini, F. Calignano, P. Fino, S. Lorenzi, M. Lorusso, D. Manfredi, C. Testa, and T. Pastore, *Materials* 1051. https://doi.org/10.3390/ma11071051 (2018).

33. R.I. Revilla, J. Liang, S. Godet, and I.D. Graeve, *J. Electrochem. Soc.* C27. https://doi.org/10.1149/2.0461702jes (2016).